UNIVERSITY OF CALIFORNIA
SANTA CRUZ

THE MAGNETOHYDRODYNAMICS OF THE SOLAR TACHOCLINE

A dissertation submitted in partial satisfaction of the
requirements for the degree of

DOCTOR OF PHILOSOPHY

in

APPLIED MATHEMATICS AND STATISTICS

by

Luis Antonio Acevedo-Arreguín

June 2012

The Dissertation of Luis Antonio Acevedo-Arreguín
is approved:

Professor Pascale Garaud, Chair

Professor Nicholas H. Brummell

Professor Gary A. Glatzmaier

Dr. Tyrus Miller
Vice Provost and Dean of Graduate Studies

Table of Contents

List of Figures vi

List of Tables xiii

Abstract xiv

Dedication xv

Acknowledgments xviii

Introduction 1

I Theoretical Framework 5

1 The Structure of the Sun 6
1.1 Solar oscillations and Helioseismology . . . 6
1.1.1 The solar rotation profile . . . 7
1.2 The solar tachocline . . . 8
1.2.1 The thickness of the tachocline . . . 8
1.2.2 Mixing in the tachocline . . . 9

2 Hydrodynamic Modeling 12
2.1 The Spiegel and Zahn's model . . . 12
2.1.1 The hydrodynamics equations . . . 13
2.1.2 Tachocline spreading . . . 16
2.1.3 Anisotropic turbulent viscosity . . . 18
2.2 The problem with the Spiegel and Zahn model . . . 19

3 Hydromagnetic Modeling 21
3.1 First models of the solar tachocline . . . 22
3.2 The Gough and McIntyre model . . . 23
3.2.1 The MHD equations . . . 24
3.2.2 The tachocline force balance . . . 24
3.2.3 The tachopause force balance . . . 25
3.2.4 Approximate solutions for the tachopause . . . 26
3.3 Numerical models of the Radiative Zone . . . 27

3.3.1 Simulations with no magnetic confinement 27
3.3.2 Simulations with magnetic confinement 29

II Model Development 31

4 Hydrodynamics of the Tachocline: Analytical Solutions 34
4.1 Introduction 34
4.2 A Cartesian model 37
4.2.1 Model setup 37
4.2.2 Model equations 38
4.2.3 The unstratified case 42
4.2.4 The stratified case 56
4.3 A "solar" model 64
4.3.1 Description of the model 64
4.3.2 The weakly stratified case 68
4.3.3 The stratified case 69
4.4 Implications of this work for solar and stellar mixing 71
4.4.1 Context for stellar mixing 71
4.4.2 Qualitative summary of our results 74
4.4.3 Applications to the Sun and other stars 76

5 Magnetohydrodynamics: Numerical Solutions 83
5.1 The Model 85
5.1.1 The background state 85
5.1.2 The model equations 85
5.1.3 The diffusivity profiles 86
5.1.4 The stratification parameter σ and the selection of N^2 87
5.1.5 Non-dimensional equations 89
5.1.6 The forcing terms 91
5.1.7 Boundary conditions 93
5.1.8 The Newton-Raphson-Kantorovich method 96
5.2 Model sensitivity to turbulent magnetic diffusivity in the convection zone 97
5.3 Fiducial model results 101
5.3.1 A first glimpse of the solar tachocline 102
5.3.2 Thermal wind balance in the radiative interior 107
5.3.3 The azimuthal force balance in the tachocline 107
5.3.4 Estimating the thickness of the tachopause and the tachocline 110
5.3.5 Magnetic confinement 112
5.3.6 Toroidal field 113
5.4 Numerical experiments at different parameter regimes 114
5.4.1 The effect of thermal diffusivity 114
5.4.2 The effect of magnetic diffusivity 117
5.4.3 Relationship to previous models 122

6 Conclusions **131**
6.1 Our fiducial model: The importance of parameter selection . . . 132
6.2 Our fiducial model: the internal magnetic field . . . 133
6.3 The tachopause-tachocline structure and its underlying assumptions . . . 134

A Computing the mean rotation rate Ω_0 of the solar interior **148**

B Derivation of the radial component for the background magnetic field **149**

C Chebyshev polynomials **151**
C.1 Integration and differentiation of $T_n(\mu)$ . . . 151
C.2 An example: Differentiation of u_ϕ . . . 153

D How to plot the potential magnetic field **154**
D.0.1 Differentiation of Chebyshev Modes . . . 155
D.0.2 Integration of Chebyshev modes . . . 156

E The Chebyshev transformation of the integrated induction equation **162**
E.0.3 The integrated induction equation . . . 162
E.0.4 Chebyshev expansion of the fields . . . 163
E.0.5 Projection onto the radial direction . . . 165

F The Force Balances in the Tachocline **168**
F.1 Force balances from the momentum equation . . . 168
F.1.1 Coriolis Force . . . 169
F.1.2 Advection term . . . 170
F.1.3 Lorentz force . . . 172
F.1.4 Gyroscopic Pumping term . . . 173
F.1.5 Viscous stresses . . . 174
F.2 Balances from the vorticity equation . . . 179
F.2.1 Coriolis term . . . 180
F.2.2 Advection term . . . 181
F.2.3 Thermal Wind, Stratification, and Baroclinicity terms . . . 182
F.2.4 Lorentz term . . . 182
F.2.5 Gyroscopic Pumping term . . . 184
F.2.6 Viscous stress term . . . 185
F.2.7 High order derivatives of expressions involving $T_{2n-1}(\mu)$ . . . 191

G `NRK_ParaSol`: The User's Guide **194**
G.1 Description of the package . . . 194
G.1.1 Installation . . . 195
G.1.2 Directory `Workdir` . . . 195
G.1.3 User-defined subroutines . . . 197
G.2 Examples . . . 198
G.2.1 Example 1 . . . 198
G.2.2 Example 2 . . . 202
G.2.3 Example 3 . . . 206
G.2.4 Example 4 . . . 209

List of Figures

0.1 The rotational profile of the Sun as inferred by Helioseismology (Schou et al. , 1998; Christensen-Dalsgaard and Thompson , 2007). 2

0.2 Spatial temporal histogram of the solar magnetic activity showing cycles of approximately eleven years (from NASA). Prediction of solar weather from these observations becomes complicated as cycles approach their end because determinations of the minimum are not sufficiently accurate yet. 3

1.1 The rotational profile of the Sun as inferred by statistical analysis of the solar oscillation frequencies (Schou et al. , 1998) using 4 different types of kernels. . . 8

1.2 The solar rotation profile at 5 different latitudes (from Howe *et al.*, 2000), where a sharp transition of the angular velocity $\Omega/2\pi$ is observed around $0.70R_{\odot}$. The region where this change occurs is the solar tachocline. 9

1.3 Difference (symbol points) between helioseismic inferences of sound speed and values computed with Christensen-Dalsgaard's Model S are compared with the difference (solid line) between helioseismic observations and values computed by the model by Elliot and Gough (1999), which includes a well-mixed tachocline. . 10

2.1 The evolution of the tachocline thickness h depends on the form of the function $t^{1/n}$. For $n = 4$, the blue curve models the hyperviscous spreading (as a function of $t^{1/4}$), whereas for $n = 2$, the red curve models the viscous spreading (as a function of $t^{1/2}$). 17

3.1 This picture of a meridional quadrant of the Sun shows the tachocline and adjacent regions according to Gough and McIntyre's theory. Here, we see meridional flows generated inside the convection zone (the orange region), and some of them enter the tachocline (green) at high latitudes. These meridional flows are deflected by the magnetic field in a diffusive boundary layer (blue) located in the bottom of the tachocline, and then return to the convection zone at mid-latitudes. In the meantime, the radiative region (pink) remains rotating as a solid body due to the poloidal field (red lines) trapped there by the meridional circulation in the tachocline, a mechanism in place for most of the Sun's lifetime. 22

3.2 Magnetic field confinement (left lower panel) caused by flows penetrating the radiative region (left upper panel), obtained numerically by Garaud and Garaud (2008). The temperature perturbations and the angular velocity are shown in the right, upper and lower panel, respectively. 30

4.1 Cartesian model geometry and intended correspondence with the spherical case. The shaded area marks the convective region, where forcing is applied. The $y = 0$ and $y = \pi/2$ lines mark the "poles" and the "equator". The system is assumed to be periodic with period π in the $y-$direction. 38
4.2 Numerical (solid) and analytical (dashed) solutions for $|\hat{w}(z)|$, in the case of a stress-free bottom boundary. From the uppermost to lowermost curves, $E_\nu = 10^{-3}$, 10^{-4}, 10^{-5} and 10^{-6} respectively, confirming the analytical scaling that $\hat{w}(z) \propto \mathrm{E}_\nu z$ in the radiative zone while $\hat{w}(z)$ becomes independent of E_ν in the convection zone. These solutions were obtained with forcing defined by the parameters $\Delta = 10^{-4}$, $\Lambda = 10$, $U_0(z) = S(z - h)$ and $S = 1$. 48
4.3 2D visualization of the flow for $E_\nu = 10^{-4}$, in the case of a stress-free bottom boundary. Shown as solid and dotted line respectively are linearly spaced streamlines of counter-clockwise and clockwise meridional flows. As predicted, the flows appear to return entirely within the convection zone and carry a negligible mass flux into the radiative zone. Meanwhile the azimuthal velocity ($\hat{u}$) as displayed in the filled contours is constant along the rotation axis ($z-$axis) below the interface ($z = h = 0.7$), but is strongly sheared at the interface. This solution was obtained with forcing defined by the parameters $\Delta = 10^{-4}$, $\Lambda = 10$, $U_0(z) = S(z - h)$ and $S = 1$, as in Figure 4.2. 49
4.4 Numerical (solid) and analytical (dashed) solutions for $\hat{u}(z)$, in the case of a stress-free bottom boundary. From the lowermost to uppermost curves, $E_\nu = 10^{-3}$, 10^{-4}, 10^{-5} and 10^{-6} respectively, confirming that $\hat{u}(z)$ tends to a constant in the radiative zone, while sustaining a finite discontinuity at the radiative-convective interface ($z = h = 0.7$). These solutions were obtained with forcing defined by the parameters $\Delta = 10^{-4}$, $\Lambda = 10$, $U_0(z) = S(z - h)$ and $S = 1$, as in Figure 4.2. 50
4.5 Numerical (solid) and analytical (dashed) solutions for $|\hat{w}(z)|$, in the case of a no-slip bottom boundary. From the uppermost to lowermost curves (as seen in the radiative zone), $E_\nu = 10^{-3}$, 10^{-4}, 10^{-5} and 10^{-6} respectively, confirming the analytical scaling that $\hat{w}(z) \propto \mathrm{E}_\nu^{1/2}$ in the radiative zone while $\hat{w}(z)$ becomes independent of E_ν in the convection zone. These solutions were obtained with forcing defined by the parameters $\Delta = 10^{-4}$, $\Lambda = 10$, $U_0(z) = S(z - h)$ and $S = 1$, as in Figure 4.2. For comparison, the previous simulations with stress-free bottom boundary, for the same parameters, are shown as dotted lines. 53
4.6 The same as for Figure 4.3 but for no-slip boundary conditions. The Ekman layer near the lower boundary is clearly visible. For ease of comparison, the same streamlines are shown in the two plots. The two figures illustrate how the nature of the lower boundary condition influences the mass flux through the radiative zone. 54
4.7 Comparison of numerical simulations (solid lines) with analytical prediction (dashed line) for a no-slip bottom boundary, for $\mathrm{E}_\nu = 10^{-6}$, and forcing functions defined with $\Lambda = 10$, $S = 0$ and $U_0(h) = 1$. The three numerical solutions are obtained for various values of the overshoot layer depth: from lowermost to uppermost curves (as seen in the convective zone), $\Delta = 10\mathrm{E}_\nu^{1/2}$, $\mathrm{E}_\nu^{1/2}$, and $0.1\mathrm{E}_\nu^{1/2}$. The analytical solution assumes an infinitely thin overshoot layer and is therefore independent of Δ. Note that the analytical solution in the convection zone is only a good approximation to the true solution if $\Delta \ll \mathrm{E}_\nu^{1/2}$. The overall scalings in the radiative zone, however, are preserved. 57

4.8 Numerical solutions of (4.9) with the following parameters: $\Delta = 0.01$, $\Lambda = 10$, $S = 0$, $U = 1$, Pr $= 0.01$ and $D_0 = 10$. Stress-free bottom boundary conditions are used. The solid lines correspond to the "strongly" stratified case with $\mathrm{Ro_{rz}}$ $= 10$, with $\mathrm{E}_\nu = 10^{-5}$ and 10^{-6} for the top and bottom curves respectively. The dashed lines correspond to the "weakly" stratified case, with $\mathrm{Ro_{rz}} = 1$, with $\mathrm{E}_\nu = 10^{-5}$ and 10^{-6} for the top and bottom curves respectively. Note that for $k = 2$, λ_2 is simply equal to $\mathrm{Pr}^{1/2}\mathrm{Ro_{rz}}$. For comparison, the unstratified case ($\mathrm{Ro_{rz}} = 0$) is shown as dotted lines. At these parameters and with these boundary conditions, $\mathrm{Ro_{rz}} = 1$ already belongs to the weakly stratified limit. 62

4.9 This figure shows the power α in the expression $\hat{w} \propto \mathrm{E}_\nu^\alpha$, as a function of λ_2 (see main text for detail). In the weakly stratified limit, $\alpha \to 1/2$ while in the strongly stratified limit $\alpha \to 1$ as predicted analytically. This calculation was done for no-slip boundary conditions, and the following parameters were held constant: $\Delta = 0.01$, $\Lambda = 10$, $S = 1$, $U_0(h) = 1$, Pr $= 0.01$ and $D_0 = 10$ 63

4.10 Variation of λ_2/k $=\mathrm{Pr}^{0.5}N/\Omega_\odot$ in the Sun, as determined from Model S of Christensen-Dalsgaard *et al.* (1996). The Prandtl number Pr is calculated using Model S together with the formulae provided by Gough (2007) for the microscopic values of the viscosity $\hat{\nu}$ and the thermal conductivity κ_T (see also Garaud & Garaud, 2008). The inset zooms into the region near the base of the convection zone, which is the only region of the radiative zone where $\lambda_2 \leq 1$ (aside from $r \to 0$). 65

4.11 Vertical velocity at 80° latitude in units of $R_\odot\Omega_\odot$ for an artificially weakly stratified simulation (where $\bar{N}$ was uniformly divided by 10^3 everywhere). The solid lines show three simulations for $f = 10^{11}$, $f = 10^{10}$ and $f = 10^9$ (from top to bottom) for the no-slip case. These correspond to $\mathrm{E}_\nu = 2 \times 10^{-4}$, $\mathrm{E}_\nu = 2 \times 10^{-5}$ and $\mathrm{E}_\nu = 2 \times 10^{-6}$ at the base of the convection zone respectively, hence showing how $u_r \propto \mathrm{E}_\nu^{1/2}$. The dotted lines show simulations with stress-free boundary conditions for the same parameters, showing $u_r \propto \mathrm{E}_\nu$. In this calculation the overshoot depth Δ was selected to be $0.01R_\odot$, and $\Lambda = 10$. The value of D_0 is irrelevant in this very weakly stratified simulation. 69

4.12 Normalized angular velocity ($\tilde{\Omega}/\Omega_{\mathrm{eq}}$) and streamlines solutions to equations (4.34) for an artificially weak stratification (see Figure 4.11), and for $f = 10^9$ (corresponding to $\mathrm{E}_\nu = 2 \times 10^{-6}$ at the base of the convection zone). On the left, we show the solution with no-slip lower boundary conditions, and on the right the stress-free solution. Dotted lines represent clockwise flows, and solid lines counter-clockwise flows. In this calculation, the overshoot layer depth Δ was selected to be $0.01R_\odot$, and $\Lambda = 10$. The value of D_0 is irrelevant in this very weakly stratified simulation. 70

4.13 Vertical velocity (in units of $R_\odot\Omega_\odot$) in nine different simulations, at latitude 80°. The background stratification in each case is solar, but the position of the lower boundary is moved through the radiative zone from $0.65R_\odot$ to $0.35R_\odot$ and $0.1R_\odot$. The solid-line plots are for no-slip lower boundary conditions while the dotted lines are for stress-free lower boundary conditions. Three simulations are shown in each case: (from lowest to highest curve) for $f = 10^8$, $f = 10^9$ and $f = 10^{10}$ corresponding to $\mathrm{E}_\nu = 2 \times 10^{-7}$ to $\mathrm{E}_\nu = 2 \times 10^{-5}$. The logarithmic scale clearly shows that u_r scales with E_ν in the radiative zone in the stress-free cases for all values of r_{in} while in the no-slip case, r_{in} scales with E_ν if $r_{\mathrm{in}} < 0.6$, as expected from Figure 4.10. 71

5.1 This plot shows the diffusivity profiles for our fiducial model. The non-dimensional diffusivities in the radiative zone are $E_\nu = 5.0 \times 10^{-9}$, $E_\eta = 1.5 \times 10^{-8}$, and $E_\kappa = 5.0 \times 10^{-7}$. The diffusion parameters are kept constant inside the radiative region, and both the magnetic and thermal diffusivities are sharply increased in the convection zone. 88
5.2 This plot shows the computed buoyancy frequency profile needed to recover the solar σ profile in our numerical experiments. The plot shown here corresponds to non-dimensional diffusivities $E_\nu = 5.0\times10^{-9}$, $E_\eta = 1.5\times10^{-8}$, and $E_\kappa = 5.0\times10^{-7}$. 89
5.3 Plot of the magnetic field lines that result from the definition of an electric current density in the azimuthal direction near the core. 94
5.4 Effect of the location where the magnetic diffusivity becomes turbulent on the geometry of the magnetic field. Here we see, on the left panel, that when the magnetic diffusivity starts its turbulent behavior at the base of the convection zone, the steady-state resulting magnetic field is open. On the other hand, when the point of turbulent magnetic diffusivity shifts upward as a small distance as $\delta_{cz} = 0.002R_\odot$, the steady-state configuration of the magnetic field exhibits confinement at the base of the convection zone, as we see on the right panel. 98
5.5 This plots shows the magnetic Reynolds number, $\mathrm{Rm} = u_r L/\eta$, with $L = 0.10R_\odot$, as computed for the two cases illustrated in Figure 5.4. As we can see in this zoomed in region near the base of the convection zone, $\mathrm{Rm} \gg 1$ for the pre-confined field case (dotted line), which indicates that the flows are interacting with the magnetic field to a great extent within the convection zone. On the other hand, $\mathrm{Rm} \ll 1$ for the open case (dashed line), which corresponds to a situation where there is no flow-magnetic field interaction. 100
5.6 These plots show the mass flux at 80^o latitude for the two cases depicted in Figure 5.4, respectively. First, we see in the left panel how the downwelling mass flux remains high in amplitude even at very deep zones in the radiative zone. This happens when the magnetic field remains open at the radiative-convective interface. On the other hand, we see in the right panel how a pre-confined magnetic field at the radiative-convective interface affects the downwelling mass flux to the extent that the fluid in the radiative zone stops its burrowing at depths not so far from the interface. 101
5.7 This plots shows the steady-state solution of the equations governing the magnetohydrodynamics of the solar tachocline in our fiducial model (see Table 5.1). Starting from the top left panel and going clockwise, we show plots of the streamlines, temperature perturbations, angular velocity, and magnetic field lines. The top left panel shows that large-scale meridional flows generated in the convection zone are able to penetrate into the radiative interior at high latitudes. These downwelling flows are deflected by the internal magnetic field in the tachopause and, in turn, confine the field. This results in solid-body rotation of the radiative interior below the tachopause, as depicted in the bottom right panel. 103
5.8 This plot shows the magnetic Reynolds number, $\mathrm{Rm} = u_r L/\eta$, with $L = 0.10R_\odot$. Thick contour lines correspond to $\mathrm{Rm} = \{1.0, 10.0, 100.0\}$, and emphasize the region below the radiative-convective interface where the advection of the field is expected to dominate over diffusion. 104

5.9 This figure shows a comparison of the various terms contributing to the global force balance in the azimuthal vorticity equation in our fiducial model. Note that these plots show the balance in the radiative region only (the convection zone appears in white). The rotational shear, as expressed in the left hand side of Equation 5.44 is shown in the top left panel, and is clearly in balance with the baroclinicity terms (right hand side of the same equation), as we can see in the top right panel. The remaining terms in the vorticity equation are shown in the two lower panels, and confirm that both viscous (left) and magnetic (right) stress-related terms are negligible. 106
5.10 This figure shows the various terms that contribute to the azimuthal force balance in the radiative zone in our fiducial model . Note that these plots show the balance in the radiative region only (the convection zone appears in white). Shown are the Coriolis force (top left panel), Lorentz force (top right panel), viscous-stresses (bottom left panel), and the inertial term (bottom right panel). These plots illustrate the balance between Coriolis and Lorentz forces, while the viscous stresses and the non-linear advection term remain negligible. Note how the tachocline is mostly force-free while the tachopause stands out as the region where strong Coriolis and Lorentz forces balance out. 108
5.11 Downwelling meridional mass flux $|\bar{\rho}u_r|$ at 80 degrees latitude. We observe that it is constant from the convective-radiative interface down to about $r = 0.58R_\odot$, a region we identify as the tachocline. Below $0.58R_\odot$, $|\bar{\rho}u_r|$ starts decreasing. We identify the region between the base of the tachocline and the first zero of $|\bar{\rho}u_r|$ as the tachopause (here at $r = 0.525R_\odot$). 110
5.12 This figure shows the magnetic confinement parameter $|B_r/B_{0,r}|$ (see the main text for details) and clearly illustrates efficient magnetic confinement at high latitudes in the tachocline. 112
5.13 The toroidal field in the radiative zone. 113
5.14 The effect of varying the non-dimensional thermal diffusivity E_κ profile on the dynamics of the tachocline. Here we see the steady-state results for $E_\kappa = 0.49E_{\kappa,REF}$ on the left panel and for $E_\kappa = 2.25E_{\kappa,REF}$ on the right panel. . . . 115
5.15 The thermal wind balance and the thermal energy balance in the tachocline are tested by computing the ratio $E_\kappa/|\bar{\rho}u_r|_0 D^3$, where $|\bar{\rho}u_r|_0$ is the downwelling mass flux in the tachocline. In the top panel we see the variation of the mass flux $|\bar{\rho}u_r|_0$ and the quantity $D = r_0 - r_t$ with respect to E_κ, where r_t is the base of the tachopause. Both $|\bar{\rho}u_r|_0$ and D increase with thermal diffusivity. The lower panel shows that the thermal spreading ratio $E_\kappa/|\bar{\rho}u_r|_0 D^3$ is almost independent of E_κ as predicted by Gough and McIntyre. Both panels show a vertical line indicating where $E_{\kappa,REF}$ is located within the interval under study. 118

5.16 The balance between the advection and the diffusion of the magnetic field in the tachocline is tested by computing the ratio $E_\eta/|u_r|_t\delta$, where $|u_r|_t$ is the downwelling radial velocity at the base of the tachocline, and δ is the thickness of the tachopause as defined in Section 5.3.4. In the top panel we see the variation of $|u_r|_t$ (curve with blue circles) and $E_\eta/|u_r|_t\delta$ (curve in red squares) with respect to E_η. Both quantities increase with magnetic diffusivity, although the ratio $E_\eta/|u_r|_t\delta$ remains almost constant for mid and low values of E_η. The lower panel shows the position of the base of the tachopause (black curve at the bottom), the base of the tachocline (red dashed curve at the middle), and the base of the convection zone (blue curve at the top). As the magnetic diffusivity reduces, the tachocline becomes much thicker than the tachopause, as predicted by Gough and McIntyre. Both panels show a vertical line indicating where $E_{\eta,REF}$ is located within the interval under study, which satisfies two more assumptions of the Gough and McIntyre model. 120
5.17 The effect of the non-dimensional magnetic diffusivity E_η profile on the dimensions of the tachopause. Here we see the steady-state results for $E_\eta = 7.5 \times 10^{-10}$ and $E_\eta = 5.0 \times 10^{-9}$ on the left and right panels, respectively. We can see how the tachocline-tachopause region changes in dimension with E_η. However, the effect of E_η on the thickness of the tachopause can only be assessed by looking at Figure 5.16. 121
5.18 On the left panel, we show the diffusivity profile from the model by Strugarek, Brun, and Zahn (2011). See the text for the exact parameterization of these profiles. On the right panel, we show the computed sigma profile corresponding to their model. 124
5.19 This plot shows the steady-state solution obtained in a parameter regime close to the one used by Strugarek, Brun, and Zahn (2011). Starting from the top left panel and going clockwise, we show plots of the streamlines, temperature perturbations, angular velocity, and magnetic field lines. The top left panel shows that large-scale meridional flows generated in the convection zone are not able to penetrate into the radiative interior at high latitudes. As a result, the magnetic field is not confined and the differential rotation pattern of the convection zone is communicated to the radiative interior. 125
5.20 This figure shows the various terms that contribute to the azimuthal force balance in the radiative zone in the simulation presented in Figure 5.19. Shown are the Coriolis force (top left panel), Lorentz force (top right panel), viscous-stresses (bottom left panel), and the inertial term (bottom right panel). These plots illustrate the balance between Coriolis force and viscous stresses just below the convection zone, while the Lorentz force only becomes important when η drops to its radiative zone value (here around $r = 0.62R_\odot$). By contrast with our fiducial model, however, viscous stresses are everywhere important. The nonlinear advection term remains negligible. 126
5.21 Downwelling meridional mass flux $|\bar{\rho}u_r|$ at 80 degrees latitude for the simulation presented in Figure 5.19. This model failed to develop a tachocline because the large-scale meridional flows decay rapidly to zero at the radiative-convective interface. The dash-dotted line is the exponential function $e^{-\sigma_t(x_0-x)}$, where $\sigma_t = 100$, which illustrates the rapid exponential decay of downwelling flows when $\sigma \gg 1$. . 127
5.22 In the new experiment discussed here, the magnetic diffusivity profile is moved up into the convection zone to pre-confine the magnetic field in the convection zone. 127

5.23 As in Figure 5.19 but with a "pre-confined" field. Starting from the top left panel and going clockwise, we show plots of the streamlines, temperature perturbations, angular velocity, and magnetic field lines. The top left panel shows that even though the magnetic field lines are forced to be confined in the convection zone, the large-scale meridional flows generated there are not able to penetrate into the radiative zone. As a result, the magnetic field is NOT confined below the radiative-convective interface, so the differential rotation pattern of the convection zone is communicated to the radiative interior. 128
5.24 Downwelling meridional mass flux $|\bar{\rho}u_r|$ at 80 degrees latitude. We observe that the mass flux crossing the convective-radiative interface decays abruptly. The dash-dotted line is the exponential function $e^{-\sigma_t(x_0-x)}$, where $\sigma_t = 100$, which illustrates the rapid exponential decay of downwelling flows when $\sigma \gg 1$. 129
5.25 This plot shows the confinement parameter $|B_r/B_{0,r}|$ (see Section 5.3.5 for details) for the numerical experiment where we reproduce the model by Strugarek, Brun, and Zahn (2011) with pre-confinement. 129
5.26 This figure shows the various terms that contribute to the azimuthal force balance in the radiative zone in the viscous-stress driven model with imposed magnetic pre-confinement in the convection zone. Shown are the Coriolis force (top left panel), Lorentz force (top right panel), viscous-stresses (bottom left panel), and the inertial term (bottom right panel). These plots illustrate that viscous stresses balance this time both Coriolis and Lorentz forces. 130

D.1 Contour plots showing streamlines (left upper panel), perturbations of the temperature background (right upper panel), magnetic field lines (left lower panel), and the ratio of angular velocity in the solar interior with respect to the equatorial angular velocity in the solar surface (right lower panel). The magnetic field lines were plotted by using A_n modes obtained by a process of differentiation with respect to μ, as indicated in the text. 158
D.2 Contour plots showing streamlines (left upper panel), perturbations of the temperature background (right upper panel), magnetic field lines (left lower panel), and the ratio of angular velocity in the solar interior with respect to the equatorial angular velocity in the solar surface (right lower panel). The magnetic field lines were plotted by using A_n modes obtained by a process of differentiation with respect to r, as indicated in the text. 159
D.3 Contour plots showing streamlines (left upper panel), perturbations of the temperature background (right upper panel), magnetic field lines (left lower panel), and the ratio of angular velocity in the solar interior with respect to the equatorial angular velocity in the solar surface (right lower panel). The magnetic field lines were plotted by using A_n modes obtained by a process of integration with respect to μ, as indicated in the text. 160
D.4 Contour plots showing streamlines (left upper panel), perturbations of the temperature background (right upper panel), magnetic field lines (left lower panel), and the ratio of angular velocity in the solar interior with respect to the equatorial angular velocity in the solar surface (right lower panel). The magnetic field lines were plotted by using A_n modes obtained by a process of coefficient inversion, as indicated in the text. 161

List of Tables

1.1 **Solar parameters in the vicinity of the tachocline as determined by Gough (2007).** 11

5.1 **Non-dimensional parameters for the fiducial model.** Here, $r_0 = 0.7127R_\odot$ is the location of the radiative-convective interface, $r_1 = 0.7130R_\odot$ is the location where thermal and magnetic diffusivities start increasing, and r_2 and Δ_{rz} define the transition from laminar to turbulent diffusivities. Also, r_0 and Δ_{rz} are parameters of the transition of $\sigma(r)$ to zero near the base of the convection zone. The domain for this model runs from $r_{in} = 0.05R_\odot$ to $r_{out} = 0.90R_\odot$. 102

Abstract

The Magnetohydrodynamics of the Solar Tachocline

by

Luis Antonio Acevedo-Arreguín

According to helioseismic inversions, the Sun exhibits two different rotational regimes. The inner radiative region rotates almost uniformly whereas the outer convection zone rotates differentially with the rotation rate decreasing with latitude. The transition region, which is located in the vicinity of the radiative-convective interface, is a very thin layer known as the solar tachocline. Both hydrodynamical and magnetohydrodynamical theories have been proposed to explain such a sharp rotational transition. This thesis presents and analyzes numerical simulations of the solar tachocline that explain the rotational regimes of the interior of the Sun as the result of the interaction between fluid in motion and magnetic fields.

To my parents Ana María Arreguín Vega and Vicente Acevedo Sagredo;

to María de la Luz Cabrera López, my dear wife for 11 years;

to my daughters Ana Luz and Laura Isabel Acevedo-Cabrera, the best motivational speakers I ever had;

to my brothers Armando, Eduardo, sisters Angélica, Ana Lilia, for keeping our family strong;

to my sisters-in-law Irma, Gloria, Cristina, Susana, and Adriana, as well as my brothers-in-law Guillermo, Severino, Rubén, and Gerardo;

to all my relatives in Mexico City and Querétaro; ...

en especial, dedico esta tesis a mis abuelitas Susana (q.e.p.d.) y Felícitas (q.e.p.d.), así como mis abuelitos Vicente (q.e.p.d.) y Leandro (q.e.p.d.);

A mis tías Fe, Clara, Reynalda (q.e.p.d.), Isaura (q.e.p.d.), Basilisa (q.e.p.d.), y María de Jesús, así como a mis tíos Raúl, Vicente, Fortunato (q.e.p.d.), Roberto (q.e.p.d.), Luis y Bernardino

A mis primos Gabriel (Ana Elena e Isaac), Raúl (y Patricia), David, Alejandro, Adrián, Susana, Manuel Felipe (y Luz Elena);

to the Latino community in Castroville, California.

Acknowledgments

The text of this thesis includes reprint[s] of the following previously published material: Garaud P. and Acevedo-Arreguin L. A., *On the Penetration of Meridional Circulation below the Solar Convection Zone II: Models with Convection Zone, the Taylor-Proudman constraint and Applications to Other Stars*, The Astrophysical Journal, **704**:1-16, 2009 October 10. The co-author listed in this publication directed and supervised the research which forms the basis for the thesis.

I want to thank all my professors in the Department of Applied Mathematics and Statistics, Baskin School of Engineering, University of California Santa Cruz, for their words of encouragement throughout my graduate apprenticeship. Especially, I thank Professor Pascale Garaud for her guidance and support for my research, and professors Nicholas Brummell, Gary Glatzmaier, and Marc Mangel for all their recommendations to improve my graduate work.

In the AMS department, I met a lot of kind people. My classmates and later friends Adrienne Traxler, Erinna Chen, Benjamin Byington, and Katelyn White, made my life much easier as a graduate student. They treated me as part of their group despite my being much older than they. I thank Adrienne for guiding me in my transition from the statistics track to the applied mathematics track, and also for revising my first writings. I thank Ben for always providing solutions and recommendations to improve my computer code even though he was overwhelmed by his own work. I am in debt to Marian Farah, Kassie Fronczyk, and Francisco Beltran for their kindness in the time of my advancement to candidacy, which was a crucial time for my graduate work. I especially thank Dr. Toby Wood for his valuable contributions to my research work.

My family, friends, and community also contributed to my academic success. María Luz not only cared for our children Ana Luz and Laura Isabel when my research required most

of my time; she also reminded me that science and our beliefs in God nurture our understanding of the universe. I thank María Luz for her prayers for me, and my daughters Ana Luz and Laura Isabel for not letting me give up my dreams.

Mis padres, Vicente y Ana María, así como mis hermanos Armando, Eduardo, Angélica y Ana Lilia son la familia que me vio crecer como persona y como profesionista en mi natal México. Recuerdo siempre cómo demostraban su orgullo por los diferentes logros en mi vida académica y, cuando emigré a los Estados Unidos de América, nunca dudaron que culminarían con el doctorado. Para ellos mi eterno agradecimiento por recordarme mis orígenes y por mantener unida a la familia. Un saludo para toda la gente de mi Querétaro lindo.

Finally, I have words of gratitude for members of my community in the United States. Among them, Sally Childs played a significant role in the final stages of my graduate work. She had the patience to read and proof read my manuscripts, either a paper for publication or my thesis, and always had the time to explain to me how to improve my English proficiency. She has been like an angel for my family in the US. With her help, my daughters and I have found the path to success in America.

Royal Oaks, California, Jun 11, 2012.

Introduction

Solar physics has seen remarkable progress since the mid-90s thanks to helioseismology. This new scientific field, whose theoretical foundation is briefly described in Chapter 1, relies on detailed measurements of the solar surface obtained over long periods of time. These observations of the solar disk are statistically analyzed to infer some properties of the solar interior. The structure thus revealed distinguishes two important regions in the Sun: a quiet, radiative, inner zone and a turbulent, convective, outer envelope. The interface between these two regions is located at the radius $r_0 = 0.7127 R_\odot$, where $R_\odot$ is the radius of the Sun (Gough , 2007).

One of the most important helioseismic discoveries is the unexpected rotation profile of the Sun. Inversions of the angular velocity profile of the solar interior show that the convection zone is differentially rotating while the radiative zone is rotating almost uniformly, a remarkable distinction observable in Figure 0.1 (Schou et al. , 1998; Christensen-Dalsgaard and Thompson , 2007). The tachocline is the very thin layer where these sharp changes in angular velocity occur. The phenomena underlying this rotational behavior have put the tachocline in the center of a quite a few scientific endeavors in modern times.

The importance of the tachocline cannot be understood without looking at the solar magnetic cycle. Since Galileo's time, dark spots on the solar surface have captured the attention of astronomers, and NASA currently keeps a daily record of their appearance, number, and location. Approximately every eleven years, sunspots start emerging at latitudes around 30

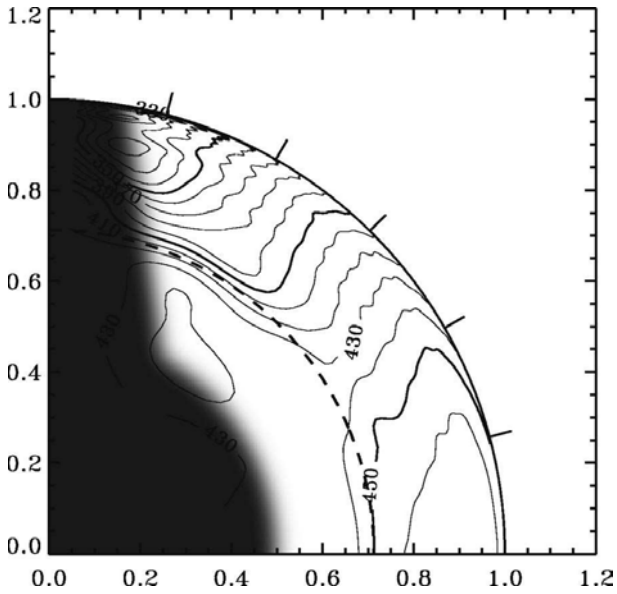

Figure 0.1: The rotational profile of the Sun as inferred by Helioseismology (Schou et al. , 1998; Christensen-Dalsgaard and Thompson , 2007).

degrees, and throughout the cycle their peak location moves toward the equator (Figure 0.2). The current paradigm explains that the solar cycle is generated by a solar dynamo, a mechanism in which electrical currents driven by plasma in motion create a magnetic field. Analysis of the records of the solar magnetic cycle, combined with mathematical models, suggests the location of the solar dynamo to be near the base of the convection zone in the region of the tachocline (Tobias and Weiss , 2007).

The magnetic activity associated with sunspots affects anything beyond the protective terrestrial atmosphere. Astronauts performing maneuvers in space, and electronic equipment carried by communication satellites are examples of possible targets vulnerable to solar magnetic storms. Hence, the study of the dynamics of the tachocline is important to understand and predict the solar weather, to attenuate its harmful effects on human life.

This research project aims to develop numerical simulations of the solar tachocline and explain the solar internal rotation profile as the result of the interaction between fluid in motion

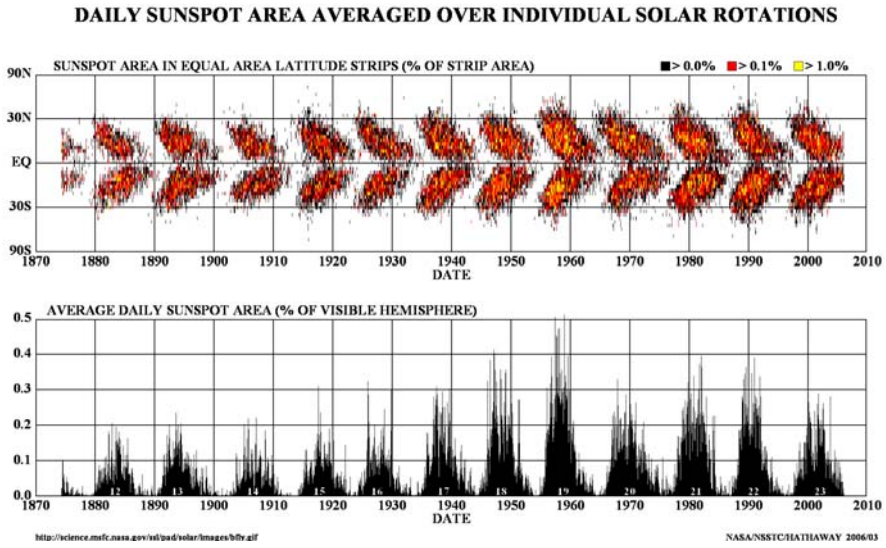

Figure 0.2: Spatial temporal histogram of the solar magnetic activity showing cycles of approximately eleven years (from NASA). Prediction of solar weather from these observations becomes complicated as cycles approach their end because determinations of the minimum are not sufficiently accurate yet.

and magnetic fields.

In the first part, we examine the existing mathematical models, which basically can be classified in hydrodynamic and hydromagnetic models, as a way to justify the theoretical framework for our own numerical model. Chapter 1 presents an overview of the solar structure as inferred by helioseismology. Chapter 2 then introduces the theory underlying the hydrodynamic models. There, we provide some details of the work by Ed Spiegel and Jean Paul Zahn, which proposes a hydrodynamical explanation for the existence of the tachocline, its evolution, and a model for its angular velocity shear. Chapter 3 deals with the hydromagnetic models and presents the theory by Gough and McIntyre, where magnetic fields and large-scale meridional flows interacting around the convective-radiative interface form the tachocline. The rest of our work will be based on the Gough and McIntyre model.

The second part describes different stages of the construction of our model. Chapter

4 introduces the hydrodynamical component of the model in a Cartesian coordinate system. In Chapter 5, we study the magnetohydrodynamics of the radiative interior in a spherical framework and perform some numerical experiments to identify the effect of some parameters on the structure of the solar tachocline. We also present results, conclusions, and recommendations for future research.

Part I

Theoretical Framework

Chapter 1

The Structure of the Sun

This chapter provides a review of what is known about the interior of the Sun as inferred from helioseismic observations. Section 1.1 briefly describes the principles of helioseismology. Then, we present in section 1.1.1 the rotational profile of the Sun and other characteristics of the tachocline as obtained by helioseismic inversions.

1.1 Solar oscillations and Helioseismology

The Sun supports a vast spectrum of acoustic oscillations, with the fundamental radial mode having a period of approximately 1 hour and with the vast majority of observed modes exhibiting periods around 5 minutes. The study of these solar oscillations constitutes the field of helioseismology.

Solar oscillations are stochastically excited by turbulent convection within a layer right below the solar surface (Gough et al. , 1996). The waves then travel through different regions of the solar interior, so their frequencies can provide information about these regions.

Measurements of the solar atmosphere are used to characterize the solar oscillations.

First, time series of the radial velocity at each point of the solar surface are obtained (by determining the Doppler shift of a certain spectral emission line). The results are projected on to spherical harmonics and then Fourier transformed in time to determine the oscillation frequencies ω_{nlm} [1].

The experimental frequencies ω_{nlm} are compared with frequencies ω_{nl} computed from perturbations of a spherically symmetric, standard solar model, which assumes a non rotating Sun, to infer the sound speed profile $c(r)$ within the solar interior. The effect of rotation manifests itself through a variation of the frequencies with azimuthal wave number m, which results in the inversion problem defined by

$$\delta\omega_{nlm} = m \int_0^{R_\odot} \int_0^{\pi} K_{nlm}(r,\theta)\Omega(r,\theta) r \mathrm{d}r \mathrm{d}\theta \ , \tag{1.1}$$

where $R_\odot$ is the radius of the Sun, Ω is its angular velocity, and $\delta\omega_{nlm} = \omega_{nlm} - \omega_{nl0}$. The smoothing kernels $K_{nlm}(r,\theta)$ are determined from the eigenfunctions for the nonrotating model (Christensen-Dalsgaard , 2002). In this way, the estimation of the angular velocity of the Sun reduces to a spatio-temporal statistics problem.

1.1.1 The solar rotation profile

Figure 1.1 shows the angular velocity of the Sun inferred by using different smoothing kernels. The radiative interior rotates with a period of approximately 27 days, whereas the convective region rotates faster at the equator ($\approx$ 25 days) than at the poles ($>$ 30 days) (Gough , 2007). Also, as shown in Figures 1.1 and 1.2, the radiative interior and the convective region at 30 degrees exhibit almost the same rotation rate, which is worth noting because it is at this latitude that sunspots emerge at the start of a new magnetic cycle (Gough , 2010).

[1] Here, the oscillation modes are characterized by three wave numbers: the degree l and azimuthal order m which describe the wave properties on a sphere (horizontal direction), and the radial order n which describes the properties in the radial direction.

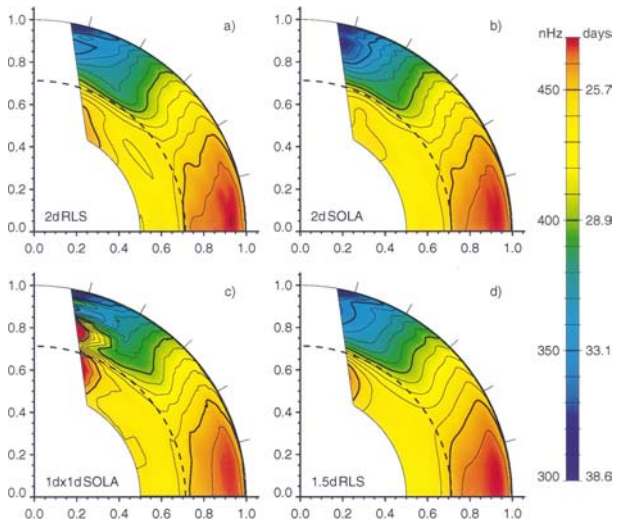

Figure 1.1: The rotational profile of the Sun as inferred by statistical analysis of the solar oscillation frequencies (Schou et al. , 1998) using 4 different types of kernels.

1.2 The solar tachocline

Figure 1.2 shows two regions exhibiting thin shear layers. In the sub-surface shear layer, the rotation rate at all latitudes increases sharply with depth within the outer 5% of the solar radius, then matches on to the rotation profile of the bulk of the convection zone. Another shear layer is visible near the base of the convection zone where the angular velocity profile rapidly converges to an internal uniform value in the radiative region. This shear layer is the solar tachocline.

1.2.1 The thickness of the tachocline

Given the low resolution of helioseismic inversions, the mere determination of the tachocline thickness has been a challenging task. As a result, instead of using full 2D direct inversions of the angular velocity profile, the tachocline thickness is usually estimated by assuming a 1D or 2D profile and then constraining its unknown coefficients by fitting predicted oscillation frequencies with observed ones. Regression models with different fitting equations

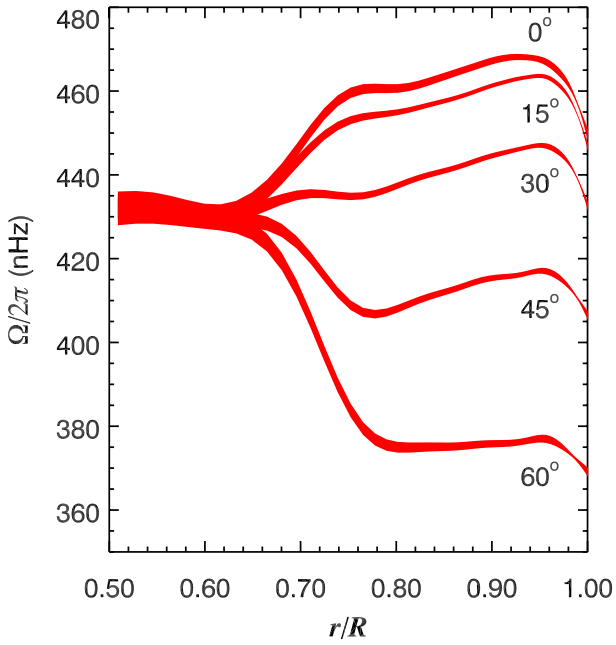

Figure 1.2: The solar rotation profile at 5 different latitudes (from Howe *et al.*, 2000), where a sharp transition of the angular velocity $\Omega/2\pi$ is observed around $0.70R_{\odot}$. The region where this change occurs is the solar tachocline.

provide different estimates of the thickness of the tachocline. This is why estimates have ranged from $0.03R_{\odot}$ to $0.09R_{\odot}$ (for more details on these regression models see Kosovichev , 1996; Charbonneau et. al , 1999, and Antia and Basu , 2011).

Charbonneau et. al (1999) also found the tachocline to be *prolate*, i.e. having a difference in central radius of about $0.024R_{\odot}$ between latitude 60 degrees and the equator, and more recently, Antia and Basu (2011) found that the tachocline exhibits no rotational radial shear around 30^{o} latitude.

1.2.2 Mixing in the tachocline

Following a different approach, Elliot and Gough (1999) estimated the tachocline thickness by studying the difference between observed and theoretical sound speed profiles in the Sun. They assumed that the tachocline is a well mixed region, which has the same chemical

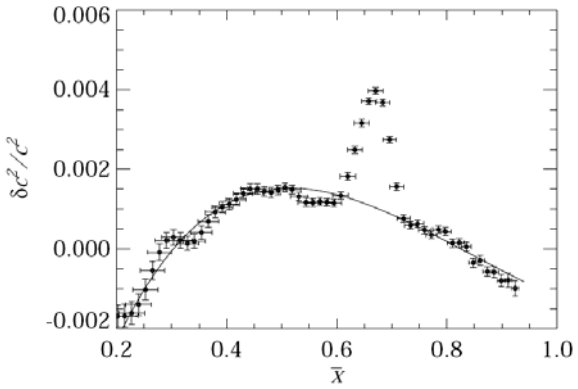

Figure 1.3: Difference (symbol points) between helioseismic inferences of sound speed and values computed with Christensen-Dalsgaard's Model S are compared with the difference (solid line) between helioseismic observations and values computed by the model by Elliot and Gough (1999), which includes a well-mixed tachocline.

composition as the convection zone. This implies a molecular weight profile that is different from the ones assumed by standard solar models. This mixing affects, for instance, the Helium settling below the base of the convection zone, so the levels of this element in the tachocline are indeed lower than the predicted values from the standard solar model S. Figure 1.3 shows how this difference in Helium concentration affects the sound speed in a manner that is more significant in the tachocline region. The depth of the well-mixed radiative region right below the base of the convection zone was calibrated to fit the sound speed data. This way, Elliot and Gough found the tachocline to be very thin, i.e. extending from $0.677R_{\odot}$ to $0.693R_{\odot}$, which represents a thickness of $0.016R_{\odot}$.

The existence of mixing regions beneath the convection zone also explains the difference between the Lithium concentrations at the solar surface and the expected levels of Lithium according to stellar evolution modeling. The measurements of Lithium from spectroscopic analysis of the solar surface differ from their expected concentrations (the abundances found in meteorites) by a factor of 150 (Christensen-Dalsgaard , 2002). However, the temperatures near the base of the solar convection zone are too low to burn Lithium. This chemical element

density	ρ	0.21	g cm^{-3}
pressure	p	6.7×10^{13}	g cm^{-2} s^{-2}
temperature	T	2.3×10^{6}	K
sound speed	c	2.3×10^{7}	cm s^{-1}
opacity	$\hat{\kappa}$	19	g^{-1} cm^{2}
gravitational acceleration	g	5.4×10^{4}	cm s^{-2}
adiabatic exponent	γ_1	1.665	
magnetic diffusivity	η	4.1×10^{2}	cm^{2} s^{-1}
kinematic viscosity	ν	2.7×10^{1}	cm^{2} s^{-1}
thermal diffusivity	κ	1.4×10^{7}	cm^{2} s^{-1}
helium diffusion coefficient	χ	8.7	cm^{2} s^{-1}
buoyancy frequency	N	8.0×10^{-4}	s^{-1}

Table 1.1: **Solar parameters in the vicinity of the tachocline as determined by Gough (2007).**

burns at 2.5×10^6 K, a temperature reachable at much deeper regions in the Sun. Hence, models incorporating mixing in the tachocline can account for the Lithium depletion problem (Christensen-Dalsgaard , 2002). Interestingly, the fact that Beryllium burns at deeper regions than Lithium and shows only moderate depletion at the solar surface also supports the notion of a thin tachocline.

Finally, Table 1.1 shows some other properties of the Sun near the base of the convection zone, as compiled by Gough (2007).

Chapter 2

Hydrodynamic Modeling

Two families of models have been proposed to characterize and describe the dynamics of the solar tachocline: hydrodynamic models and hydromagnetic models. This chapter aims to provide a brief overview of the theory that explains the solar tachocline as a hydrodynamical phenomenon, for both historical and pedagogical reasons.

2.1 The Spiegel and Zahn's model

Spiegel and Zahn (1992) proposed the first model of the tachocline, which was based on a purely hydrodynamical mechanism. They studied the evolution of large-scale flows in the radiative zone when the latter is subjected to a rotational shear imposed by the convection zone above. Let us first look at the equations governing the hydrodynamics of the solar interior. This will allow us to set the mathematical framework we will use throughout the rest of this thesis.

2.1.1 The hydrodynamics equations

The equations governing the hydrodynamics of a stably-stratified region, in a steadily rotating frame are the momentum equation:

$$\rho\frac{\partial \mathbf{u}}{\partial t} + \rho(\mathbf{u}\cdot\nabla)\mathbf{u} + 2\rho\mathbf{\Omega}_0\times\mathbf{u} = -\nabla p - \rho\nabla\Phi + \nabla\cdot\mathbf{\Pi}\ , \tag{2.1}$$

the energy equation:

$$\rho T\frac{\partial S}{\partial t} + \rho T\mathbf{u}\cdot\nabla S = \nabla\cdot(k\nabla T)\ , \tag{2.2}$$

the mass conservation law:

$$\frac{\partial \rho}{\partial t} + \nabla\cdot(\rho\mathbf{u}) = 0\ , \tag{2.3}$$

and the ideal gas law:

$$p = \frac{\rho R T}{\mathcal{M}}\ . \tag{2.4}$$

Here, $\mathbf{u}$ is the velocity field, $\mathbf{\Omega}_0$ is the rotation rate of the frame, t is time, ρ is mass density, p is pressure, T is temperature, S is entropy, Φ is the gravitational potential, $\mathbf{\Pi}$ is the viscous stress tensor, and $\mathcal{M}$ is the molecular weight of the gas. The thermal conductivity is represented by k and the ideal gas constant by R. We consider a spherically symmetric, time-independent background state.

Once the system is perturbed, the variables of interest can be decomposed as:

$$q(r,\theta,\phi,t) = \bar{q}(r) + \tilde{q}(r,\theta,\phi,t)\ , \tag{2.5}$$

where q stands for any field, the bar indicating the background state and the tilde indicating the perturbations to such an equilibrium state. If the thermodynamic perturbations are small, the governing equations can be linearized around the background state.

Spiegel and Zahn then also make the following assumptions: axial symmetry, the anelastic approximation, small Rossby number, a very thin tachocline, and geostrophic flow.

In addition, they assume that the system has already reached thermal equilibrium via a fast adiabatic adjustment phase. Then, by introducing a stream function for the meridional flow with u_r and u_θ defined by

$$\frac{\partial \psi}{\partial \mu} = \bar{\rho} r^2 u_r \tag{2.6}$$

$$\frac{\partial \psi}{\partial r} = \bar{\rho} r \sqrt{1-\mu^2} u_\theta \ , \tag{2.7}$$

they express the system of governing equations in spherical coordinates as:

$$-\frac{1}{\bar{\rho}} \frac{\partial \tilde{p}}{\partial r} + \bar{g} \frac{\tilde{T}}{\bar{T}} = 0 \tag{2.8}$$

$$-2\Omega_0 \tilde{\Omega} r \mu = \frac{1}{\bar{\rho} r} \frac{\partial \tilde{p}}{\partial \mu} \tag{2.9}$$

$$\begin{aligned} \bar{\rho} r^2 (1-\mu^2) \frac{\partial \tilde{\Omega}}{\partial t} + 2\Omega_0 \mu \frac{\partial \psi}{\partial r} &= \frac{(1-\mu^2)}{r^2} \frac{\partial}{\partial r} \left[\bar{\rho} \nu r^4 \frac{\partial \tilde{\Omega}}{\partial r} \right] \\ &\quad + \bar{\rho} \frac{\partial}{\partial \mu} \left[\nu (1-\mu^2)^2 \frac{\partial \tilde{\Omega}}{\partial \mu} \right] \end{aligned} \tag{2.10}$$

$$\frac{N^2}{\bar{g}} \frac{\bar{T}}{\bar{\rho} r^2} \frac{\partial \psi}{\partial \mu} = \frac{1}{\bar{\rho} c_p r^2} \frac{\partial}{\partial r} \left(k r^2 \frac{\partial \tilde{T}}{\partial r} \right) \tag{2.11}$$

$$0 = \frac{\tilde{\rho}}{\bar{\rho}} + \frac{\tilde{T}}{\bar{T}} \ , \tag{2.12}$$

where $\mu = \cos\theta$ and $\mathbf{u}(r, \theta, \phi) = (u_r, u_\theta, r \sin\theta \tilde{\Omega})$ is the velocity field.

These equations governing the hydrodynamics of the solar interior are solved only for the radiative zone by imposing top boundary conditions at the radiative-convective interface ($r = r_0$). The boundary conditions are expressed in terms of the angular velocity as:

$$\tilde{\Omega}(r, \mu, t) = \Omega_{eq}(1 - a\mu^2 - b\mu^4) - \Omega_0 \text{ at } r = r_0 \tag{2.13}$$

$$\frac{\partial \tilde{\Omega}(r, \mu, t)}{\partial r} = 0 \text{ at } r = r_0 \tag{2.14}$$

$$\tilde{\Omega}(r, \mu, t) \rightarrow 0 \text{ for } r \rightarrow 0 \ , \tag{2.15}$$

Here, the expression $\Omega_{eq}(1-a\mu^2-b\mu^4)$ models the differential rotation at the radiative-convective interface, where a and b are constants determined from helioseismic information, and where Ω_{eq} is the equatorial rate. Spiegel and Zahn used the expression derived by Goode *et al.* (1991), which has $\Omega_0 = 462$ nHz, $a = 64/462$, and $b = 73/462$ for $\Omega_{eq}/2\pi$.

It is important to note that Equations 2.8 and 2.9 indicate that the system in Spiegel and Zahn's model is in thermal wind balance, whereas Equation 2.11 emphasizes the balance between radiative diffusion and transport of the background entropy gradient, which means that the system is also in thermal equilibrium. We examine these conditions next.

2.1.1.1 The thermal-wind balance

We first obtain the azimuthal component of the vorticity equation for this system by performing

$\frac{1}{r}\frac{\partial}{\partial r}\,(r\ \text{Equation 2.9}) - \frac{1}{r}\frac{\partial}{\partial \theta}\,(\text{Equation 2.8})$,

which yields

$$-2\Omega_0 r\sin\theta\left[\cos\theta\frac{\partial\tilde{\Omega}}{\partial r} - \frac{\sin\theta}{r}\frac{\partial\tilde{\Omega}}{\partial\theta}\right] = \frac{1}{r\bar{\rho}^2}\frac{\partial\bar{\rho}}{\partial r}\frac{\partial\tilde{p}}{\partial\theta} - \frac{\bar{g}}{r\bar{T}}\frac{\partial\tilde{T}}{\partial\theta} \tag{2.16}$$

$$2s\Omega_0\frac{\partial\tilde{\Omega}}{\partial z} \approx \frac{\bar{g}}{r\bar{T}}\frac{\partial\tilde{T}}{\partial\theta}\ , \tag{2.17}$$

where $z = r\cos\theta$ and $s = r\sin\theta$. This is the so-called thermal wind equation, which relates the rotational shear along the polar axis to the latitudinal temperature gradient for systems in geostrophic and hydrostatic equilibrium.

2.1.1.2 The impact of thermal equilibrium

Equation 2.11, which can also be written as

$$\frac{\bar{N}^2\bar{T}}{\bar{g}}u_r \approx \frac{1}{\bar{\rho}\bar{c_p}}\frac{1}{r^2}\frac{\partial}{\partial r}\left(r^2 k\frac{\partial\tilde{T}}{\partial r}\right)\ , \tag{2.18}$$

indicates that in stratified systems, there is a balance between advection of the background stratification and radiative diffusion. In particular, any temperature perturbation resulting from thermal wind balance must be compensated by radial flows to keep the system in thermal equilibrium. The amplitude of those flows is constrained by stratification and rotation. The overall effect is a chemically well-mixed tachocline.

Spiegel and Zahn (1992) solve the system of governing equations 2.8 - 2.12 and associated boundary conditions for two distinct scenarios for the tachocline. They found expressions for the angular velocity perturbation $\tilde{\Omega}(r, \theta, t)$ for the cases where viscosity in the tachocline is isotropic and strongly anisotropic, respectively.

2.1.2 Tachocline spreading

If viscous stresses are assumed to be isotropic and if the tachocline is very thin, then the angular momentum conservation equation becomes

$$\bar{\rho} r^2 (1-\mu^2) \frac{\partial \tilde{\Omega}_0}{\partial t} + 2\Omega\mu \frac{\partial \psi}{\partial r} = \frac{(1-\mu^2)}{r^2} \frac{\partial}{\partial r} \left[\bar{\rho} \nu r^4 \frac{\partial \tilde{\Omega}}{\partial r} \right] \ . \tag{2.19}$$

By assuming a solution of the form

$$\tilde{\Omega} = \sum_{i>0} \hat{\Omega}_i(r,t) f_i(\mu) \ , \tag{2.20}$$

where $f_i(\mu)$ are eigenfunctions to be numerically determined, Spiegel and Zahn combine Equations 2.8, 2.9, 2.11, 2.12, and 2.19 to find an expression for the perturbations $\hat{\Omega}_i(r,t)$ as

$$\frac{\partial \hat{\Omega}_i}{\partial t} + \kappa \left(\frac{2\Omega_0}{N} \right)^2 \left(\frac{r_0}{\lambda_i} \right)^2 \frac{\partial^4 \hat{\Omega}_i}{\partial r^4} - \nu \frac{\partial^2 \hat{\Omega}_i}{\partial r^2} = 0 \ , \tag{2.21}$$

where the thermal diffusivity $\kappa = k/\bar{\rho} c_p$, and λ_i is an eigenvalue. Equation 2.21 indicates that no steady-state is attainable, which means that the differential rotation will continue to spread toward the center of the Sun and the tachocline will thicken over time. Two dynamical regimes are possible: thermal and viscous spreading. The second term of Equation 2.21 models a

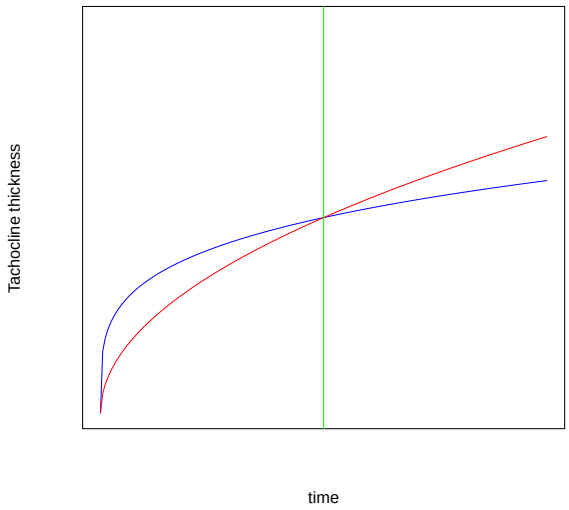

Figure 2.1: The evolution of the tachocline thickness h depends on the form of the function $t^{1/n}$. For $n = 4$, the blue curve models the hyperviscous spreading (as a function of $t^{1/4}$), whereas for $n = 2$, the red curve models the viscous spreading (as a function of $t^{1/2}$).

hyperviscous spreading of thermal origin (Zahn , 2007), which takes place on a local Eddington-Sweet timescale t_{ES}, with

$$t_{ES} = \left(\frac{N}{2\Omega}\right)^2 \frac{r_0^2}{\kappa} \ . \tag{2.22}$$

The last term of Equation 2.21 represents a more standard viscous spreading, which takes place on a timescale $t_\nu = r_0^2/\nu$ where ν is the viscosity, which was assumed isotropic.

Each of these two regimes can be studied individually. By introducing the similarity variable $u = (r - r_0)/t^{1/n}$, then viscous spreading yields

$$-\frac{1}{2}u\frac{\mathrm{d}\hat{\Omega}}{\mathrm{d}u} - \nu_r\frac{\mathrm{d}^2\hat{\Omega}}{\mathrm{d}u^2} = 0 \ , \tag{2.23}$$

with $n = 2$, which indicates that $\hat{\Omega}(r, t)$ is just a function of $(r - r_0)/t^{1/2}$. Similarly, when $n = 4$, hyperviscous spreading reduces to:

$$-\frac{1}{2}u\frac{\mathrm{d}\hat{\Omega}}{\mathrm{d}u} + \kappa\left(\frac{2\Omega_0}{N}\right)^2\left(\frac{r_0}{\lambda}\right)^2\frac{\mathrm{d}^4\hat{\Omega}}{\mathrm{d}u^4} = 0 \ , \tag{2.24}$$

which indicates that $\hat{\Omega}(r,t)$ is just a function of $(r-r_0)/t^{1/4}$. This suggests that the thickness of the tachocline varies as:

$$h = r_0 \left(\frac{t}{t_\nu}\right)^{\frac{1}{2}} \text{ [viscosity driven system]}, \tag{2.25}$$

$$h = r_0 \left(\frac{t}{t_{ES}}\right)^{\frac{1}{4}} \text{ [hyperviscosity driven system]}, \tag{2.26}$$

where r_0 is the radius of the convection zone. Both regimes are shown in Figure 2.1. We see that the effect of viscosity is negligible at early times, whereas viscosity drives the thickening of the tachocline at later times. It is important to note that the thickness of the tachocline h at the intersection of these two curves corresponds to

$$h = \left(\frac{t_\nu}{t_{ES}}\right)^{\frac{1}{2}} r_0 = \frac{r_0}{\sigma} \ , \tag{2.27}$$

where $\sigma = \sqrt{\mathrm{Pr}}N/\Omega_0$ is a stratification parameter governing the dynamics of meridional flows in the radiative zone (Garaud and Acevedo-Arreguin , 2009), and $\mathrm{Pr} = \nu/\kappa$ is the Prandtl number. Hence, the growth of the tachocline is driven by meridional flows (thermoviscous spreading) when $h < r_0/\sigma$ and by molecular friction (viscous spreading) when $h > r_0/\sigma$.

By considering only the contribution of the various terms in Equation 2.21, Spiegel and Zahn (1992) estimated (a) the tachocline is still in the thermal spreading phase, and (b) the thickness of the tachocline, $h \approx r_0(t/t_{ES})^{1/4}$, as of 2×10^5 km after 4.6×10^9 years, by considering $t_{ES} = 2.2 \times 10^{11}$ years.

2.1.3 Anisotropic turbulent viscosity

Since thermal spreading has to be taking place in the Sun, the fact that the tachocline is so thin means that some mechanism must actively prevent it.

Spiegel and Zahn then proposed that the growth of the tachocline could be halted if anisotropic turbulent stresses were operating along the base of the convection zone. They

modeled these stresses by assuming that they take the form of a viscosity, but with different values of ν in the radial and latitudinal direction (ν_r and ν_θ, respectively). If the contribution of ν_θ dominates the other viscous term in Equation 2.10, then a steady state can be achieved, satisfying

$$\left(\frac{2\Omega_0}{N}\right)^2 \frac{\kappa}{\nu_\theta}\left(\frac{r_0}{\lambda_i}\right)\frac{\mathrm{d}^4\hat{\Omega}_i}{\mathrm{d}r^4} + \hat{\Omega}_i = 0 \ , \tag{2.28}$$

from which the tachocline thickness can be estimated as

$$h = \frac{3\pi}{2\lambda_{min}} r_0 \left(\frac{\Omega_0}{N}\right)^{\frac{1}{2}} \left(\frac{\kappa}{\nu_\theta}\right)^{\frac{1}{4}} \ , \tag{2.29}$$

where λ_{min} is the smallest non-zero eigenvalue of the eigenfunction associated with a solution similar to Equation 2.20, but now for Equation 2.10 with $\nu_r = 0$.

By using some values from Table 1.1 and assuming a tachocline thickness $h = 0.03 R_\odot =$ 20880 km, we can compute the order of magnitude of the horizontal, turbulent viscosity to be of 7.89×10^9 cm^2 s^{-1}.

2.2 The problem with the Spiegel and Zahn model

Spiegel and Zahn (1992) introduced the notion of a 2-D eddy viscosity to justify an accelerated transport of angular momentum in the latitudinal direction. However, it is now recognized that this mechanism cannot explain the uniformly rotating radiative interior because Reynolds stresses smooth out potential vorticity, not angular velocity (Gough , 2007). Contrary to the idea conveyed by eddy viscosity, turbulent motions drive a rotating, stratified fluid away from solid-body rotation. This phenomenon had been already observed in the laboratory by Plumb and McEwan (1978), as reported by (McIntyre , 2003).

Even if the concept of 2-D eddy viscosity somehow holds, the next question is whether a viscosity $\nu_\theta \approx 7.89 \times 10^9$ cm^2 s^{-1} is realistic or not [1]. We believe it is unlikely.

[1] This value increases almost four times if we use the thickness of the tachocline calculated by Elliot and Gough

In Chapter 3, we review the models considering magnetic stresses to explain the thinness of the solar tachocline.

(1999).

Chapter 3

Hydromagnetic Modeling

The inadequacy of hydromodels in reproducing observations suggested the necessity for other forces to be incorporated. The most commonly-accepted paradigm for the tachocline today involves magnetic fields. Indeed, magnetic fields and fluids in motion can affect one another. In cases where there is no magnetic dissipation, i.e. the fluid is highly conductive, the magnetic field lines are forced to be aligned with the flow (Alfven's theorem). The opposite is also true, so when the poloidal component of an axially symmetric field acts on a rotating fluid and the system reaches the equilibrium, the resulting angular velocity should be constant on magnetic field lines according to Ferraro (1937):

$$\mathbf{B} \cdot \nabla \Omega = 0, \tag{3.1}$$

where $\mathbf{B}$ is the axisymmetric magnetic field, and Ω is the angular velocity . This property of magnetized fluids inspired the idea that some configurations of magnetic field lines might force the radiative zone to rotate uniformly (Mestel , 1953; Mestel and Weiss , 1987).

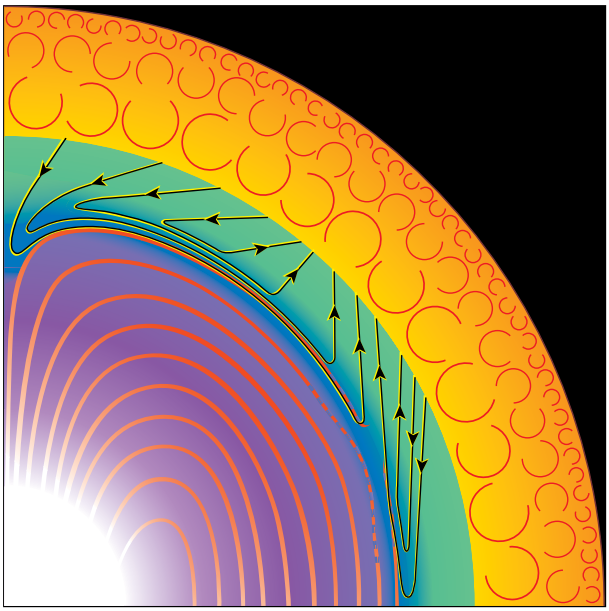

Figure 3.1: This picture of a meridional quadrant of the Sun shows the tachocline and adjacent regions according to Gough and McIntyre's theory. Here, we see meridional flows generated inside the convection zone (the orange region), and some of them enter the tachocline (green) at high latitudes. These meridional flows are deflected by the magnetic field in a diffusive boundary layer (blue) located in the bottom of the tachocline, and then return to the convection zone at mid-latitudes. In the meantime, the radiative region (pink) remains rotating as a solid body due to the poloidal field (red lines) trapped there by the meridional circulation in the tachocline, a mechanism in place for most of the Sun's lifetime.

3.1 First models of the solar tachocline

Rüdiger and Kitchatinov (1997) proposed the first magnetic model of the tachocline and showed that a confined, primordial magnetic field can force the angular velocity of the radiative interior of the Sun to be constant. For simplicity, they assumed the existence of a prescribed poloidal magnetic field, confined entirely within the radiative zone, and studied its interaction with zonal flows through the azimuthal components of the momentum and induction equations. They found that this interaction can result in a solar-like rotation profile with a thin tachocline. Using a very similar model, MacGregor and Charbonneau (1999) showed that the field *had* to be confined for a tachocline to exist. A poloidal field with a nonzero

component normal to the radiative-convective interface transmits differential rotation to the radiative interior instead of suppressing it.

However, while providing an interesting look into the problem, these two models failed in two fundamental aspects. Firstly, neither of these works elaborated on the mechanisms for magnetic confinement. Secondly, by neglecting meridional flows in the system, both sets of results placed an unphysical emphasis on viscous stresses, since they become the only force available to balance the Lorentz force in the ϕ-component of the momentum equation. In the real Sun, however, viscous stresses are not expected to be important.

3.2 The Gough and McIntyre model

Gough and McIntyre (1998) were the first to describe self-consistently the existence of the tachocline as the result of an interaction between large-scale flows and a primordial magnetic field (Figure 3.1). In their model, meridional flows are driven in the convection zone by the gyroscopic pumping effect induced by differential rotation, and penetrate into the top of the radiative region. These meridional flows first travel across a region with no significant presence of magnetic field (the tachocline), and then reach a deeper magnetically dominated region (the tachopause). There, the interaction between the downwelling meridional flows and the magnetic field becomes important for the dynamics of the region. The Lorentz and Coriolis forces, in the azimuthal component of the momentum equation, are in balance. The flows decrease in amplitude whereas the field is distorted, so streamlines and field lines run horizontally. The field is then prevented from diffusing outward and the meridional flows stop their burrowing into the interior.

Gough and McIntyre argue that the governing equations must be completed by incorporating the energy equation to model the tachocline meridional flows correctly. In absence of

azimuthal forces, the transport of angular momentum in the tachocline is thermally driven, as described by Spiegel and Zahn (see Chapter 2).

3.2.1 The MHD equations

For a system in steady state and negligible presence of inertial force, the equations governing its magnetohydrodynamics are:

$$2\bar{\rho}\mathbf{\Omega}_0 \times \mathbf{u} = -\nabla\tilde{p} - \tilde{\rho}\mathbf{g} + \mathbf{j} \times \mathbf{B} + \nabla \cdot \mathbf{\Pi} \tag{3.2}$$

$$\bar{\rho}\bar{T}\mathbf{u} \cdot \nabla\bar{S} = \nabla \cdot (k\nabla\tilde{T}) \tag{3.3}$$

$$\nabla \cdot (\bar{\rho}\mathbf{u}) = 0 \tag{3.4}$$

$$\nabla \times (\mathbf{u} \times \mathbf{B}) = \nabla \times (\eta\nabla \times \mathbf{B}) \tag{3.5}$$

$$\nabla \cdot \mathbf{B} = 0 \tag{3.6}$$

$$\frac{\tilde{p}}{\bar{p}} = \frac{\tilde{\rho}}{\bar{\rho}} + \frac{\tilde{T}}{\bar{T}} \, , \tag{3.7}$$

The magnetic field is represented by $\mathbf{B} = (B_r, B_\theta, B_\phi)$, whereas the electric current density by $\mathbf{j}$. The magnetic diffusivity is η, and the rest of the variables were already defined in Chapter 2.

3.2.2 The tachocline force balance

As in Spiegel and Zahn , Gough and McIntyre assume hydrostatic and geostrophic balance in the radial and latitudinal components of the momentum equation. The tachocline is therefore in thermal-wind balance (see Equation 2.17). Assuming that the tachocline is thin and that its thickness is Δ, a boundary-layer approximation yields

$$\frac{\tilde{T}}{\bar{T}} \approx \frac{\alpha\Omega_0^2 r_0^2}{\bar{g}L\Delta} \, , \tag{3.8}$$

where the rotational shear is approximated as $\partial\Omega/\partial z \approx (\Omega_{cz} - \Omega_0)/\Delta \approx \alpha\Omega_0/\Delta$, and the latitudinal temperature perturbation as $\partial\tilde{T}/\partial\theta \approx L\tilde{T}$, where L is a number of order unity.

According to Spiegel and Zahn and Gough and McIntyre , the tachocline is also in thermal equilibrium, so Equation 2.18 yields

$$u_r \propto \frac{\kappa\bar{g}}{\bar{N}^2\Delta^2}\left(\frac{\tilde{T}}{\bar{T}}\right) , \tag{3.9}$$

where $\partial/\partial r \propto 1/\Delta$ and $\kappa = k/\bar{\rho}\bar{c_p}$.

From these two equilibriums, Gough and McIntyre deduce that

$$u_r \propto \frac{\alpha r_0^2\kappa}{L}\frac{\Omega_0^2}{\bar{N}^2}\left(\frac{1}{\Delta^3}\right) . \tag{3.10}$$

This equation is very important because relates the amplitude of the downwelling meridional flows in the tachocline to its thickness. We will return to this equation in Chapter 5.

3.2.3 The tachopause force balance

Gough and McIntyre assume the tachopause is still in thermal wind balance and in thermal equilibrium. In addition, the Lorentz and Coriolis forces now become significant terms in the azimuthal momentum equation. The ϕ-component of the momentum equation, when expressed in spherical coordinates, is

$$2\Omega_0 u_\theta \cos\theta + 2\Omega_0 u_r \sin\theta = \frac{1}{4\pi\bar{\rho}}\left[\frac{B_\theta}{r\sin\theta}\frac{\partial}{\partial\theta}(B_\phi \sin\theta) - \frac{B_r}{r}\frac{\partial}{\partial r}(rB_\phi)\right] . \tag{3.11}$$

By assuming the poloidal magnetic field to be horizontal, i.e. $B_r = 0$ and $B_\theta = B_0$, and the meridional flows to run parallel in the tachopause, Gough and McIntyre reduce Equation 3.11 to:

$$2\Omega_0 u_\theta \cos\theta \approx \frac{B_0}{4\pi\bar{\rho}r\sin\theta}\frac{\partial}{\partial\theta}(B_\phi \sin\theta) . \tag{3.12}$$

The left-hand side of this equation expresses the magnitude of the Coriolis force as a function

of u_θ. The right-hand side expresses the magnitude of the Lorentz force as a function of the magnetic field strength and the rate of change of the toroidal field with latitude.

The differential rotation twists and stretches the poloidal field in the tachopause to generate the toroidal field. This can be modeled by the zonal component of the magnetic induction equation:

$$\frac{\partial}{\partial r}[u_\phi B_r - u_r B_\phi] + [u_\phi B_r - u_r B_\phi] - \frac{1}{r}\frac{\partial}{\partial \theta}[u_\theta B_\phi - u_\phi B_\theta] = -\eta\left[\nabla^2 B_\phi - \frac{1}{r^2 \sin^2\theta} B_\phi\right] \ , \quad (3.13)$$

which Gough and McIntyre simplified by considering again the meridional flows and the poloidal magnetic field being horizontal and almost constant. These assumptions and the fact that perturbations of the toroidal field and of the angular velocity change rapidly in the tachopause yield:

$$-B_0 \sin\theta \frac{\partial \tilde{\Omega}}{\partial \theta} \approx \eta \frac{\partial^2 B_\phi}{\partial r^2} \ . \quad (3.14)$$

Here, any reduction of rotational shear is directly balanced by generation of toroidal field.

3.2.4 Approximate solutions for the tachopause

The equations derived in section 3.2.1 along with the thermal wind and energy equations (Equations 2.17 and 2.18, respectively) were examined by Gough and McIntyre . Using a boundary-layer analysis, they showed that

$$\frac{\partial^6 \tilde{T}}{\partial r^6} - \frac{1}{\delta^6}\tilde{T} \approx 0 \ , \quad (3.15)$$

where the tachopause thickness δ is given by

$$\delta = \left(\frac{8\pi\bar{\rho}\eta\kappa\Omega_0^2}{B_0^2 r_0^2 \bar{N}^2 L^4}\right)^{\frac{1}{6}} r_0 \ . \quad (3.16)$$

This expression can be used with the magnetic advection-diffusion balance

$$|u_r| \approx \frac{\eta}{\delta} \quad (3.17)$$

to relate the thickness of the tachocline with the strength of the magnetic field at its base:

$$\frac{|B_0|}{\sqrt{4\pi\bar{\rho}}} \propto \frac{\alpha^3}{L^5}\left(\frac{\kappa}{\eta}\right)^3\left(\frac{\Omega_0}{\bar{N}}\right)^7\left(\frac{r_0}{\Delta}\right)^9\frac{\sqrt{\kappa\eta}}{r_0}\ , \tag{3.18}$$

which simply suggests that

$$\Delta \propto |B_0|^{-1/9}\ . \tag{3.19}$$

Gough and McIntyre estimated that, given present tachocline thickness of the order of $0.018R_\odot$, B_0 should be of the order of 10^{-4} Tesla. This is consistent with what we would expect of a primordial field strength from flux conservation during stellar formation.

3.3 Numerical models of the Radiative Zone

Since Gough and McIntyre published their theory in 1998, the implementation of numerical experiments to verify it became an important line of investigation. A few attempts were made using different techniques. They are reviewed here in two groups depending on whether magnetic confinement was achieved or not.

3.3.1 Simulations with no magnetic confinement

The first time-dependent, 3-D simulations of the tachocline were conducted by Brun and Zahn (2006) using the ASH code[1]. ASH solves the anelastic magnetohydrodynamic equations for a stratified, rotating, spherical shell of ionized gas. Brun and Zahn (2006) ran numerical simulations of a model of the radiative interior only, under the influence of a fixed differential rotation profile imposed by the convection zone on the top, as modeled through boundary conditions. At time $t = 0$, the radiative interior is rotating uniformly and is threaded by a confined, purely poloidal magnetic field. They subsequently evolved this system to see whether or not it

[1]The ASH code was developed by modifying Glatzmaier's code (Glatzmaier , 1985) for modeling convection in a spherical shell.

would reach the steady state proposed by Gough and McIntyre (1998). Brun and Zahn (2006) found that, regardless of initial conditions, the magnetic field always eventually diffuses outward and opens up into the convection zone. When this happens, the imposed differential rotation propagates into the interior.

Gough (2010) discussed Brun and Zahn's results and argued that at their selected parameters, the thicknesses of the tachocline and the tachopause are roughly equal. This is markedly different from the Gough and McIntyre's criterion $\delta \ll \Delta$ and indicates the absence of a magnetic-free region between the radiative interior and the convection zone (Gough , 2010), i.e. in the strict sense of the definition, no tachocline at all was simulated by Brun and Zahn .

Before that, Garaud and Garaud (2008) also pointed out that by assuming the convective-radiative interface to be closed to meridional flows, Brun and Zahn (2006) prevented the very mechanism that is supposed to maintain the magnetic field confined to the radiative interior.

Strugarek, Brun, and Zahn (2011) then upgraded their first 3-D simulations by incorporating the convection zone into the model and generating meridional circulations self-consistently. However, they still found that the initially confined magnetic field diffused into the convection zone and that the flows were unable to confine the field. In fact, they found that the evolution of the magnetic field had significant effects on the meridional circulation patterns in the radiative zone. The internal magnetic field was so strong that the polar radiative region was not in thermal-wind balance. Large-scale meridional flows were not generated by differential rotation near the poles. Inspection of the azimuthal component of the vorticity equation (see Figure 17 in their paper) showed, however, that the tachocline dynamics were still dominated by viscous stresses. In terms of Spigel and Zahn's work, the tachocline is now in the viscous spreading regime (see Equation 2.27), where $\sigma = \sqrt{\mathrm{Pr}}N/\Omega_0 \gg 1$.

Rogers (2011) ran similar simulations, but this time using a 2.5-D model. She included

a forcing term in the momentum equation to drive differential rotation in the convection zone. In her simulations, by contrast with Strugarek, Brun, and Zahn (2011), the magnetic field was very weak and had little effect on Ω. The viscous stresses were also dominating the system (again the stratification parameter $\sigma \gg 1$). It is not clear why the tachocline in Roger's model remained thin.

In all 3-D global models presented here, the fact that viscous stresses dominate the dynamics of the system is an important clue to the claim that the parameters have not been chosen correctly. As seen in Section 2.1.2, in absence of anisotropic turbulent viscosity (or magnetic stresses as discussed in this chapter), the tachocline dynamics is governed by either thermal or viscous spreading. The parameter $\sigma = \sqrt{\mathrm{Pr}}N/\Omega_0$ indicates which of the two regimes is in operation, i.e. thermal spreading when $\sigma \ll 1$ or viscous spreading when $\sigma \gg 1$. Since thermal spreading occurs in the early stages of the tachocline formation, any simulation involving viscous spreading models an unrealistic tachocline.

In the next part of this thesis, we will discuss in more detail the problem of parameter selection.

3.3.2 Simulations with magnetic confinement

To investigate whether interaction between magnetic field and meridional flows in the radiative zone is possible, Garaud and Garaud (2008) developed a code to perform 2-D simulations of the radiative zone only. They imposed a boundary condition at the radiative-convective interface to reproduce the downwelling flows at high latitudes described by the Gough and McIntyre theory. An internal magnetic field was prescribed and steady-state solutions were obtained for the MHD equations. Garaud and Garaud found that the meridional flows were able to confine the field (Figure 3.2).

Since Garaud and Garaud kept the buoyancy frequency $\bar{N}$ with its solar profile and

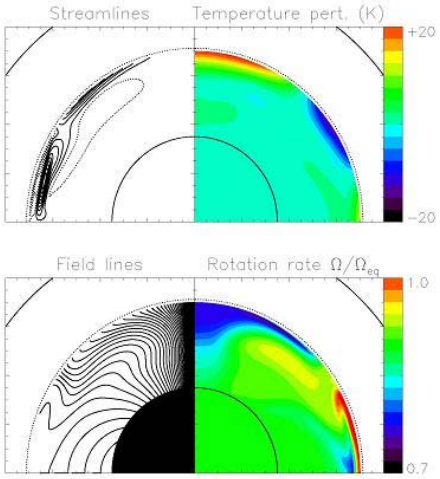

Figure 3.2: Magnetic field confinement (left lower panel) caused by flows penetrating the radiative region (left upper panel), obtained numerically by Garaud and Garaud (2008). The temperature perturbations and the angular velocity are shown in the right, upper and lower panel, respectively.

used the right combination of diffusivities, their simulations were indeed within a parameter space that corresponded to a thermally-driven tachocline, i.e. $\sigma \ll 1$. However, the meridional flows associated with this thermal condition were already in the tachocline by definition. It remained then to be investigated whether these flows could actually penetrate the radiative-convective interface if they were generated in the convection zone instead.

Part II

Model Development

One of the main discoveries of helioseismology is the solar tachocline. In Chapter 1, we learned that the tachocline is too thin to be resolved by helioseismic inversions. Understanding the tachocline dynamics requires the help of theory.

Thanks to the work by Spiegel and Zahn (1992), we learned in Chapter 2 that, in the absence of magnetic fields or other anisotropic stresses, the tachocline thickens over time as a result of advection by meridional flows burrowing into the radiative region. The dynamics of these flows is controlled by thermal-wind balance and thermal equilibrium. Spiegel and Zahn showed that the tachocline would grow and eventually span the entire radiative interior.

Gough and McIntyre (1998) first proposed a self-consistent theory to explain the way an internal magnetic field may prevent the tachocline from growing indefinitely. The field imposes uniform rotation through Ferraro's law. Meridional flows driven by differential rotation in the convection zone travel across the radiative-convective interface to stop the internal magnetic field from diffusing outside the radiative region. Although these flows cannot block completely the field from reaching the convection zone, their action is sufficient to create a tachopause, a sort of magnetic wall that divides the radiative interior in two regions: a magnetically dominated and uniformly rotating region below, and the tachocline, with just traces of magnetic field, above.

In this thesis, we develop a numerical model of the Gough and McIntyre theory, based on the original work of Garaud and Garaud (2008). Our goal is to obtain answers for some of the following questions:

1. Under which conditions can large-scale meridional flows generated in the convection zone cross the convective-radiative interface?

2. Under which conditions can large-scale meridional flows circulating in the tachocline confine an internal magnetic field?

3. Which assumptions of the theory by Gough and McIntyre (1998) are verifiable by numerical simulations?

In Chapter 4, we study question 1. We focus in the hydrodynamical part of the phenomenon underlying the formation of the tachocline. We investigate how large-scale meridional flows can move from the convection zone into the radiative zone, and especially how these flows can reach deeper regions within the radiative zone.

In Chapter 5, we study the last two questions. We build and run a 2-D model of a sphere of an ideal gas, whose dynamics is governed by the MHD equations. We then analyze the results in the light of the Gough and McIntyre theory.

Chapter 4

Hydrodynamics of the Tachocline: Analytical Solutions

Based on the discussion of Chapter 3, section 3.3, we began to study more systematically the gyroscopic pumping mechanisms, and under which conditions it can indeed drive sufficiently high amplitude flows from the convection zone to the radiative zone. A first purely hydrodynamic study was published in the Astrophysical Journal, *On the penetration of meridional circulation below the solar convection zone. II. Models with convection zone, the Taylor-Proudman constraint, and applications to other stars*, by Garaud and Acevedo-Arreguin (2009), and forms the content of this chapter.

4.1 Introduction

Various related mechanisms are thought to contribute to the generation and maintenance of large-scale meridional flows in the solar convection zone. The effect of rotation on turbulent convection induces a relatively strong anisotropy in the Reynolds stresses (Kippen-

hahn 1963), in particular near the base of the convection zone where the convective turnover time is of the order of the solar rotation period. The divergence of these anisotropic stresses can directly drive large-scale meridional flows (see Rüdiger, 1989, for a discussion of this effect). It also drives large-scale zonal flows (more commonly referred to as differential rotation) which then induce meridional forcing through the bias of the Coriolis force, a mechanism referred to as "gyroscopic pumping" (McIntyre 2007). Indeed, the polar regions of the convection zone are observed to be more slowly rotating than the bulk of the Sun (Schou *et al.* 1998), so that the associated Coriolis force in these regions drives fluid *towards* the polar axis. Meanwhile, equatorial regions are rotating more rapidly than the average, and are therefore subject to a Coriolis force pushing fluid *away* from the polar axis. The most likely flow pattern resulting from the combination of these forces is one with an equatorial upwelling, a surface poleward flow and a deep return flow. This pattern is indeed observed near the solar surface: poleward surface and sub-surface flows with velocities up to a few tens of meters per second have been observed by measurements of photospheric line-shifts (Labonte & Howard 1982) and by time-distance helioseismology (Giles et al. 1997) respectively.

The amplitude and spatial distribution of these meridional flows deeper in the convection zone remains essentially unknown, as the sensitivity of helioseismic methods rapidly drops below the surface. As a result, the question of whether some of the pumped mass flux actually penetrates into the underlying radiative zone is still open, despite its obvious importance for mixing of chemical species (Pinsonneault, 1997; Elliott & Gough, 1999), and its presumed role in the dynamical balance of the solar interior (Gough & McIntyre 1998, McIntyre, 2007, Garaud, 2007, Garaud & Garaud, 2008) and in some models of the solar dynamo (see Charbonneau, 2005 for a review).

In Paper I (Garaud & Brummell, 2008), we began a systematic study of the penetration of meridional flows from the convection zone into the radiative zone by considering a related but

easier question: *assuming that the amplitude and geometry of meridional flows in the convection zone are both known*, what is their influence on the underlying radiative zone? This simpler question enabled us to study the dynamics of the radiative zone only by assuming a flow profile at the radiative–convective interface (instead of having to include the more complex convection zone in the calculation). The overwhelming conclusion of that first study was that the degree to which flows penetrate into the stratified interior (in the model) is *very* sensitive to the interfacial conditions selected. Hence, great care must be taken when using a "radiative-zone-only" model to make definite predictions about interior flow amplitudes. In addition, that approach makes the implicit assumption that the dynamics of the radiative zone do not in return influence those of the convection zone, but the only way to verify this is to construct a model which includes both regions. This was the original purpose of the present study; as we shall see, the combined radiative–convective model we construct here provides insight into a much broader class of problems.

We therefore propose a simplified model of the Sun which includes both a "convective" region and a "radiative" region, where the convective region is forced in such a way as to promote gyroscopic pumping of meridional flows. We calculate the flow solution everywhere and characterize how it scales in terms of governing parameters (e.g. stellar rotation rate, stratification, diffusivities, etc..), focusing in particular on the flows which are entering the radiative zone. We begin with a simple Boussinesq Cartesian model (Section 4.2), first in the unstratified limit (Section 4.2.3) and then in the more realistic case of a radiative–convective stratification (Section 4.2.4). Although the Cartesian results essentially illustrate most of the relevant physical phenomena, we confirm our analysis with numerical solutions of the full set of equations in a spherical geometry in Section 4.3. We then use this information in Section 4.4 to discuss the effects of mixing by meridional flows both in the Sun and in other Main Sequence stars.

4.2 A Cartesian model

4.2.1 Model setup

As in Paper I, we first study the problem in a Cartesian geometry. Since our primary aim is to understand the behavior of the meridional flows generated (e.g. scaling of the solutions) in terms of the governing parameters, this approach is sufficient and vastly simplifies the required algebra. In Section 4.3, we turn to numerical simulations to study the problem in a spherical geometry.

In this Cartesian model section, distances are normalized to the solar radius $R_\odot$, and velocities to $R_\odot\Omega_\odot$ where $\Omega_\odot$ is the mean solar angular velocity (the exact value is not particularly relevant here). The coordinate system is (x, y, z), where x should be thought of as the azimuthal coordinate ϕ, with $x \in [0, 2\pi]$; y represents minus the co-latitude and spans the interval $y \in [0, \pi]$ (the poles are at $y = 0$ and $y = \pi$ while the equator is at $y = \pi/2$). Finally the z-direction is the radial direction with $z \in [0, 1]$, and represents the direction of (minus) gravity so that $z = 0$ is the interior, and $z = 1$ is the surface.

In this framework, the system rotates with mean angular velocity $\mathbf{\Omega} = (0, 0, 1)$, thereby implicitly assuming that the rotation axis is everywhere aligned with gravity. This assumption induces another "geometric" error in the velocity estimates for the meridional flows, comparable with the error made in reducing the problem to a Cartesian analysis; it does not influence the predicted scalings (except in small equatorial regions which we ignore here).

We divide the domain in two regions, by introducing the dimensionless constant h to represent the radiative–convective interface. Thus $z \in [0, h]$ represents the "radiative zone" while $z \in [h, 1]$ represents the "convection zone". From here on, $h = 0.7$. Figure 4.1 illustrates the geometry of the Cartesian system.

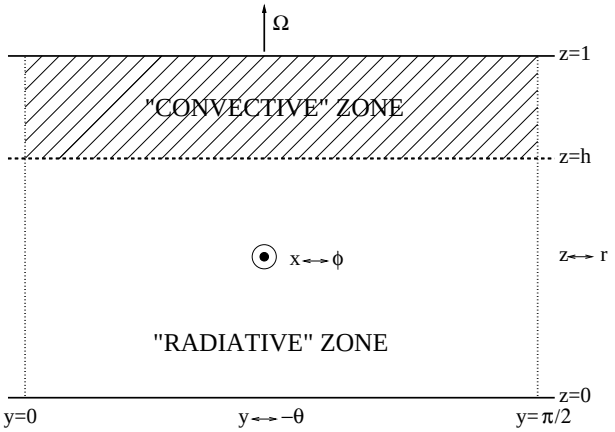

Figure 4.1: Cartesian model geometry and intended correspondence with the spherical case. The shaded area marks the convective region, where forcing is applied. The $y = 0$ and $y = \pi/2$ lines mark the "poles" and the "equator". The system is assumed to be periodic with period π in the $y-$direction.

4.2.2 Model equations

For this simple Cartesian approach, we work with the Boussinesq approximation (this assumption is dropped in the spherical model but doesn't affect the predicted scalings). The background state is assumed to be stratified, steady, and in hydrostatic equilibrium. The background density and temperature profiles are denoted by $\bar{T}(z)$ and $\bar{\rho}(z)$ respectively. Density and temperature perturbations to this background state (ρ and T) are then assumed to be linearly related: $\rho = -\alpha_T(z)T$, where $\alpha_T(z)$ is the coefficient of thermal expansion. For simplicity, we will assume that the background temperature gradient $\bar{T}_z$ is constant throughout the domain $z \in [0, 1]$, and treat the convection zone as a region where $\alpha_T \to 0$ while the radiative zone has $\alpha_T \neq 0$ (see below). The alternative option of using a constant α_T and a varying $\bar{T}_z$ yields qualitatively equivalent scalings for the meridional flows (a statement which is verified in Section 4.3) although the algebra is trickier.

The set of equations governing the system in this approximation are the momentum,

mass and thermal energy conservation equations respectively:

$$\begin{aligned}
\frac{\partial \mathbf{u}}{\partial t} + \mathbf{u}\cdot\nabla\mathbf{u} + 2\mathbf{e}_z \times \mathbf{u} &= -\nabla p + \mathrm{Ro}^2(z) T \mathbf{e}_z + \mathrm{E}_\nu \nabla^2 \mathbf{u} \ , \\
\nabla \cdot \mathbf{u} &= 0 \ , \\
\frac{\partial T}{\partial t} + \mathbf{u}\cdot\nabla T + \mathbf{u}\cdot\mathbf{e}_z &= \frac{\mathrm{E}_\nu}{\mathrm{Pr}} \nabla^2 T \ ,
\end{aligned} \tag{4.1}$$

where $\mathbf{u} = (u, v, z)$ is the velocity field. In these equations, temperature perturbations have been normalized to the background temperature difference across the box $R_\odot \bar{T}_z$. The governing non-dimensional parameters are:

$$\begin{aligned}
\mathrm{Ro}(z) &= N(z)/\Omega_\odot \text{ the Rossby number} \ , \\
\mathrm{E}_\nu &= \frac{\nu}{R_\odot^2 \Omega_\odot} \text{ the Ekman number} \ , \\
\mathrm{Pr} &= \frac{\nu}{\kappa_T} \text{ the Prandtl number} \ ,
\end{aligned} \tag{4.2}$$

where the dimensional quantity $N^2(z) = \alpha_T(z)\bar{T}_z g$ is the square of the Brunt-Väisälä frequency (g is the magnitude of gravity and is assumed to be constant). The microscopic diffusion coefficients ν (the viscosity) and κ_T (the thermal conductivity) are both assumed to be constant. In the Sun, near the radiative–convective interface, $\mathrm{E}_\nu \simeq 2 \times 10^{-15}$ and $\mathrm{Pr} \simeq 2 \times 10^{-6}$ (Gough, 2007).

As mentioned earlier, the transition between the model radiative zone and convection zone is measured by the behavior of $\alpha_T(z)$, which goes from 0 for $z > h$ to a finite value for $z < h$. This can be modeled in a non-dimensional way through the Rossby number, which we assume is of the form:

$$\mathrm{Ro}(z) = \frac{\mathrm{Ro}_{\mathrm{rz}}}{2}\left[1 + \tanh\left(\frac{h - z}{\Delta}\right)\right] \ , \tag{4.3}$$

where $\mathrm{Ro}_{\mathrm{rz}}$ is constant. The lengthscale Δ may be thought of as the thickness of the "overshoot" region near the base of the convection zone, but in practice is mostly used to ensure continuity and smoothness of the background state through the tanh function.

In what follows, we further restrict our study to an "axially" symmetric ($\partial/\partial x = 0$), steady-state ($\partial/\partial t = 0$) problem. Within the radiative zone, the nonlinear terms $\mathbf{u}\cdot\nabla\mathbf{u}$ and $\mathbf{u}\cdot\nabla T$ are assumed to be negligible. Within the convection zone on the other hand, anisotropic turbulent stresses are thought to drive the observed differential rotation[1]. We model this effect in the simplest possible way, replacing the divergence of the stresses by a linear relaxation towards the observed convection zone profile:

$$\mathbf{u}\cdot\nabla\mathbf{u} \rightarrow \mathbf{F}_{\rm turb} = \frac{\mathbf{u}-\mathbf{u}_{\rm cz}}{\tau} \ , \tag{4.4}$$

where $\mathbf{u}_{\rm cz} = u_{\rm cz}(y,z)\mathbf{e}_x$ and the function $u_{\rm cz}(y,z)$ models the observed azimuthal velocity profile in the solar convection zone. This is analogous to the prescription used by Spiegel & Bretherton (1968) in their study of the effect of a convection zone on solar spin-down, although in their model the convection zone was not differentially rotating. The dimensionless relaxation timescale τ can be thought of, for example, as being of the same order of magnitude as the convective turnover time divided by the rotation period. It is modeled as:

$$\tau^{-1}(z) = \frac{\Lambda}{2}\left[1+\tanh\left(\frac{z-h}{\Delta}\right)\right] \ . \tag{4.5}$$

Note that in the real solar convection zone, τ varies by orders of magnitudes between the surface ($\tau\sim 10^{-3}$) and the bottom of the convection zone ($\tau\sim 1$). Here, we assume that Λ is constant for simplicity.

We adopt the following profile for $u_{\rm cz}(y,z)$:

$$\begin{aligned} u_{\rm cz}(y,z) &= \frac{U_0(z)}{2}\left[1+\tanh\left(\frac{z-h}{\Delta}\right)\right]e^{iky} = \hat{u}_{\rm cz}(z)e^{iky} \ , \\ U_0(z) &= U_0(h) + S(z-h) \ , \end{aligned} \tag{4.6}$$

where $k=2$ to match the equatorial symmetry of the observed solar rotation profile. The tanh function once again is merely added to guarantee continuity of the forcing across the overshoot

[1]Note that for slowly rotating stars, such as the Sun, the direct generation of meridional flows by anisotropic stresses is a much weaker effect in the bulk of the convection zone. We neglect it here.

layer. The function $U_0(z)$ describes the imposed "vertical shear", and is for simplicity taken to be a linear function of z. If $U_0(h) = 0$, the forcing effectively vanishes at the base of the convection zone. If $U_0(h) \neq 0$ on the other hand, a strong azimuthal shear is forced at the interface. The observed solar rotation profile appears to be consistent with $U_0(h)$ and S both being non-zero (and of the order of 0.1, although since we are studying a linear problem, the amplitude of the forcing is somewhat irrelevant). Note that if $S = 0$ the forcing velocity $\mathbf{u}_{\rm cz}$ has zero vorticity.

Finally, the observed asphericity in the temperature profile is negligible in the solar convection zone; this is attributed to the fact that the turbulent convection very efficiently mixes heat both vertically and horizontally. We model this effect as:

$$\mathbf{u} \cdot \nabla T \rightarrow -D(z)\nabla^2 T \ , \tag{4.7}$$

where the turbulent heat diffusion coefficient is modeled as

$$D(z) = \frac{D_0}{2}\left[1 + \tanh\left(\frac{z-h}{\Delta}\right)\right] \ , \tag{4.8}$$

and thus vanishes beneath the overshoot layer. We will assume that the diffusion timescale $1/D_0$ (in non-dimensional units) is much smaller than any other typical timescale in the system ($D_0 \gg 1$).

Projecting the remaining equations into the Cartesian coordinate system, and seeking

solutions in the form $q(y,z) = \hat{q}(z)e^{iky}$ for each of the unknown quantities yields

$$
\begin{aligned}
-2\hat{v} &= \mathrm{E}_\nu \left(\frac{\mathrm{d}^2\hat{u}}{\mathrm{d}z^2} - k^2\hat{u} \right) - \frac{\hat{u} - \hat{u}_{\mathrm{cz}}}{\tau} \ , \\
2\hat{u} &= -ik\hat{p} + \mathrm{E}_\nu \left(\frac{\mathrm{d}^2\hat{v}}{\mathrm{d}z^2} - k^2\hat{v} \right) - \frac{\hat{v}}{\tau} \ , \\
0 &= -\frac{\mathrm{d}\hat{p}}{\mathrm{d}z} + \mathrm{Ro}^2(z)\hat{T} + \mathrm{E}_\nu \left(\frac{\mathrm{d}^2\hat{w}}{\mathrm{d}z^2} - k^2\hat{w} \right) - \frac{\hat{w}}{\tau} \ , \\
ik\hat{v} &+ \frac{\mathrm{d}\hat{w}}{\mathrm{d}z} = 0 \ , \\
\hat{w} &= \left(\frac{\mathrm{E}_\nu}{\mathrm{Pr}} + D(z) \right) \left(\frac{\mathrm{d}^2\hat{T}}{\mathrm{d}z^2} - k^2\hat{T} \right) \ ,
\end{aligned} \tag{4.9}
$$

Note that as required, the imposed forcing term drags the fluid in the azimuthal direction: for $\tau \to 0$, $\hat{u} \to \hat{u}_{\mathrm{cz}}$ in the convection zone. The meridional flows $\hat{v}$ and $\hat{w}$ on the other hand are generated by the $y-$component of the Coriolis force and by mass conservation respectively (the essence of gyroscopic pumping, see McIntyre 2007).

We now proceed to solve these equations to gain a better understanding of the meridional flows and their degree of penetration into the radiative zone below. We use a dual approach, solving these equations first analytically under various limits, and then exactly using a simple Newton-Raphson-Kantorovich (NRK) two-point boundary value algorithm. The analytical approximations yield predictions for the relevant scalings of the solutions in terms of the governing parameters (an in particular, the Ekman number and the Rossby number) which are then confirmed by the exact numerical solutions.

4.2.3 The unstratified case

Although this limit is not a priori relevant to the physics of the solar interior, we begin by studying the case of an unstratified region, setting $\mathrm{Ro}_{\mathrm{rz}} = 0$ (in this case, the thermal energy equation can be discarded). This simpler problem, as we shall demonstrate, contains the essence of the problem.

In order to find analytical approximations to the solutions, we solve the governing equations separately in the convective zone and in the radiative zone. At this point, it may be worth pointing out that in the unstratified case, the nomenclatures "convective" and "radiative" merely refer to regions which respectively are and are not subject to the additional forcing.

We assume that the transition region is very thin[2]. In this case, $\tau^{-1} = \Lambda$ for $z > h$ while $\tau^{-1} = 0$ for $z < h$. Similarly, $\hat{u}_{\rm cz}(z) = U_0(h) + S(z-h)$ in the convection zone while $\hat{u}_{\rm cz}(z) = 0$ in the radiative zone. Once obtained, the solutions are patched at the radiative–convective interface.

4.2.3.1 Solution in the convection zone

In the convection zone, the equations reduce to

$$\begin{aligned} -2\hat{v} &= -\Lambda(\hat{u} - \hat{u}_{\rm cz}) \ , \\ 2\hat{u} &= -ik\hat{p} - \Lambda\hat{v} \ , \\ 0 &= -\frac{\mathrm{d}\hat{p}}{\mathrm{d}z} - \Lambda\hat{w} \ , \\ ik\hat{v} &+ \frac{\mathrm{d}\hat{w}}{\mathrm{d}z} = 0 \ , \end{aligned} \tag{4.10}$$

where we have neglected the viscous dissipation terms in favor of the forcing terms since $E_\nu \ll \Lambda$ for all reasonable solar parameters. Combining them yields

$$\frac{\mathrm{d}^2\hat{w}}{\mathrm{d}z^2} = \frac{k^2\Lambda^2}{4+\Lambda^2}\hat{w} + 2ik\frac{\Lambda}{4+\Lambda^2}\frac{\mathrm{d}\hat{u}_{\rm cz}}{\mathrm{d}z} \ . \tag{4.11}$$

This second-order ordinary differential equation[3] for $\hat{w}(z)$ suggests the introduction of a new lengthscale

$$\delta = \frac{\sqrt{4+\Lambda^2}}{k\Lambda} \ , \tag{4.12}$$

[2] More precisely, $\Delta \ll \mathrm{E}_\nu^{1/2}$, see Section 4.2.3.5.

[3] The original order of the system is much reduced in the convection zone since we ignored the effect of viscous terms there.

so that the general solution to (4.10) is

$$\begin{aligned}
\hat{w}(z) &= Ae^{z/\delta} + Be^{-z/\delta} - \frac{2iS}{k\Lambda} \ , \\
\hat{v}(z) &= -\frac{1}{ik\delta}\left[Ae^{z/\delta} - Be^{-z/\delta}\right] \ , \\
\hat{u}(z) &= \hat{u}_{\rm cz}(z) - \frac{2}{ik\Lambda\delta}\left[Ae^{z/\delta} - Be^{-z/\delta}\right] \ , \\
\hat{p}(z) &= -\frac{2}{ik}\hat{u}_{\rm cz}(z) - \delta\Lambda\left[Ae^{z/\delta} - Be^{-z/\delta}\right] \ .
\end{aligned} \tag{4.13}$$

The constants A and B are integration constants which must be determined by applying boundary conditions (at $z = 1$) and matching conditions (at $z = h$). Note from the $\hat{u}$-equation that the actual rotation profile approaches the imposed (observed) profile $\hat{u}_{\rm cz}$ provided A and B tend to 0, or when $\Lambda \gg 2$ (in which case $\delta \to 1/k$).

4.2.3.2 Solution in the radiative zone with stress-free lower boundary, and matching

In the radiative region, the equations reduce to

$$\begin{aligned}
-2\hat{v} &= \mathrm{E}_\nu\left(\frac{\mathrm{d}^2\hat{u}}{\mathrm{d}z^2} - k^2\hat{u}\right) \ , \\
2\hat{u} &= -ik\hat{p} \ , \\
\frac{\mathrm{d}\hat{p}}{\mathrm{d}z} &= 0 \ , \\
ik\hat{v} + \frac{\mathrm{d}\hat{w}}{\mathrm{d}z} &= 0 \ ,
\end{aligned} \tag{4.14}$$

if we neglect viscous stresses in both y and z components of the momentum equation. Note that viscous stresses in the $x-$equation cannot be dropped since they are the only force balancing

the Coriolis force. These equations are easily solved:

$$\begin{aligned}
\hat{p}(z) &= p_{\rm rz} \ , \\
\hat{u}(z) &= -\frac{ik}{2} p_{\rm rz} \ , \\
\hat{v}(z) &= -\frac{iE_\nu k^3}{4} p_{\rm rz} \ , \\
\hat{w}(z) &= w_{\rm rz} - \frac{E_\nu k^4}{4} p_{\rm rz} z \ ,
\end{aligned} \tag{4.15}$$

where $p_{\rm rz}$ and $w_{\rm rz}$ are two additional integration constants. Here, we recover the standard Taylor-Proudman constraint where in the absence diffusion or any other stresses, the velocity must be constant along the rotation axis (here, $\mathbf{e}_z$); in the limit $\mathrm{E}_\nu \to 0$, $\hat{u}(z)$ and $\hat{w}(z)$ become independent of z, while $\hat{v}(z) \to 0$.

We are now able to match the solution in the radiative zone to that of the convection zone. The two constants $p_{\rm rz}$ and $w_{\rm rz}$ form, together with A and B, a set of 4 unknown constants which are determined by application of boundary and matching conditions. Since we have neglected viscous effects in the convection zone, we cannot require any boundary or matching condition on the horizontal fluid motions. On the other hand, we are allowed to impose impermeability $\hat{w} = 0$ at the surface ($z = 1$) and at the bottom ($z = 0$). Moreover, we request the continuity of the radial (vertical) velocity and of the pressure at the interface ($z = h$). Applying these conditions yields the set of equations

$$\begin{aligned}
w_{\rm rz} &= 0 \ , \\
Ae^{h/\delta} + Be^{-h/\delta} - \frac{2iS}{k\Lambda} &= w_{\rm rz} - \frac{\mathrm{E}_\nu k^4}{4} p_{\rm rz} h \ , \\
-\frac{2}{ik} U_0(h) - \delta\Lambda \left[Ae^{h/\delta} - Be^{-h/\delta} \right] &= p_{\rm rz} \ , \\
Ae^{1/\delta} + Be^{-1/\delta} - \frac{2iS}{k\Lambda} &= 0 \ ,
\end{aligned} \tag{4.16}$$

which have the following solution for A and B:

$$A = \frac{\frac{\mathrm{E}_\nu h k^3}{2i} U_0(h) + \frac{2iS}{k\Lambda}\left[1 - e^{(1-h)/\delta}\left[1 + \frac{E_\nu k^4}{4} h\delta\Lambda\right]\right]}{e^{h/\delta}\left[1 - \frac{E_\nu k^4}{4} h\delta\Lambda\right] - e^{(2-h)/\delta}\left[1 + \frac{E_\nu k^4}{4} h\delta\Lambda\right]} ,$$

$$B = \frac{2iS}{k\Lambda} e^{1/\delta} - A e^{2/\delta} . \tag{4.17}$$

These can be substituted back into (4.13) to obtain the meridional flow velocities in the convection zone. While the exact form of A and B are not particularly informative, we note that in the limit $S = 0$ (i.e. the forcing velocity has no azimuthal vorticity), both A and B scale as E_ν. This implies that the amplitude of meridional flows everywhere in the solar interior scales like E_ν (even in the convection zone). The physical interpretation of this somewhat surprising limit is discussed in Section 4.2.3.4, but turns out to be of academic interest only (Section 4.2.3.5).

When $S \neq 0$ then A and B are of order $S/k\Lambda$ in the convection zone regardless of the Ekman number, and respectively tend to

$$A = \frac{2iS}{k\Lambda} \frac{1 - e^{(1-h)/\delta}}{e^{h/\delta} - e^{(2-h)/\delta}} + O(\mathrm{E}_\nu) ,$$

$$B = \frac{2iS}{k\Lambda} \frac{1 - e^{(h-1)/\delta}}{e^{-h/\delta} - e^{(h-2)/\delta}} + O(\mathrm{E}_\nu) , \tag{4.18}$$

as $\mathrm{E}_\nu \to 0$. This implies that $\hat{w}$ is of order $S/k\Lambda$ in the convection zone. Since significant flows are locally generated, one may reasonably expect a fraction of the forced mass flux to penetrate into the lower region, especially in this unstratified case.

Using (4.17) in (4.16), solving for p_{rz}, then plugging p_{rz} into (4.15), we find that the general expression for $\hat{w}(z)$ *in the radiative zone* $z \in [0, h]$ is

$$\hat{w}(z) = -\frac{iE_\nu k^3}{2}\left(U_0(h) + \frac{\cosh((1-h)/\delta) - 1}{\sinh((1-h)/\delta)} \delta S\right) z . \tag{4.19}$$

This implies that only a *tiny* fraction of the large mass flux circulating in the convection zone actually enters the radiative zone. Instead, the system adjusts itself in such a way as to ensure that most of the meridional flows return above the base of the convection zone.

We now compare this a priori counter-intuitive[4] analytical result with exact numerical solutions of the governing equations. The numerical solutions were obtained by solving (4.9) for $\mathrm{Ro_{rz}} = 0$ (unstratified case), and are uniformly calculated in the whole domain (i.e. there is nothing special about the interfacial point $z = h$). The boundary conditions used are impermeable boundary conditions at the top and bottom of the domain for $\hat{w}$, and stress-free boundary conditions for $\hat{u}$ and $\hat{v}$.

In Figure 4.2 we compare numerical and analytical solutions for $\hat{w}(z)$, in a case where the forcing function parameters are $\Delta = 10^{-4}$, $\Lambda = 10$, $U_0(h) = 0$ and $S = 1$, for four values of the Ekman number. The analytical solution is described by equations (4.13) and (4.17) (for the convection zone) and (4.15) (for the radiative zone). As $\mathrm{E}_\nu \to 0$ the numerical solution approaches the analytically derived one, confirming in particular that $\hat{w}(z) \propto z\mathrm{E}_\nu$ in the radiative zone. The convection zone solution is also well-approximated in this case by the analytical formula.

A full 2D visualization of the flow for $\mathrm{E}_\nu = 10^{-4}$ but otherwise the same governing parameters is shown in Figure 4.3. This figure illustrates more clearly the fact that the meridional flows are negligible below the interface, and mostly return within the convection zone. Note that given our choice of the forcing function $u_{\mathrm{cz}}(y, z) \propto \cos(2y)$, the induced Coriolis force does not vanish at $y = 0$ or $y = \pi$ (the "poles"). This explains why the meridional flows apparently cross the polar axis in this simple model. This is merely a geometric effect: in a true spherical geometry the forcing azimuthal velocity $u_{\mathrm{cz}}(r, \theta)$ would be null at the poles, and meridional flows cannot cross the polar axis. More realistic calculations in spherical geometry are discussed in Section 4.3.

Finally, it is interesting to note that the analytical solution for the azimuthal velocity

[4] but a posteriori obvious, see Section 4.2.3.4

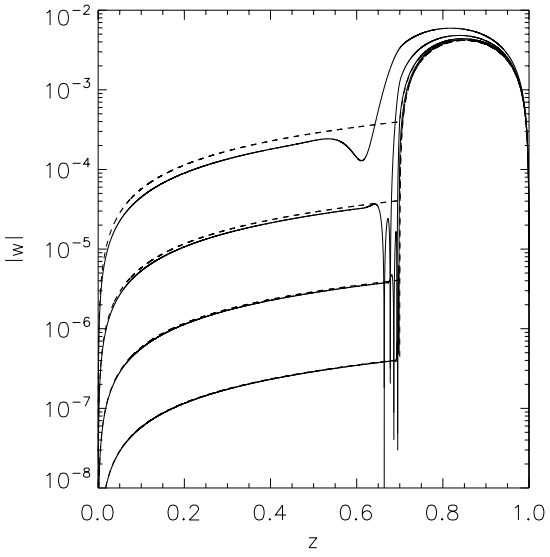

Figure 4.2: Numerical (solid) and analytical (dashed) solutions for $|\hat{w}(z)|$, in the case of a stress-free bottom boundary. From the uppermost to lowermost curves, $E_\nu = 10^{-3}$, 10^{-4}, 10^{-5} and 10^{-6} respectively, confirming the analytical scaling that $\hat{w}(z) \propto \mathrm{E}_\nu z$ in the radiative zone while $\hat{w}(z)$ becomes independent of E_ν in the convection zone. These solutions were obtained with forcing defined by the parameters $\Delta = 10^{-4}$, $\Lambda = 10$, $U_0(z) = S(z-h)$ and $S = 1$.

$\hat{u}(z)$ exhibits a "discontinuity" across the base of the convection zone, which tends to

$$\hat{u}(h^+) - \hat{u}(h^-) = \left(\frac{2}{ik\delta\Lambda} + \frac{ik\delta\Lambda}{2}\right)\left(Ae^{h/\delta} - Be^{-h/\delta}\right) \tag{4.20}$$

as $\mathrm{E}_\nu \to 0$. The numerical solutions of course are continuous, but the continuity is only assured by the viscosity in the system (in the $y-$ direction) and the fact that the overshoot layer depth is finite. This is shown in Figure 4.4, together with a comparison of the numerical solutions with the analytical solution, again confirming the analytical approximation derived.

This highlights another and equally a priori counter-intuitive property of the system: the value of u_{rz} in the radiative zone is markedly different from the imposed $\hat{u}_{\mathrm{cz}}(h) = U_0(h)$ at the interface:

$$u_{\mathrm{rz}} = U_0(h) + \frac{ik\delta\Lambda}{2}\left(Ae^{h/\delta} - Be^{-h/\delta}\right) \ . \tag{4.21}$$

Hence, even if the imposed differential rotation is exactly 0 at the radiative–convective interface

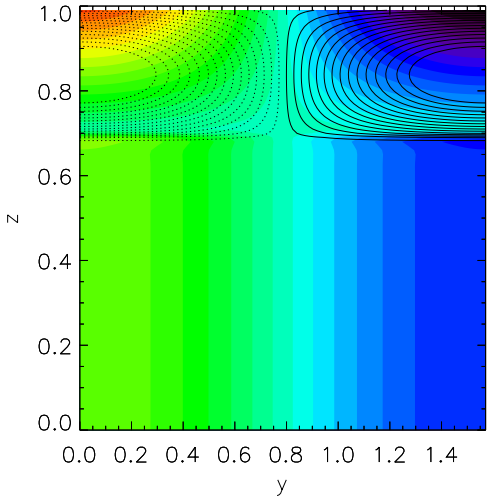

Figure 4.3: 2D visualization of the flow for $E_\nu = 10^{-4}$, in the case of a stress-free bottom boundary. Shown as solid and dotted line respectively are linearly spaced streamlines of counter-clockwise and clockwise meridional flows. As predicted, the flows appear to return entirely within the convection zone and carry a negligible mass flux into the radiative zone. Meanwhile the azimuthal velocity ($\hat{u}$) as displayed in the filled contours is constant along the rotation axis ($z-$axis) below the interface ($z = h = 0.7$), but is strongly sheared at the interface. This solution was obtained with forcing defined by the parameters $\Delta = 10^{-4}$, $\Lambda = 10$, $U_0(z) = S(z-h)$ and $S = 1$, as in Figure 4.2.

(as it is the case in the simulation presented in Figure 4.4 since $U_0(z) = S(z-h)$), a large-scale latitudinal shear measured by $u_{\rm rz}$ may be present in the radiative zone, as illustrated in Figure 4.3. This shows that the propagation of the azimuthal shear into the radiative zone is non-local (i.e. does not rely on the presence of shear at the interface), and is instead communicated by the long-range pressure gradient.

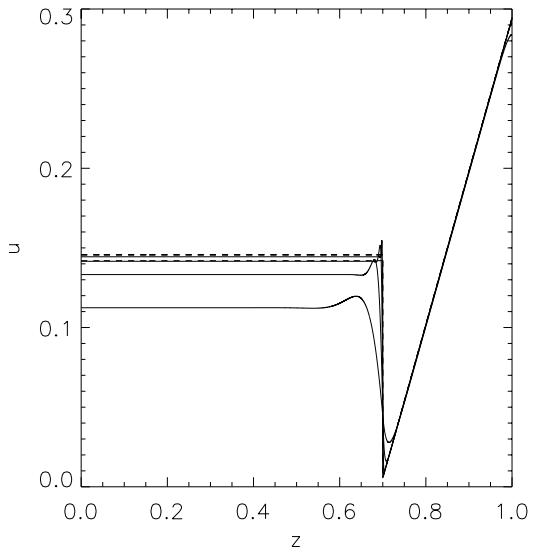

Figure 4.4: Numerical (solid) and analytical (dashed) solutions for $\hat{u}(z)$, in the case of a stress-free bottom boundary. From the lowermost to uppermost curves, $E_\nu = 10^{-3}$, 10^{-4}, 10^{-5} and 10^{-6} respectively, confirming that $\hat{u}(z)$ tends to a constant in the radiative zone, while sustaining a finite discontinuity at the radiative-convective interface ($z = h = 0.7$). These solutions were obtained with forcing defined by the parameters $\Delta = 10^{-4}$, $\Lambda = 10$, $U_0(z) = S(z-h)$ and $S = 1$, as in Figure 4.2.

4.2.3.3 Solution in the case of no-slip bottom boundary

The stress-free bottom boundary conditions studied in the previous Section are at first glance the closest to what one may expect in the real Sun, where the "bottom" boundary merely represents the origin of the spherical coordinate system. However, let us now explore for completeness (and for further reasons that will be clarified in the next Section) the case of

no-slip bottom boundary conditions.

When the lower boundary is a no-slip boundary, the nature of the solution in the whole domain changes. This change is induced by the presence of an Ekman boundary layer, which forms near $z = 0$. Just above the boundary layer, in the bulk of the radiative zone, the solution described in 4.2.3.2 remains valid. However, matching the bulk solution with the boundary conditions can no longer be done directly; one must first solve for the boundary layer dynamics to match the bulk solution with the boundary conditions *across* the boundary layer. This is a standard procedure (summarized in Appendix A for completeness), and leads to the well-known "Ekman jump" relationship between the jump in $\hat{w}(z)$ and the jump in $\hat{u}(z)$ across the boundary layer:

$$\hat{u}_{\text{bulk}} - \hat{u}(0) = \frac{2i}{k} E_\nu^{-1/2} (\hat{w}_{\text{bulk}} - \hat{w}(0)) \ . \tag{4.22}$$

By impermeability, $\hat{w}(0) = 0$. Moreover, by assuming that the total angular momentum of the lower boundary is the same as that of the convection zone, we require that $\hat{u}(0) = 0$. Meanwhile, $\hat{u}_{\text{bulk}} = u_{\text{rz}}$ and $\hat{w}_{\text{bulk}} = w_{\text{rz}}$ in the notation of equation (4.15). So finally, for no-slip boundary conditions, we simply replace the impermeability condition ($w_{\text{rz}} = 0$) in (4.16) by

$$u_{\text{rz}} = \frac{2i}{k} E_\nu^{-1/2} w_{\text{rz}} \ , \tag{4.23}$$

and solve for the unknown constants A, B, w_{rz} and p_{rz} as before.

The exact expressions for the resulting integration constants A and B are now slightly different from those given in (4.17), but are without particular interest. However, it can be shown that they have the same limit as in the stress-free case as $\mathrm{E}_\nu \to 0$ (with $S \neq 0$). This implies that the meridional flows driven *within the convection zone*, in the limit $\mathrm{E}_\nu \to 0$, and with $S \neq 0$, are independent of the boundary condition selected at the bottom of the radiative

zone. However, we now have the following expression for $\hat{w}(z)$ in the bulk of the radiative zone:

$$\begin{aligned}\hat{w}(z) &= -\left(\frac{k^2}{4}E_\nu^{1/2} + \frac{E_\nu k^4}{4}z\right)p_{\rm rz}\ , \\ &= -\frac{ik}{2}E_\nu^{1/2}\left(U_0(h) + \frac{\cosh((1-h)/\delta)-1}{\sinh((1-h)/\delta)}\delta S\right) + O(\mathrm{E}_\nu)z\ , \end{aligned} \tag{4.24}$$

which has one fundamental consequence: the amplitude of the flows allowed to penetrate into the radiative zone is now of order $E_\nu^{1/2}$ instead of being $O(\mathrm{E}_\nu)$. This particular statement is actually true even if $S = 0$, although in that case both convection zone and radiative zone flows scale with $E_\nu^{1/2}$.

Figure 4.5 shows a comparison between the approximate analytical formula and the numerical solution for the same simulations as in Figure 4.2, but now using no-slip bottom boundary conditions. For ease of comparison, the results from the stress-free numerical simulations (for exactly the same parameters) have also been drawn, highlighting the much larger amplitude of the meridional flows down-welling into the radiative zone in the no-slip case, and their scaling with $E_\nu^{1/2}$. Figure 4.6 shows an equivalent 2D rendition of the solution, and illustrates the presence of large-scale mixing in the bulk of the radiative zone when the bottom-boundary is no-slip.

4.2.3.4 Physical interpretation

The various sets of solutions derived above can be physically understood in the following way. Let us first discuss the solution in the convection zone. In the limit where $u_{\rm cz}(y,z)$ is independent of z (equivalently, $S = 0$), the azimuthal ($x-$) component of the vorticity of the forcing is zero. In that case there is no injection of $x-$vorticity into the system aside from that induced in the viscous boundary layers, and the amplitude of the meridional flows generated in the convection zone scales with E_ν. This limit is somewhat academic in the case of the Sun, however given the observed rotation profile (see also Section 4.2.3.5). When $S \neq 0$, the

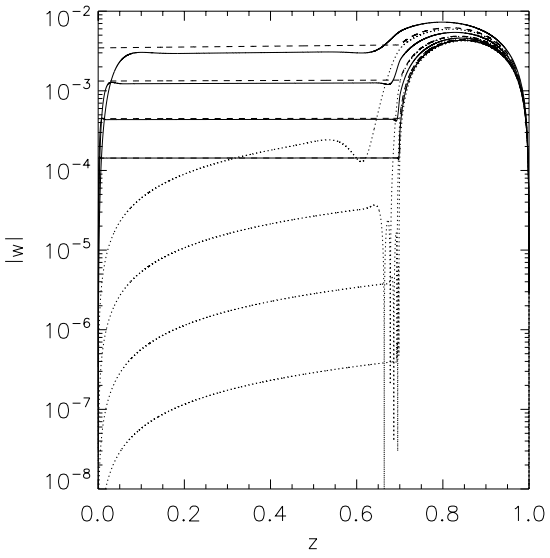

Figure 4.5: Numerical (solid) and analytical (dashed) solutions for $|\hat{w}(z)|$, in the case of a no-slip bottom boundary. From the uppermost to lowermost curves (as seen in the radiative zone), $E_\nu = 10^{-3}$, 10^{-4}, 10^{-5} and 10^{-6} respectively, confirming the analytical scaling that $\hat{w}(z) \propto \mathrm{E}_\nu^{1/2}$ in the radiative zone while $\hat{w}(z)$ becomes independent of E_ν in the convection zone. These solutions were obtained with forcing defined by the parameters $\Delta = 10^{-4}$, $\Lambda = 10$, $U_0(z) = S(z-h)$ and $S = 1$, as in Figure 4.2. For comparison, the previous simulations with stress-free bottom boundary, for the same parameters, are shown as dotted lines.

amplitude of the induced meridional flows in the convection zone scales linearly with S and is independent of viscosity.

In the radiative zone, the Taylor-Proudman constraint enforces invariance of the flow velocities along the rotation axis, except in regions where other forces balance the Coriolis force. In the non-magnetic, unstratified situation discussed in the two previous sections, the only agent capable of breaking the Taylor-Proudman constraint are viscous stresses, which are only significant in two thin boundary layers: one right below the convection zone and the other one near the bottom boundary. *These two layers are the only regions where flows down-welling into the radiative zone are allowed to return to the convection zone.* The question then remains of what fraction of the mass flux entering the radiative zone returns within the upper Ekman

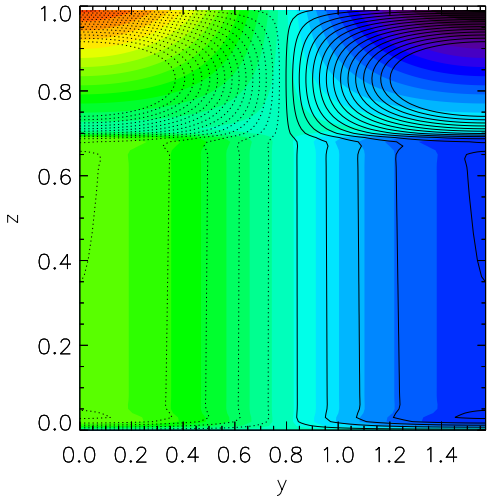

Figure 4.6: The same as for Figure 4.3 but for no-slip boundary conditions. The Ekman layer near the lower boundary is clearly visible. For ease of comparison, the same streamlines are shown in the two plots. The two figures illustrate how the nature of the lower boundary condition influences the mass flux through the radiative zone.

layer, and what fraction returns within the lower Ekman layer. The latter, of course, permits large-scale mixing within the radiative zone.

In the first case studied, the bottom boundary was chosen to be stress-free. This naturally suppresses the lower viscous boundary layer so that the only place where flows are allowed to return is at the radiative-convective interface. As a result, only a tiny fraction of the mass flux penetrates below $z = h$, and the turnover time of the remaining flows within the radiative zone is limited to a viscous timescale of the order of $1/\mathrm{E}_\nu\Omega_\odot$.

Following this reasoning, we expect and indeed find quite a different behavior when the bottom boundary is no-slip. In that case viscous stresses within the lower boundary layer break the Taylor-Proudman constraint and allow a non-zero mass flux (of order $\mathrm{E}_\nu^{1/2}$) to return near $z = 0$. This flow then mixes the entire radiative zone as well, with an overall turnover time of order of $1/\mathrm{E}_\nu^{1/2}\Omega_\odot$ (in dimensional units).

To summarize, in this unstratified steady-state situation, the amount of mixing induced within the radiative zone by convective zone flows depends (of course) on the amplitude of the convection zone forcing, but also on the existence of a mechanism to break the Taylor-Proudman constraint somewhere within the radiative zone. That mechanism is needed in order to allow downwelling flows to return to the convection zone. But more crucially, this phenomenon implies that the dynamics of the lower boundary layer entirely control the mass flux through the system.

Here, we studied the case of viscous stresses only. One can rightfully argue that there are no expected "solid" boundaries in a stellar interior and that the overall behavior of the system should be closer to the one discussed in the stress-free case than the no-slip case. *However, we chose here to study viscous stresses simply because they are the easiest available example.* In real stars viscous stresses are likely to be negligible compared with a variety of other possible stresses: turbulent stresses at the interface with another convection zone, magnetic forces, etc. Nevertheless, these stresses will play a similar role in allowing flows to mix the radiative zone if they become comparable in amplitude with the Coriolis force, and help break the Taylor-Proudman constraint. This issue is discussed in more detail in Section 4.4.

4.2.3.5 The thickness of the overshoot layer

Before moving on to the more realistic stratified case, note that this unstratified system holds one final subtlety. In all simulations presented earlier, the overshoot layer depth was selected to be very small – and in particular, smaller than the Ekman layer thickness. In that case, the transition in the forcing at the base of the convection zone is indeed close to being a discontinuity, and the analytical solutions presented in Sections 4.2.3.1 and 4.2.3.2 are a good fit to the true numerical solution.

In the Sun, the overshoot layer depth Δ is arguably always thicker than an Ekman lengthscale $E_\nu^{1/2}$. When this happens, the solution "knows" about the exact shape of the forcing

function within the transition region, and therefore depends on it. This limit turns out to be rather difficult to study analytically, and since in the case of the Sun we do not know the actual profile of $\tau^{-1}(z)$, there is little point in exercise anyway.

We can explore the behavior of the system numerically, however, for the profile $\tau^{-1}(z)$ discussed in equation (4.5), in the limit where $\Delta > \mathrm{E}_\nu^{1/2}$. The example for which this effect matters the most is the somewhat academic limit where $S = 0$ in the convection zone, but $U_0(h) \neq 0$. In this case, the asymptotic analysis predicts that the meridional flow amplitudes are $O(\mathrm{E}_\nu^{1/2})$ in both the convection zone and in the radiative zone for the no-slip case. We see in Figure 4.7 that this is indeed the case in simulations where $\Delta \ll \mathrm{E}_\nu^{1/2}$. However, when the overshoot thickness is progressively increased and becomes larger than the Ekman layer thickness, the amplitude of the meridional circulation in the convection zone is no longer $O(\mathrm{E}_\nu^{1/2})$ but much larger. Meanwhile, the scaling of the radiative zone solutions with E_ν remain qualitatively correct. The difference with the analytical solution in the convection zone can simply be attributed to the fact that when the system knows about the shear *within* the overshoot layer the limit $S = 0$ is no longer relevant.

4.2.4 The stratified case

While the previous section provides interesting insight into the problem, notably on the role of the Taylor-Proudman constraint, we now move to the more realistic situation where stratification plays a role in the flow dynamics. In this section, we generalize our Cartesian study to take into account the stratification of the lower region ($\mathrm{Ro}_{\mathrm{rz}} \neq 0$). For this purpose, we go back to studying the full system of equations (4.9). As before, we first find approximate analytical solutions to derive the overall scaling of the solutions with governing parameters, and then compare them to the full numerical solutions of (4.9). The analytical solutions are obtained by solving the system in the convective region and radiative region separately, and matching

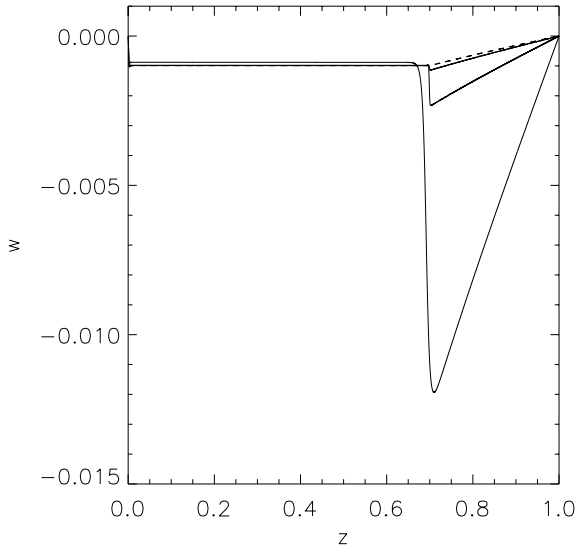

Figure 4.7: Comparison of numerical simulations (solid lines) with analytical prediction (dashed line) for a no-slip bottom boundary, for $\mathrm{E}_\nu = 10^{-6}$, and forcing functions defined with $\Lambda = 10$, $S = 0$ and $U_0(h) = 1$. The three numerical solutions are obtained for various values of the overshoot layer depth: from lowermost to uppermost curves (as seen in the convective zone), $\Delta = 10\mathrm{E}_\nu^{1/2}$, $\mathrm{E}_\nu^{1/2}$, and $0.1\mathrm{E}_\nu^{1/2}$. The analytical solution assumes an infinitely thin overshoot layer and is therefore independent of Δ. Note that the analytical solution in the convection zone is only a good approximation to the true solution if $\Delta \ll \mathrm{E}_\nu^{1/2}$. The overall scalings in the radiative zone, however, are preserved.

them at $z = h$.

4.2.4.1 Convection zone solution

The equations in the convection zone are now given by

$$\begin{aligned}
-2\hat{v} &= -\Lambda(\hat{u} - \hat{u}_{\mathrm{cz}}) \ , \\
2\hat{u} &= -ik\hat{p} - \Lambda\hat{v} \ , \\
0 &= -\frac{\mathrm{d}\hat{p}}{\mathrm{d}z} - \Lambda\hat{w} \ , \\
\hat{w} &= D_0\left(\frac{\mathrm{d}^2\hat{T}}{\mathrm{d}z^2} - k^2\hat{T}\right) \ , \\
ik\hat{v} &+ \frac{\mathrm{d}\hat{w}}{\mathrm{d}z} = 0 \ ,
\end{aligned} \tag{4.25}$$

where we have assumed that $D_0 \gg \mathrm{E}_\nu/\mathrm{Pr}$. Eliminating variables one by one yields the same equation for $\hat{w}(z)$ in the convection zone as before (4.11), as well as a Poisson equation for $\hat{T}$ once $\hat{w}$ is known. The solutions are then as (4.13), together with

$$\hat{T}(z) = T_0 e^{kz} + T_1 e^{-kz} + \frac{\delta^2 \left[A e^{z/\delta} + B e^{-z/\delta} \right]}{D_0(1-\delta^2 k^2)} + \frac{2iS}{k^3 \Lambda D_0} \ , \tag{4.26}$$

where the integration constants T_0 and T_1 remain to be determined. For the sake of analytical simplicity, we will assume that $D_0 \gg 1$ in all that follows (i.e. very large thermal diffusivity in the convection zone), and thus neglect the third and fourth terms in (4.26). This limit is relevant for the Sun.

4.2.4.2 Radiative zone solution

The radiative zone equations are now

$$\begin{aligned} -2\hat{v} &= E_\nu \left(\frac{\mathrm{d}^2 \hat{u}}{\mathrm{d}z^2} - k^2 \hat{u} \right) \ , \\ 2\hat{u} &= -ik\hat{p} \ , \\ 0 &= -\frac{\mathrm{d}\hat{p}}{\mathrm{d}z} + \mathrm{Ro}_{\mathrm{rz}}^2(z)\hat{T} \ , \\ \hat{w} &= \frac{\mathrm{E}_\nu}{\mathrm{Pr}} \left(\frac{\mathrm{d}^2 \hat{T}}{\mathrm{d}z^2} - k^2 \hat{T} \right) \ , \\ ik\hat{v} &+ \frac{\mathrm{d}\hat{w}}{\mathrm{d}z} = 0 \ , \end{aligned} \tag{4.27}$$

and can be combined to yield

$$\frac{\mathrm{d}^4 \hat{u}}{\mathrm{d}z^4} - k^2 \left(1 + \frac{\mathrm{PrRo_{rz}}^2}{4} \right) \frac{\mathrm{d}^2 \hat{u}}{\mathrm{d}z^2} + k^4 \frac{\mathrm{PrRo_{rz}}^2}{4} \hat{u} = 0 \ , \tag{4.28}$$

and similarly for $\hat{T}$. The characteristic polynomial is

$$(\lambda^2 - k^2) \left(\lambda^2 - \frac{\mathrm{PrRo_{rz}}^2}{4} k^2 \right) = 0 \ , \tag{4.29}$$

with solutions

$$\pm\lambda_1 = \pm k \ ,$$

$$\pm\lambda_2 = \pm\sqrt{\mathrm{Pr}}\frac{\mathrm{Ro_{rz}}}{2}k \ . \tag{4.30}$$

These solutions are the same as those presented in Paper I, and will be referred to as the "global-scale" mode and the thermo-viscous mode respectively. Note that here, λ_2 corresponds to k_2 in Paper I.

In this steady-state study, the quantity λ_2 summarizes the effect of stratification. It is important to note that it contains information about the rotation rate of the star as well as the Prandtl number, in addition to the buoyancy frequency. If $\lambda_2 \ll 1$, then the thermo-viscous mode essentially spans the whole domain: the system appears to be "unstratified", and is again dominated by the Taylor-Proudman constraint. On the other hand, if $\lambda_2 \gg 1$ then the flows only penetrate into the radiative zone within a small thermo-viscous boundary layer of thickness $1/\lambda_2$ as a result of the strong stratification of the system. The Taylor-Proudman constraint is irrelevant in this limit, since the magnitude of the buoyancy force is much larger than that of the Coriolis force.

The calculation above was made in the limit where the viscous terms in the latitudinal and radial components of the momentum equation are discarded. Paper I shows that two additional Ekman modes are also present if they are instead kept. By analogy with the unstratified case, we expect that these Ekman modes do not influence the solution for stress-free boundary conditions, but that additional care must be taken for no-slip boundary conditions.

Note that the equation for $\hat{w}$ instead simplifies to

$$\frac{\mathrm{d}^2\hat{w}}{\mathrm{d}z^2} = k^2\frac{\mathrm{PrRo_{rz}}^2}{4}\hat{w} \ , \tag{4.31}$$

and similarly for $\hat{v}$ (i.e. both equations are only second order in z, and only contain the thermo-

viscous mode). The radiative zone ($z \in [0, h]$) solutions are now

$$\begin{aligned}
\hat{u}(z) &= u_1 e^{kz} + u_2 e^{-kz} + u_3 e^{\lambda_2 z} + u_4 e^{-\lambda_2 z} \ , \\
\hat{v}(z) &= \frac{E_\nu}{2}(k^2 - \lambda_2^2)\left[u_3 e^{\lambda_2 z} + u_4 e^{-\lambda_2 z}\right] \ , \\
\hat{w}(z) &= -ik\frac{E_\nu}{2}\frac{(k^2 - \lambda_2^2)}{\lambda_2}\left[u_3 e^{\lambda_2 z} - u_4 e^{-\lambda_2 z}\right] \ , \\
\hat{p}(z) &= -\frac{2}{ik}\left[u_1 e^{kz} + u_2 e^{-kz} + u_3 e^{\lambda_2 z} + u_4 e^{-\lambda_2 z}\right] \ , \\
\hat{T}(z) &= -\frac{2}{ik\mathrm{Ro}_{\mathrm{rz}}^2}\left[k u_1 e^{kz} - k u_2 e^{-kz} + \lambda_2 u_3 e^{\lambda_2 z} - \lambda_2 u_4 e^{-\lambda_2 z}\right] \ . \qquad (4.32)
\end{aligned}$$

where the 4 constants $\{u_i\}_{i=1,4}$ are integration constants, to be determined.

4.2.4.3 The stratified stress-free case

We now proceed to match the solutions in the two regions, assuming stress-free boundary conditions near the lower boundary. Since there are in total 8 unknown constants (including A, B, T_0 and T_1 from the convection zone solution and $\{u_i\}_{i=1,4}$ from the radiative zone solution), we need a total of 8 matching and boundary conditions.

At the lower boundary ($z = 0$) we take $\hat{w} = \mathrm{d}\hat{u}/\mathrm{d}z = 0$; this condition in turn implies that $\hat{T} = 0$. At the surface ($z = 1$), we take as before $\hat{w} = 0$, and select in addition $\hat{T} = 0$. We then need 4 matching conditions across the interface: these are given by the continuity of $\hat{w}$, $\hat{p}$, $\hat{T}$ and $\mathrm{d}\hat{T}/\mathrm{d}z$. Note that it is important to resist the temptation of requiring the continuity of $\hat{v}$, since viscous stresses have been neglected in the analytical treatment of the $y-$ component of the momentum equation in both radiative and convective zones. Moreover, we know that in the unstratified limit, $\hat{u}$ actually becomes discontinuous at the interface in the limit $\mathrm{E}_\nu \to 0$. Since we expect the stratified solution to tend to the unstratified one uniformly as $\mathrm{Ro}_{\mathrm{rz}} \to 0$, we cannot require the continuity of $\hat{u}$ at the interface[5].

The equations and resulting solutions for the integration constants are fairly compli-

[5] a fact which is again only obvious in hindsight

cated. The most important ones are reported in the Appendix B for completeness, and are used to justify mathematically the following statements:

- In the limit of $\mathrm{Ro_{rz}} \to 0$, we find as expected that the solutions uniformly tend to the unstratified solution summarized in equations (4.13), (4.15), and (4.17). Indeed, in that case $\lambda_2 \to 0$ and the thermo-viscous solution spans the whole radiative zone (mathematically, it tends to the linear solution found in the unstratified case).

- In the strongly stratified case (defined as $\lambda_2 \gg k$), as described earlier, $\hat{w}$ in the radiative zone decays exponentially with depth on a lengthscale $1/\lambda_2$, with an amplitude which scales as E_ν/λ_2. The flows are therefore very strongly suppressed, and return to the convection zone within a small thermo-viscous layer. Note that $\mathrm{E}_\nu/\lambda_2 = \mathrm{Ra}^{-1/2}$ where Ra is the usually defined Rayleigh number.

The two limits are illustrated in Figure 4.8, which shows the numerical solution to (4.9) for two values of the Rossby number $\mathrm{Ro_{rz}}$, but otherwise identical parameters. In the strongly stratified limit ($\lambda_2 = 10$, using $\mathrm{Pr} = 0.01$ and $\mathrm{Ro_{rz}} = 10^2$) we see that the solution decays exponentially below the interface, with an amplitude which scales as E_ν/λ_2 as predicted analytically. In the weakly stratified case ($\lambda_2 = 0.1$, using $\mathrm{Pr} = 0.01$ and $\mathrm{Ro_{rz}} = 1$) the solution tends to the unstratified limit and scales as $\mathrm{E}_\nu z$.

4.2.4.4 Matching in the no-slip case

By analogy with the previous section, we expect to recover the unstratified limit when $\lambda_2 \to 0$, so that $\hat{w}(z) \propto \mathrm{E}_\nu^{1/2}$ in this no-slip case. In the strongly stratified limit on the other hand, the amplitude of the flows decays exponentially with depth below the interface as a result of the thermo-viscous mode and is negligible by the time they reach the lower boundary. In that case, we do not expect the applied lower boundary conditions to affect the solution, so that the

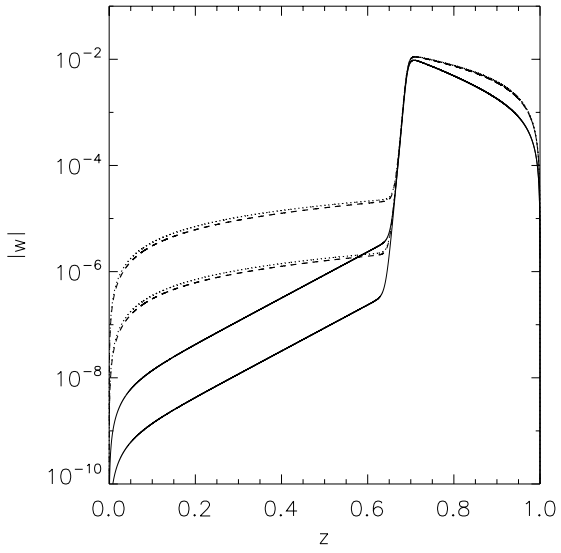

Figure 4.8: Numerical solutions of (4.9) with the following parameters: $\Delta = 0.01$, $\Lambda = 10$, $S = 0$, $U = 1$, $\mathrm{Pr} = 0.01$ and $D_0 = 10$. Stress-free bottom boundary conditions are used. The solid lines correspond to the "strongly" stratified case with $\mathrm{Ro_{rz}} = 10$, with $\mathrm{E}_\nu = 10^{-5}$ and 10^{-6} for the top and bottom curves respectively. The dashed lines correspond to the "weakly" stratified case, with $\mathrm{Ro_{rz}} = 1$, with $\mathrm{E}_\nu = 10^{-5}$ and 10^{-6} for the top and bottom curves respectively. Note that for $k = 2$, λ_2 is simply equal to $\mathrm{Pr}^{1/2}\mathrm{Ro_{rz}}$. For comparison, the unstratified case ($\mathrm{Ro_{rz}} = 0$) is shown as dotted lines. At these parameters and with these boundary conditions, $\mathrm{Ro_{rz}} = 1$ already belongs to the weakly stratified limit.

scalings found in the strongly stratified limit with *stress-free* boundary conditions should still apply: $\hat{w}(z) \propto \mathrm{E}_\nu/\lambda_2$.

These statements are verified in Figure 4.9. There, we show the results of a series of numerical experiments for no-slip boundary conditions where we extracted from the simulations the power α in the expression $\hat{w} \propto \mathrm{E}_\nu^\alpha$, and plotted it as a function of stratification (λ_2). To do this, we integrated the solutions to equations (4.9) for the following parameters: $\Delta = 0.01$, $\Lambda = 10$, $S = 1$, $U_0(h) = 1$, $\mathrm{Pr} = 0.01$ and $D_0 = 10$ and calculated $\hat{w}(z = 0.5)$ for 4 values of E_ν: 10^{-6}, 10^{-7}, 10^{-8} and 10^{-9}. We estimated α by calculating the quantity

$$\alpha = \log_{10} \frac{\hat{w}(z = 0.5, \mathrm{E}_\nu = 10^{-6})}{\hat{w}(z = 0.5, \mathrm{E}_\nu = 10^{-7})} \tag{4.33}$$

for the ($E_\nu = 10^{-6}$, $E_\nu = 10^{-7}$) pair (diamond symbols) and similarly for the pairs ($E_\nu = 10^{-7}$, $E_\nu = 10^{-8}$) (triangular symbols) and ($E_\nu = 10^{-8}$, $E_\nu = 10^{-9}$) (star symbols). In the weakly stratified limit ($\lambda_2 \to 0$), we find that $\alpha \to 1/2$ while in the strongly stratified limit ($\lambda_2 \gg 1$), $\alpha \to 1$, thus confirming our analysis. The transition between the two regimes appears to occur for slightly lower-than expected values of λ_2, namely 0.1 instead of 1.

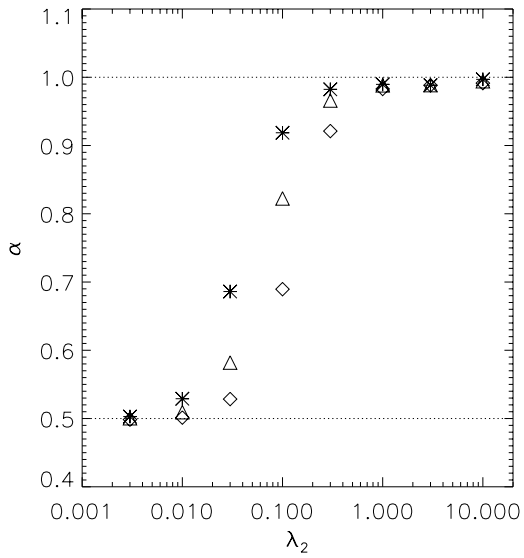

Figure 4.9: This figure shows the power α in the expression $\hat{w} \propto E_\nu^\alpha$, as a function of λ_2 (see main text for detail). In the weakly stratified limit, $\alpha \to 1/2$ while in the strongly stratified limit $\alpha \to 1$ as predicted analytically. This calculation was done for no-slip boundary conditions, and the following parameters were held constant: $\Delta = 0.01$, $\Lambda = 10$, $S = 1$, $U_0(h) = 1$, Pr $= 0.01$ and $D_0 = 10$

A final summary of our findings for the stratified case together with its implications for mixing between the solar convection zone and the radiative interior, is deferred to Section 4.4. There, we also discuss the consequences in terms of mixing in other stars. But first, we complete the study by releasing some of the simplifying assumptions made, and moving to more realistic numerical solutions to confirm our simple Cartesian analysis.

4.3 A "solar" model

In this section we improve on the Cartesian analysis by moving to a spherical radiative–convective model. The calculations are thus performed in an axisymmetric spherical shell, with the outer radius $r_{\rm out}$ selected to be near the solar surface, and the inner radius $r_{\rm in}$ somewhere within the radiative interior. This enables us to gain a better understanding of the effects of the geometry of the system on the spatial structure of the flows generated. In addition, we use more realistic input physics in particular in terms of the background stratification, and no longer use the Boussinesq approximation for the equation of state. We expect that the overall scalings derived in Section 4.2 still adequately describe the flow amplitudes in this new calculation. However, the use of a more realistic background stratification adds an additional complication to the problem: the background temperature/density gradients are no longer constant, so that the measure of stratification λ_2 varies with radius (see Figure 4.10, for an estimate of λ_2 in the Sun). This aim of this section is therefore to study the impact of both geometry and non-uniform stratification on the system dynamics.

4.3.1 Description of the model

The spherical model used is analogous to the radiative-zone-only model presented in Paper I and described in detail (including the magnetic case) by Garaud & Garaud (2008). The salient points are repeated here for completeness, together with the added modifications made to include the "convective" region.

We consider a spherical coordinate system (r, θ, ϕ) where the polar axis is aligned with rotation axis of the Sun. The background state is assumed to be spherically symmetric and in hydrostatic equilibrium. The background thermodynamical quantities such as density, pressure, temperature and entropy are denoted with bars (as $\bar{\rho}(r)$, $\bar{p}(r)$, $\bar{T}(r)$ and $\bar{s}(r)$ respectively), and

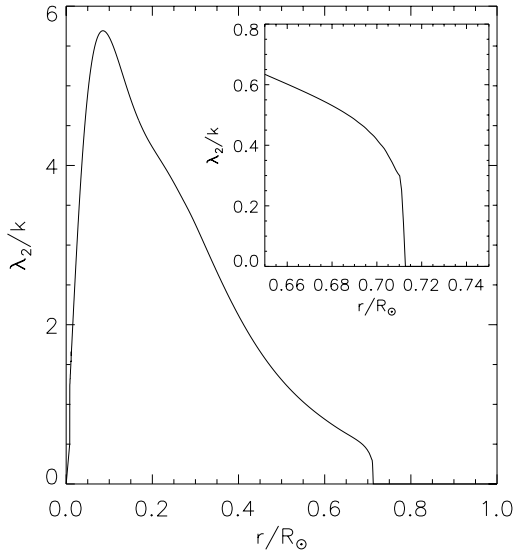

Figure 4.10: Variation of λ_2/k $=\mathrm{Pr}^{0.5}N/\Omega_\odot$ in the Sun, as determined from Model S of Christensen-Dalsgaard *et al.* (1996). The Prandtl number Pr is calculated using Model S together with the formulae provided by Gough (2007) for the microscopic values of the viscosity $\hat{\nu}$ and the thermal conductivity κ_T (see also Garaud & Garaud, 2008). The inset zooms into the region near the base of the convection zone, which is the only region of the radiative zone where $\lambda_2 \leq 1$ (aside from $r \to 0$).

extracted from the standard solar model of Christensen-Dalsgaard *et al.* (1996). Perturbations to this background induced by the velocity field $\mathbf{u} = (u_r, u_\theta, u_\phi)$ are denoted with tildes. In the frame of reference rotating with angular velocity $\Omega_\odot$, in a steady state, the linearized perturbation equations become

$$\begin{aligned}
&\nabla \cdot (\bar{\rho}\mathbf{u}) = 0 \ , \\
&2\bar{\rho}\boldsymbol{\Omega}_\odot \mathbf{e}_z \times \mathbf{u} = -\nabla\tilde{p} + \tilde{\rho}\mathbf{g} + f\nabla\cdot\Pi - \bar{\rho}\Omega_\odot \frac{\mathbf{u}-\mathbf{u}_{\rm cz}}{\tau(r)} \ , \\
&\frac{\bar{\rho}\bar{c}_{\rm p}\bar{T}\bar{N}^2}{g} u_r = \nabla\cdot\left[(f\bar{k}_T + R_\odot^2\Omega_\odot D(r))\nabla\tilde{T}\right] \ , \\
&\frac{\tilde{p}}{\bar{p}} = \frac{\tilde{\rho}}{\bar{\rho}} + \frac{\tilde{T}}{\bar{T}} \ ,
\end{aligned} \tag{4.34}$$

where $\bar{c}_{\rm p}$ is the specific heat at constant pressure, $\bar{k}_T(r) = \bar{\rho}\bar{c}_{\rm p}\bar{\kappa}_T$ is the thermal conductivity in the solar interior, Π is the viscous stress tensor (which depends on the background viscosity $\bar{\nu}$)

and $\mathbf{g} = -g(r)\mathbf{e}_r$ is gravity. Note that this set of equations is given in dimensional form here, although the numerical algorithm used further casts them into a non-dimensional form. Also note that both diffusion terms (viscous diffusion and heat diffusion) have been multiplied by the same factor f. This enables us to vary the effective Ekman number $\mathrm{E}_\nu(r) = f\mathrm{E}_\nu^\odot = f\bar{\nu}(r)/R_\odot^2\Omega_\odot$ while maintaining a solar Prandtl number at every radial position. As a result, the quantity λ_2 used in the simulations and represented in Figure 4.10 is the true solar value (except where specifically mentioned).

As in the Cartesian case, we model the dynamical effect of turbulent convection in the convection zone through a relaxation to the observed profile in the momentum equation, and a turbulent diffusion in the thermal energy equation. The expressions for the non-dimensional quantities $\tau(r)$ and $D(r)$ are the same as in equations (4.5) and (4.8) with z replaced by $r/R_\odot$, and $h = 0.713$ instead of $h = 0.7$ (Christensen-Dalsgaard *et al.* 1996). In what follows, we take Δ to be 0.01 (i.e. the overshoot layer depth is 1% of the solar radius) although the choice of Δ has little influence on the scalings derived. The rotation profile in the convection zone $\mathbf{u}_{\mathrm{cz}}$ is selected to be

$$\mathbf{u}_{\mathrm{cz}}(r,\theta) = r\sin\theta\Omega_{\mathrm{cz}}(\theta)\ \mathbf{e}_\phi\ , \tag{4.35}$$

where

$$\Omega_{\mathrm{cz}}(\theta) = \Omega_{\mathrm{eq}}\left(1 - a_2\cos^2\theta - a_4\cos^4\theta\right)\ , \tag{4.36}$$

with

$$\begin{aligned} a_2 = 0.17\ ,\ a_4 = 0.08\ ,\\ \frac{\Omega_{\mathrm{eq}}}{2\pi} = 463\ \mathrm{nHz}\ , \end{aligned} \tag{4.37}$$

which is a simple approximation to the helioseismically determined profile (Schou *et al.* 1998; Gough, 2007). Here, Ω_{eq} is the observed equatorial rotation rate. As in Paper I, we finally select

$\Omega_\odot$ to be

$$\Omega_\odot = \Omega_{\rm eq}\left(1 - \frac{a_2}{5} - \frac{3a_4}{35}\right) , \tag{4.38}$$

to ensure that the system has the same specific angular momentum as that of the imposed profile $\mathbf{u}_{\rm cz}(r,\theta)$.

The computational domain is a spherical shell with the outer boundary located at $r_{\rm out} = 0.9R_\odot$. It is chosen to be well below the solar surface to avoid complications related to the very rapidly changing background in the region $r > 0.95R_\odot$. The position of the lower boundary will be varied.

The upper and lower boundaries are assumed to be impermeable. The upper boundary is always stress-free, while the lower boundary is assumed to be either no-slip or stress-free depending on the calculation. In the no-slip case, the rotation rate of the excluded core is an eigenvalue of the problem, calculated in such a way as to guarantee that the total torque applied to the core is zero. Finally, the boundary conditions on temperature are selected in such a way as to guarantee that $\nabla^2\tilde{T} = 0$ outside of the computational domain, as in Garaud & Garaud (2008). We verified that the selection of the temperature boundary conditions only has a qualitative influence on the results, and doesn't affect the scalings derived.

The numerical method of solution is based on the expansion of the governing equations onto the spherical coordinate system, followed by their projection onto Chebyshev polynomials $T_n(\cos\theta)$, and finally, solution of the resulting ODE system in r using a Newton-Raphson-Kantorovich algorithm. The typical solutions shown have 3000 meshpoints and 60-80 Fourier modes. For more detail, see Garaud (2001) and Garaud & Garaud (2008).

4.3.2 The weakly stratified case

We first consider the artificial limit of weak stratification. In the following numerical experiment, we use the available solar model background state, but divide the buoyancy frequency $\bar{N}$ by 10^3 everywhere in the computational domain (all other background quantities remain unchanged). As a result, the new value of λ_2 in the domain is artificially reduced from the one presented in Figure 4.10 by 10^3, and is everywhere much smaller than one. The position of the lower boundary is arbitrarily chosen to be at $r_{\rm in} = 0.35 R_\odot$.

Two sets of solutions are computed for no-slip lower boundary and for stress-free lower boundary. Figure 4.11 is equivalent to Figure 4.5: it displays the radial velocity u_r as a function of radius near the poles (latitude of 80°) for various values of f – in other words, E_ν – and clearly illustrates the scalings of $u_r \propto E_\nu^{1/2}$ in the radiative zone for the no-slip case, and $u_r \propto E_\nu$ for the stress-free case.

Figure 4.12 illustrates the geometry of the flow in both no-slip and stress-free cases for $f = 10^9$ (which corresponds to an Ekman number near the radiative–convective interface of about 2×10^{-6}). The geometrical pattern of the flows observed within the convection zone show a single-cell, with poleward flows near the surface and equatorward flows near the bottom of the convection zone. Below the convection zone we note the presence of three distinct regions: the polar region, a Stewardson layer region (at the tangent cylinder) and an equatorial region. Flows within the equatorial region are weak regardless of the lower boundary conditions. In the stress-free case, even in the tangent cylinder the flows tend to return mostly within the convection zone. If the lower boundary is no-slip on the other hand, flows within the tangent cylinder are stronger, although the effect is not as obvious as in the Cartesian case because of the anelastic mass conservation equation used here.

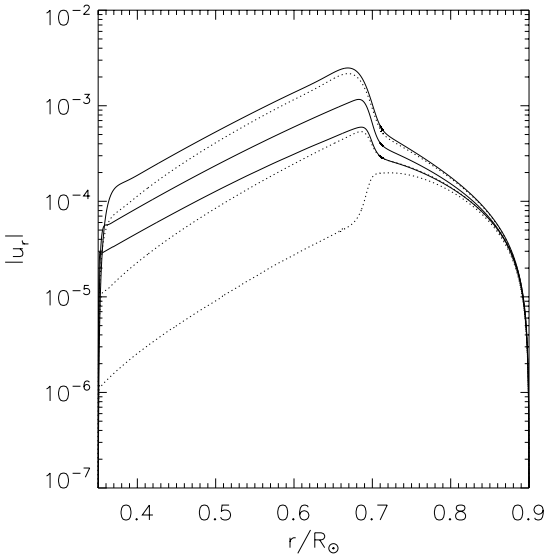

Figure 4.11: Vertical velocity at 80° latitude in units of $R_\odot\Omega_\odot$ for an artificially weakly stratified simulation (where $\bar{N}$ was uniformly divided by 10^3 everywhere). The solid lines show three simulations for $f = 10^{11}$, $f = 10^{10}$ and $f = 10^9$ (from top to bottom) for the no-slip case. These correspond to $\mathrm{E}_\nu = 2 \times 10^{-4}$, $\mathrm{E}_\nu = 2 \times 10^{-5}$ and $\mathrm{E}_\nu = 2 \times 10^{-6}$ at the base of the convection zone respectively, hence showing how $u_r \propto \mathrm{E}_\nu^{1/2}$. The dotted lines show simulations with stress-free boundary conditions for the same parameters, showing $u_r \propto \mathrm{E}_\nu$. In this calculation the overshoot depth Δ was selected to be $0.01R_\odot$, and $\Lambda = 10$. The value of D_0 is irrelevant in this very weakly stratified simulation.

4.3.3 The stratified case

Let us now consider the case of a true solar stratification. Since λ_2 increases rapidly with depth beneath the convection zone (from 0 to about 10 in the case of the Sun), the radius at which $\lambda_2 \simeq 1$ (r_1 for short) plays a special role: we expect the dynamics of the system to depend on the position of the lower boundary r_{in} compared with $r_1 \simeq 0.55R_\odot$.

This is indeed observed in the simulations, as shown in Figure 4.13. If $r_{\mathrm{in}} > r_1$, then $\lambda_2 < 1$ everywhere in the modeled section of the radiative zone. In this case, the dynamics follow the scaling for the unstratified case, and depend on the nature of the lower boundary ($u_r \propto \mathrm{E}_\nu$ if the lower boundary is stress-free, and $u_r \propto \mathrm{E}_\nu^{1/2}$ if the lower boundary is no-slip).

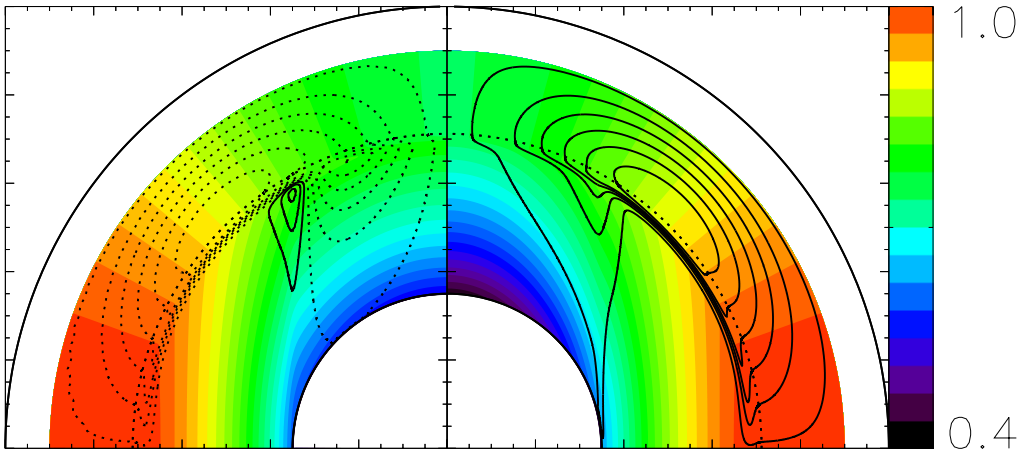

Figure 4.12: Normalized angular velocity ($\tilde{\Omega}/\Omega_{\rm eq}$) and streamlines solutions to equations (4.34) for an artificially weak stratification (see Figure 4.11), and for $f = 10^9$ (corresponding to $\mathrm{E}_\nu = 2 \times 10^{-6}$ at the base of the convection zone). On the left, we show the solution with no-slip lower boundary conditions, and on the right the stress-free solution. Dotted lines represent clockwise flows, and solid lines counter-clockwise flows. In this calculation, the overshoot layer depth Δ was selected to be $0.01 R_\odot$, and $\Lambda = 10$. The value of D_0 is irrelevant in this very weakly stratified simulation.

On the other hand, if $r_{\rm in} < r_1$ then the flows are strongly quenched by the stratification before they reach the lower boundary. As a result, the radial velocities scale with E_ν/λ_2 regardless of the applied boundary conditions.

The implications of this final result, namely the importance of the *location* of the stresses involved in breaking the Taylor-Proudman constraint in relation to the radius at which $\lambda_2 \simeq 1$, are discussed in Section 4.4.3.

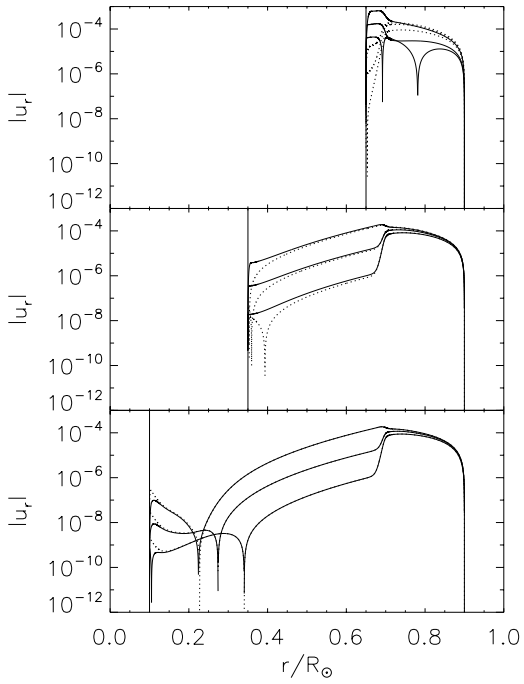

Figure 4.13: Vertical velocity (in units of $R_\odot\Omega_\odot$) in nine different simulations, at latitude 80°. The background stratification in each case is solar, but the position of the lower boundary is moved through the radiative zone from $0.65R_\odot$ to $0.35R_\odot$ and $0.1R_\odot$. The solid-line plots are for no-slip lower boundary conditions while the dotted lines are for stress-free lower boundary conditions. Three simulations are shown in each case: (from lowest to highest curve) for $f = 10^8$, $f = 10^9$ and $f = 10^{10}$ corresponding to $\mathrm{E}_\nu = 2 \times 10^{-7}$ to $\mathrm{E}_\nu = 2 \times 10^{-5}$. The logarithmic scale clearly shows that u_r scales with E_ν in the radiative zone in the stress-free cases for all values of $r_{\rm in}$ while in the no-slip case, $r_{\rm in}$ scales with E_ν if $r_{\rm in} < 0.6$, as expected from Figure 4.10.

4.4 Implications of this work for solar and stellar mixing

4.4.1 Context for stellar mixing

The presence of mixing in stellar radiative zones has long been inferred from remaining discrepancies between models-without-mixing and observations (see Pinsonneault 1997 for a review). The most commonly used additional mixing source is convective overshoot, whereby strong convective plumes travel beyond the radiative–convective interface and cause intense but

very localized (both in time and space) mixing events (Brummell, Clune & Toomre, 2002). The typical depth of the layer thus mixed, the "overshoot layer", is assumed to be a small fraction of a pressure scaleheight in most stellar models.

A related phenomenon is wave-induced mixing (Schatzman, 1996). While most of the energy of the impact of a convective plume hitting the stably stratified fluid below is converted into local buoyancy mixing, a fraction goes into the excitation of a spectrum of gravity waves, which may then propagate much further into the radiative interior. Where and when the waves eventually cause mixing (either through mutual interactions, thermal dissipation or by transferring momentum to the large-scale flow) depends on a variety of factors. It has recently been argued that the interaction of the gravity waves with the local azimuthal velocity field (the differential rotation) would dominate the mixing process (Charbonnel & Talon 2005), although this statement is not valid unless the wave-spectrum is near-monochromatic. For the typically flatter wave spectra self-consistently generated by convection, wave-induced mixing has much more turbulent characteristics (Rogers, MacGregor & Glatzmaier 2008), and is again fairly localized below the convection zone.

Mixing induced by large-scale flows comes in two forms: turbulent mixing resulting from instabilities of the large-scale flows, and direct transport by the large-scale flows themselves. The former case is the dominant mechanism in the early stages of stellar evolution when the star is undergoing rapid internal angular-momentum "reshuffling" caused by external angular-momentum extraction (disk-locked and/or jet phase, early magnetic breaking phase). In these situations, regions of strong radial angular-velocity shear develop, which then become unstable and cause local turbulent mixing of both chemical species and angular momentum. Studies of these processes were initiated by the work of Endal & Sofia (1978). Later, Chaboyer & Zahn (1992) refined the analysis to consider the effect of stratification on the turbulence, and showed how this can differentially affect chemical mixing and angular-momentum mixing. Fi-

nally, Zahn (1992) proposed the first formalism which combines mixing by large-scale flows and mixing by (two-dimensional) turbulence. In addition to the flows driven by angular-momentum redistribution, he also considered flows driven by the local baroclinicity of the rotating star, and showed that their effect can be represented as a hyperdiffusion term in the angular velocity evolution equation. In a quasi-steady, uniformly rotating limit, the flows described are akin to a local Eddington-Sweet circulation. His formalism is used today in stellar evolution models with rotation (Maeder & Meynet, 2000).

In all cases described above, mixing is either localized near the base of the convection zone (overshoot, gravity-wave mixing), or significant only in very rapidly rotating stars (local Eddington-Sweet circulations) or stars which are undergoing major angular-momentum redistribution (during phases of gravitational contraction, spin-down, mass loss, etc..). In this paper, we have identified another potential cause of mixing, where the original energy source is the differential rotation in the stellar convective region: gyroscopic pumping (induced by the Coriolis force associated with the differential rotation, see McIntyre 2007) drives large-scale meridional flows which may – under the right circumstances – penetrate the radiative region and cause a global circulation.

This source of mixing is intrinsically *non-local* to the radiative zone. The simplest way of seeing this is to consider a thought-experiment where the radiative–convective interface is impermeable: as shown in Paper I, the amplitude of the meridional flows generated locally (i.e. below the interface) is then much smaller than the one calculated here. The origin of the flows is also clearly independent of the baroclinicity (since the same phenomenon is observed in the unstratified limit), although the flows themselves can be influenced by the stratification. This implies that they are not related to Eddington-Sweet flows. Finally, contrary to some of the other mixing sources listed above, the one described here does not rely on the system being out-of-equilibrium: it is an inherently quasi-steady phenomenon, implying that this process is

an ideal candidate for "deep mixing" for stars on the Main Sequence.

The process together with the conditions under which strong mixing might occur, are now summarized and discussed.

4.4.2 Qualitative summary of our results

The differential rotation observed in stellar convective envelopes (e.g. Barnes *et al.* 2005) is thought to be maintained by anisotropic Reynolds stresses, arising from rotationally constrained convective eddies (Kippenhahn, 1963). The details of this particular process are beyond the scope of this study, but are the subject of current investigation by others (Kitchatinov & Rüdiger, 1993, 2005; Rempel, 2005). Instead, we have assumed here the simplest possible type of forcing which *mimics* the effect of convective Reynolds stresses in driving the system towards a differentially rotating state. Using this model, we then derive the expected mixing caused by large-scale meridional flows[6].

We first found that large-scale flows are indeed self-consistently driven by gyroscopic pumping in the convection zone, as expected (McIntyre, 2007). The amplitude of these flows *within the convection zone* scales roughly as

$$V_{\rm cz} \sim \tau R_\star (\Delta\Omega) \ , \tag{4.39}$$

where $(\Delta\Omega)$ is the observed equator-to-pole differential rotation, $R_\star$ is the stellar radius, and τ is, as discussed in Section 4.2.2, related to the ratio of the convective turnover time divided by the rotation period. Note that for the Sun, with $(\Delta\Omega) \sim 0.1\Omega_\odot$, the typical amplitude of the corresponding meridional flows would be of the order of 200 τ m/s – which doesn't seem too unreasonable given the observations of subsurface flows (Giles *et al.* 1997) and the typical values of τ in the solar convection zone (see Section 4.2.2).

[6]It is worth noting here that while we expect the details of the flow structure and amplitude to be different when a more realistic forcing mechanism is taken into account, the overall scalings derived should not be affected.

Next, we studied how much mixing these flows might induce in the underlying radiative zone. *In this quasi-steady formalism*, we found that the magnitude of convection-zone-driven flows decays exponentially with depth below the radiative–convective interface on the lengthscale l_2, where $l_2 = R_\odot/\mathrm{Pr}^{1/2}\mathrm{Ro}_{\mathrm{rz}}$, as determined in Section 4.2.4.2 (see also Gilman & Miesch, 2004 and Garaud & Brummell, 2008). This penetration corresponds (in the linear regime) to a so-called "thermo-viscous" mode. The limit $l_2 \ll R_\odot$ corresponds to a strongly stratified limit, where the flow velocities are rapidly quenched beneath the convection zone. The limit $l_2 \gg R_\odot$ corresponds to the weakly stratified case, where the thermo-viscous mode spans the whole radiative interior and the stratification has little effect on the flow. It is important to note that "weakly stratified" regions in this context can either correspond to regions with weak temperature stratification (small $\bar{N}$), *or* in rapid rotation, *or* with small Prandtl number – this distinction will be used later.

The amplitude of the flows upon entering the radiative zone V_{rz}, together with l_2, uniquely define the global circulation timescale in the interior (roughly speaking, l_2/V_{rz}). In the weakly stratified/rapidly rotating limit, we find that the fraction of the meridional mass flux pumped in the convection zone which is allowed to *enter* the radiative zone is strongly constrained by Taylor-Proudman's theorem. This theorem, which holds when the pressure gradient[7] and the Coriolis force are the two dominant forces and are therefore in balance, enforces the invariance of all components of the flow velocities along the rotation axis. Hence, flows which enter the radiative zone cannot *return* to the convection zone unless the Taylor-Proudman constraint is broken. However, additional stresses (such as Reynolds stresses, viscous stresses, magnetic stresses) are needed to break this constraint. As a result, two regimes may exist. If the (weakly stratified/rapidly rotating) radiative zone is in *pure* Taylor-Proudman balance, then the system adjusts itself, by adjusting the pressure field, in such a way as to ensure that the convection zone

[7] more precisely, the perturbation to the pressure gradient around hydrostatic equilibrium

flows remain entirely within the convection zone. On the other hand, if there are other sources of stresses somewhere in the radiative zone to break the Taylor-Proudman balance, then significant large-scale mixing is possible since flows entering the radiative zone are allowed to return to the convection zone. Furthermore, the resulting meridional mass flux in the radiative zone depends rather sensitively on the nature of the mechanism which breaks the Taylor-Proudman constraint (see next section).

The strongly stratified/slowly rotating limit exhibits a very different behavior. Because of the strong buoyancy force, the Taylor-Proudman balance becomes irrelevant, the flows are exponentially suppressed, and the induced radiative zone mixing is independent of the lower boundary conditions. However, note that since $\bar{N}$ tends to 0 at a radiative–convective interface, there will always be a "weakly stratified" region in the vicinity of any convective zone. In that region the dynamics described in the previous paragraph apply.

4.4.3 Applications to the Sun and other stars

In the illustrative model studied here, the only stresses available to break the Taylor-Proudman constraint are viscous stresses, which are only significant within the thin Ekman layer located near an artificial impermeable inner boundary. We do not advocate that this is a particularly relevant mechanism for the Sun! However, it is a useful example of the sensitive dependence of the global circulation mass flux on the mechanism responsible for breaking the Taylor-Proudman constraint.

In the limit of weak stratification, we found that if the inner boundary is a stress-free boundary then the global turnover time within the radiative zone is the viscous timescale. This is because stress-free boundary conditions effectively suppress the Ekman layer. On the other hand if the boundary layer is no-slip, then *the global mass flux through the radiative zone is equal to the mass flux allowed to return through the Ekman layer.* In that case, and according

to well-known Ekman layer dynamics, the overall turnover time within the bulk of the domain is the geometric mean of the viscous timescale and the rotation timescale ($1/\mathrm{E}_\nu^{1/2}\Omega_\odot$), which correspond to a few million years only.

Going beyond simple Ekman dynamics, a much more plausible related scenario for the solar interior was studied by Gough & McIntyre (1998). They considered the same mechanism for the generation of large-scale flows within the convection zone, studied how these flows down-well into the radiative zone and interact with an embedded large-scale primordial magnetic field. They showed that the field can prevent the flows from penetrating too deeply into the radiative zone, while the flows confine the field within the interior. In their model, this nonlinear interaction occurs in a thin thermo-magnetic diffusion layer, located somewhat below the radiative–convective interface. One can therefore see an emerging analogy with the dynamics discussed here: in the Gough & McIntyre model, the field does act as a somewhat impermeable barrier, and provides an efficient and elegant mechanism for breaking the Taylor-Proudman constraint within the radiative zone. The only significant difference is that the artificial Ekman layer is replaced by a more convincing thermo-magnetic diffusion layer: the mass flux allowed to down-well into the radiative zone, and mix its upper regions, is now controlled by a balance between the Coriolis force and magnetic stresses (instead of the viscous stresses). With this new balance, they find that the global turnover time for the circulation in the region between the base of the convection zone and the thermo-magnetic diffusion layer is of the order of a few tens of millions of years (which is still short compared with the nuclear evolution timescale).

This mixed region is the solar tachocline. By relating their model with observations, Gough & McIntyre were able to identify the position of the magnetic diffusion layer to be just at the base of the observed tachocline (around $0.68 \pm 0.01 R_\odot$, see Charbonneau *et al.* 1999). This turns out to be close enough to the base of the convection zone for the dynamics of the radiative region to be weakly-stratified in the sense used in this paper (see Figure 4.10 and Section 4.3.3)

so that the meridional flows are indeed able to penetrate, and do so with "significant" amplitude (about 10^{-5} cm/s) down to the magnetic diffusion layer. However, it is rather interesting to note that the Gough & McIntyre model could not have worked had today's tachocline been observed to be much thicker. It is also interesting to note that for younger, more rapidly rotating solar-type stars, a much larger region of the radiative zone can be considered "weakly stratified", possibly leading to much deeper mixed regions if these stars also host a large-scale primordial field. The implications of these findings for Li burning, together with a few other interesting ideas, will be discussed in a future publication.

Acknowledgments

This work was funded by NSF-AST-0607495, and the spherical domain simulations were performed on the UCSC Pleiades cluster purchased with an NSF-MRI grant. The authors thank N. Brummell and S. Stellmach for many illuminating discussions, and D. Gough for the original idea.

Appendix A: Ekman jump condition

Equation (4.15) provides the solution "far" from the lower boundary, in the bulk of the fluid. Let us refer to the limit of bulk solutions as $z \to 0$ as $\hat{u}_{\rm bulk}(0^+)$ (and similarly for the other quantities). We now derive the Ekman solution close to the boundary, for the unstratified case. Let's study the problem using the stream-function ψ with

$$(\hat{u}, \hat{v}, \hat{w}) = \left(\hat{u}, \frac{\mathrm{d}\hat{\psi}}{\mathrm{d}z}, -ik\hat{\psi} \right) \ . \tag{4.40}$$

Moreover, let us assume that within the boundary layer, $\mathrm{d}\hat{\psi}/\mathrm{d}z \gg k\hat{\psi}$. The governing equations are then approximated by

$$\begin{aligned} -2\frac{\mathrm{d}\hat{\psi}}{\mathrm{d}z} &= E_\nu \frac{\mathrm{d}^2\hat{u}}{\mathrm{d}z^2} \ , \\ 2\hat{u} &= -ik\hat{p} + E_\nu \frac{\mathrm{d}^3\hat{\psi}}{\mathrm{d}z^3} \ , \\ \frac{\mathrm{d}\hat{p}}{\mathrm{d}z} &= -ikE_\nu \frac{\mathrm{d}^2\hat{\psi}}{\mathrm{d}z^2} \ , \end{aligned} \tag{4.41}$$

which simplify to

$$\frac{\mathrm{d}^5\hat{\psi}}{\mathrm{d}z^5} = -4\frac{\mathrm{d}\hat{\psi}}{\mathrm{d}z} \ , \tag{4.42}$$

with solutions

$$\begin{aligned} \hat{\psi}(z) &= \psi_0 + \psi_1 e^{\lambda_3} + \psi_2 e^{-\lambda_3 z} + \psi_3 e^{\lambda_4 z} + \psi_4 e^{-\lambda_4 z} \ , \\ \hat{u}(z) &= u_0 - \frac{2}{E_\nu}\left[\frac{1}{\lambda_3}\psi_1 e^{\lambda_3 z} - \frac{1}{\lambda_3}\psi_2 e^{-\lambda_3 z} + \frac{1}{\lambda_4}\psi_3 e^{\lambda_4 z} - \frac{1}{\lambda_4}\psi_4 e^{-\lambda_4 z}\right] \ , \end{aligned} \tag{4.43}$$

where

$$\lambda_3 = (1+i)\mathrm{E}_\nu^{-1/2} \ , \ \lambda_4 = (1-i)\mathrm{E}_\nu^{-1/2} \ . \tag{4.44}$$

The growing exponentials are ignored to match the solution far from the boundary layer; it then becomes clear that $u_0 = \hat{u}_{\mathrm{bulk}}(0^+)$, while $-ik\psi_0 = \hat{w}_{\mathrm{bulk}}(0^+)$. Requiring no-slip, impermeable conditions at $z = 0$ implies

$$\begin{aligned} \psi_0 + \psi_2 + \psi_4 &= 0 \ , \\ \lambda_3\psi_2 + \lambda_4\psi_4 &= 0 \ , \\ u_0 - \frac{2}{E_\nu}\left[-\frac{1}{\lambda_3}\psi_2 - \frac{1}{\lambda_4}\psi_4\right] &= 0 \ , \end{aligned} \tag{4.45}$$

which in turn implies

$$\begin{aligned} \psi_4 &= -\frac{\lambda_3}{\lambda_4}\psi_2 \ , \\ \psi_2 &= \frac{\lambda_4}{\lambda_3 - \lambda_4}\psi_0 \ , \\ u_0 &= \frac{2}{E_\nu}\frac{\lambda_3 + \lambda_4}{\lambda_3\lambda_4}\psi_0 = 2E_\nu^{-1/2}\psi_0 \ . \end{aligned} \tag{4.46}$$

This last equation then uniquely relates the limit of the bulk solution $\hat{u}(0^+)$ and $\hat{w}(0^+)$ as $z \to 0$ as

$$\hat{u}_{\rm bulk}(0^+) = \frac{2i}{k} E_\nu^{-1/2} \hat{w}_{\rm bulk}(0^+) \ , \tag{4.47}$$

yielding the standard *Ekman jump condition*.

Appendix B: Stratified stress-free solution

The boundary conditions discussed in Section 4.2.3.3 imply the following set of equations. At $z = 0$, $\hat{w} = 0$ and $\hat{u}_z = 0$ (alternatively, $\hat{T} = 0$):

$$\begin{aligned} 0 &= u_3 - u_4 \ , \\ 0 &= k u_1 - k u_2 + \lambda_2 u_3 - \lambda_2 u_4 \ . \end{aligned} \tag{4.48}$$

At $z = 1$: $\hat{w} = 0$ and $\hat{T} = 0$:

$$0 = A e^{1/\delta} + B e^{-1/\delta} - \frac{2iS}{k\Lambda} \ , \tag{4.49}$$

$$0 = T_0 e^k + T_1 e^{-k} \ . \tag{4.50}$$

Finally, matching conditions on $\hat{w}$, $\hat{p}$, $\hat{T}$ and $\mathrm{d}\hat{T}/\mathrm{d}z$ at $z = h$:

$$\begin{aligned} -ikE_\nu \frac{k^2 - \lambda_2^2}{\lambda_2} u_3 \sinh(\lambda_2 h) &= A e^{h/\delta} + B e^{-h/\delta} - \frac{2iS}{k\Lambda} \ , \\ 2u_1 \cosh(kh) + 2u_3 \cosh(\lambda_2 h) &= U_0(h) + \frac{ik}{2} \delta\Lambda \left[A e^{h/\delta} - B e^{-h/\delta} \right] \ , \\ T_0 e^{kh} + T_1 e^{-kh} &= -\frac{4}{ik \mathrm{Ro}_{\rm rz}^2} \left[k u_1 \sinh(kh) + \lambda_2 u_3 \sinh(\lambda_2 h) \right] \ , \\ T_0 e^{kh} - T_1 e^{-kh} &= -\frac{4}{ik^2 \mathrm{Ro}_{\rm rz}^2} \left[k^2 u_1 \cosh(kh) + \lambda_2^2 u_3 \cosh(\lambda_2 h) \right] \ , \end{aligned} \tag{4.51}$$

where u_4 and u_2 were already eliminated using equations (4.50). We now proceed to eliminate A, B, T_0 and T_1, which leaves two equations for u_1 and u_3:

$$\begin{aligned}
&2G\left[u_1\cosh(kh)+u_3\cosh(\lambda_2 h)\right]-\delta\Lambda k^2 E_\nu\frac{k^2-\lambda_2^2}{2\lambda_2}u_3\sinh(\lambda_2 h)\ ,\\
&\quad=\delta S\left(e^{(h-1)/\delta}(1-G)-1\right)+GU_o(h)\ ,\\
&(F-1)\,ku_1\sinh(kh)+ku_1\cosh(kh)=-\frac{\lambda_2^2}{k}u_3\cosh(\lambda_2 h)-(F-1)\,\lambda_2 u_3\sinh(\lambda_2 h)
\end{aligned}\tag{4.52}$$

where the functions $F(h,k)$ and $G(h,h)$ are geometric factors defined as

$$\begin{aligned}
F(h,k)&=\frac{2}{1-e^{2k(h-1)}}\ ,\\
G(h,k)&=\frac{e^{(h-2)/\delta}-e^{-h/\delta}}{e^{(h-2)/\delta}+e^{-h/\delta}}\ .
\end{aligned}\tag{4.53}$$

These equations form a linear system for u_1 and u_3 with

$$\begin{aligned}
u_1&=-Hu_3\ ,\\
u_3&=\frac{\delta S\left(e^{(h-1)/\delta}(1-G)-1\right)+GU_o(h)}{2G\left[-H\cosh(kh)+\cosh(\lambda_2 h)\right]-\delta\Lambda k^2 E_\nu\frac{k^2-\lambda_2^2}{2\lambda_2}\sinh(\lambda_2 h)}\ ,
\end{aligned}\tag{4.54}$$

and where the function $H(h,k,\lambda_2)$ is given as

$$H(h,k,\lambda_2)=\frac{\lambda_2}{k}\frac{\frac{\lambda_2}{k}\cosh(\lambda_2 h)+(F-1)\sinh(\lambda_2 h)}{\cosh(kh)+(F-1)\sinh(kh)}\ .\tag{4.55}$$

These rather opaque solutions can be clarified a little by looking at the various relevant limits. For weakly stratified fluids $\lambda_2\to 0$. Then $H(h,k,\lambda_2)=O(\lambda_2^2)\to 0$, and so

$$u_3=\frac{\delta S\left(e^{(h-1)/\delta}(1-G)-1\right)+GU_o(h)}{2G-\delta\Lambda k^4 E_\nu\frac{h}{2}}+O(\lambda_2^2)\ .\tag{4.56}$$

In the limit $\mathrm{E}_\nu\to 0$ this then becomes

$$\begin{aligned}
u_1&=O(\lambda_2^2)\ ,\\
u_3&=\frac{1}{2}\left[U_o(h)-\delta S\frac{1-\cosh((1-h)/\delta)}{\sinh((1-h)/\delta)}\right]\ .
\end{aligned}\tag{4.57}$$

Folding this back into the original solution in the radiative zone then yields

$$\hat{w}(z) = -ik^3 E_\nu u_3 z = -\frac{ik^3 E_\nu}{2}\left[U_o(h) - \delta S \frac{1-\cosh((1-h)/\delta)}{\sinh((1-h)/\delta)}\right] z \ , \tag{4.58}$$

which is identical to equation (4.19).

In the opposite, strongly stratified limit, $\lambda_2 \gg k$. Then we have instead

$$H(h,k,\lambda_2) \simeq \frac{\lambda_2^2}{k^2}\frac{\cosh(\lambda_2 h)}{\cosh(kh) + (F-1)\sinh(kh)} \ , \tag{4.59}$$

so that this time $u_3 = O(\lambda_2^{-2}) \to 0$, and in the limit $\mathrm{E}_\nu \to 0$

$$u_1 = \frac{1}{2\cosh(kh)}\left[U_o(h) - \delta S \frac{1-\cosh((1-h)/\delta)}{\sinh((1-h)/\delta)}\right] \ . \tag{4.60}$$

Folding this back into the equation for $\hat{w}(z)$ in the radiative zone now yields

$$\hat{w}(z) = -\frac{ik^3 \mathrm{E}_\nu}{2\lambda_2}\frac{\sinh(\lambda_2 z)}{\cosh(\lambda_2 h)}\left(1 - \frac{\tanh(kh)}{\tanh(k(1-h))}\right)\left[U_o(h) - \delta S \frac{1-\cosh((1-h)/\delta)}{\sinh((1-h)/\delta)}\right] \ , \tag{4.61}$$

therefore justifying the scaling discussed in 4.2.4.3.

Chapter 5

Magnetohydrodynamics:

Numerical Solutions

This chapter is in preparation for publication of the paper *2-D Numerical simulations of the Solar Tachocline* in the Astrophysical Journal. It focuses on the development of a numerical model to validate the Gough and McIntyre theory on the solar tachocline. The model solves for the interaction between large-scale meridional flows generated in the convection zone with an internal magnetic field residing in the radiative zone. We have found solutions that have qualitative similarity with observations. An analysis of the forces dominating the dynamics of the radiative zone confirms the assumptions and predictions about the tachopause and the tachocline in the Gough and McIntyre's theory.

Our model is built upon the work of Garaud and Garaud (2008, referred to as GG08 hereafter). GG08 developed a code to find 2-D steady state, axisymmetric solutions of the MHD equations in the radiative zone only. They started from a spherically symmetric background state in hydrostatic equilibrium derived from 1-D solar standard models, and studied perturbations to the system caused by a differential rotation imposed from an overlying convection zone and

an internal, primordial magnetic field. They included perturbations of all thermodynamical quantities as well as the velocity and magnetic fields. The system solved was fully non-linear in terms of velocity and magnetic field perturbations, but was linearized in the thermodynamic perturbations.

Their computational domain was a spherical shell with r in $[0.35, r_0]$. The background state was computed from model S Christensen-Dalsgaard, Gough, and Thompson (1991), and the diffusivities using formulae derived by Gough (2007). It is important to note that all the forcing (differential rotation and magnetic field) was applied through the boundary conditions. The radiative-convective interface was assumed to be differentially rotating, and inflow/outflow boundary conditions were used to model the effects of an overlying convection zone in driving large-scale azimuthal and meridional flows. GG08 also assumed the presence of a primordial field maintained by a point dipole located at the origin. The core field was matched onto the computational domain field at the lower boundary.

Under the point dipole assumption, unfortunately, the magnetic field $\mathbf{B}$ reaches unrealistically high amplitudes near the center, leading to numerical convergence difficulties and driving artificial MHD instabilities near the lower boundary. This ultimately prevented GG08 from obtaining solutions at low enough diffusivities to exhibit a Gough and McIntyre-like tachocline.

In order to improve the stability of the numerical scheme and model the dynamics of the complete system, including both the convection zone and the radiative zone, we revisit their model extending the computational domain and introducing body terms to drive the flows and maintain the field. The equations governing the dynamics of the system, all variables of interest, boundary conditions, and the method of solution are described in the following section.

5.1 The Model

5.1.1 The background state

As in GG08, our background state is a non-rotating, non-magnetic Sun in hydrostatic equilibrium. We interpolate Model S (Christensen-Dalsgaard etal., 1996) to obtain the density $\bar{\rho}$, temperature $\bar{T}$, pressure $\bar{p}$, gravity $\bar{g}$, and heat capacity at constant pressure $\bar{c_p}$ of the background fluid as a function of radius r.

Our computational domain is larger than that of GG08, and consists of a spherical shell with r ranging from $r_{in} = 0.05R_\odot$ to $r_{out} = 0.95R_\odot$. The system is assumed to be rotating with mean angular velocity

$$\Omega_\odot = \Omega_{\rm eq}\left[1 - \frac{1}{5}a_2 - \frac{3}{35}a_4\right] \ , \tag{5.1}$$

where $\Omega_{\rm eq}$, a_2, and a_4 were defined in Section 4.3.1. This expression results from assuming the total angular momentum of the convection zone to be zero in the rotating frame (Gilman, Morrow and Deluca, 1989).

Our goal is to study how this background changes under forcing by the differential rotation in the convection zone and by a large-scale primordial field.

5.1.2 The model equations

To find steady-state solutions for the equations governing the magnetohydrodynamics (MHD) of the solar interior, we assume that all resulting fluid motions are sufficiently slow to apply the anelastic approximation and assume axial symmetry. In spherical coordinates (r, θ, ϕ), perturbed thermodynamical fields q are written as $q(r,\theta) = \bar{q}(r) + \tilde{q}(r,\theta)$, where the bar indicates the background state and the tilde refers to the (small) perturbations.

Under these assumptions, the system of governing equations can be written as:

$$2\bar{\rho}(r)\mathbf{\Omega}\times\mathbf{u} = -\nabla\tilde{p}-\tilde{\rho}\bar{g}(r)\mathbf{e}_r+\mathbf{j}\times\mathbf{B}+\nabla\cdot\mathbf{\Pi}-\frac{1}{\tau(r)}(\mathbf{u}-\mathbf{u}_{cz}) \quad (5.2)$$

$$\bar{\rho}(r)\bar{T}(r)\mathbf{u}\cdot\nabla\bar{s}(r) = \nabla\cdot(k(r)\nabla\tilde{T}) \quad (5.3)$$

$$\nabla\times(\mathbf{u}\times\mathbf{B}) = \nabla\times[\eta(r)(\nabla\times\mathbf{B}-4\pi\mathbf{j_0})] \quad (5.4)$$

$$\frac{\tilde{p}}{\bar{p}(r)} = \frac{\tilde{\rho}}{\bar{\rho}(r)}+\frac{\tilde{T}}{\bar{T}(r)} \quad (5.5)$$

$$\nabla\cdot(\bar{\rho}(r)\mathbf{u}) = 0 \quad (5.6)$$

$$\nabla\cdot\mathbf{B} = 0\ , \quad (5.7)$$

where $\mathbf{u}$ is the velocity of the fluid, $\mathbf{B}$ the magnetic field, $\mathbf{j}$ the electric current density, η the magnetic diffusivity, and k the thermal conductivity. The viscous stress tensor $\mathbf{\Pi}$ incorporates the contribution of the viscosity ν:

$$\mathbf{\Pi}=\bar{\rho}(r)\nu(r)\left[\nabla\mathbf{u}+(\nabla\mathbf{u})^{\mathbf{T}}-\frac{\mathbf{2}}{\mathbf{3}}(\nabla\cdot\mathbf{u})\mathbf{I}\right]\ , \quad (5.8)$$

where $\mathbf{I}$ is the identity matrix.

The non-linear advection term in the momentum equation is neglected in the radiative region. In the convection zone, its main effect is assumed to be the driving of the differential rotation. For this reason we replace $(\mathbf{u}\cdot\nabla)\mathbf{u}$ by the body force term $-\frac{1}{\tau}(\mathbf{u}-\mathbf{u}_{cz})$ where $1/\tau$ vanishes in the radiative zone (see Section 5.1.6.1 for more detail). Similarly, we introduce a forcing term $\mathbf{j}_0$ in the magnetic induction equation to maintain a background magnetic field (see Section 5.1.6.2 for detail).

5.1.3 The diffusivity profiles

In all what follows, we use r_0 to denote the radius of the radiative-convective interface. For simplicity, diffusivities in the radiative zone ($r < r_0$) are assumed to be constant, with values ν_{rz}, η_{rz}, and κ_{rz}. In the convection zone, we assume that magnetic and thermal diffusivities

both increase to model the effects of the turbulence on the field and on heat transport [1]. Thus, for $r > r_0$:

$$\nu(r) = \nu_{rz} \tag{5.9}$$

$$\eta(r) = \eta_{rz} + \eta_{turb}(r) \tag{5.10}$$

$$\kappa(r) = \kappa_{rz} + \kappa_{turb}(r) \ , \tag{5.11}$$

where

$$\eta_{turb}(r) = \frac{1}{2}(\eta_{cz,max} - \eta_{rz})\frac{r - r_1}{r_{out} - r_1}\left[\tanh\left(\frac{r - r_2}{\Delta_{cz}}\right) + 1\right] \tag{5.12}$$

$$\kappa_{turb}(r) = \frac{1}{2}(\kappa_{cz,max} - \kappa_{rz})\frac{r - r_1}{r_{out} - r_1}\left[\tanh\left(\frac{r - r_2}{\Delta_{cz}}\right) + 1\right] \ , \tag{5.13}$$

where r_1 is the location where thermal and magnetic diffusivities start increasing. Note that r_1 does not necessarily have to be equal to the radius of the radiative-convective interface r_0. In fact, we choose $r_1 > r_0$ for the reasons explained in Section 5.2. The selection of the offset $\delta_{cz} = r_1 - r_0$ is also discussed in Section 5.2. In addition, we include a tanh term in the diffusivity profiles with midpoint r_2 and width Δ_{cz}. This smoothes out the transition of diffusion from laminar to turbulent regimes. In all that follows, we take $r_2 = 0.7427 R_\odot$ and $\Delta_{cz} = 0.02 R_\odot$.

5.1.4 The stratification parameter σ and the selection of N^2

In Chapter 4 (see also Wood, McCaslin, and Garaud , 2011), we showed the importance of the stratification parameter $\sigma = \sqrt{\mathrm{Pr}} N/\Omega_\odot$ in setting the vertical scale of the penetration of the flows into the radiative interior. If σ is too large, flows are rapidly damped and will not be able to confine the magnetic field. We therefore have to ensure that σ is of the same order as in

[1] We do not increase the viscosity in the convection zone to prevent the formation of Ekman layers near the radiative-convective interface, which might drive flows not associated with the differential rotation. By keeping $\nu = \nu_{rz}$ across the convection zone, we guarantee that the meridional flows generated in the convection zone are the result of gyroscopic pumping only, as recommended by Gough and McIntyre (1998)

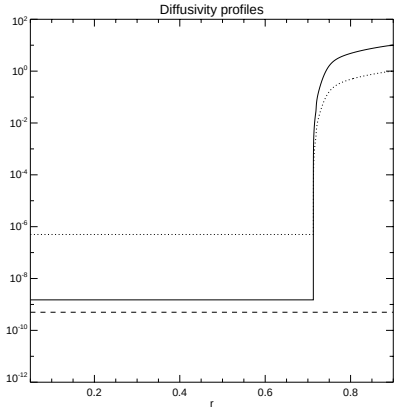

Figure 5.1: This plot shows the diffusivity profiles for our fiducial model. The non-dimensional diffusivities in the radiative zone are $E_\nu = 5.0 \times 10^{-9}$, $E_\eta = 1.5 \times 10^{-8}$, and $E_\kappa = 5.0 \times 10^{-7}$. The diffusion parameters are kept constant inside the radiative region, and both the magnetic and thermal diffusivities are sharply increased in the convection zone.

the Sun. Since our Prandtl number is *not* solar, we chose to modify the background stratification profile N in the simulation in such a way to ensure that $\sigma(r)$ is the actual solar σ profile, $\sigma_\odot(r)$, as computed from Model S. We proceed as follows.

First, we compute the "true" background diffusivities $\nu_\odot(r)$ and $\kappa_\odot(r)$ in the radiative zone by using the expressions derived by Gough (2007). Then, we compute the solar profile for the stratification parameter

$$\sigma_\odot(r) = \sqrt{\frac{\nu_\odot(r)}{\kappa_\odot(r)}} \left(\frac{\bar{N}_\odot(r)}{\Omega_\odot} \right) , \tag{5.14}$$

where $\bar{N}_\odot(r)$ is the solar profile for the buoyancy frequency from standard Model S.

Once the numerical diffusivity profiles $\nu(r)$ and $\kappa(r)$ have been selected (see Section 5.1.3), we construct an artificial buoyancy frequency profile $\bar{N}^2$ satisfying:

$$N(r) = \begin{cases} \frac{1}{2}\sigma_\odot(r)\Omega_\odot \sqrt{\frac{\kappa_{rz}}{\nu_{rz}}} \left[1 - \tanh\left(\frac{r - r_3}{\Delta_{rz}} \right) \right] & , \text{for } r < r_0 \\ 0 & \text{otherwise.} \end{cases}$$

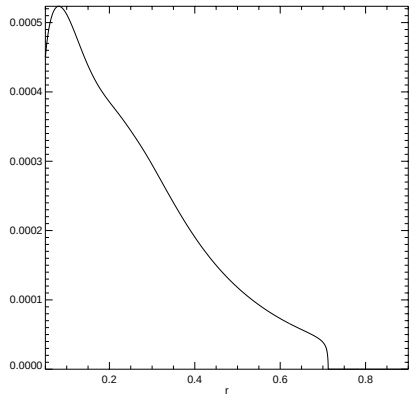

Figure 5.2: This plot shows the computed buoyancy frequency profile needed to recover the solar σ profile in our numerical experiments. The plot shown here corresponds to non-dimensional diffusivities $E_\nu = 5.0 \times 10^{-9}$, $E_\eta = 1.5 \times 10^{-8}$, and $E_\kappa = 5.0 \times 10^{-7}$.

The added tanh profile and its parameters r_3 and Δ_{rz} are chosen to smooth out the N profile a little bit compared with that of Model S. Indeed, the latter is too sharp, which is particularly difficult to treat numerically and is furthermore known to be likely sharper than the true solar profile. In what follows, we take $r_3 = 0.7127 R_\odot$ and $\Delta_{rz} = 0.02 R_\odot$. Figure 5.2 shows the modified buoyancy frequency used in our fiducial model.

5.1.5 Non-dimensional equations

The variables are non-dimensionalized as follows: distances with respect to the solar radius $R_\odot$, time to the inverse of the mean solar rotation rate $\Omega_\odot$, velocities to $R_\odot \Omega_\odot$, density to $\rho_0 = 1\ g\ cm^{-3}$, temperature to $T_0 = 1\ K$, pressure to $\rho_0 R_\odot^2 \Omega_\odot^2$, and the magnetic field B is normalized to $\mathcal{B}_0$, which is the value of the imposed primordial field in the core (see Section 5.1.6.2).

The non-dimensionalization of the governing equations yields the following non-dimensional

(constant) model parameters:

$$\begin{aligned}
\Lambda &= \frac{\mathcal{B}_0^2}{4\pi\rho_0 R_\odot^2 \Omega_\odot^2} \\
E_\kappa &= \frac{\kappa_{rz}}{R_\odot^2 \Omega_\odot} \\
E_\eta &= \frac{\eta_{rz}}{R_\odot^2 \Omega_\odot} \\
E_\nu &= \frac{\nu_{rz}}{R_\odot^2 \Omega_\odot} \ . \qquad (5.15)
\end{aligned}$$

Under these circumstances and omitting the notation (r) for the radial dependency of all background quantities for simplicity, the system of equations becomes:

$$\begin{aligned}
2\mathbf{e}_r \times \hat{\mathbf{u}} &= -\frac{\rho_0}{\bar{\rho}}\nabla\hat{p} + \frac{\rho_0\hat{\rho}}{\bar{\rho}}\frac{\bar{g}}{R_\odot\Omega_\odot^2}\mathbf{e}_r + \frac{\Lambda}{\bar{\rho}}(\nabla\times\hat{\mathbf{B}})\times\hat{\mathbf{B}} \qquad (5.16) \\
&\quad + \frac{1}{\bar{\rho}}\nabla\cdot\mathbf{\Pi} - \frac{1}{\tau}(\hat{\mathbf{u}} - \hat{\mathbf{u}}_{cz}) \qquad (5.17) \\
\frac{N^2}{\bar{g}}\frac{\bar{T}}{T_0}\hat{\mathbf{u}}\cdot\mathbf{e}_r &= \frac{1}{\bar{\rho}\bar{c_p}}\nabla\cdot[\bar{\rho}\bar{c_p}(E_\kappa + E_{\kappa,turb})\nabla\hat{T}] \qquad (5.18) \\
\nabla\times(\hat{\mathbf{u}}\times\hat{\mathbf{B}}) &= \nabla\times[(E_\eta + E_{\eta,turb})(\nabla\times\hat{\mathbf{B}} - 4\pi\hat{\mathbf{j}}_0)] \qquad (5.19) \\
\rho_0 R_\odot^2\Omega_\odot^2\frac{\hat{p}}{\bar{p}} &= \rho_0\frac{\hat{\rho}}{\bar{\rho}} + T_0\frac{\hat{T}}{\bar{T}} \qquad (5.20) \\
\nabla\cdot(\bar{\rho}\hat{\mathbf{u}}) &= 0 \qquad (5.21) \\
\nabla\cdot\hat{\mathbf{B}} &= 0 \ , \qquad (5.22)
\end{aligned}$$

where the non-dimensional, computed perturbation fields are denoted by hats. Here

$$\begin{aligned}
E_{\eta,turb} &= \frac{\eta_{turb}}{R_\odot^2\Omega_\odot} \qquad (5.23) \\
E_{\kappa,turb} &= \frac{\kappa_{turb}}{R_\odot^2\Omega_\odot} \ . \qquad (5.24)
\end{aligned}$$

5.1.6 The forcing terms

5.1.6.1 Convection zone forcing

With the available code we cannot model the short-term turbulent flows that characterize the convection zone. As such, we cannot model the generation of the large-scale differential rotation self-consistently either. Instead, we use a forcing term that drives large-scale zonal flows to reproduce the observed differential rotation, i.e.

$$\mathbf{u}_{cz} = x \sin\theta R_\odot \frac{\Omega_{\rm cz}(x,\theta)}{\Omega_\odot} \mathbf{e}_\phi \ , \tag{5.25}$$

where $x = r/R_\odot$. This forced shear flow in the azimuthal direction also guarantees a continuous gyroscopic pumping of meridional flows in the convection zone (GAA09; Garaud and Bodenheimer , 2010), with downwelling in polar regions and upwelling near the equator[2].

The forcing is imposed as

$$-\frac{1}{\tau}(\mathbf{u} - \mathbf{u}_{cz}) \ , \tag{5.26}$$

where the relaxation timescale τ is defined such that

$$\frac{1}{\tau(x)} = \frac{1}{\tau_{cz}} \left[\frac{x - x_0}{x_{out} - x_0} \right] \ , \text{for } x > x_0 \ . \tag{5.27}$$

The quantity τ_{cz} can be interpreted as the turnover time for the convective flows[3]. We have chosen the τ profile so that $1/\tau(x)$ starts increasing linearly exactly from the base of the convection zone upward. By gradually increasing the forcing, we prevent the formation of boundary layers at the radiative-convective interface that a step function, as

$$\frac{1}{\tau(x)} = \begin{cases} \frac{1}{\tau_{cz}} & \text{, for } x > x_0 \ , \\ 0 & \text{otherwise,} \end{cases}$$

[2] According to Gough and McIntyre (1998), one of the main conditions in modeling the dynamics of the solar interior is the existence of large-scale meridional flows generated by gyroscopic pumping in the convection zone.

[3] Note that the forcing term in the momentum equation is similar to the one used by Garaud and Bodenheimer (2010) and by Rogers (2011) in their modeling of the hydrodynamics of the convection zone.

might otherwise generate (see GAA09).

The shape and magnitude of the of the function $\tau(x)$ has little direct impact on the resulting dynamics in the radiative interior (Wood, McCaslin, and Garaud , 2011).

5.1.6.2 The new magnetic background

Another modification to GG08's model is in the treatment of the background magnetic field. Instead of maintaining it through boundary conditions, we assume the presence of an azimuthal electric current density in the region where $r_a \leq r \leq r_b$, which induces a magnetic field $\mathbf{B}_0$. With $x = r/R_\odot$ again, the non-dimensional expression for this current density is chosen to be:

$$\hat{\mathbf{j}}_0(x,\theta) = \begin{cases} J_0(x-x_a)(x-x_b)\sin\theta\mathbf{e}_\phi & \text{, for } x_a < x < x_b \\ 0 & \text{everywhere else} \end{cases}$$

where x_a and x_b are both far below the region where the tachocline is expected to form. In all that follows, we take $x_a = 0.1$ and $x_b = 0.3$. This generates a dipolar magnetic field, whose exact radial dependence is shown in Appendix B. By restricting this forcing term to a short radial interval within the radiative zone, we reduced the scope for numerical instabilities near the core, which created difficulties in GG08.

The non-dimensional, electric current density amplitude J_0 is specifically chosen so that the induced non-dimensional magnetic field within the core sphere ($x < x_a$) is constant and equal to 1. This is done in the following way.

The magnetic potential $\hat{A}_0$[4], solution of

$$\hat{\mathbf{j}}_0 = \nabla \times \nabla \times \left(\frac{\hat{A}_0}{4\pi x \sin\theta} \hat{\mathbf{e}}_\phi \right) \tag{5.28}$$

[4]We define the magnetic vector potential as in Garaud and Guervilly (2009).

is:

$$\hat{A}_0(x,\theta) = \begin{cases} \frac{1}{2}x^2 \sin^2\theta & , 0 \le x \le x_a \\ -8\pi J_0 x^2 \left[\frac{1}{18}x^3 - \frac{1}{10}(x_a+x_b)x^2 + \frac{1}{4}x_a x_b x + \frac{c_1}{3} + \frac{c_2}{x^3}\right]\sin^2\theta & , x_a \le x \le x_b \\ \frac{c_3}{2x}\sin^2\theta & , x_b \le x \end{cases} \tag{5.29}$$

thus guaranteeing that the field in the core ($x < x_a$) is $\mathbf{B}_0 = \hat{\mathbf{e}}_z$.

J_0 and the other constants c_1, c_2, and c_3 are then obtained by requiring continuity of B_r and $\mathrm{d}B_r/\mathrm{d}x$ at $x = x_a$ and $x = x_b$, which results in:

$$c_1 = -\left[\frac{1}{3}x_b^3 - \frac{1}{2}(x_a+x_b)x_b^2 + x_a x_b^2\right] \tag{5.30}$$

$$3c_2 = \frac{1}{6}x_a^6 - \frac{1}{5}(x_a+x_b)x_a^5 + \frac{1}{4}x_a x_b x_a^4 \tag{5.31}$$

$$3c_3 = 8\pi J_0\left[\frac{1}{6}(x_b^6 - x_a^6) - \frac{1}{5}(x_a+x_b)(x_b^5 - x_a^5) + \frac{1}{4}x_a x_b (x_b^4 - x_a^4)\right] , \tag{5.32}$$

and

$$J_0 = \frac{3}{8\pi\left[\frac{1}{3}(x_b^3 - x_a^3) - \frac{1}{2}(x_a+x_b)(x_b^2 - x_a^2) + x_a x_b (x_b - x_a)\right]} . \tag{5.33}$$

For our fiducial model with $x_a = 0.1$ and $x_b = 0.3$, we have $J_0 = -1125/4\pi = -89.52466$, $c_1 = 0.00000$, $c_2 = 3.88889 \times 10^{-8}$, and $c_3 = 8.25556 \times 10^{-6}$. Figure 5.3 shows contour lines of the magnetic potential A_0 induced by this forcing term $\mathbf{j}_{0,\phi}$.

5.1.7 Boundary conditions

The bottom boundary at x_{in} is considered impermeable and stress-free. The core angular velocity, Ω_{in}, is chosen in such a way as to guarantee that the fluid exerts a zero total

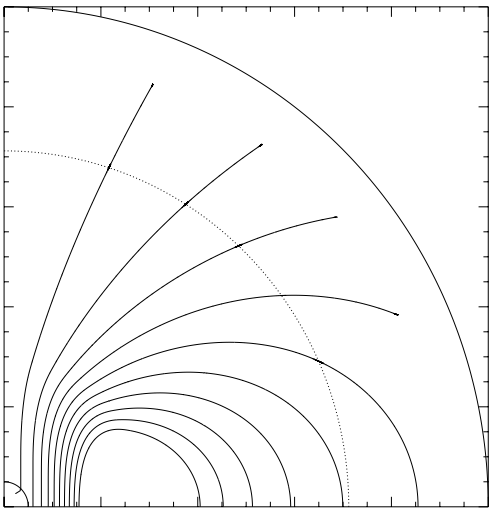

Figure 5.3: Plot of the magnetic field lines that result from the definition of an electric current density in the azimuthal direction near the core.

torque on the core. This implies:

$$\hat{u}_r(x_{in},\theta) = 0 \tag{5.34}$$

$$\frac{\partial \hat{u}_\theta(x_{in},\theta)}{\partial x} = 0 \tag{5.35}$$

$$\int_{-\pi/2}^{\pi/2} \left(\frac{\bar{\rho}}{\rho_0} E_\nu x_{in}^2 \frac{\partial \hat{\Omega}}{\partial x} \sin^2\theta + \frac{\hat{B}_r \hat{B}_\phi}{4\pi} x_{in} \sin\theta \right) \sin\theta \mathrm{d}\theta = 0 \ . \tag{5.36}$$

The inner core ($x < x_{in}$) is also considered as a thermally conducting solid (out of the computational domain) with the same thermal diffusivity as the fluid close to the bottom boundary ($x = x_{in}$). The temperature perturbations in the core satisfy the Laplace equation:

$$\nabla^2 \tilde{T}(x_{in},\theta) = 0 \ . \tag{5.37}$$

Requiring continuity of $\tilde{T}$ and $\mathrm{d\tilde{T}/dx}$ at the interface between the core and the bottom region of the system, the solutions of Equation 5.37 are matched onto the solutions of the computational domain at the boundary $x = x_{in}$.

Similarly, the inner core is electrically conducting and with the same electric current density and electric conductivity as the fluid near the bottom boundary of the radiative zone. The magnetic field perturbations also satisfy the Laplace equation in the core:

$$\nabla^2 \mathbf{B}(x_{in},\theta) = 0 \ . \tag{5.38}$$

Requiring continuity of B_r and B_θ at the interface core-model domain, the solutions in the computational domain are matched onto the core solution at the bottom boundary.

The inner core boundary conditions are completed with the following equations for the top boundary at x_{out}:

$$\hat{u}_r(x_{out},\theta) = 0 \tag{5.39}$$

$$\hat{u}_\theta(x_{out},\theta) = 0 \tag{5.40}$$

$$\hat{u}_\phi(x_{out},\theta) = x_{out}\sin\theta\hat{\Omega}_{\rm cz}(\theta) \tag{5.41}$$

$$\nabla^2\tilde{T}(x_{out},\theta) = 0 \tag{5.42}$$

$$\nabla^2\mathbf{B}(x_{out},\theta) = 0\ , \tag{5.43}$$

which simply indicate that we model a impermeable, no-slip top boundary with temperature perturbations and the magnetic field satisfying the Laplace equation outside the domain. The top boundary condition for the zonal flow indicates that we assume the fluid to rotate with the angular velocity as estimated from helioseismic inversions, namely $\hat{\Omega}_{\rm cz}(x,\theta) \approx \Omega_{\rm eq}(x)(1 - a_2(x)\cos^2\theta - a_4(x)\cos^4\theta)$ with $x = x_{out}$, $a_2 = 0.17$, and $a_4 = 0.08$.

5.1.8 The Newton-Raphson-Kantorovich method

Once the parameterization for the model is set, the system of partial differential equations governing the magnetohydrodynamics of the solar interior is numerically solved by using the algorithm developed by GG08. The details on how these equations are solved and implemented in our model are well described in GG08. Here, we give a brief description of th method for completeness.

The system of governing equations and boundary conditions is expanded in terms of Chebyshev polynomials and projected onto the radial coordinate to generate a system of ordinary differential equations. Numerical solutions of these coupled nonlinear ODEs are obtained by the parallel implementation of the Newton-Raphson-Kantorovich method, coded in FORTRAN 77, by Garaud and Garaud (2008). This research project used the same FORTRAN routines. Appendix G provides several examples on how to use the NRK method.

5.2 Model sensitivity to turbulent magnetic diffusivity in the convection zone

Flows of significant amplitude are driven in the convection zone by gyroscopic pumping. As a result, the geometry and the structure of the magnetic field in the convection zone is very sensitive to the assumed magnetic diffusivity profile, $E_{\eta,turb}(r)$, in that region. In this section, we describe the impact that small changes in the magnetic diffusivity profile have on the overall magnetic field configuration.

By testing different profiles while keeping the rest of the parameters unchanged, we noticed that small changes near the base of the convection zone led to major changes in the magnetic field configuration in the steady-state solution. More precisely, we varied $\delta_{cz} = r_1 - r_0$, the offset between the position r_1 (see Equation 5.12) where the magnetic diffusivity starts increasing above its basic radiation zone value, and the radius of the radiative-convective interface r_0. Figure 5.4 illustrates the two possible scenarios in terms of the resulting configuration of the magnetic field. In both cases, the functional form of the diffusion parameters is similar to the one described in Table 5.1, with $E_{\nu,rz} = 5.0 \times 10^{-9}$, $E_{\eta,rz} = 1.5 \times 10^{-8}$, and $E_{\kappa,rz} = 5.0 \times 10^{-6}$.

When the magnetic diffusivity turns turbulent at the radiative-convective interface (i.e. when $\delta_{cz} = 0.000$), we see that the field remains open. On the other hand, when we move up the point of transition even a tiny distance into the convection zone ($\delta_{cz} = 0.002 R_\odot$), the magnetic field is confined by the convection zone flows, just above the radiative-convective interface. For the sake of clarity, in all that follows we will call this confinement by convection zone flows "pre-confinement" to contrast it with the effect of confinement by meridional flows deeper in the radiative zone. Pre-confinement is quite different from the dynamics described by Gough and McIntyre for the reasons pointed out below.

However, let us first describe why such a small offset δ_{cz} of the $E_{\eta,turb}$ profile results in

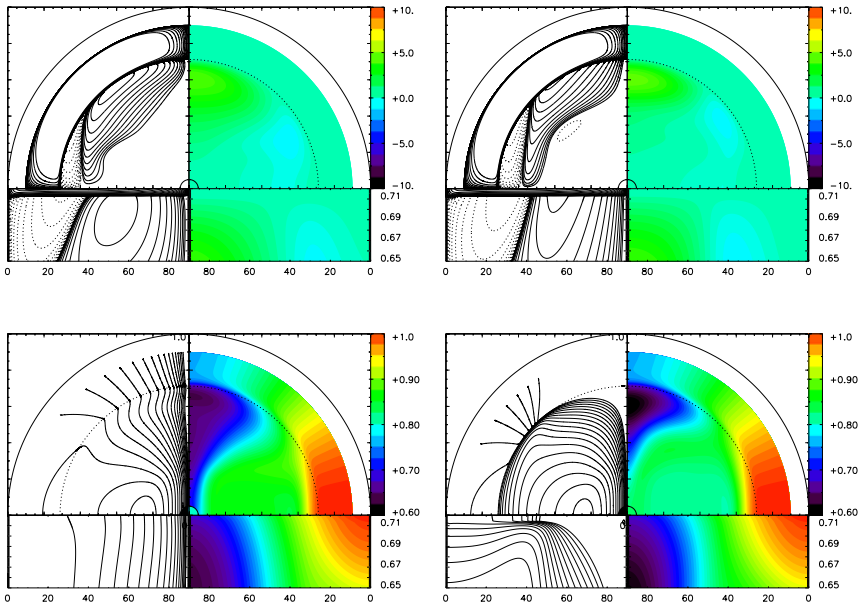

Figure 5.4: Effect of the location where the magnetic diffusivity becomes turbulent on the geometry of the magnetic field. Here we see, on the left panel, that when the magnetic diffusivity starts its turbulent behavior at the base of the convection zone, the steady-state resulting magnetic field is open. On the other hand, when the point of turbulent magnetic diffusivity shifts upward as a small distance as $\delta_{cz} = 0.002 R_{\odot}$, the steady-state configuration of the magnetic field exhibits confinement at the base of the convection zone, as we see on the right panel.

magnetic pre-confinement in the lower convection zone by contrast with the unconfined solution when $\delta_{cz} = 0$. We compute the magnetic Reynolds number $\mathrm{Rm} = u_r L/\eta$, where L is arbitrarily selected to be $L = 0.10 R_\odot$, for both simulations shown in Figure 5.4. The results are shown in Figure 5.5. Since downwelling flows reaching the lower convection zone show similar profiles in both cases (see Figure 5.6), the magnetic Reynolds number Rm is mostly controlled by the value of the magnetic diffusivity. In the case where $\delta_{cz} = 0.000$, the flow amplitude drops to zero, approaching the base of the convection zone, at the same rate (more or less) as E_η, leading to $\mathrm{Rm} < 1$ in the entire convection zone, as shown in Figure 5.5. On the other hand, when $\delta_{cz} = 0.002 R_\odot$, the location where magnetic diffusivity turns turbulent moves higher up into the convection zone, and a shallow region $r_0 < r < 0.7145 R_\odot$ appears where strong meridional flows, combined with a sufficiently low magnetic diffusivity, yield $\mathrm{Rm} \gg 1$. This indicates a strong interaction between flows and magnetic field, which results in magnetic field "pre-confinement" in the convection zone.

In the absence of any other dynamics, this "pre-confinement" model is not dissimilar from the one described by Kitchatinov and Rüdiger (2006), who built a model of the radiative region with meridional flows only penetrating an Ekman layer of the order of 100 meters (when microscopic viscosity is assumed). They argued that these meridional flows are suficiently strong to confine the field. However, any meridional flows in the bulk of the radiative interior were neglected. As a result, their tachocline is *very* different from the one described by the Gough and McIntyre model, because it is a laminar layer in magnetoviscous balance. In essence, it is more like a "tachopause" than a "tachocline" (see Gough and McIntyre , 1998). The quantitative difference between "pre-confinement-only" models *a la* Kitchatinov and Rüdiger and the Gough and McIntyre model is discussed in more detail in Section 5.4.3.2. What is interesting, however, is that pre-confinement appears to be needed to facilitate the deeper Gough and McIntyre's confinement process. Indeed, with pre-confinement, we are able to find deeply confined solutions

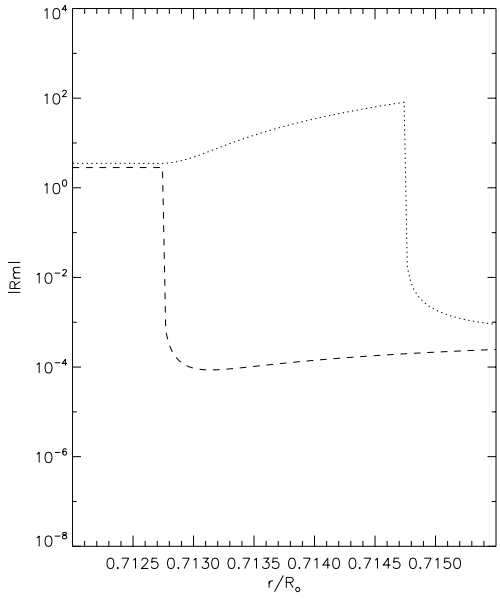

Figure 5.5: This plots shows the magnetic Reynolds number, Rm $= u_r L/\eta$, with $L = 0.10 R_\odot$, as computed for the two cases illustrated in Figure 5.4. As we can see in this zoomed in region near the base of the convection zone, Rm $\gg 1$ for the pre-confined field case (dotted line), which indicates that the flows are interacting with the magnetic field to a great extent within the convection zone. On the other hand, Rm $\ll 1$ for the open case (dashed line), which corresponds to a situation where there is no flow-magnetic field interaction.

as described in Section 5.3.

Is magnetic field pre-confinement in the convection zone a possible scenario in the real Sun? Brummell, Clune, and Toomre (2001), as well as Garaud and Rogers (2007) proposed that magnetic "pre-confinement" could be the result of turbulent pumping of magnetic field by overshooting plumes crossing the radiative-convective interface. Since the transport of angular momentum and magnetic fields can only be modeled in three dimensions, Wood and Brummell (2012 submitted) have performed 3-D numerical simulations of the vicinity of the radiative-convective interface. Their preliminary results show that "horizontal" magnetic field in the equatorial region can be pre-confined by convective plumes regardless the presence of meridional flows. In the case of "polar" magnetic field, however, the confinement can only be achieved by

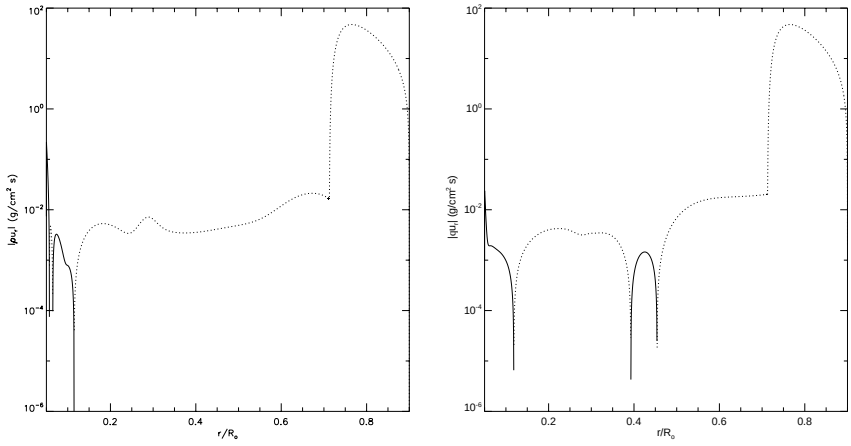

Figure 5.6: These plots show the mass flux at 80^o latitude for the two cases depicted in Figure 5.4, respectively. First, we see in the left panel how the downwelling mass flux remains high in amplitude even at very deep zones in the radiative zone. This happens when the magnetic field remains open at the radiative-convective interface. On the other hand, we see in the right panel how a pre-confined magnetic field at the radiative-convective interface affects the downwelling mass flux to the extent that the fluid in the radiative zone stops its burrowing at depths not so far from the interface.

meridional flows, as suggested by Wood and McIntyre (2011).

Since we cannot self-consistently model turbulent pumping in our simulation, we will use a non-zero δ_{cz} to force magnetic pre-confinement in the lower convection zone. In our fiducial model, we therefore fix $\delta_{cz} = 0.0003 R_\odot$ unless otherwise indicated.

5.3 Fiducial model results

We present in this section the results of our fiducial model. The governing parameters for this reference case were selected after a series of experiments starting from a parameter regime similar to the one proposed by Wood, McCaslin, and Garaud (2011) and gradually reducing all parameters simultaneously. The model selected is our best outcome for a well-resolved simulation. The parameterization of our fiducial model is summarized in Table 5.1. We

Parameter	Radiative Zone	Convection Zone
E_ν	5.0×10^{-10}	5.0×10^{-10}
E_η	1.5×10^{-9}	$1.5 \times 10^{-9} + 5.0\frac{r-r_1}{r_{out}-r_1}\left[\tanh\left(\frac{r-r_2}{\Delta_{rz}}\right)+1\right]$
E_κ	5.0×10^{-7}	$5.0 \times 10^{-7} + 0.5\frac{r-r_1}{r_{out}-r_1}\left[\tanh\left(\frac{r-r_2}{\Delta_{rz}}\right)+1\right]$
σ	$\sigma_\odot(r)\left[1-\tanh\left(\frac{r-r_0}{\Delta_{rz}}\right)\right]$	0.0
$\frac{1}{\tau}$	0.0	$\frac{1}{\tau_{cz}}\left[\frac{r-r_0}{r_{out}-r_0}\right]$
Λ	1.0×10^{-3}	1.0×10^{-3}

Table 5.1: **Non-dimensional parameters for the fiducial model.** Here, $r_0 = 0.7127R_\odot$ is the location of the radiative-convective interface, $r_1 = 0.7130R_\odot$ is the location where thermal and magnetic diffusivities start increasing, and r_2 and Δ_{rz} define the transition from laminar to turbulent diffusivities. Also, r_0 and Δ_{rz} are parameters of the transition of $\sigma(r)$ to zero near the base of the convection zone. The domain for this model runs from $r_{in} = 0.05R_\odot$ to $r_{out} = 0.90R_\odot$.

will first describe its qualitative properties and then analyze it more quantitatively by studying the balance of dominant forces responsible for the formation of the tachocline, and by comparing our findings with theoretical expectations from previous semi-analytical models (e.g. Gough and McIntyre , 1998; Wood, McCaslin, and Garaud , 2011).

5.3.1 A first glimpse of the solar tachocline

Figure 5.7 shows the steady-state solution of the flow field, temperature perturbation, magnetic field, and angular velocity, and demonstrates that magnetic confinement below the radiative-convective interface is possible.

The top left figure shows the steady-state meridional flows generated in the model. From the surface to the center, we identify three main regions. In the convection zone, the flows are driven by the gyroscopic pumping effect of the imposed zonal flow. We observe a single meridional cell with surface flows moving toward the poles and fluid near the base of the convection zone moving toward the equator.

The tachocline is located below the radiative-convective interface. Since the radiative region in our fiducial model is weakly stratified in terms of the parameter σ, a fraction of the

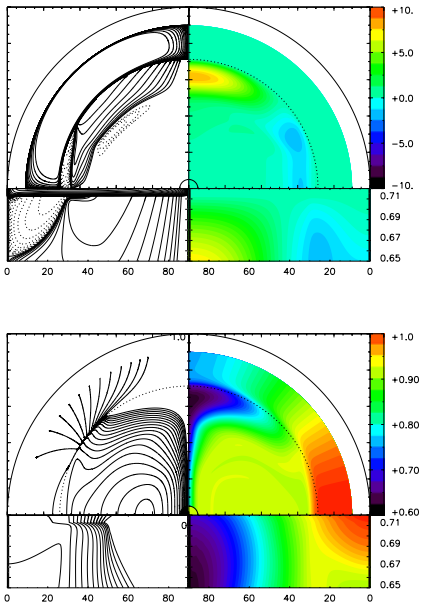

Figure 5.7: This plots shows the steady-state solution of the equations governing the magneto-hydrodynamics of the solar tachocline in our fiducial model (see Table 5.1). Starting from the top left panel and going clockwise, we show plots of the streamlines, temperature perturbations, angular velocity, and magnetic field lines. The top left panel shows that large-scale meridional flows generated in the convection zone are able to penetrate into the radiative interior at high latitudes. These downwelling flows are deflected by the internal magnetic field in the tachopause and, in turn, confine the field. This results in solid-body rotation of the radiative interior below the tachopause, as depicted in the bottom right panel.

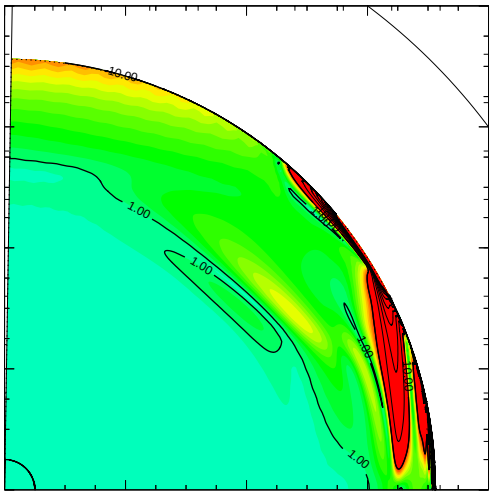

Figure 5.8: This plot shows the magnetic Reynolds number, $\mathrm{Rm} = u_r L/\eta$, with $L = 0.10 R_\odot$. Thick contour lines correspond to $\mathrm{Rm} = \{1.0, 10.0, 100.0\}$, and emphasize the region below the radiative-convective interface where the advection of the field is expected to dominate over diffusion.

meridional mass flux driven in the convection zone downwells into the tachocline. We observe two cells, including a large polar cell with meridional flows circulating clockwise, and a small equatorial cell with meridional flows circulating in the opposite direction. Both extend down to about $0.50 R_\odot$. The downwelling flows in the large cell, although weak in amplitude, are sufficiently strong to distort the magnetic field (see below). Below the tachocline, we observe a large meridional counter-cell. We show later that it is part of the tachopause. Below that region, the velocities are negligible.

The bottom left figure shows the effect of these flows on the poloidal magnetic field. In the upper part of the convection zone, the magnetic diffusivity is high and the flows do not affect the field. By contrast, we see that the field lines are strongly distorted by the flows in the lower

part of the convection zone, where the magnetic diffusivity drops and the magnetic Reynolds number increases above 10. Equatorward flows advect field lines from high to low latitudes, so their geometry in the vicinity of the base of the convection zone is mostly horizontal. This is what we call magnetic *pre-confinement* and was extensely discussed in Section 5.2.

Despite the fact that the flow velocities are much smaller within the tachocline than in the convection zone, the local magnetic Reynolds number remains relatively high (again, see Figure 5.8). Polar field lines are bent horizontally and advected toward mid-latitudes (roughly 30 degrees) as predicted by Gough and McIntyre (1998) and studied by Wood, McCaslin, and Garaud (2011). Below the tachopause at $r = 0.5R_\odot$, by contrast, we see that the field is not affected by the flows and is more or less equal to the imposed primordial field (see Figure 5.3).

The right bottom panel of Figure 5.7 illustrates the steady-state configuration of the angular velocity. The convection zone, as expected, rotates with the imposed differential rotation. Most of the radiative zone, by contrast, exhibits a uniform angular velocity, namely $\Omega \approx 0.92\Omega_{eq}$, which extends from the base of the tachocline to the core albeit with some shear near the polar axis. The tachocline lies between these two regions and matches their respective rotation profiles, although not necessarily monotonically (see in particular the polar sub-rotating region).

The remaining plot in Figure 5.7 provides the temperature perturbation computed by our fiducial model. The temperature perturbations are negligible in the magnetically dominated part of the radiative region, below the tachopause. By contrast, the tachocline exhibits a strong latitudinal temperature gradient consistent with thermal wind balance (see below).

We now analyze the results of the fiducial model more quantitatively to determine the dominant balances in each region, and verify whether this model satisfies the Gough and McIntyre's, as well as Wood, McCaslin, and Garaud's models.

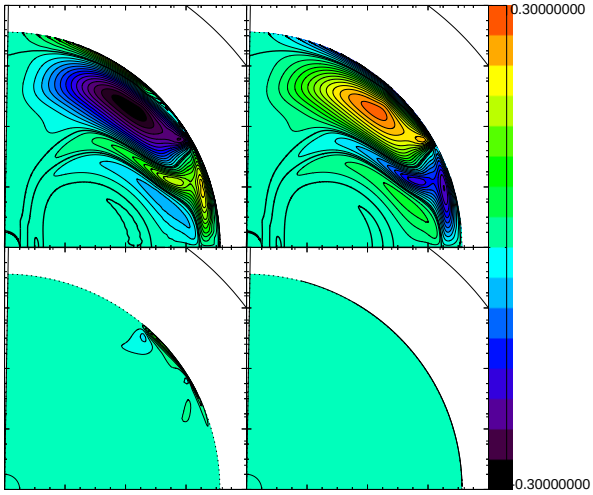

Figure 5.9: This figure shows a comparison of the various terms contributing to the global force balance in the azimuthal vorticity equation in our fiducial model. Note that these plots show the balance in the radiative region only (the convection zone appears in white). The rotational shear, as expressed in the left hand side of Equation 5.44 is shown in the top left panel, and is clearly in balance with the baroclinicity terms (right hand side of the same equation), as we can see in the top right panel. The remaining terms in the vorticity equation are shown in the two lower panels, and confirm that both viscous (left) and magnetic (right) stress-related terms are negligible.

5.3.2 Thermal wind balance in the radiative interior

The first aspect of Gough and McIntyre's theory that we verify is the assumption of thermal-wind balance. This equilibrium occurs when the system satisfies the hydrostatic and geostrophic balances. Taking the curl of the steady-state momentum equation divided by the background density $\bar{\rho}$, we obtain:

$$-2\Omega r\sin\theta\left[\cos\theta\frac{\partial\tilde{\Omega}}{\partial r}-\frac{\sin\theta}{r}\frac{\partial\tilde{\Omega}}{\partial\theta}\right]=\frac{1}{r\bar{\rho}^2}\frac{\partial\bar{\rho}}{\partial r}\frac{\partial\tilde{p}}{\partial\theta}-\frac{g}{r\bar{T}}\frac{\partial\tilde{T}}{\partial\theta}$$
$$+\left[\nabla\times\left(\frac{1}{\bar{\rho}}\mathbf{j}\times\mathbf{B}\right)\right]_\phi+\left[\nabla\times\left(\frac{1}{\bar{\rho}}\nabla\cdot\mathbf{\Pi}\right)\right]_\phi-\left[\nabla\times\left(\frac{\mathbf{u}-\mathbf{u}_{cz}}{\bar{\rho}\tau}\right)\right]_\phi, \tag{5.44}$$

where the left-hand side term represents the rotational shear[5], and the first two terms of the right-side account for the total baroclinicity. The balance between rotational shear and total baroclinicity is the thermal wind equation. The remaining terms on the right side are the magnetic and viscous torques as well as the curl of the gyroscopic pumping term. The latter is included for completeness but is zero in the radiative interior.

The two top panels in Figure 5.9 show the rotational shear (left panel) and the baroclinicity term (right panel), which clearly balance each other. The bottom panels, which show the viscous (left) and magnetic (right) terms, confirm that their respective contribution to the azimuthal vorticity equation is negligible. Hence, the assumption of thermal wind balance is valid.

5.3.3 The azimuthal force balance in the tachocline

The second aspect of Gough and McIntyre's theory that we examine is the angular momentum transport balance by studying the azimuthal component of the momentum equation.

[5]These two terms can be reduced to $2s\Omega\frac{\partial\tilde{\Omega}}{\partial z}$ when $s=r\sin\theta$ and $z=r\cos\theta$, which better represent the rotational shear along the polar axis

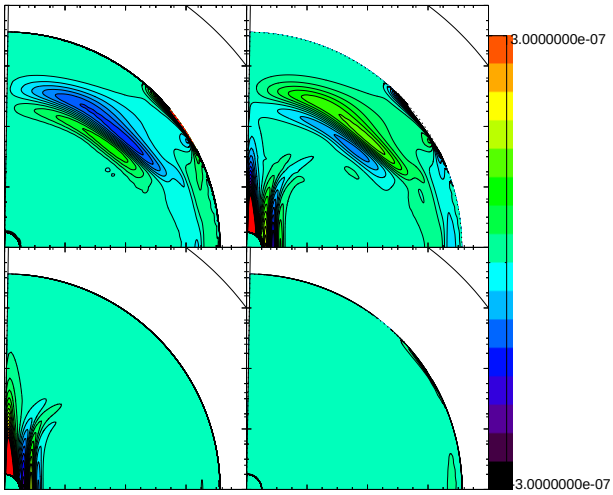

Figure 5.10: This figure shows the various terms that contribute to the azimuthal force balance in the radiative zone in our fiducial model . Note that these plots show the balance in the radiative region only (the convection zone appears in white). Shown are the Coriolis force (top left panel), Lorentz force (top right panel), viscous-stresses (bottom left panel), and the inertial term (bottom right panel). These plots illustrate the balance between Coriolis and Lorentz forces, while the viscous stresses and the non-linear advection term remain negligible. Note how the tachocline is mostly force-free while the tachopause stands out as the region where strong Coriolis and Lorentz forces balance out.

The following forces operate in the azimuthal direction:

$$
\begin{aligned}
-2\rho\Omega_{\odot}(u_\theta \cos\theta + u_r \sin\theta) \qquad & \text{(Coriolis)} \\
-\rho\left[u_r\frac{\partial u_\phi}{\partial r} + \frac{u_\theta}{r}\frac{\partial u_\phi}{\partial \theta} + \frac{1}{r}u_\phi u_r + \frac{\cos\theta}{r\sin\theta}u_\phi u_\theta\right] \qquad & \text{(Inertial)} \\
j_r B_\theta - j_\theta B_r \qquad & \text{(Lorentz)} \\
-\frac{\rho}{\tau}[u_\phi - u_{CZ}] \qquad & \text{(Gyroscopic pumping)} \\
(\nabla \cdot \mathbf{\Pi})_\phi \qquad & \text{(Viscous stresses)}
\end{aligned}
$$

Here, $\mathbf{\Pi} = \rho\nu[\nabla\mathbf{u} + (\nabla\mathbf{u})^T - \frac{2}{3}\nabla\cdot\mathbf{u}\mathbf{I}]$.

Figure 5.10 shows each of these terms individually (i.e. except the pumping term, which does not act in the radiative zone). We verified that their sum is zero, as expected in steady state.

First and foremost, note that the viscous stresses are negligible in the tachocline, confirming the theoretical expectation that viscosity should play no role in its dynamics [6]. This finding contrasts with the results obtained by Strugarek, Brun, and Zahn (2011) and Rogers (2011). Their 3-D, time-dependent simulations show a viscous tachocline unable to confine an internal magnetic field. We discuss in Chapter 6 the reason for this difference with our own model results.

The top panels of Figure 5.10 show, from left to right, the azimuthal component of the Coriolis and Lorentz forces, which are clearly in balance in the most of the radiative zone. This is consistent with the assumptions from Gough and McIntyre (1998) and Wood, McCaslin, and Garaud (2011). In addition, we see that the tachocline is mostly force-free by contrast with the tachopause below, where we see a strong presence of Lorentz and Coriolis forces.

[6] Viscous stresses are significant in the proximity of the polar axis, in a thin boundary layer where they balance the Lorentz forces associated with the interaction of the primordial field with the boundary near the inner core. However, we do not expect these stresses to occur in the real Sun.

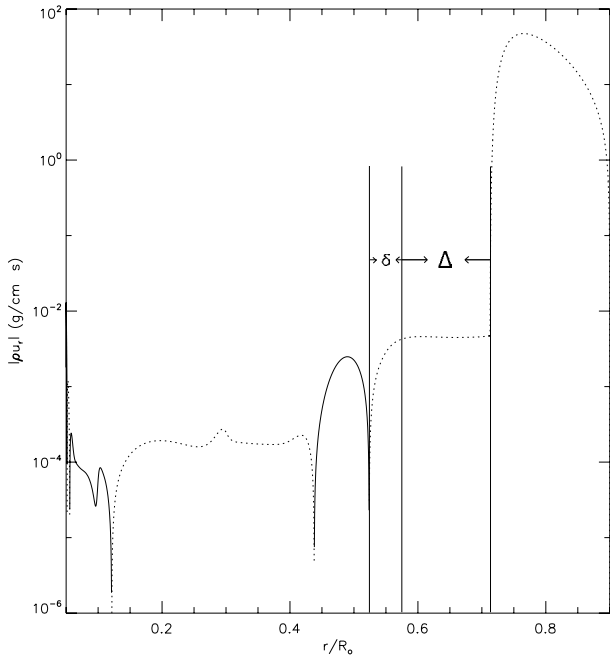

Figure 5.11: Downwelling meridional mass flux $|\bar{\rho}u_r|$ at 80 degrees latitude. We observe that it is constant from the convective-radiative interface down to about $r = 0.58R_\odot$, a region we identify as the tachocline. Below $0.58R_\odot$, $|\bar{\rho}u_r|$ starts decreasing. We identify the region between the base of the tachocline and the first zero of $|\bar{\rho}u_r|$ as the tachopause (here at $r = 0.525R_\odot$).

5.3.4 Estimating the thickness of the tachopause and the tachocline

The fact that the tachocline is magnetic-free (in the sense that the Lorentz force is negligible) has implications on the mass flux coming from the convection zone (see Wood, McCaslin, and Garaud , 2011 for a complete discussion). Indeed, taking the curl of the momentum equation and combining it with the mass conservation law yields:

$$-2(\mathbf{\Omega}\cdot\nabla)(\bar{\rho}\mathbf{u}) = \nabla\tilde{\rho}\times\mathbf{g} + \nabla\times(\mathbf{j}\times\mathbf{B}) \ , \tag{5.45}$$

(where viscous stresses were neglected). The radial component of this expression reduces to:

$$-2\Omega\frac{\mathrm{d}}{\mathrm{d}z}(\bar{\rho}u_r) - \frac{2}{r}\Omega u_\theta\sin\theta = [\nabla\times(\mathbf{j}\times\mathbf{B})]_r \ , \tag{5.46}$$

where $z = r\cos\theta$. Note that $u_\theta \sin\theta$ is negligible at high latitudes. This expression therefore indicates that in absence of magnetic stresses in the tachocline, the change of radial mass flux along the polar axis is zero. This is illustrated in Figure 5.11, which shows the mass flux $|\rho u_r|$ at 80 degrees latitude. We see that $|\rho u_r|$ is constant between the radiative-convective interface and $r \approx 0.58 R_\odot$ and then decreases rapidly to zero as a result of the effect of the magnetic field.

We can therefore use Figure 5.11 to *identify* the tachocline and the tachopause regions. In what follows, we define the base of the tachocline to be located at the depth where $|\bar{\rho} u_r|$ drops by 5% from its value just below the convection zone, as measured at 80^o latitude. Based on Figure 5.11, we find that the base of the tachocline is at $r_T = 0.575 R_\odot$ in the fiducial model.

Then, we define the tachopause as the region located between the base of the tachocline and the depth at which the mass flux equals zero. From Figure 5.11, we find that this happens at $r_t = 0.525 R_\odot$. Hence, we found in our fiducial model that the thickness of the tachocline is roughly three times the thickness of the tachopause, which marks an important distinction between our model and others where the tachopause is thicker than the tachocline (Kitchatinov and Rüdiger, 2006; Strugarek, Brun, and Zahn, 2011).

These definitions are arguably somewhat arbitrary: one could equally well define the base of the tachocline to be where the mass flux drops by Q%, where Q is any number between 0 and say, 20. Furthermore, since the radial mass flux in the tachopause varies sinusoidally with depth (Wood, McCaslin, and Garaud , 2011), we could equally well define the base of the tachopause to be the position of the second zero, or the maximum between them. In this sense, the values obtained for the respective thicknesses of the tachocline and the tachopause should be viewed as rough estimates rather than precise measurements. However, the hope is that the manner in which both thicknesses vary with governing parameters (e.g. E_κ, E_η) should be independent of our strategy to estimate them.

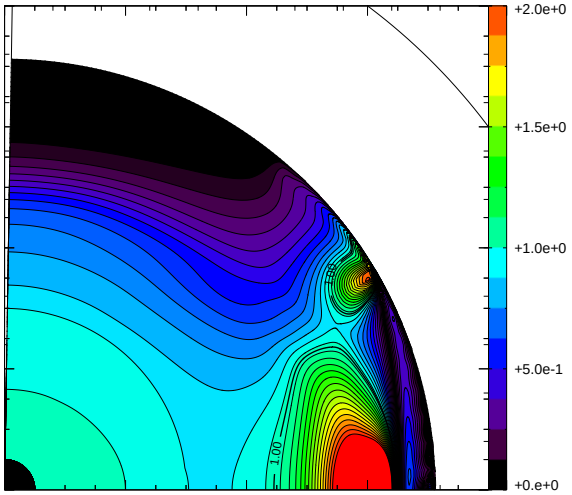

Figure 5.12: This figure shows the magnetic confinement parameter $|B_r/B_{0,r}|$ (see the main text for details) and clearly illustrates efficient magnetic confinement at high latitudes in the tachocline.

5.3.5 Magnetic confinement

Another way of quantifying magnetic confinement is by constructing the parameter $|B_r/B_{0,r}|$ (shown in Figure 5.12), as defined by Garaud and Garaud (2008), where B_r is the radial component of the magnetic field in the fiducial model, whereas $B_{0,r}$ is the radial component of the imposed, background magnetic field. From this plot, we see that the field is strongly confined at high latitudes.

From the results discussed in Sections 5.3.3, 5.3.4, and this one, we say that the model achieved magnetic confinement by the tachocline meridional flows, as predicted by Gough and McIntyre (1998).

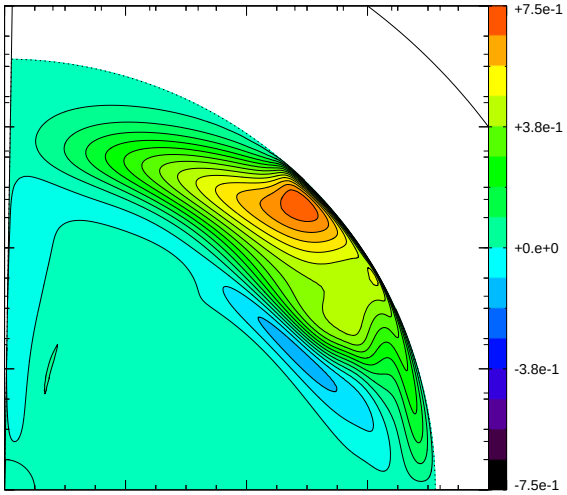

Figure 5.13: The toroidal field in the radiative zone.

5.3.6 Toroidal field

The final aspect of the Gough and McIntyre's theory that we investigate is the distribution of toroidal fields in the tachocline and in the tachopause. Strong toroidal fields are expected to be generated as poloidal magnetic field is twisted by the azimuthal flows. Gough and McIntyre argue that this effect should be most important in the tachopause (where the azimuthal shear winds up the primordial field).

Figure 5.13 shows the distribution of toroidal field in the radiative region for our fiducial model. As expected, we find that strong fields are indeed generated in the tachopause and in a localized region of the tachocline, around 45^o latitude. Interestingly, this region is somewhat closer to the poles than the center of the upwelling region around 30^o. In fact, we do not expect the presence of toroidal field in the so-called upwelling region in the tachocline because it is a

shear-free region.

5.4 Numerical experiments at different parameter regimes

5.4.1 The effect of thermal diffusivity

Let us first vary E_κ, keeping all other parameters fixed (in particular, without changing E_ν or N^2). This implies that σ changes as well, but in all cases presented we made sure that σ remains smaller than 1 to guarantee that the effects of viscosity are always negligible in the tachocline and tachopause. The results are shown in Figure 5.14. On the left panel, we see the effect of a reduction of E_κ from the fiducial model value by a factor of 0.49. Since the tachocline is in thermal equilibrium, this reduction in the thermal diffusivity directly affects the amplitude of the downwelling meridional flows in the tachocline and therefore the depth at which these flows confine the field. We see in the streamline plot that the tachocline is now narrower than in the reference case (see Figure 5.7 for comparison). Also, the field exhibits less distortion in the tachocline than in the fiducial model. On the other hand, the right panel shows the effects on field and flows of an increment of E_κ by a factor of 2.25 with respect to the fiducial model. This time, flows and magnetic field are able to interact at deeper regions in the radiative zone. The streamline plot shows a tachopause-tachocline region thicker than the one in the fiducial case, and the distortion of the field by meridional flows is greater. We now study these trends more quantitatively.

As discussed by Spiegel and Zahn (1992) and Gough and McIntyre (1998), thermal wind balance and thermal equilibrium imply specific scalings for the tachocline. Indeed, thermal-wind balance implies

$$2s\Omega_0 \frac{\partial \tilde{\Omega}}{\partial z} \approx \frac{\bar{g}}{r\bar{T}} \frac{\partial \tilde{T}}{\partial \theta} \ , \tag{5.47}$$

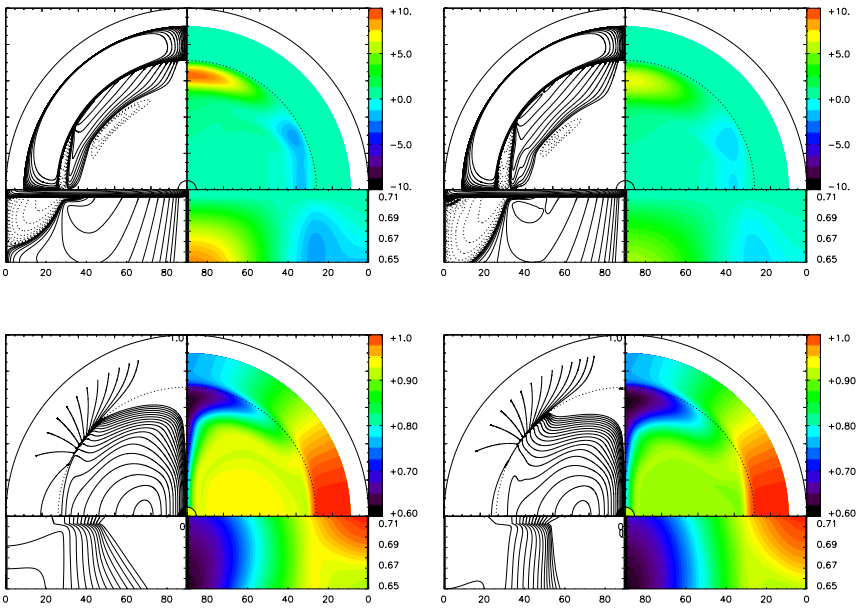

Figure 5.14: The effect of varying the non-dimensional thermal diffusivity E_κ profile on the dynamics of the tachocline. Here we see the steady-state results for $E_\kappa = 0.49E_{\kappa,REF}$ on the left panel and for $E_\kappa = 2.25E_{\kappa,REF}$ on the right panel.

where $z = r\cos\theta$ and $s = r\sin\theta$. Assuming that the tachocline is thin and that its thickness is Δ, a boundary-layer approximation yields

$$\frac{\tilde{T}}{\bar{T}} \approx \frac{\alpha\Omega_0^2 r_0^2}{\bar{g}L\Delta} \ , \tag{5.48}$$

where the rotational shear is approximated as $\partial\Omega/\partial z \approx (\Omega_{cz} - \Omega_0)/\Delta \approx \alpha\Omega_0/\Delta$, and the latitudinal temperature perturbation as $\partial\tilde{T}/\partial\theta \approx L\tilde{T}$, where L is a number of order unity. If the tachocline is also in thermal equilibrium, then

$$\frac{\bar{N}^2\bar{T}}{\bar{g}}u_r \approx \frac{1}{\bar{\rho}\bar{c_p}}\frac{1}{r^2}\frac{\partial}{\partial r}\left(r^2 k\frac{\partial\tilde{T}}{\partial r}\right) \ , \tag{5.49}$$

which yields

$$u_r \propto \frac{\kappa\bar{g}}{\bar{N}^2\Delta^2}\left(\frac{\tilde{T}}{\bar{T}}\right) \ , \tag{5.50}$$

when $\partial/\partial r \propto 1/\Delta$ and $\kappa = k/\bar{\rho}\bar{c_p}$.

From these two equilibria, Gough and McIntyre deduce that

$$u_r \propto \frac{\alpha r_0^2\kappa}{L}\frac{\Omega_0^2}{\bar{N}^2}\left(\frac{1}{\Delta^3}\right) \ . \tag{5.51}$$

This equation is very important because relates the amplitude of the downwelling meridional flows in the tachocline to its thickness under very plausible assumptions. It is a generic property of many models (Spiegel and Zahn , 1992; Gough and McIntyre , 1998; Wood, McCaslin, and Garaud , 2011). Using the measurement technique for the thickness of the tachocline and tachopause described earlier, we can check its validity. However, first note that in the original derivation by Gough and McIntyre , they assume that the tachopause is much thinner than the tachocline, so that they did not need to differentiate between Δ (tachocline thickness only) and $\Delta + \delta$ (tachocline and tachopause) in Equation 5.51. Here, δ is approximately of the same order of magnitude than Δ, so we must decide whether Equation 5.51 or

$$u_r \propto \frac{\alpha r_0^2\kappa}{L}\frac{\Omega_0^2}{\bar{N}^2}\left[\frac{1}{(\delta+\Delta)^3}\right] \tag{5.52}$$

is more appropriate. Indeed, since the tachopause is *also* in thermal equilibrium and in thermal wind balance, both equations are plausible. We consider Equation 5.52 to better represent the dynamics of the tachocline and tachopause in our model for two reasons. First, in the approximation of the rotational shear,

$$\frac{\partial \Omega}{\partial z} \approx \frac{\Omega_{cz} - \Omega_0}{D} \approx \frac{\alpha \Omega_0}{D} \ , \tag{5.53}$$

Gough and McIntyre consider the depth D (from the radiative-convective interface) at which the rotation becomes uniform (Ω_0), which in our model corresponds to the base of the tachopause. Similarly, for the boundary layer analysis of the energy equation, they approximate

$$\frac{\partial \hat{T}}{\partial r} \approx \frac{\hat{T}}{D} \ , \tag{5.54}$$

where D is again a lengthscale, this time associated with the region in thermal equilibrium. Since both the tachopause and the tachocline are in thermal-wind balance and in thermal equilibrium, $D = \Delta + \delta$.

The relationship among E_κ, the amplitude of the mass flux in the tachocline $|\rho u_r|_0$, and the thickness of the tachocline-tachopause region $D = r_0 - r_t = \delta + \Delta$ is shown in Figure 5.15[7]. The top panel shows that the downwelling mass flux $|\bar{\rho} u_r|_0$ and the thickness D both increase with thermal diffusivity. As E_κ increases, temperature perturbations diffuse faster reaching deeper regions in the radiative zone. The lower panel shows that the thermal spreading ratio $E_\kappa / |\bar{\rho} u_r|_0 D^3$ is constant for varying E_κ, as predicted by Gough and McIntyre (1998) as well as Wood, McCaslin, and Garaud (2011) with the minor correction for D noted before.

5.4.2 The effect of magnetic diffusivity

We tested the effect of the magnetic diffusivity on our fiducial model by decreasing and increasing the reference value $E_\eta = 1.5 \times 10^{-9}$. Figure 5.17 shows the cases where $E_\eta =$

[7]Both in Gough and McIntyre (1998) and Wood, McCaslin, and Garaud (2011), D is assumed to be the tachocline thickness Δ only.

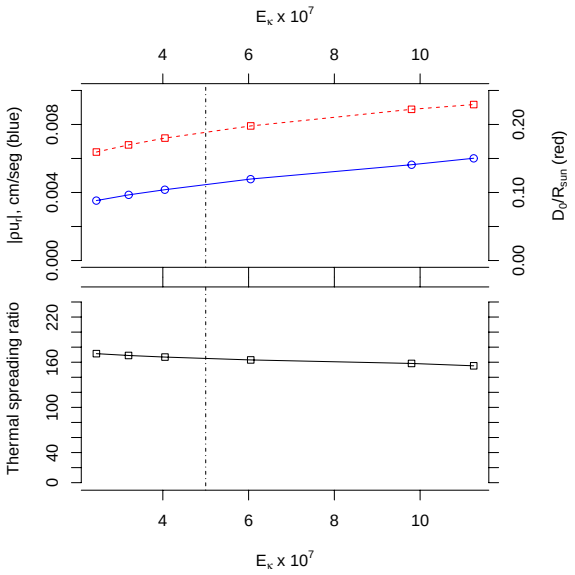

Figure 5.15: The thermal wind balance and the thermal energy balance in the tachocline are tested by computing the ratio $E_\kappa/|\bar{\rho}u_r|_0 D^3$, where $|\bar{\rho}u_r|_0$ is the downwelling mass flux in the tachocline. In the top panel we see the variation of the mass flux $|\bar{\rho}u_r|_0$ and the quantity $D = r_0 - r_t$ with respect to E_κ, where r_t is the base of the tachopause. Both $|\bar{\rho}u_r|_0$ and D increase with thermal diffusivity. The lower panel shows that the thermal spreading ratio $E_\kappa/|\bar{\rho}u_r|_0 D^3$ is almost independent of E_κ as predicted by Gough and McIntyre. Both panels show a vertical line indicating where $E_{\kappa,REF}$ is located within the interval under study.

7.5×10^{-10} and $E_\eta = 5 \times 10^{-9}$. There, we can appreciate how the thickness of the tachopause-tachocline region changes with E_η. From the streamline plots (top left panels), we see that the tachocline looks slightly thicker for the case with lower magnetic diffusivity. The same case shows also a greater distortion of the magnetic field (see bottom left panels).

To quantify this change, let us look at the balance between the advection and the diffusion of the magnetic field in the radiative region. In steady-state, Gough and McIntyre (1998) argued that (in dimensional terms)

$$|u_r| \approx \frac{\eta}{\delta} \, , \tag{5.55}$$

which relates the downwelling meridional flow velocity to the thickness of the tachopause and magnetic diffusivity. We computed the ratio $E_\eta/|u_r|_t\delta$ for a series of simulations where E_η varied from 5×10^{-10} to 1×10^{-8}, and $|u_r|_t$ was the radial velocity at the base of the tachocline r_T. We use our definition of the tachocline and tachopause, described in Section 5.3.4, to estimate δ and $|u_r|_t$. The results are plotted in Figure 5.16.

The bottom panel of Figure 5.16 shows that the dimensions of the tachocline and the tachopause change significantly with magnetic diffusivity. It is interesting to note that as E_η decreases, the base of the tachopause remains roughly at the same place; however, the geometry of the tachocline/tachopause system changes with the tachopause becoming thinner whereas the tachocline thickens. As a result, the ratio δ/Δ decreases. As the magnetic diffusivity is lowered, the steady-state solution approaches the condition $\delta \ll \Delta$ assumed by Gough and McIntyre (1998).

The top panel shows that the downwelling radial velocity u_r at the base of the tachopause r_t decreases as the magnetic diffusivity is reduced. We also found that the ratio of diffusion/advection of the magnetic field is independent of E_η, as shown in the top panel of Figure 5.16, which is in agreement with another assumption of the Gough and McIntyre model. This

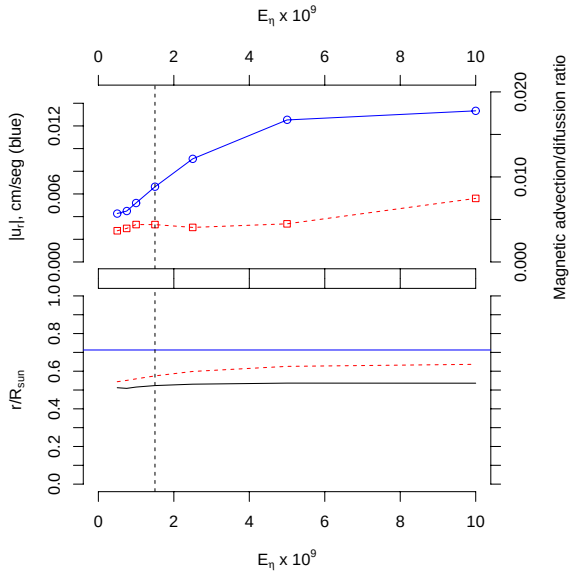

Figure 5.16: The balance between the advection and the diffusion of the magnetic field in the tachocline is tested by computing the ratio $E_\eta/|u_r|_t\delta$, where $|u_r|_t$ is the downwelling radial velocity at the base of the tachocline, and δ is the thickness of the tachopause as defined in Section 5.3.4. In the top panel we see the variation of $|u_r|_t$ (curve with blue circles) and $E_\eta/|u_r|_t\delta$ (curve in red squares) with respect to E_η. Both quantities increase with magnetic diffusivity, although the ratio $E_\eta/|u_r|_t\delta$ remains almost constant for mid and low values of E_η. The lower panel shows the position of the base of the tachopause (black curve at the bottom), the base of the tachocline (red dashed curve at the middle), and the base of the convection zone (blue curve at the top). As the magnetic diffusivity reduces, the tachocline becomes much thicker than the tachopause, as predicted by Gough and McIntyre. Both panels show a vertical line indicating where $E_{\eta,REF}$ is located within the interval under study, which satisfies two more assumptions of the Gough and McIntyre model.

relationship only departs from its constant value for high magnetic diffusivity values.

The results discussed so far prove that the assumptions in the model of Gough and McIntyre are correct. Our fiducial model reproduces for the first time the tachocline and the tachopause as described by their theory. Unfortunately, our parameter regime is in the borderline where numerical instabilities arise, so we are unable to obtain sufficient data to verify their scalings. Their relationships between the tachocline thickness and and field strength, as well as the tachopause thickness and the magnetic diffusivity require simulations with parameters varying in domains still computationally intractable. However, since we have already validated

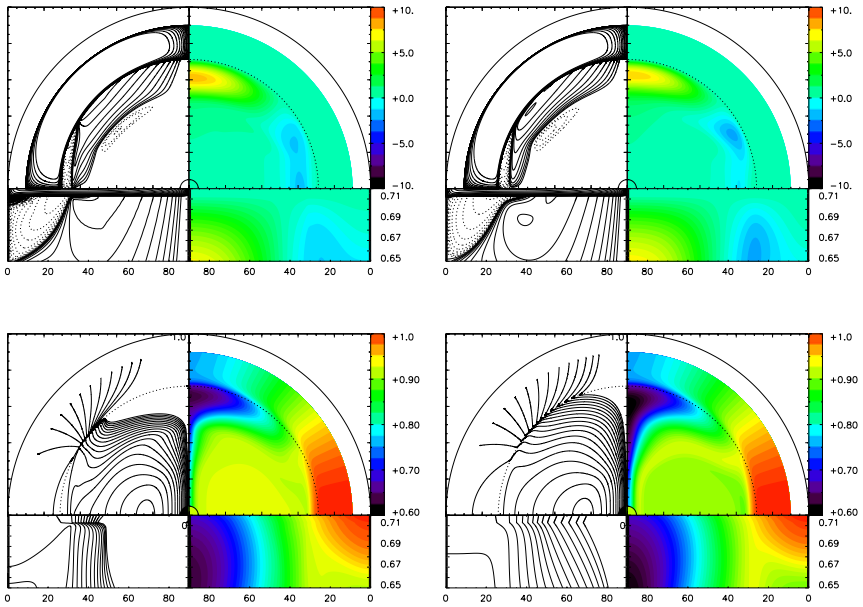

Figure 5.17: The effect of the non-dimensional magnetic diffusivity E_η profile on the dimensions of the tachopause. Here we see the steady-state results for $E_\eta = 7.5 \times 10^{-10}$ and $E_\eta = 5.0 \times 10^{-9}$ on the left and right panels, respectively. We can see how the tachocline-tachopause region changes in dimension with E_η. However, the effect of E_η on the thickness of the tachopause can only be assessed by looking at Figure 5.16.

their model, we have gone a long way towards showing that those scalings are also correct.

5.4.3 Relationship to previous models

5.4.3.1 Basic Strugarek, Brun, and Zahn model

In this section, we now revisit the results of Strugarek, Brun, and Zahn (2011) and explain why they could not achieve magnetic confinement and, at the same time why their simulations were viscously dominated. We ran numerical experiments in a parameter regime as close as possible to that of Strugarek, Brun, and Zahn. We adopted their diffusion parameters

$$\nu(r) = 8.0 \times 10^9 + 8.0 \times 10^{12} \left[1.0 + \tanh\left(\frac{r - 0.6753 R_\odot}{0.01 R_\odot}\right)\right] \tag{5.56}$$

$$\eta(r) = 8.0 \times 10^{10} + 1.6 \times 10^{13} \left[1.0 + \tanh\left(\frac{r - 0.6753 R_\odot}{0.01 R_\odot}\right)\right] \tag{5.57}$$

$$\kappa(r) = 8.0 \times 10^{12} + 3.2 \times 10^{13} \left[1.0 + \tanh\left(\frac{r - 0.6753 R_\odot}{0.01 R_\odot}\right)\right] \ , \tag{5.58}$$

which are shown in non-dimensional form in Figure 5.18 (left panel). They used the solar profile for the buoyancy frequency N. The corresponding profile for the stratification parameter σ is therefore quite different from the solar profile $\sigma_\odot$ as shown in Figure 5.18 (right panel). As we can see, $\sigma \gg 1$ in the entire radiative region. We imposed differential rotation in the convection zone by using a similar forcing term as in our fiducial model. While Strugarek, Brun, and Zahn model a time-dependent decaying magnetic field, we still have to impose a background magnetic field in our simulation to get steady-state solutions. We do this in a similar way to the one described in Section 5.1.6.2, but with $\Lambda = 334$. A much larger value of Λ is needed in their model in comparison with our fiducial model to guarantee that the rotational Elsasser number Λ/E_η will be greater than one in the radiative zone. Since their E_η is much larger than ours, their field must also be larger.

The resulting steady-state solution for this case is shown in Figure 5.19. We can immediately see that the downwelling flows penetrating the radiative zone from above decay

rapidly into the interior and are unable to confine the internal magnetic field, so the latter diffuses across the convection zone. As a result, the radiative zone is differentially rotating, in a Ferraro state.

Figure 5.20 shows the forces operating in the azimuthal momentum equation. It is clear, by contrast with our fiducial model, that Coriolis force and viscous stresses are in balance just below the radiative-convective interface. As suggested by GAA09, this balance implies that any meridional flows crossing the interface must decay on a lengthscale $R_\odot/\sigma$. This is confirmed in Figure 5.21, which shows the downwelling mass flux $|\bar{\rho}u_r|$ below the interface.

The fact that Lorentz force does not play a role in the angular momentum balance just beneath the convection zone is due to the fact that their η is still very large in that region. Further down, η drops to its radiative zone value and the Lorentz force becomes important.

Finally, since the stratification parameter $\sigma \gg 1$ for Strugarek, Brun, and Zahn model, any meridional flows downwelling into the radiative region must decay rapidly, so interaction between those flows and the internal field in the radiative zone is not possible. Hence, the field lines connecting the radiative and the convective zones help transport angular momentum from the convection zone into the radiative region, so differential rotation spreads to the interior.

5.4.3.2 Strugarek, Brun, and Zahn model with pre-confinement

So far, we have compared Strugarek, Brun, and Zahn model with our fiducial model and found that they cannot reproduce confinement. However, we note that one of the main differences between ours and their model is preconfinement. The question that then arises is whether a pre-confinement of the magnetic field would lead to a more tachocline-like structure in the Strugarek, Brun, and Zahn model. To answer this question, we ran simulations with the same parameters except that the magnetic diffusivity profile was shifted up as we did in our fiducial model (see Section 5.2) to pre-confine the field in the convection zone. Thus, the new

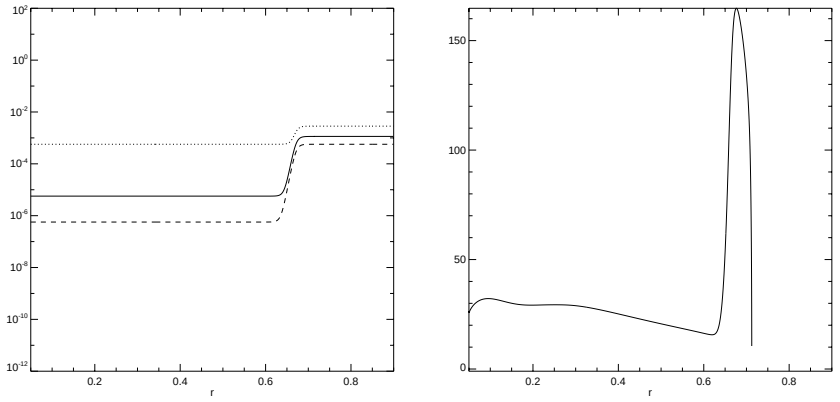

Figure 5.18: On the left panel, we show the diffusivity profile from the model by Strugarek, Brun, and Zahn (2011). See the text for the exact parameterization of these profiles. On the right panel, we show the computed sigma profile corresponding to their model.

E_η profile had its transition point at $r = 0.8127 R_\odot$ instead of the original $r = 0.6753 R_\odot$ as we see in Figure 5.22.

Figure 5.23 shows the results for this new experiment. Even though the magnetic field is now indeed somewhat pre-confined, as the bottom left panel illustrates, the field *in the radiative zone* remains unaffected by the meridional flows downwelling from the convection zone. The top left panel shows that, as in Section 5.4.3.1, these flows decay rapidly with distance from the interface, on the same lengthscale $R_\odot/\sigma$. In fact, comparing Figure 5.21 and Figure 5.24, we see that in both cases the field hardly affects the flows. We can also look at the magnetic confinement plot in Figure 5.25 to confirm that the interaction between meridional flows and the background magnetic field is circumscribed to the region very close to the radiative-convective interface.

Looking at the force balance in the radiative zone (Figure 5.26), we now see that the latter is quite different from that of Section 5.4.3.1. The main force balance is between

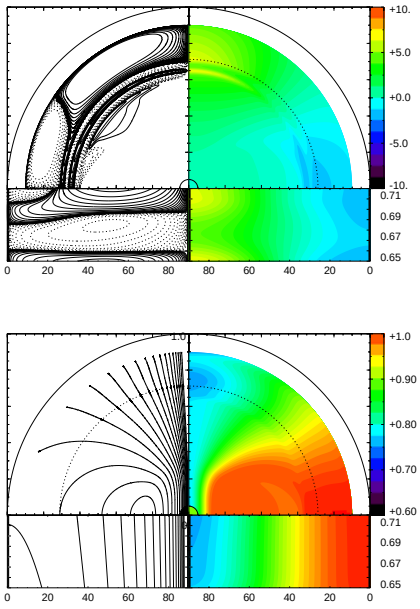

Figure 5.19: This plot shows the steady-state solution obtained in a parameter regime close to the one used by Strugarek, Brun, and Zahn (2011). Starting from the top left panel and going clockwise, we show plots of the streamlines, temperature perturbations, angular velocity, and magnetic field lines. The top left panel shows that large-scale meridional flows generated in the convection zone are not able to penetrate into the radiative interior at high latitudes. As a result, the magnetic field is not confined and the differential rotation pattern of the convection zone is communicated to the radiative interior.

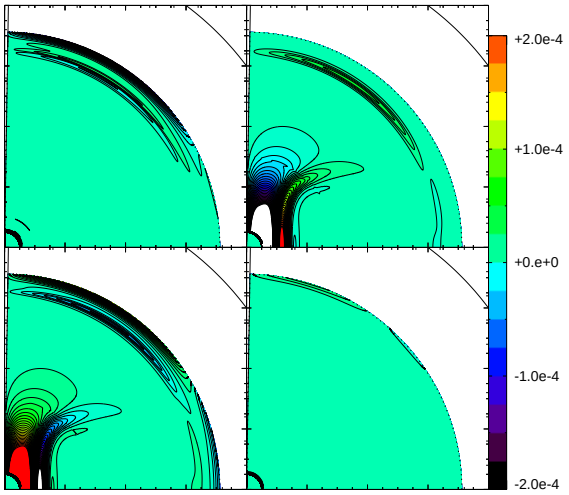

Figure 5.20: This figure shows the various terms that contribute to the azimuthal force balance in the radiative zone in the simulation presented in Figure 5.19. Shown are the Coriolis force (top left panel), Lorentz force (top right panel), viscous-stresses (bottom left panel), and the inertial term (bottom right panel). These plots illustrate the balance between Coriolis force and viscous stresses just below the convection zone, while the Lorentz force only becomes important when η drops to its radiative zone value (here around $r = 0.62R_\odot$). By contrast with our fiducial model, however, viscous stresses are everywhere important. The non-linear advection term remains negligible.

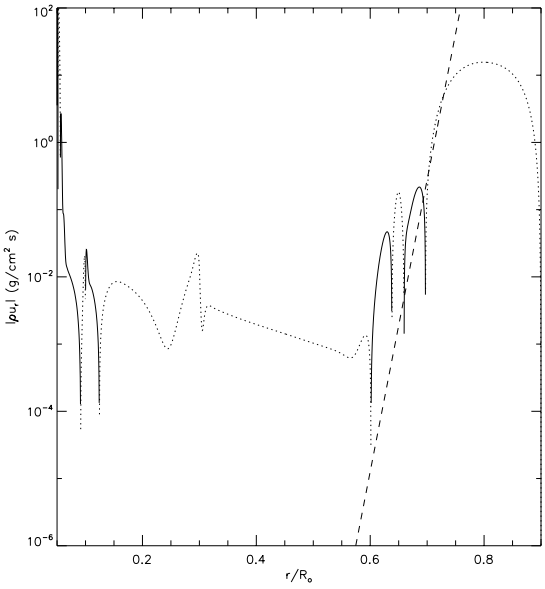

Figure 5.21: Downwelling meridional mass flux $|\bar{\rho}u_r|$ at 80 degrees latitude for the simulation presented in Figure 5.19. This model failed to develop a tachocline because the large-scale meridional flows decay rapidly to zero at the radiative-convective interface. The dash-dotted line is the exponential function $e^{-\sigma_t(x_0-x)}$, where $\sigma_t = 100$, which illustrates the rapid exponential decay of downwelling flows when $\sigma \gg 1$.

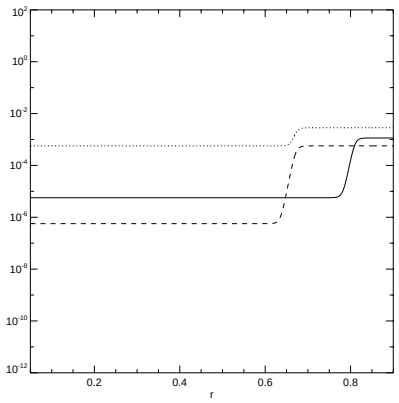

Figure 5.22: In the new experiment discussed here, the magnetic diffusivity profile is moved up into the convection zone to pre-confine the magnetic field in the convection zone.

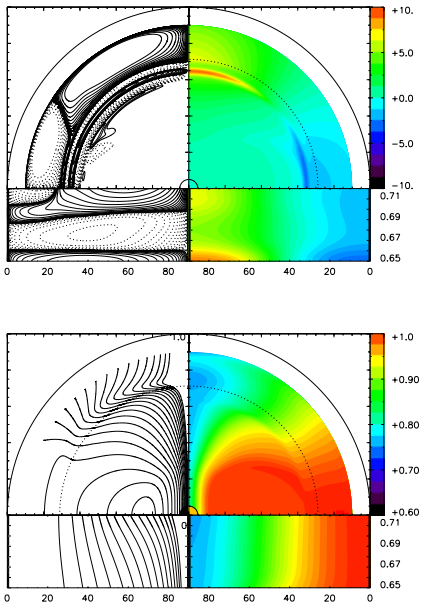

Figure 5.23: As in Figure 5.19 but with a "pre-confined" field. Starting from the top left panel and going clockwise, we show plots of the streamlines, temperature perturbations, angular velocity, and magnetic field lines. The top left panel shows that even though the magnetic field lines are forced to be confined in the convection zone, the large-scale meridional flows generated there are not able to penetrate into the radiative zone. As a result, the magnetic field is NOT confined below the radiative-convective interface, so the differential rotation pattern of the convection zone is communicated to the radiative interior.

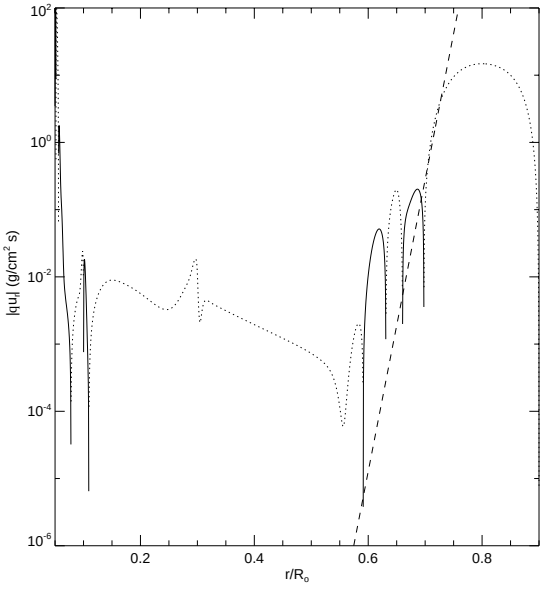

Figure 5.24: Downwelling meridional mass flux $|\bar{\rho}u_r|$ at 80 degrees latitude. We observe that the mass flux crossing the convective-radiative interface decays abruptly. The dash-dotted line is the exponential function $e^{-\sigma_t(x_0-x)}$, where $\sigma_t = 100$, which illustrates the rapid exponential decay of downwelling flows when $\sigma \gg 1$.

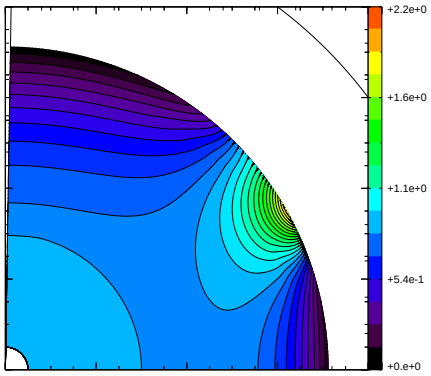

Figure 5.25: This plot shows the confinement parameter $|B_r/B_{0,r}|$ (see Section 5.3.5 for details) for the numerical experiment where we reproduce the model by Strugarek, Brun, and Zahn (2011) with pre-confinement.

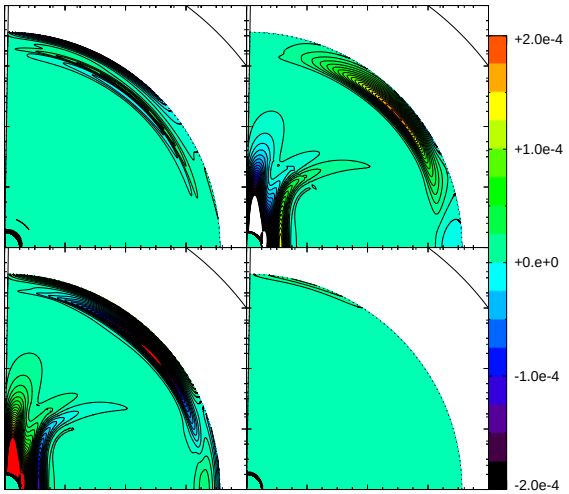

Figure 5.26: This figure shows the various terms that contribute to the azimuthal force balance in the radiative zone in the viscous-stress driven model with imposed magnetic pre-confinement in the convection zone. Shown are the Coriolis force (top left panel), Lorentz force (top right panel), viscous-stresses (bottom left panel), and the inertial term (bottom right panel). These plots illustrate that viscous stresses balance this time both Coriolis and Lorentz forces.

the viscous stresses and the Lorentz force; this time the Elsasser number near the interface is greater than one because the magnetic diffusivity remains low in that region. Given this magnetoviscous balance and the rapid decay of large-scale meridional flows below the interface, the tachocline thus obtained is much more similar to that of Kitchatinov and Rüdiger (2006) than the tachocline of the Gough and McIntyre model.

As we have demonstrated in this chapter, a careful parameter selection makes Gough and McIntyre-like solutions possible. Another important finding is that pre-confinement helps obtain those solutions more easily. Hence, the development of tachopause-tachocline structures as described by the Gough and McIntyre theory relies not only on the presence of a primordial magnetic field in the interior, but also on the nature of the assumed radiative interior and the effect of the convective zone flows on the primordial field..

Chapter 6

Conclusions

Our fiducial model and its associated numerical experiments, which we described in Chapter 5, demonstrate that the model proposed by Gough and McIntyre in 1998 to explain self-consistently the dynamics of the solar tachocline is based on correct assumptions. Our model reproduces the interactions between magnetic fields and meridional flows below the radiative-convective interface as described by the Gough and McIntyre theory. Its results show an almost uniformly rotating radiative interior and a differentially rotating convection zone coupled by two layers: a thin, non-viscous, and magnetic-free tachocline, and a much thinner, magnetically dominated, tachopause. Here we summarize the key components of our model and briefly discuss why this simple 2-D model yields the best numerical simulations that validate the Gough and McIntyre theory.

Even though Spiegel and Zahn (1992) proposed the first model of the tachocline based on purely hydrodynamical mechanisms, and Rüdiger and Kitchatinov (1997) studied the first magnetic model of the solar interior with no presence of meridional flows in the radiative zone, Gough and McIntyre (1998) provided the first self-consistent explanation of the dynamics of the tachocline based on the interaction between meridional flows and a primordial magnetic

field. Based on this notion of a dual mechanism (flows acting on the field and field reacting on the flows, all happening below the radiative-convective interface), we proceed to describe our fiducial model.

6.1 Our fiducial model: The importance of parameter selection

In Chapter 4, we tackled the problem of modeling the dynamics of the tachocline by analyzing its purely hydrodynamic mechanisms to learn the circumstances under which large-scale meridional flows might circulate through the interior of the Sun. Garaud and Brummell (2008) had anticipated the role of the stratification-rotation parameter $\sigma = \sqrt{Pr}\frac{N}{\Omega}$ in the dynamics of meridional flows crossing the radiative-convective interface. These flows can penetrate the radiative zone to a depth $R_\odot/\sigma$, which opens the possibility of interactions between flows and magnetic field. In a model by Garaud and Garaud (2008), meridional flows were forced at the interface, penetrated a radiative region with solar σ profile, and confined the internal magnetic field. In a sequel of that study, we ran some numerical experiments to confirm that large-scale meridional flows, this time generated in the convection zone by gyroscopic pumping, can downwell into the radiative zone only if $\sigma \ll 1$. When this criterion is not satisfied, any internal magnetic field will not be confined by large-scale meridional flows. This is the reason why the 3-D time-dependent numerical simulations by Strugarek, Brun, and Zahn (2011) ended up with the initial strong magnetic field diffused throughout the radiative and convection zones, and with no evidence of a tachocline. A similar model by Rogers (2011) did not set a weakly stratified radiative zone, so the addition of a weak magnetic field did not have any impact on the dynamics of the zone either.

The reason previous numerical simulations accidentally used $\sigma \gg 1$ was because they

focused on lowering the diffusivities to very small values, the smallest possible, and on using as many as possible parameters from a standard solar model. They did so as if by reaching the most solar-like computational domain, they would obtain the most solar-like tachocline. That did not work. Wood, McCaslin, and Garaud (2011) found that more importantly than getting the solar parameterization, the model should reproduce the force balances that contribute to the formation and evolution of the tachocline. We built our fiducial model starting from the diffusion parameterization suggested by Wood, McCaslin, and Garaud and completed with a solar σ profile and few more parameters from Model S.

A weakly stratified radiative zone and a correct parameter regime are just the first steps to facilitate large-scale meridional flows to circulate the radiative region. Models need a mechanism to generate these flows in the convection zone. Kitchatinov and Rüdiger (2006) and Garaud and Garaud (2008) implemented each a model with boundary conditions driving meridional flows along the radiative-convective interface. Contrary to this approach, we included a forcing term in the momentum equation to model gyroscopic pumping, which is the mechanism described by Gough and McIntyre (1998) as the main source of meridional flows in the convection zone. Thus, the incorporation of the convection zone (with a gyroscopic pumping mechanism) and the radiative zone (with the appropriate conditions of diffusion and stratification) into our model satisfy the hydrodynamical conditions in the Gough and McIntyre model.

6.2 Our fiducial model: the internal magnetic field

The next piece of the model is the internal primordial magnetic field. We replaced the boundary condition approach used by Garaud and Garaud (2008) to impose the background magnetic field by a "forcing" term approach. We induced an internal magnetic field by defining an electric current density profile in such a way to prevent numerical instabilities near the core.

The field thus generated was of the dipolar type with field lines connecting both the radiative and convective zones. The field was then pre-confined by choosing an appropriate magnetic diffusivity profile. This "pre-confinement" step is very important for large-scale meridional flows entering the radiative zone to confine the internal magnetic field more efficiently. It certainly helps our model from a computational perspective, but magnetic pre-confinement is not an unrealistic phenomenon at all.

Tobias, Brummell, Clune, and Toomre (2001) ran 3-D numerical simulations to investigate the transport of magnetic field by turbulent flows in the convection zone. They found that the magnetic field is preferentially transported from the convection zone into the radiative region by overshooting plumes, where the field finds a more stable region to reside. The depth of penetration, however, is limited to the overshoot region. Large-scale meridional flows can also confine the field in the lower convection zone, and these flows can be originated either by turbulent flows or by large-scale zonal flows. In any case, we considered that field confinement in the convection zone (by turbulent magnetic pumping or large-scale meridional flows) should be taken into account, but only as an intermediate step in the process of getting magnetic confinement at much deeper zones below the radiative-convective interface. Even though our 2-D model is unable to model turbulent flows, choosing the appropriate magnetic diffusivity profile can model pre-confinement.

6.3 The tachopause-tachocline structure and its underlying assumptions

With all these ingredients in place, our fiducial model could provide steady-state solutions for the MHD equations modeling the dynamics of the solar interior. Its results show the presence of two important layers in the radiative interior that were predicted by Gough and

McIntyre (1998): the tachocline and the tachopause. By defining a method to determine the location of the tachocline and the tachopause, we proceeded to verify the main assumptions in the Gough and McIntyre theory that describe these layers. We found that both the tachocline and the tachopause are in thermal-wind balance and thermal equilibrium. We did it by computing the quantity

$$GMI_1 = \frac{E_\kappa}{|\bar{\rho} u_r|_0 (\Delta + \delta)^3} \ , \tag{6.1}$$

which must be constant to satisfy both equilibria.

We also found a magnetic-free tachocline and a strong magnetically dominated tachopause just by looking at a mass flux plot at 80^o latitude as well as a plot of the terms in the azimuthal momentum equation. The latter shows that Lorentz and Coriolis forces are in balance in the tachopause-tachocline region. Also, by varying the magnetic diffusivity and by using our definition of the tachopause and tachocline, we verified the assumption of magnetic advection/diffusion balance in the tachopause. We did it by computing the quantity

$$GMI_2 = \frac{E_\eta}{|u_r|_T \delta} \ , \tag{6.2}$$

which must also be constant.

We verified that GMI_1 and GMI_2 remained constant for numerical experiments varying the thermal diffusivity and the magnetic diffusivity, respectively. We could not verify other scalings proposed by the Gough and McIntyre theory, such as the relationship between the tachocline thickness and the magnetic strength B_0, but we can argue that by having validated their main assumptions, those scalings might also be correct.

Therefore, we conclude that our fiducial model is the first numerical model that self-consistently reproduces the solar tachocline (and tachopause) described by the Gough and McIntyre theory. Our fiducial model reproduces the uniformly rotating radiative interior and the rotational transition observed in the tachocline. It confirms that the azimuthal balance between

Coriolis and Lorentz forces is at the core of this rotational transition, and that the tachopause separates the magnetically dominated radiative interior from the magnetic-free tachocline. It also verifies that both the tachopause and the tachocline are in thermal equilibrium and in thermal-wind balance, and that viscous stresses play no role in the dynamics of the radiative zone.

It is important to note that our fiducial model provides evidence of the key role of the stratification parameter σ for the interaction between meridional flows and magnetic field in the radiative zone. Since σ is a function of the rotation rate among other parameters, our fiducial model might be used to infer tachopause-tachocline structures of other stars rotating faster or slower than the Sun. We might expect, for example, that a star rotating slower than the Sun might have no tachocline. Our model could also be used to infer the internal structure of the Sun in previous or future ages. But more importantly perhaps, our 2-D fiducial model might provide more complicated 3-D models with starting parameter regimes, so computational resources could be better applied in the study of the dynamics of the Sun and other stars.

Bibliography

Antia H. M., Basu S., and Chitre S. M.

Solar internal rotation rate and the latitudinal variation of the tachocline

Mon. Not. R. Astron. Soc. **298**: 543-556 (1998)

Abramowitz, M., Stegun, I.A.: 1972, *Handbook of Mathematical Functions*, Dover Publications, New York, 332.

Antia H. M. and Basu S.

The Astrophysical Journal, **720**:494 (2010)

Antia H. M. and Basu S.

Revisiting the solar tachocline: Average properties and temporal variations

The Astrophysical Journal Letters, **735** Number 2 (2011)

Balbus S. A. and Hawley J. F.

A powerful local shear instability in weakly magnetized disks. I. Linear analysis.

The Astrophysical Journal, **376**:214-222 (1991)

Batchelor, G.K.: 1970, *An Introduction to Fluid Dynamics*, Cambridge University Press, Great Britain, 601.

Brummell, N.H., Clune, T.L., Toomre, J.

The Astrophysical Journal, **511**, 466 (2002)

Brun A. S. and Zahn J.-P.,

Magnetic confinement of the solar tachocline,

Astronomy & Astrophysics, **457**: 665-674 (2006)

Charbonneau P., Christensen-Dalsgaard J., Henning R., Larsen R. M., Schou J., Thompson M. J., and Tomczyk S.

Helioseismic constraints of the structure of the solar tachocline

The Astrophysical Journal, **527**:445-460 (1999)

Christensen-Dalsgaard J. and Schou J.,

Seismology of the Sun and Sun-like Stars,

Edited by V. Domingo and E. J. Rolfe

ESA-SP286, p. 149

Christensen-Dalsgaard, J., etal.: 1996, *Science*, **272**, 1286.

Christensen-Dalsgaard, J.

Helioseismology

Reviews of Modern Physics, **74**:1073-1129 (2002)

Christensen-Dalsgaard, J.

Stellar Oscillations

Institut for Fysik og Astronomi, Aarhus Universitet, May 2003 http://astro.phys.au.dk/∼jcd/oscilnotes/

Christensen-Dalsgaard J., Gough D. O., and Thompson M. J.

The depth of the solar convection zone,

The Astrophysical Journal, **378**:413-437 (1991)

Christensen-Dalsgaard J. and Thompson M. J.

Observational results and issues concerning the tachocline,

In chapter 3 of The Solar Tachocline,

Edited by Hughes, Rosner, and Weiss,

Cambridge, 2007

Christensen-Dalsgaard, J., Thompson, M. J.: 2007, in Hughes, D., Rosner, R., Weiss, N. (eds.),

The Solar Tachocline, Cambridge University Press, United Kingdom, 53.

Elliott J. R. and Gough D. O.,

Calibration of the thickness of the solar tachocline,

The Astrophysical Journal, **516**:475-481 (1999)

The non-uniform rotation of the Sun and its magnetic field

MNRAS, **97**:458-472 (1937)

Fogiel, M.

The Differential equations Problem Solver

Research & Education Association, 1996, pp. 1261-1263

Forgács-Dajka E. and Petrovay K.

Dynamics of the fast solar tachocline

Astronomy & Astrophysics **389**:629-640 (2002)

Garaud, P.,

Dynamics of the solar tachocline,

PhD Thesis, University of Cambridge, Trinity College, 2000

Garaud, P.,

Dynamics of the solar tachocline: an incompressible study,

MNRAS, 329, 1-17, 2002

Garaud, P.,

Two-point boundary value solver using the Newton-Raphson-Kantorovich method (NRK),

May 5, 2006

Garaud P.,

Magnetic Confinement of the solar tachocline,

In chapter 7 of The Solar Tachocline,

Edited by Hughes, Rosner, and Weiss,

Cambridge, 2007

Garaud P. and Garaud J.-D.,

A Friendly and Free Parallel Block-Tridiagonal Solver: User Manual,

October 1, 2007

Garaud P. and Rogers T.

in Unsolved Problems in Stellar Physics

American Institute of Physics Conference Series 947, 237-248 (2007)

Garaud P. and Garaud J. D.

Dynamics of the solar tachocline II. The stratified case

MNRAS 391, 1239-1258 (2008)

Garaud P. and Brummell N. H. ,

On the Penetration of Meridional Circulation below the Solar Convection Zone,

The Astrophysical Journal, 674:498-510, 2008 February 10

Garaud P. and Guervilly C.,

The rotation rate of the solar radiative zone,

The Astrophysical Journal, 695:799-808, 2009 April 20

Garaud P. and Acevedo-Arreguin L. A.,

On the Penetration of Meridional Circulation below the Solar Convection Zone II: Models with Convection Zone, the Taylor-Proudman constraint and Applications to Other Stars,

The Astrophysical Journal, 704:1-16, 2009 October 10

Garaud P. and Bodenheimer P.,

Gyroscopic Pumping of Large-Scale Flows in Stellar Interiors and application to Lithium-Dip Stars,

The Astrophysical Journal, 719:313-334, 2019 August 10

Gilman, P.A., Morrow, C.A., Deluca, E.E.: 1989, *Astrophys. J.*, **338**, 528.

Gilman and Miesch,

Limits to penetration of meridional circulation below the solar convection zone,

The Astronomical Journal, 611:568-574, 2004 August 10

Glatzmaier, G.A.: 1984, *J. Comp. Phys.*, **55**, 461.

Glatzmaier G. A.

Numerical simulations of stellar convective dynamos. II. Field propagation in the convection zone

The Astrophysical Journal, **291**:300-307 (1985)

Gough D. O., Spiegel E. A., and Toomre J.

Highly stretched meshes as functional of solutions

In Lecture Notes in Physics 35,

Edited by Ehlers, Hepp, and Weidenmúller, Springer-Verlag, Heidelberg, 1975

Gough D. O., Leibacher J. W., Scherrer P. H., and Toomre J.

Perspectives in Helioseismology,

Science, Vol. 272, 5266:1281-1283, 31 May 1996

Gough and McIntyre,

Inevitability of a magnetic field in the Sun's radiative interior,

Nature, Vol. 394, 20 August 1998

Gough D.,

An introduction to the solar tachocline,

In chapter 1 of The Solar Tachocline,

Edited by Hughes, Rosner, and Weiss,

Cambridge, 2007

Gough D.,

Angular Momentum Coupling through the Tachocline,

In Magnetic Coupling between the Interior and the Atmosphere of the Sun,

Edited by Hasan and Rutten,

Springer-Verlag, Heidelberg, 2010

Howe R.,Christensen-Dalsgaard J., Hill F., Komm R. W., Larsen R. M., Schou J., Thompson M. J., and Toomre J.

Dynamic Variations at the Base of the Solar Convection Zone

Science, **287**: 2456-2460 (2000)

Howe R., Komm R., Hill F., Christensen-Dalsgaard J., Larson T. P., Schou J., Thompson M.

J., and Toomre J.

Rotation-rate variations at the tachocline: an update

Journal of Physics: Conference Series, **271**:1-4 (2011)

Kitchatinov, L.L.: 2005, *Physics–Uspekhi*, **48**, (5) 449.

Kitchatinov, L.L., Rüdiger, G.: 2005, textitAstron. Nachr. AN, textbf326, (6), 379.

Rüdiger G. and Kitchatinov L. L.,

Kitchatinov, L.L., Rüdiger, G.: 2006, textitAstronomy & Astrophysics, textbf453, 329.

Kosovichev A. G.

Helioseismic constraints on the gradient of angular velocity at the base of the solar convection zone

The Astrophysical Journal, **469**:L61-L64 (1996)

MacGregor K. B. and Charbonneau P.,

Angular momentum transport in magnetized stellar radiative zones. IV. Ferraro's Theorem and the solar tachocline

The Astrophysical Journal, **519**:911-917 (1999)

Mason J. C. and Handscomb D. C.

Chebyshev Polynomials

Chapman & Hall/CRC, Boca Raton, Florida, 2003

McIntyre, M. E.

Solar tachocline dynamics: eddy viscosity, anti-friction, or something in between?

In chapter 8 of Stellar Astrophysical Fluid Dynamics

Edited by Thompson and Christensen-Dalsgaard

Cambridge, 2003

Mestel, L.: 1953, *Mon. Not. R. astr. Soc.*, **6**, 716.

Mestel, L., Weiss, N.O.: 1987, *Mon. Not. R. astr. Soc.*, **226**, 123.

Miesch M. S.

Large-Scale Dynamics of the Convection Zone and Tachocline

Max Plack Institute for Solar System Research, Germany

http://solarphysics.livingreviews.org/lrsp-2005-1

Press, Teukolsky, Vetterling, and Flannery

Numerical Recipes

Cambridge University Press, 2007, pp. 964-970

Rempel, M.

Solar differential rotation and meridional flow: The role of a subadiabatic tachocline for the

Taylor-Proudman balance,

The Astrophysical Journal, 622:1320-1332, 2005 Abril 1

Rivlin, T. J.

The Chebyshev Polynomials

John Wiley & Sons, 1974, pp. 4, 31

Rogers, T.M.: 2011, *Astrophys. J.*, **733**, 12.

Rüdiger G. and Kitchatinov L. L.,

The slender solar tachocline: a magnetic model,

Astron. Nachr., **318** 5, 273-279 (1997)

Schnack Dalton D.

Lectures in Magnetohydrodynamics

Springer-Verlag, Berlin Heidelberg (2009)

Schou *et al.*,

Helioseismic Studies of Differential Rotation in the Solar Envelope by the Solar Oscillations Investigation Using the Michelson Doppler Imager

The Astrophysical Journal, 505:390-417, 1998

Schou, J.: 1998, *Astrophys. J.*, **505**, 390.

Schultz, Lee, and Boyd,

Chebyshev Pseudospectral Method of Viscous Flows with Corner Singularities,

Journal of Scientific Computing, Vol. 4, No. 1, 1989

Spiegel E. A. and Zahn J.-P.,

The Solar Tachocline,

Astronm. Astrophys. 265, 106-144 (1992)

Spiegel E. A.,

Reflections on the solar tachocline,

In chapter 2 of The Solar Tachocline,

Edited by Hughes, Rosner, and Weiss,

Cambridge, 2007

Strugarek, A., Brun, A.S., Zahn, J.-P.: 2011, *Astron. Astrophys.*, **532**, A34.

Thompson, M.J., Toomre, J., Anderson, E.R., Antia, H.M., Berthomieu, G., Burtonclay, D., Chitre, S.M., Christensen-Dalsgaard, J., Corbard, T., DeRosa, M., Genovese, C.R., Gough, D.O., Haber, D.A., Harvey, J.W., Hill, F., Howe, R., Korzennik, S.G., Kosovichev, A.G., Leibacher, J.W., Pijpers, F.P., Provost, J., Rhodes Jr., E.J., Schou, J., Sekii, T., Stark, P.B., Wilson, P.R. : 1996, *Science*, textbf272, (5266), 1300.

Tobias, S.M., Brummell, N.H., Clune, T.L., Toomre, J.

The Astrophysical Journal, **549**, 1183 (2001)

Tobias and Weiss,

The solar dynamo and the tachocline,

In chapter 13 of The Solar Tachocline,

Edited by Hughes, Rosner, and Weiss,

Cambridge, 2007

Tobias Steven M., Diamond Patrick H., and Hughes David W.,

β-Plane Magnetohydrodynamic turbulence in the solar Tachocline

The Astrophysical Journal, **667**:L113-L116 (2007)

Weinberger, H. F.

A First Course in Partial Differential equations

John Wiley & Sons, 1965, pp. 120, 415

Weinberger, H.F.: 1965, *A First Course in Partial Differential Equations*, John Wiley & Sons,

New York, 188.

Wilson, P.R., Burtonclay, D., Li, Y.: 1996, *Astrophys. J.*, **470**, 621.

The Sun's meridional circulation and interior magnetic field

The Astrophysical Journal, **738**:47 (2011)

Polar confinement of the Sun's interior magnetic field by laminar magnetostrophic flow

J. Fluid Mech., **677**:445-482 (2011)

Zahn J.-P.,

Hydrodynamic models of the tachocline,

In chapter 4 of The Solar Tachocline,

Edited by Hughes, Rosner, and Weiss,

Cambridge, 2007

Appendix A

Computing the mean rotation rate Ω_0 of the solar interior

To have a system rotating with zero net angular momentum,

$$\begin{aligned} \int_0^\pi L_0 \sin\theta \mathrm{d}\theta &= 0 \\ \int_0^\pi (L_{CZ} - L_\odot) \sin\theta \mathrm{d}\theta &= 0 \\ \int_0^\pi r^2 \sin^2\theta (\Omega_{CZ} - \Omega_\odot) \sin\theta \mathrm{d}\theta &= 0 \ , \end{aligned} \tag{A.1}$$

where $\Omega_{CZ} = \Omega_{eq}(1 - a\cos^2\theta - b\cos^4\theta)$, with a and b estimated from helioseismic observations. Then, by the change of variable $\mu = \cos\theta$, we find:

$$\begin{aligned} \int_{-1}^1 (1-\mu^2)[\Omega_{eq}(1 - a\mu^2 - b\mu^4) - \Omega_\odot]\mathrm{d}\mu &= 0 \\ 2\int_0^1 [(1-\mu^2)(\Omega_{eq} - \Omega_\odot) - a(\mu^2 - \mu^4)\Omega_{eq} - b(\mu^4 - \mu^6)\Omega_{eq}]\mathrm{d}\mu &= 0 \\ (\Omega_{eq} - \Omega_\odot) - \frac{1}{3}(\Omega_{eq} - \Omega_\odot) - a(\frac{1}{3} - \frac{1}{5})\Omega_{eq} - b(\frac{1}{5} - \frac{1}{7})\Omega_{eq} &= \ , \end{aligned} \tag{A.2}$$

which yields:

$$\Omega_0 = 1 - \frac{\Omega_\odot}{\Omega_{eq}} = \frac{3}{15}a + \frac{3}{35}b \ . \tag{A.3}$$

Appendix B

Derivation of the radial component for the background magnetic field

We derive the background magnetic field $\mathbf{B}$, which we assumed to be poloidal only, by integrating twice the given expression for the electric current density $\mathbf{j}_0$. The background magnetic field $\mathbf{B}$ with no toroidal component can be expressed in terms of its poloidal components

$$B_r = b_r \cos\theta \tag{B.1}$$

$$B_\theta = b_\theta \sin\theta \ , \tag{B.2}$$

where b_r and b_θ are functions of r. To induce a poloidal magnetic field we force an electric current density in the azimuthal direction:

$$j_\phi = -\frac{1}{4\pi}[\nabla \times \mathbf{B}]_\phi = J_0(r - r_a)(r - r_b) \ , \ r_a \leq r \leq r_b \ , \tag{B.3}$$

with $j_\phi = 0$ everywhere else.

We combine then the ϕ-component of $\nabla \times \mathbf{B}$ with the solenoidal condition $\nabla \cdot \mathbf{B} = 0$

to eliminate b_θ, and obtain the following differential equation:

$$-\left[r\frac{\partial^2 b_r}{\partial r^2}+4\frac{\partial b_r}{\partial r}\right]\sin\theta = 2J_0(r-r_a)(r-r_b)\sin\theta\ ,\ r_a\le r\le r_b\ , \tag{B.4}$$

which by a first integration with respect to r, in $r_a \le r \le r_b$, yields:

$$\begin{aligned}\frac{\mathrm{d}}{\mathrm{dr}}\left[r\frac{\mathrm{db_r}}{\mathrm{dr}}+3b_r\right] &= -8\pi J_0\left[r^2-(r_a+r_b)r+r_a r_b\right]\\ \frac{\mathrm{db_r}}{\mathrm{dr}}+\frac{3}{r}b_r &= -8\pi J_0\left[\frac{r^2}{3}-\frac{(r_a+r_b)}{2}r+r_a r_b+\frac{c_1}{r}\right]\ .\end{aligned} \tag{B.5}$$

We integrate again with respect to r to obtain:

$$\begin{aligned}\frac{\mathrm{d}}{\mathrm{dr}}\left[r^3 b_r\right] &= -8\pi J_0\left[\frac{1}{3}r^5-\frac{1}{2}(r_a+r_b)r^4+r_a r_b r^3+c_1 r^2\right]\\ b_r &= -8\pi J_0\left[\frac{r^3}{18}=\frac{r_a+r_b)}{10}r^2+\frac{r_a r_b}{4}r+\frac{c_1}{3}+\frac{c_2}{r^3}\right]\ ,\end{aligned} \tag{B.6}$$

which is the solution for the interval $r_a \le r \le r_b$. We also obtain

$$b_r = c_0+\frac{c_3}{r^3} \tag{B.7}$$

for the remaining domain.

By applying the conditions $b_r \to 0$ as $r\to\infty$, continuity of b_r and $\mathrm{db_r/dr}$ at $r=r_a$ and $r=r_b$, and $b_r=1$ at the core, we end up with the solution:

$$B_r(r,\theta)=\begin{cases} c_0\cos\theta & ,\ 0\le r\le r_a\\ -8\pi J_0\left[\frac{1}{18}r^3-\frac{1}{10}(r_a+r_b)r^2+\frac{1}{4}r_a r_b r+\frac{c_1}{3}+\frac{c_2}{r^3}\right]\cos\theta & ,\ r_a\le r\le r_b\\ \frac{c_3}{r^3}\cos\theta & ,\ r_b\le r\end{cases} \tag{B.8}$$

where constants c_0, c_1, c_2, and c_3 are functions of the geometric parameters r_a and r_b. Note that the solution guarantees the amplitude of the magnetic field at the center of the sphere to be finite, an advantage from a computational perspective over the expression for a dipole point used by GG08.

Appendix C

Chebyshev polynomials

C.1 Integration and differentiation of $T_n(\mu)$

Garaud (2000) provides the following identities (Garaud , 2000):

$$\begin{aligned}
(1-\mu^2)T_n &= \frac{T_n}{2} - \frac{T_{n+2}}{4} - \frac{T_{n-2}}{4} \\
(1-\mu^2)\frac{\mathrm{d}T_n}{\mathrm{d}\mu} &= \frac{n}{2}(T_{n-1} - T_{n+1}) \\
\frac{\mathrm{d}}{\mathrm{d}\mu}[(1-\mu^2)T_n] &= \frac{n-2}{2}T_{n-1} - \frac{n+2}{2}T_{n+1} \\
T_m T_n &= \frac{1}{2}T_{m+n} + \frac{1}{2}T_{m-n} \qquad \text{(C.1)} \\
\int_{-1}^{+1} \frac{T_h(\mu)T_{2k}(\mu)}{\sqrt{1-\mu^2}}\mathrm{d}\mu &= \begin{cases} \frac{\pi}{2} & \text{if} \quad h = 2k \neq 0 \\ \pi & \text{if} \quad h = 2k = 0 \\ 0 & \text{if} \quad h \neq 2k \end{cases} . \qquad \text{(C.2)}
\end{aligned}$$

Here, we have some useful identities from Mason and Handscomb's (2003) book (Mason

and Handscomb , 2003)]:

$$\frac{\mathrm{d}^2 T_n(\mu)}{\mathrm{d}\mu^2} = \left(\frac{n}{4}\right)\left[\frac{(n+1)T_{|n-2|}(\mu) - 2nT_n(\mu) + (n-1)T_{n+2}(\mu)}{(1-\mu^2)^2}\right] \tag{C.3}$$

$$\int T_n(\mu)\mathrm{d}\mu = \begin{cases} \frac{1}{2}\left[\frac{T_{n+1}(\mu)}{n+1} - \frac{T_{|n-1|}(\mu)}{n-1}\right] & \text{if} \quad n \neq 1 \\ \frac{1}{2}\left[\frac{T_{n+1}(\mu)}{n+1}\right] & \text{if} \quad n = 1 \end{cases} . \tag{C.4}$$

Another identities I derived:

$$(1-\mu^2)\frac{\mathrm{d}^2 T_n(\mu)}{\mathrm{d}\mu^2} = \mu\frac{\mathrm{d}T_n(\mu)}{\mathrm{d}\mu} - n^2 T_n(\mu) \tag{C.5}$$

$$(1-\mu^2)\frac{\mathrm{d}^3 T_n(\mu)}{\mathrm{d}\mu^3} = 3\mu\frac{\mathrm{d}^2 T_n(\mu)}{\mathrm{d}\mu^2} + (1-n^2)\frac{\mathrm{d}T_n(\mu)}{\mathrm{d}\mu} \tag{C.6}$$

$$(1-\mu^2)\frac{\mathrm{d}^4 T_n(\mu)}{\mathrm{d}\mu^4} = 5\mu\frac{\mathrm{d}^3 T_n(\mu)}{\mathrm{d}\mu^3} + [3+(1-n^2)]\frac{\mathrm{d}^2 T_n(\mu)}{\mathrm{d}\mu^2} , \tag{C.7}$$

which can also be written as:

$$\frac{\mathrm{d}^3 T_n(\mu)}{\mathrm{d}\mu^3} = \left[\frac{3\mu^2}{(1-\mu^2)^2} + \frac{1-n^2}{1-\mu^2}\right]\frac{\mathrm{d}T_n(\mu)}{\mathrm{d}\mu} - \frac{3\mu n^2}{(1-\mu^2)^2}T_n(\mu) \tag{C.8}$$

$$\frac{\mathrm{d}^4 T_n(\mu)}{\mathrm{d}\mu^4} = \left[\frac{15\mu^3}{(1-\mu^2)^3} + \frac{5\mu(1-n^2)}{(1-\mu^2)^2} + \frac{[3+(1-n^2)]\mu}{1-\mu^2}\right]\frac{\mathrm{d}T_n(\mu)}{\mathrm{d}\mu} - \left[\frac{15\mu^2 n^2}{(1-\mu^2)^3} + \frac{[3+(1-n^2)]n^2}{1-\mu^2}\right]T_n(\mu) . \tag{C.9}$$

C.2 An example: Differentiation of u_ϕ

Provided that the non-dimensional $\hat{L} = \hat{L}(x, \mu)$, we can write:

$$u_\phi(r,\theta) = R_\odot^2 \Omega_{eq} \frac{\hat{L}}{r \sin\theta} \tag{C.10}$$

$$u_\phi(x,\mu) = R_\odot^2 \Omega_{eq} \frac{\hat{L}}{x\sqrt{1-\mu^2}} \tag{C.11}$$

$$\begin{aligned} \frac{\partial u_\phi}{\partial \theta}(r,\theta) &= = \frac{R_\odot^2 \Omega_{eq}}{r} \left[\frac{1}{\sin\theta} \frac{\partial \hat{L}}{\partial \theta} - \frac{\cos\theta}{\sin^2\theta} \hat{L} \right] \\ &= \frac{R_\odot^2 \Omega_{eq}}{r \sin\theta} \left[-\sin\theta \frac{\partial \hat{L}}{\partial \cos\theta} - \frac{\cos\theta}{\sin\theta} \hat{L} \right] \end{aligned} \tag{C.12}$$

$$-\sqrt{1-\mu^2} \frac{\partial u_\phi}{\partial \mu}(x,\mu) = = \frac{R_\odot \Omega_{eq}}{x} \left[-\frac{\partial \hat{L}}{\partial \mu} - \frac{\mu}{1-\mu^2} \hat{L} \right] \tag{C.13}$$

$$\frac{\partial^2 u_\phi}{\partial \theta^2}(r,\theta) = \frac{R_\odot^2 \Omega_{eq}}{r \sin\theta} \left[-\sin\theta \frac{\partial}{\partial \theta} \left(\frac{\partial \hat{L}}{\partial \cos\theta} \right) + \cos\theta \frac{\partial \hat{L}}{\partial \cos\theta} + \frac{2\cos^2\theta}{\sin^2\theta} \hat{L} + \hat{L} \right] \tag{C.14}$$

$$\frac{\partial^2 u_\phi}{\partial \mu^2}(x,\mu) = \frac{R_\odot \Omega_{eq}}{x\sqrt{1-\mu^2}} \left[\frac{\partial^2 \hat{L}}{\partial \mu^2} + \frac{\mu}{1-\mu^2} \frac{\partial \hat{L}}{\partial \mu} + \frac{1+\mu^2}{1-\mu^2} \hat{L} \right] . \tag{C.15}$$

Appendix D

How to plot the potential magnetic field

The potential magnetic field A and the poloidal magnetic field B_P are related in spherical coordinates through the following expression:

$$B_P = \nabla \times \left(\frac{A}{r \sin\theta} \hat{\mathbf{e}}_\phi \right) \ , \tag{D.1}$$

from which we can determine the radial and latitudinal components of the magnetic field:

$$B_r = \frac{1}{r \sin\theta} \frac{\partial}{\partial \theta} \left(\frac{A}{r} \right) = -\frac{1}{r^2} \frac{\partial A}{\partial \mu} \tag{D.2}$$

$$B_\theta = -\frac{1}{r \sin\theta} \frac{\partial A}{\partial r} = -\frac{1}{r\sqrt{1-\mu^2}} \frac{\partial A}{\partial r} \ , \tag{D.3}$$

where we made the substitution $\mu = \cos\theta$. We also define non-dimensional radial and latitudinal componentes of the magnetic field, B and b, respectively (see Garaud and Garaud, 2008), which under the Chebyshev expansion can be written as:

$$B = \sum_{n=1}^{N} B_n(r) T_{2n-1}(\mu) \tag{D.4}$$

$$b = \sum_{n=1}^{N} b_n(r)(1-\mu^2) T_{2n-2}(\mu) \ . \tag{D.5}$$

We can numerically obtain the Chebyshev modes B_n and b_n, which we then will use to compute the corresponding Chebyshev modes A_n needed to evaluate the potential magnetic field as:

$$A = \sum_{n=1}^{N} A_n(r)(1-\mu^2)T_{2n-2}(\mu) \ . \tag{D.6}$$

The computation of A_n from given B_n and b_n can be achieved either by integration or differentiation.

D.0.1 Differentiation of Chebyshev Modes

Here, we derive the relationship between A_n and B_n by taking the first derivative of equation D.6 with respect to μ, and then using the first identity of equation D.2:

$$\begin{aligned} \sum_{n=1}^{N} B_n(r)T_{2n-1}(\mu) &= -\frac{1}{r^2}\frac{\partial}{\partial\mu}\left[\sum_{n=1}^{N} A_n(r)(1-\mu^2)T_{2n-2}(\mu)\right] \\ &= -\sum_{n=1}^{N} A_n(r)\left[\frac{2n-4}{2}T_{2n-3}(\mu) - \frac{2n}{2}T_{2n-1}(\mu)\right] \ , \end{aligned} \tag{D.7}$$

where we have used some identities included in the appendix. Then, by a projection onto T_{2k-1}, we can obtain a relationship between B_n and A_n:

$$B_k = -(k-1)A_{k+1} + kA_k \ , \tag{D.8}$$

which can be used to recursively obtain A_k by assuming, for example, $A_N = 0$. A plot of the potential field obtained by using this formula is shown on the third panel of figure D.1.

Another process of differentiation can be used to determine A_n. This time, we will use b_n modes and the second identity of equation D.2 as follows:

$$\begin{aligned} \sum_{n=1}^{N} rb_n(r)(1-\mu^2)T_{2n-2}(\mu) &= -\sum_{n=1}^{N} \frac{\partial A_n(r)}{\partial r}(1-\mu^2)T_{2n-2}(\mu) \\ &= -\sum_{n=1}^{N} \frac{A_n(i+1)-A_n(i)}{r(i+1)-r(i)}(1-\mu^2)T_{2n-2}(\mu) \ , \end{aligned} \tag{D.9}$$

which reduces to the following formula relating A_n and b_n:

$$r(i)b_n(i) = \frac{A_n(i+1) - A_n(i)}{r(i+1) - r(i)} \ . \tag{D.10}$$

Alternatively, a centered finite difference scheme can be used to express $\partial A/\partial r$, which leads to the following expression for $A_n(i)$:

$$A_n(i) = A_n(i+1) + \frac{[b_n(i+1) + b_n(i)][r(i+1)^2 - r(i)^2]}{4} \ , \tag{D.11}$$

where i is an index corresponding to the discretization of r. A plot of the potential field lines obtained by using this recursion formula is shown on figure D.2.

D.0.2 Integration of Chebyshev modes

Finding relationships between A_n modes by integrating the corresponding magnetic field ones is slightly more complicated, especially with respect to r. Here, we only show how to integrate with respect to μ. In a first case, we integrate the Chebyshev expansion of B_r (see equation D.4) by using the identities provided in the appendix:

$$\begin{aligned} A(r,\mu) &= -r^2 \int_1^\mu B(r,\mu)\partial\mu \\ &= -r^2 \sum_{n=1}^{n} B_n(r) \int_1^\mu T_{2n-1}(\mu)\partial\mu \\ &= -r^2 \frac{B_1(r)}{2} \frac{T_2(\mu) - T_2(1)}{2} - r^2 \sum_{n=2}^{N} \frac{B_n(r)}{2} \left(\frac{T_{2n}(\mu)}{2n} - \frac{T_{|2n-2|}(\mu)}{2n-2} \right) \Bigg|_1^\mu \ . \end{aligned} \tag{D.12}$$

A plot of the potential field lines obtained by using this expression is shown on figure D.3.

Finally, to obtain A_n as a function of B_n, we can use the following identity:

$$-r^2 \sum_{n=1}^{N} B_n(r) \int T_{2k-1}(\mu)\partial\mu = -\sum_{n=1}^{N} \left[\frac{(k-1)B_{n+1}(r) - B_n(r)}{n} \right] (1-\mu^2) T_{2n-2}(\mu) \ , \tag{D.13}$$

which, once implemented for plotting, yields the plot of magnetic field lines shown on figure D.4, which shows a slightly different configuration. Therefore, we use any of the first three formulations to plot the magnetic potential field.

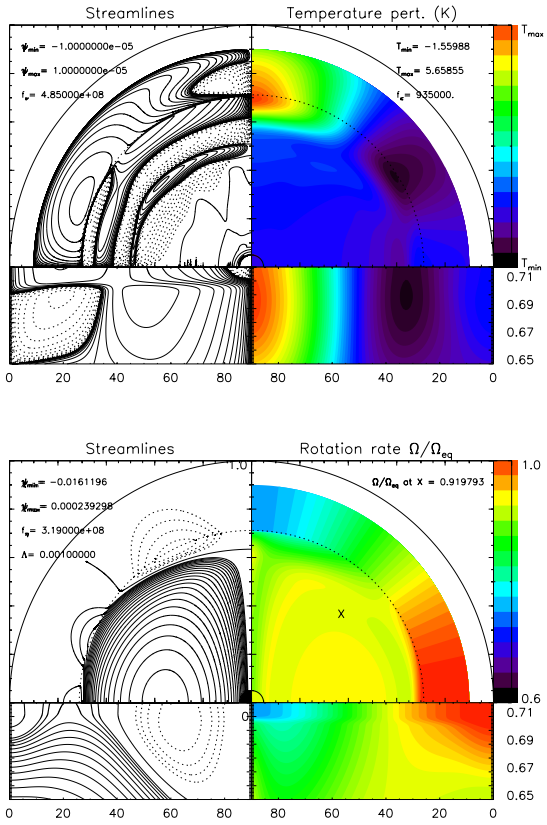

Figure D.1: Contour plots showing streamlines (left upper panel), perturbations of the temperature background (right upper panel), magnetic field lines (left lower panel), and the ratio of angular velocity in the solar interior with respect to the equatorial angular velocity in the solar surface (right lower panel). The magnetic field lines were plotted by using A_n modes obtained by a process of differentiation with respect to μ, as indicated in the text.

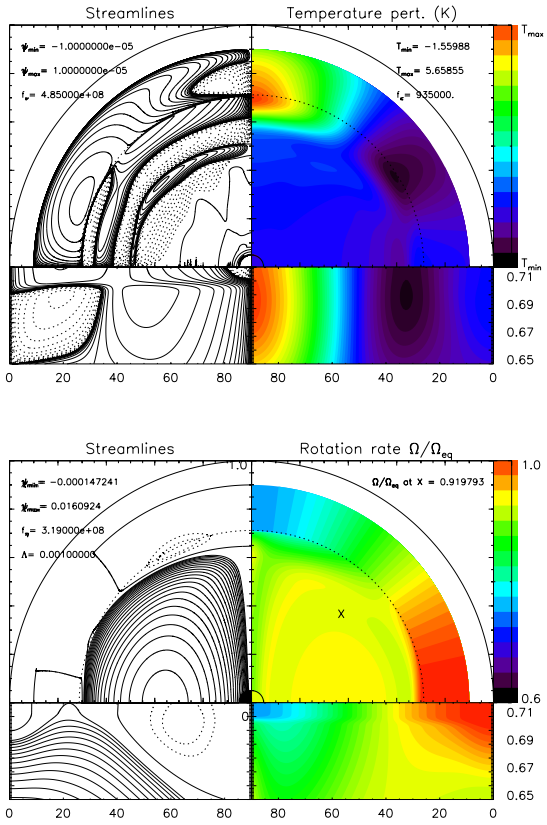

Figure D.2: Contour plots showing streamlines (left upper panel), perturbations of the temperature background (right upper panel), magnetic field lines (left lower panel), and the ratio of angular velocity in the solar interior with respect to the equatorial angular velocity in the solar surface (right lower panel). The magnetic field lines were plotted by using A_n modes obtained by a process of differentiation with respect to r, as indicated in the text.

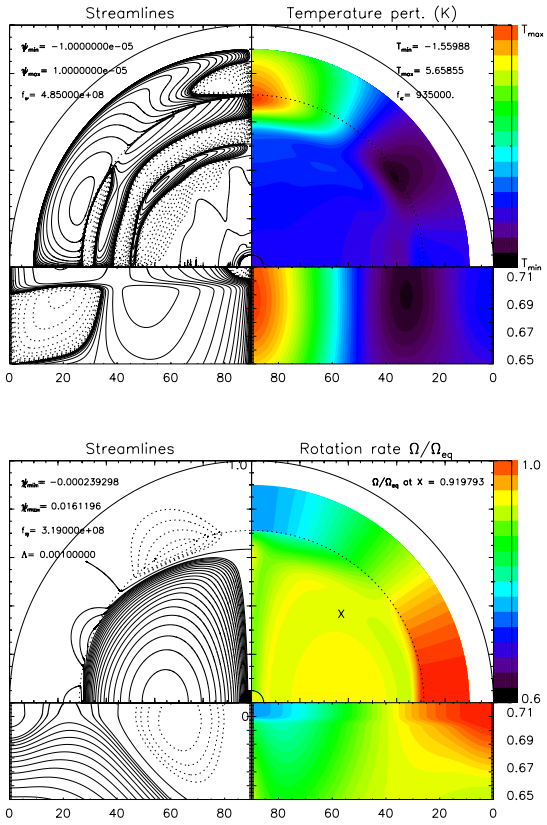

Figure D.3: Contour plots showing streamlines (left upper panel), perturbations of the temperature background (right upper panel), magnetic field lines (left lower panel), and the ratio of angular velocity in the solar interior with respect to the equatorial angular velocity in the solar surface (right lower panel). The magnetic field lines were plotted by using A_n modes obtained by a process of integration with respect to μ, as indicated in the text.

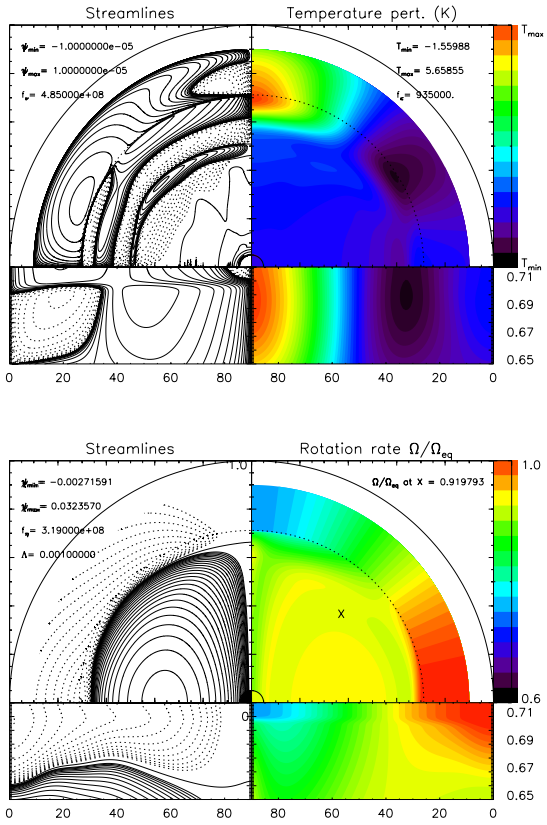

Figure D.4: Contour plots showing streamlines (left upper panel), perturbations of the temperature background (right upper panel), magnetic field lines (left lower panel), and the ratio of angular velocity in the solar interior with respect to the equatorial angular velocity in the solar surface (right lower panel). The magnetic field lines were plotted by using A_n modes obtained by a process of coefficient inversion, as indicated in the text.

Appendix E

The Chebyshev transformation of the integrated induction equation

E.0.3 The integrated induction equation

We write the additional contribution to the induction equation in terms of a prescribed background current density $\bar{j}$:

$$\nabla \times (\mathbf{u} \times \mathbf{B}) = \nabla \times (\eta \nabla \times \mathbf{B}) - 4\pi \nabla \times (\eta \bar{\mathbf{j}}) \ . \tag{E.1}$$

After integration, we obtain the ϕ-component of the integrated induction equation in spherical coordinates:

$$(\mathbf{u} \times \mathbf{B})_\phi = (\eta \nabla \times \mathbf{B})_\phi - \mathcal{B}_0 \eta \hat{j}_{0,\phi}(r) \sin\theta \ , \tag{E.2}$$

with

$$\bar{\mathbf{j}}_\phi = \frac{\mathcal{B}_0}{4\pi} \hat{j}_\phi(r) \sin\theta \mathbf{e}_\phi \ . \tag{E.3}$$

The ϕ-component of the integrated induction equation can also be written as

$$u_r B_\theta - u_\theta B_r = 4\pi f_\eta \bar{\eta}_\odot j_\phi + f_\eta \bar{\eta}_\odot \mathcal{B}_0 \hat{j}_{0,\phi}(r) \sin\theta \ , \tag{E.4}$$

where we have introduced an amplification factor f_η to facilitate the numerical computations, and the magnetic diffusivity η has been assumed without perturbation from its background state $\bar{\eta}_\odot$.

Now we make a change of variables to non-dimensionalize the equation according to Garaud and Garaud (Garaud and Garaud , 2008). They proposed:

$$\begin{aligned} E_\eta &= \frac{f_\eta \bar{\eta}}{R_\odot^2 \Omega_{eq}} \\ u &= \frac{u_r}{R_\odot \Omega_{eq}} \\ v &= \frac{u_\theta \sin\theta}{R_\odot \Omega_{eq}} \\ B &= \frac{B_r}{B_0} \\ b &= \frac{B_\theta \sin\theta}{B_0} \\ J &= \frac{4\pi r \sin\theta j_\phi}{B_0} \ . \end{aligned} \tag{E.5}$$

By applying these expressions, we obtain:

$$\frac{\mathcal{B}_0 R_\odot \Omega_{eq}}{\sin\theta}[ub - vB] = f_\eta \frac{\bar{\eta}_\odot \mathcal{B}_0}{\sin\theta}\frac{J}{r} - f_\eta \bar{\eta}_\odot \mathcal{B}_0 \hat{j}_{0,\phi}(r)\sin\theta \tag{E.6}$$

$$ub - vB = f_\eta E_\eta \frac{J}{x} - f_\eta E_\eta \hat{j}_{0,\phi}(x)\sin^2\theta \tag{E.7}$$

$$ub - vB = f_\eta E_\eta \left[\frac{J}{x} - (1-\mu^2)\hat{j}_{0,\phi}(x)\right] \ , \tag{E.8}$$

where $x = \frac{r}{R_\odot}$ and $\mu = \cos\theta$.

E.0.4 Chebyshev expansion of the fields

The next step is writting the variables of interest in terms of linear combinations of Chebyshev polynomials. Again, we use the Chebyshev identities provided by Garaud and

Garaud (Garaud and Garaud , 2008):

$$
\begin{aligned}
u(x,\mu) &= \sum_{n=1}^{N} \psi_n(x) \frac{\partial}{\partial \mu} \left[(1-\mu^2) T_{2n-1}(\mu) \right] \ , \\
v(x,\mu) &= (1-\mu^2) \sum_{n=1}^{N} v_n(x) T_{2n-1}(\mu) \ , \\
B(x,\mu) &= \sum_{n=1}^{N} B_n(x) T_{2n-1}(\mu) \ , \\
b(x,\mu) &= (1-\mu^2) \sum_{n=1}^{N} b_n(x) T_{2n-2}(\mu) \ , \\
J(x,\mu) &= (1-\mu^2) \sum_{n=1}^{N} J_n(x) T_{2n-2}(\mu) \ . \qquad \text{(E.9)}
\end{aligned}
$$

This transformation yields

$$
\begin{aligned}
\sum_{n=1}^{N} \psi_n(x) \frac{\partial}{\partial \mu} \left[(1-\mu^2) T_{2n-1}(\mu) \right] (1-\mu^2) \sum_{m=1}^{N} b_m(x) T_{2m-2}(\mu) \\
-(1-\mu^2) \sum_{n=1}^{N} v_n(x) T_{2n-1}(\mu) \sum_{m=1}^{N} B_m(x) T_{2m-1}(\mu) \\
= E_\eta \left[\frac{(1-\mu^2)}{x} \sum_{n=1}^{N} J_n(x) T_{2n-2}(\mu) - \frac{2}{x_0} (1-\mu^2) \right] \ , \qquad \text{(E.10)}
\end{aligned}
$$

which simplyfies to

$$
\begin{aligned}
\sum_{n=1}^{N} \psi_n(x) \frac{\partial}{\partial \mu} \left[(1-\mu^2) T_{2n-1}(\mu) \right] \sum_{m=1}^{N} b_m(x) T_{2m-2}(\mu) \\
- \sum_{n=1}^{N} v_n(x) T_{2n-1}(\mu) \sum_{m=1}^{N} B_m(x) T_{2m-1}(\mu) \\
= E_\eta \left[\frac{(1}{x} \sum_{n=1}^{N} J_n(x) T_{2n-2}(\mu) - \frac{2}{x_0} \right] \ . \qquad \text{(E.11)}
\end{aligned}
$$

This equation can be written now in terms of a vector $\mathbf{Y}$ containing all the dependent variables. To do that, we follow Garaud's (2000) notation:

$$\begin{aligned} \psi_n &\rightarrow Y_n \ , \\ v_n &\rightarrow Y_{N+n} \ , \\ B_n &\rightarrow Y_{6N+n} \ , \\ b_n &\rightarrow Y_{7N+n} \ , \text{ and} \\ J_n &\rightarrow Y_{10N+n} \ , \end{aligned} \tag{E.12}$$

which yields

$$\sum_{n,m} Y_n \frac{\partial}{\partial \mu} \left[(1-\mu^2) T_{2n-1} \right] Y_{7N+m} T_{2m-2} - \sum_{n,m} Y_{N+n} T_{2n-1} Y_{6N+m} T_{2m-1} = \\ = E_\eta \left[\frac{1}{x} \sum_n Y_{10N+n} T_{2n-2} - \frac{2}{x_0} \right]. \tag{E.13}$$

We use some of the identities included in Appendix D to simplify Equation E.13 into:

$$\sum_{n,m} Y_n Y_{7N+m} \left[\frac{2n-3}{2} \left(\frac{1}{2} T_{2n+2m-4} + \frac{1}{2} T_{2n-2m} \right) - \frac{2n+1}{2} \left(\frac{1}{2} T_{2n+2m-2} + \frac{1}{2} T_{2n-2m+2} \right) \right] \\ - \sum_{n,m} Y_{N+n} Y_{6N+m} \left[\frac{1}{2} T_{2n+2m-2} + \frac{1}{2} T_{2n-2m} \right] = E_\eta \sum_n \left[\frac{1}{x} Y_{10N+n} T_{2n-2} \right] - \frac{2E_\eta}{x_0} T_0 \ . \tag{E.14}$$

E.0.5 Projection onto the radial direction

We project the equation by applying the following identity (Garaud , 2000):

$$\int_{-1}^{+1} \frac{T_h(\mu) T_{2k}(\mu)}{\sqrt{1-\mu^2}} d\mu = \begin{cases} \frac{\pi}{2} & \text{if} \quad h = 2k \neq 0 \\ \pi & \text{if} \quad h = 2k = 0 \\ 0 & \text{if} \quad h \neq 2k \end{cases}$$

This results, for $2k \neq 0$, in

$$\begin{aligned}
&\frac{1}{4}\left(\frac{\pi}{2}\right)\sum_{k,m}(2k-2m+1)Y_{k-m+2}Y_{7N+m}+\frac{1}{4}\left(\frac{\pi}{2}\right)\sum_{k,m}(2k+2m-3)Y_{k+m}Y_{7N+m}\\
-&\frac{1}{4}\left(\frac{\pi}{2}\right)\sum_{k,m}(2k-2m+3)Y_{k-m+1}Y_{7N+m}-\frac{1}{4}\left(\frac{\pi}{2}\right)\sum_{k,m}(2k+2m-1)Y_{k+m-1}Y_{7N+m}\\
&-\frac{1}{2}\left(\frac{\pi}{2}\right)\sum_{k,m}Y_{N+k-m+1}Y_{6N+m}-\frac{1}{2}\left(\frac{\pi}{2}\right)\sum_{k,m}Y_{N+k+m}Y_{6N+m}\\
&=E_\eta\frac{1}{x}\left(\frac{\pi}{2}\right)\sum_{k}Y_{10N+k+1}\ . \qquad \text{(E.15)}
\end{aligned}$$

On the other hand, when $2k = 0$,

$$\begin{aligned}
&\frac{\pi}{4}\sum_{m}(-2m+1)Y_{-m+2}Y_{7N+m}+\frac{\pi}{4}\sum_{m}(2m-3)Y_{m}Y_{7N+m}\\
-&\frac{\pi}{4}\sum_{m}(-2m+3)Y_{-m+1}Y_{7N+m}-\frac{\pi}{4}\sum_{m}(2m-1)Y_{m-1}Y_{7N+m}\\
-&\frac{\pi}{2}\sum_{m}Y_{N-m+1}Y_{6N+m}-\frac{\pi}{2}\sum_{m}Y_{N+m}Y_{6N+m}=E_\eta\pi\left[\frac{1}{x}Y_{10N+1}-\frac{2}{x_0}\right]\ . \qquad \text{(E.16)}
\end{aligned}$$

Alternatively, we can derive these expressions in terms of n. For example, for $2k \neq 0$, we obtain

$$\begin{aligned}
&\frac{1}{4}\left(\frac{\pi}{2}\right)\sum_{k,n}(2n-3)Y_{n}Y_{7N+k-n+2}+\frac{1}{4}\left(\frac{\pi}{2}\right)\sum_{k,n}(2n-3)Y_{n}Y_{7N-k+n}\\
-&\frac{1}{4}\left(\frac{\pi}{2}\right)\sum_{k,n}(2n+1)Y_{n}Y_{7N-k+n+1}-\frac{1}{4}\left(\frac{\pi}{2}\right)\sum_{k,n}(2n+1)Y_{n}Y_{7N+k-n+1}\\
&-\frac{1}{2}\left(\frac{\pi}{2}\right)\sum_{k,n}Y_{N+n}Y_{6N+k-n+1}-\frac{1}{2}\left(\frac{\pi}{2}\right)\sum_{k,n}Y_{N+n}Y_{6N-k+n}\\
&=E_\eta\frac{1}{x}\left(\frac{\pi}{2}\right)\sum_{k}Y_{10N+k+1}\ . \qquad \text{(E.17)}
\end{aligned}$$

Likewise, for $2k = 0$, we obtain

$$\begin{aligned}
&\frac{\pi}{4}\sum_{n}(2n-3)Y_{n}Y_{7N-n+2}+\frac{\pi}{4}\sum_{n}(2n-3)Y_{n}Y_{7N+n}\\
-&\frac{\pi}{4}\sum_{n}(2n+1)Y_{n}Y_{7N+n+1}-\frac{\pi}{4}\sum_{n}(2n+1)Y_{n}Y_{7N-n+1}\\
&-\frac{\pi}{2}\sum_{n}Y_{N+n}Y_{6N-n+1}-\frac{\pi}{2}\sum_{n}Y_{N+n}Y_{6N+n}\\
&=E_\eta\pi\left[\frac{1}{x}Y_{10N+1}-\frac{2}{x_0}\right]\ . \qquad \text{(E.18)}
\end{aligned}$$

Note that some of the terms in the previous equations can be simplify by considering only the indexes which stay in range. However, they introduce some conditional commands in the code to guarantee the correct indexing.

Appendix F

The Force Balances in the Tachocline

Here, we derive expressions for each term of the momemtum and vorticity equations, which we use to visualize the force balances taking place in the tachocline.

F.1 Force balances from the momentum equation

The momentum equation

$$\rho\frac{\partial \mathbf{u}}{\partial t} = -\rho\mathbf{u}\cdot\nabla\mathbf{u} - 2\mathbf{\Omega}_\odot \times \mathbf{u} - \nabla p - \rho\mathbf{g} + \mathbf{j}\times\mathbf{B} + \nabla\cdot\mathbf{\Pi} \tag{F.1}$$

is one of the equations governing the magnetohydrodynamics of the solar interior. It is perturbed with respect to a background in hydrostatic equilibrium, and numerically solved within a spherical framework rotating with angular velocity Ω_0. We assume a system in steady state with axial symmetry, and with meridional flows generated in the convection zone by a force, $(\mathbf{u}-\mathbf{u}_C Z)/\tau$, driven by the differential rotation estimated from helioseismic observations. Then,

the ϕ-component of the corresponding forces are:

$$-2\rho\Omega_\odot(u_\theta\cos\theta + u_r\sin\theta) \qquad \text{(Coriolis force)} \tag{F.2}$$

$$-\rho\left[u_r\frac{\partial u_\phi}{\partial r} + \frac{u_\theta}{r}\frac{\partial u_\phi}{\partial\theta} + \frac{1}{r}u_\phi u_r + \frac{\cos\theta}{r\sin\theta}u_\phi u_\theta\right] \qquad \text{(Advection)} \tag{F.3}$$

$$j_r B_\theta - j_\theta B_r \qquad \text{(Lorentz force)} \tag{F.4}$$

$$-\frac{\rho}{\tau}[u_\phi - u_{CZ}] \qquad \text{(Gyroscopic pumping)} \tag{F.5}$$

$$(\nabla\cdot\mathbf{\Pi})_\phi = f_\nu\rho\nu[\nabla\mathbf{u} + (\nabla\mathbf{u})^T - \frac{2}{3}\nabla\cdot\mathbf{u}\mathbf{I}]_\phi \qquad \text{(Viscous stresses)} \tag{F.6}$$

We now derive these forces in terms of Chebyshev polynomials to construct the solutions from the numerically computed modes.

F.1.1 Coriolis Force

We define the components of the velocity field in terms of non-dimensional variables by using:

$$u_r = R_\odot\Omega_{eq}\hat{u} \tag{F.7}$$

$$u_\theta = \frac{R_\odot\Omega_{eq}}{\sin\theta}\hat{v}\ , \tag{F.8}$$

$$\tag{F.9}$$

which yields:

$$\begin{aligned} F_{Coriolis} &= -2\rho\Omega_\odot(u_\theta\cos\theta + u_r\sin\theta) \\ &= -2R_\odot\Omega_{eq}\rho\Omega_\odot\left[\frac{\cos\theta}{\sin\theta}\hat{v} + \hat{u}\sin\theta\right] \\ &= -2R_\odot\Omega_{eq}\rho\Omega_\odot\left[\frac{\mu}{\sqrt{1-\mu^2}}\hat{v} + \sqrt{1-\mu^2}\hat{u}\right]\ , \end{aligned} \tag{F.10}$$

where $\mu = \cos\theta$. Since $\Omega_0 = 1 - \Omega_\odot/\Omega_{eq}$ (see Appendix A),

$$\frac{F_{Coriolis}}{R_\odot\Omega_{eq}^2} = -2\rho(1-\Omega_0)\left[\frac{\mu}{\sqrt{1-\mu^2}}\hat{v} + \sqrt{1-\mu^2}\hat{u}\right]\ . \tag{F.11}$$

Then, we use the following Chebyshev transformations:

$$\begin{aligned}
\hat{u}(x,\mu) &= \sum_{n=1}^{N} \psi_n(x) \frac{\partial}{\partial \mu}[(1-\mu^2) T_{2n-1}(\mu)] \\
&= \sum_{n=1}^{N} \psi_n(x) \left[\frac{2n-3}{2} T_{2n-2}(\mu) - \frac{2n+1}{2} T_{2n}(\mu) \right] \\
&= \sum_{m=0}^{N-1} \psi_m(x) \left[\frac{2m-1}{2} T_{2m}(\mu) - \frac{2m+3}{2} T_{2m+2}(\mu) \right] \qquad \text{(F.12)} \\
\hat{v}(x,\mu) &= (1-\mu^2) \sum_{n=1}^{N} v_n(x) T_{2n-1}(\mu) \\
&= (1-\mu^2) \sum_{m=0}^{N-1} v_m(x) T_{2m+1}(\mu) \qquad \text{(F.13)}
\end{aligned}$$

to compute $F_{Coriolis}$ from the correspondig Chebyshev modes, $\psi_m(x)$ and $v_m(x)$.

F.1.2 Advection term

We define u_ϕ in terms of a non-dimensional variable $\hat{L}$ as:

$$u_\phi = R_\odot^2 \Omega_{eq} \frac{1}{r \sin\theta} \hat{L} \ , \qquad \text{(F.14)}$$

which, in conjuction with the non-dimensional expressions for u_r and u_θ, yields:

$$\begin{aligned}
F_{Advection} &= -\rho \left[u_r \frac{\partial u_\phi}{\partial r} + \frac{u_\theta}{r} \frac{\partial u_\phi}{\partial \theta} + \frac{1}{r} u_\phi u_r + \frac{\cos\theta}{r \sin\theta} u_\phi u_\theta \right] \\
&= -R_\odot \Omega_{eq}^2 \rho \left[\frac{\hat{u}}{x \sin\theta} \frac{\partial \hat{L}}{\partial x} - \frac{1}{x^2 \sin\theta} \hat{u} \hat{L} \right. \\
&\quad + \frac{1}{\sin\theta} \hat{v} \left(\frac{1}{x^2 \sin\theta} \frac{\partial \hat{L}}{\partial \theta} - \frac{\cos\theta}{x^2 \sin^2\theta} \hat{L} \right) \\
&\quad \left. + \frac{1}{x^2 \sin\theta} \hat{u} \hat{L} + \frac{\cos\theta}{x^2 \sin^2\theta} \hat{v} \hat{L} \right] \ , \qquad \text{(F.15)}
\end{aligned}$$

which simplifies to:

$$\frac{F_{Advection}}{R_\odot \Omega_{eq}^2} = -\frac{\rho}{x\sqrt{1-\mu^2}} \left[\hat{u} \frac{\partial \hat{L}}{\partial x} - \frac{1}{x} \hat{v} \frac{\partial \hat{L}}{\partial \mu} \right] \ . \qquad \text{(F.16)}$$

Here, we used:

$$\begin{aligned}
\frac{\partial u_\phi}{\partial r} &= R_\odot^2 \Omega_{eq} \left[\frac{1}{r \sin\theta} \frac{\partial \hat{L}}{\partial r} - \frac{1}{r^2 \sin\theta} \hat{L} \right] , \\
\frac{\partial u_\phi}{\partial \theta} &= R_\odot^2 \Omega_{eq} \left[\frac{1}{r \sin\theta} \frac{\partial \hat{L}}{\partial \theta} - \frac{\cos\theta}{r \sin^2\theta} \hat{L} \right] , \text{ and} \\
x &= \frac{r}{R_\odot} . \qquad \text{(F.17)}
\end{aligned}$$

In addition to $\hat{u}$ and $\hat{v}$, we will need $\hat{L}$ and its derivatives with respect to x and with respect to μ to be expressed in terms of Chebyshev polynomials:

$$\begin{aligned}
\hat{L}(x,\mu) &= (1-\mu^2) \sum_{n=1}^{N} L_n(x) T_{2n-2}(\mu) \\
&= (1-\mu^2) \sum_{m=0}^{N-1} L_m(x) T_{2m}(\mu) \qquad \text{(F.18)} \\
\frac{\partial \hat{L}(x,\mu)}{\partial x} &= (1-\mu^2) \sum_{n=1}^{N} dL_n(x) T_{2n-2}(\mu) \\
&= (1-\mu^2) \sum_{m=0}^{N-1} dL_m(x) T_{2m}(\mu) \qquad \text{(F.19)} \\
\frac{\partial \hat{L}(x,\mu)}{\partial \mu} &= \sum_{n=1}^{N} L_n(x) \frac{\partial}{\partial \mu} [(1-\mu^2) T_{2n-2}(\mu)] \\
&= \sum_{n=1}^{N} L_n(x) [(n-2) T_{|2n-3|}(\mu) - n T_{2n-1}(\mu)] \\
&= \sum_{m=0}^{N-1} L_m(x) [(m-1) T_{|2m-1|}(\mu) - (m+1) T_{2m+1}(\mu)] . \qquad \text{(F.20)}
\end{aligned}$$

This way, we will compute $F_{Advection}$ from $\psi_m(x)$, $v_m(x)$, $L_m(x)$, and $dL_m(x)$.

F.1.3 Lorentz force

We non-dimensionalize the Lorentz force expression by using[1]:

$$\begin{aligned} B_r &= B_0 \hat{B} \\ B_\theta &= \frac{B_0}{\sin\theta}\hat{b} \\ B_\phi &= \frac{B_0 R_\odot}{r\sin\theta}\hat{S} \\ \Lambda &= \frac{B_0^2}{4\pi\rho_0 R_\odot \Omega_{eq}^2} \ , \end{aligned} \tag{F.21}$$

which yields:

$$\begin{aligned} F_{Lorentz} &= j_r B_\theta - j_\theta B_r \\ &= \frac{1}{4\pi}\left[B_r\frac{\partial B_\phi}{\partial r} + \frac{1}{r}B_r B_\phi + \frac{1}{r}B_\theta\frac{\partial B_\phi}{\partial\theta} + \frac{\cos\theta}{r\sin\theta}B_\theta B_\phi\right] \\ &= \frac{B_0 R_\odot}{4\pi}B_r\left[\frac{1}{r\sin\theta}\frac{\partial\hat{S}}{\partial r} - \frac{1}{r^2\sin\theta}\hat{S} + \frac{1}{r^2\sin\theta}\hat{S}\right] \\ &\quad + \frac{B_0 R_\odot}{4\pi}\frac{B_\theta}{r}\left[\frac{1}{r\sin\theta}\frac{\partial\hat{S}}{\partial\theta} - \frac{\cos\theta}{r\sin^2\theta}\hat{S} + \frac{\cos\theta}{r\sin^2\theta}\hat{S}\right] \\ &= \frac{B_0 R_\odot}{4\pi}\frac{1}{r\sin\theta}\left[B_r\frac{\partial\hat{S}}{\partial r} + \frac{1}{r}B_\theta\frac{\partial\hat{S}}{\partial\theta}\right] \\ &= \frac{B_0^2 R_\odot}{4\pi}\frac{1}{r\sin\theta}\left[\hat{B}\frac{\partial\hat{S}}{\partial r} + \frac{1}{r\sin\theta}\hat{b}\frac{\partial\hat{S}}{\partial\theta}\right] \\ &= \frac{B_0^2}{4\pi R_\odot}\frac{1}{x\sqrt{1-\mu^2}}\left[\hat{B}\frac{\partial\hat{S}}{\partial x} - \frac{1}{x}\hat{b}\frac{\partial\hat{S}}{\partial\mu}\right] \ , \end{aligned} \tag{F.22}$$

which simplifies to:

$$\frac{F_{Lorentz}}{R_\odot\Omega_{eq}^2} = \Lambda\frac{1}{x\sqrt{1-\mu^2}}\left[\hat{B}\frac{\partial\hat{S}}{\partial x} - \frac{1}{x}\hat{b}\frac{\partial\hat{S}}{\partial\mu}\right] \ . \tag{F.23}$$

[1]Note that we assume $\rho_0 = 1$ to simplify Λ.

Then, the required Chebyshev transformations of $\hat{B}$, $\hat{b}$, as well as $\hat{S}$ and its derivatives, are:

$$\begin{aligned}
\hat{B}(x,\mu) &= \sum_{n=1}^{N} B_n(x) T_{2n-1}(\mu) \\
&= \sum_{m=0}^{N-1} B_m(x) T_{2m+1}(\mu) \qquad \text{(F.24)} \\
\hat{b}(x,\mu) &= (1-\mu^2) \sum_{n=1}^{N} b_n(x) T_{2n-2}(\mu) \\
&= (1-\mu^2) \sum_{m=0}^{N-1} b_m(x) T_{2m}(\mu) \qquad \text{(F.25)} \\
\hat{S}(x,\mu) &= (1-\mu^2) \sum_{n=1}^{N} S_n(x) T_{2n-1}(\mu) \\
&= (1-\mu^2) \sum_{m=0}^{N-1} S_m(x) T_{2m+1}(\mu) \qquad \text{(F.26)} \\
\frac{\partial \hat{S}(x,\mu)}{\partial x} &= (1-\mu^2) \sum_{n=1}^{N} dS_n(x) T_{2n-1}(\mu) \\
&= (1-\mu^2) \sum_{m=0}^{N-1} dS_m(x) T_{2m+1}(\mu) \qquad \text{(F.27)} \\
\frac{\partial \hat{S}(x,\mu)}{\partial \mu} &= \sum_{n=1}^{N} S_n(x) \frac{\partial}{\partial \mu} [(1-\mu^2) T_{2n-1}(\mu)] \\
&= \sum_{n=1}^{N} S_n(x) \left[\frac{2n-3}{2} T_{2n-2}(\mu) - \frac{2n+1}{2} T_{2n}(\mu) \right] \\
&= \sum_{m=0}^{N-1} S_m(x) \left[\frac{2m-1}{2} T_{2m}(\mu) - \frac{2m+3}{2} T_{2m+2}(\mu) \right] , \qquad \text{(F.28)}
\end{aligned}$$

which we will use to obtain $F_{Lorentz}$ from $B_m(x)$, $b_m(x)$, $S_m(x)$, and $dS_m(x)$.

F.1.4 Gyroscopic Pumping term

We write the term that drives meridional flows in the convection zone as:

$$\begin{aligned}
F_{Gyropump} &= -\frac{\rho}{\tau} [u_\phi - u_{CZ}] \\
&= -\frac{\rho R_\odot^2 \Omega_{eq}}{\tau} \frac{1}{r \sin\theta} [\hat{L} - \hat{L}_{CZ}] , \qquad \text{(F.29)}
\end{aligned}$$

which reduces to:

$$\frac{F_{Gyropump}}{R_\odot \Omega_{eq}^2} = -\frac{\rho}{\hat{\tau}} \frac{1}{x\sqrt{1-\mu^2}} [\hat{L} - x^2(1-\mu^2)\hat{\Omega}_{CZ}] \ . \tag{F.30}$$

Then, we will use the $L_m(x)$ modes, along with a and b, to find $F_{Gyropump}$.

F.1.5 Viscous stresses

To compute the viscous stresses on the azimuthal direction, we start from:

$$(\nabla \cdot \mathbf{\Pi})_\phi = \frac{\partial \Pi_{r\phi}}{\partial r} + \frac{1}{r}\frac{\partial \Pi_{\theta\phi}}{\partial \theta} + \frac{3}{r}\Pi_{r\phi} + 2\frac{\cos\theta}{r\sin\theta}\Pi_{\theta\phi} \ , \tag{F.31}$$

where:

$$\begin{aligned} \Pi_{r\phi} &= \rho\nu \left(\frac{\partial u_\phi}{\partial r} - \frac{1}{r}u_\phi \right) \\ \Pi_{\theta\phi} &= \rho\nu \left(\frac{1}{r}\frac{\partial u_\phi}{\partial \theta} - \frac{\cos\theta}{r\sin\theta}u_\phi \right) \ . \end{aligned} \tag{F.32}$$

Hence,

$$\begin{aligned} F_{Viscous} &= \rho\nu \left[\frac{\partial^2 u_\phi}{\partial r^2} - \frac{1}{r^2}\left(r\frac{\partial u_\phi}{\partial r} - u_\phi \right) \right. \\ &\quad + \frac{1}{r}\left\{ \frac{1}{r}\frac{\partial^2 u_\phi}{\partial \theta^2} - \frac{1}{r\sin^2\theta}\left(\sin\theta \frac{\partial}{\partial\theta}[u_\phi \cos\theta] - u_\phi \cos^2\theta \right) \right\} \\ &\quad + \frac{3}{r}\left(\frac{\partial u_\phi}{\partial r} - \frac{1}{r}u_\phi \right) \\ &\quad \left. + 2\frac{\cos\theta}{r\sin\theta}\left(\frac{1}{r}\frac{\partial u_\phi}{\partial\theta} - \frac{\cos\theta}{r\sin\theta}u_\phi \right) \right] \\ &\quad + \frac{\partial(\rho\nu)}{\partial r}\left[\frac{\partial u_\phi}{\partial r} - \frac{1}{r}u_\phi \right] \ , \end{aligned} \tag{F.33}$$

which reduces to:

$$\begin{aligned} F_{Viscous} &= \rho\nu \left[\frac{\partial^2 u_\phi}{\partial r^2} + \frac{2}{r}\frac{\partial u_\phi}{\partial r} - \frac{2}{r^2}u_\phi \right. \\ &\quad + \frac{1}{r^2}\frac{\partial^2 u_\phi}{\partial\theta^2} - \frac{1}{r^2}\left(-u_\phi + \frac{\cos\theta}{\sin\theta}\frac{\partial u_\phi}{\partial\theta} \right) \\ &\quad \left. + \frac{2\cos\theta}{r^2\sin\theta}\frac{\partial u_\phi}{\partial\theta} - \frac{\cos^2\theta}{r^2\sin^2\theta}u_\phi \right] \\ &\quad + \frac{\partial(\rho\nu)}{\partial r}\left[\frac{\partial u_\phi}{\partial r} - \frac{1}{r}u_\phi \right] \ , \end{aligned} \tag{F.34}$$

which simplifies to:

$$\begin{aligned} F_{Viscous} &= \rho\nu \left[\frac{\partial^2 u_\phi}{\partial r^2} + \frac{1}{r^2}\frac{\partial^2 u_\phi}{\partial \theta^2} + \frac{2}{r}\frac{\partial u_\phi}{\partial r} - \frac{1}{r^2}u_\phi \right. \\ &\quad \left. + \frac{\cos\theta}{r^2\sin\theta}\frac{\partial u_\phi}{\partial \theta} - \frac{\cos^2\theta}{r^2\sin^2\theta}u_\phi \right] + \frac{\partial(\rho\nu)}{\partial r}\left[\frac{\partial u_\phi}{\partial r} - \frac{1}{r}u_\phi\right] . \end{aligned} \tag{F.35}$$

By replacing u_ϕ by its corresponding non-dimensional expression, we find:

$$\begin{aligned} \frac{\partial u_\phi}{\partial r} &= \frac{R_\odot^2\Omega_{eq}}{r\sin\theta}\left[\frac{\partial \hat{L}}{\partial r} - \frac{1}{r}\hat{L}\right] \\ \frac{\partial^2 u_\phi}{\partial r^2} &= \frac{R_\odot^2\Omega_{eq}}{r\sin\theta}\left[\frac{\partial^2 \hat{L}}{\partial r^2} - \frac{2}{r}\frac{\partial \hat{L}}{\partial r} + \frac{2}{r^2}\hat{L}\right] \\ \frac{\partial u_\phi}{\partial \theta} &= \frac{R_\odot^2\Omega_{eq}}{r\sin\theta}\left[-\sin\theta\frac{\partial \hat{L}}{\partial\cos\theta} - \frac{\cos\theta}{\sin\theta}\hat{L}\right] \\ \frac{\partial^2 u_\phi}{\partial \theta^2} &= \frac{R_\odot^2\Omega_{eq}}{r\sin\theta}\left[-\sin\theta\frac{\partial}{\partial\theta}\left(\frac{\partial \hat{L}}{\partial\cos\theta}\right) + \cos\theta\frac{\partial \hat{L}}{\partial\cos\theta} + \frac{2\cos^2\theta}{\sin^2\theta}\hat{L} + \hat{L}\right] , \end{aligned} \tag{F.36}$$

which we then incorporate into our last expression for the viscous stresses:

$$\begin{aligned} F_{Viscous} &= \rho\nu\frac{R_\odot^2\Omega_{eq}}{r\sin\theta}\left[\frac{\partial^2 \hat{L}}{\partial r^2} - \frac{2}{r}\frac{\partial \hat{L}}{\partial r} + \frac{2}{r^2}\hat{L}\right. \\ &\quad -\frac{\sin\theta}{r^2}\frac{\partial}{\partial\theta}\left(\frac{\partial \hat{L}}{\partial\cos\theta}\right) + \frac{\cos\theta}{r^2}\frac{\partial \hat{L}}{\partial\cos\theta} + \frac{2\cos^2\theta}{r^2\sin^2\theta}\hat{L} + \frac{1}{r^2}\hat{L} \\ &\quad +\frac{2}{r}\frac{\partial \hat{L}}{\partial r} - \frac{2}{r^2}\hat{L} \\ &\quad -\frac{1}{r^2}\hat{L} \\ &\quad +\frac{\cos\theta}{r^2\sin\theta}\left(-\sin\theta\frac{\partial \hat{L}}{\partial\cos\theta} - \frac{\cos\theta}{\sin\theta}\hat{L}\right) \\ &\quad \left. -\frac{\cos^2\theta}{r^2\sin^2\theta}\hat{L}\right] \\ &\quad +\frac{R_\odot^2\Omega_{eq}}{r\sin\theta}\frac{\partial(\rho\nu)}{\partial r}\left[\frac{\partial \hat{L}}{\partial r} - \frac{1}{r}\hat{L} - \frac{1}{r}\hat{L}\right] , \end{aligned} \tag{F.37}$$

which we furtherly simplify to:

$$\begin{aligned} F_{Viscous} &= \rho\nu\frac{R_\odot^2\Omega_{eq}}{r\sin\theta}\left[\frac{\partial^2 \hat{L}}{\partial r^2} - \frac{\sin\theta}{r^2}\frac{\partial}{\partial\theta}\left(\frac{\partial \hat{L}}{\partial\cos\theta}\right)\right] \\ &\quad +\frac{R_\odot^2\Omega_{eq}}{r\sin\theta}\frac{\partial(\rho\nu)}{\partial r}\left[\frac{\partial \hat{L}}{\partial r} - \frac{2}{r}\hat{L}\right] . \end{aligned} \tag{F.38}$$

Then, a change of variables yields:

$$\begin{aligned} F_{Viscous} &= \rho\nu \frac{\Omega_{eq}}{R_\odot x\sqrt{1-\mu^2}} \left[\frac{\partial^2 \hat{L}}{\partial x^2} + \frac{1-\mu^2}{x^2}\frac{\partial^2 \hat{L}}{\partial \mu^2}\right] \\ &\quad + \frac{\Omega_{eq}}{R_\odot x\sqrt{1-\mu^2}} \frac{\partial(\rho\nu)}{\partial x}\left[\frac{\partial \hat{L}}{\partial x} - \frac{2}{x}\hat{L}\right] , \end{aligned} \tag{F.39}$$

which yields:

$$\begin{aligned} \frac{F_{Viscous}}{R_\odot \Omega_{eq}^2} &= \frac{\rho E_\nu}{x\sqrt{1-\mu^2}} \left[\frac{\partial^2 \hat{L}}{\partial x^2} + \frac{1-\mu^2}{x^2}\frac{\partial^2 \hat{L}}{\partial \mu^2}\right] \\ &\quad + \frac{1}{x\sqrt{1-\mu^2}} \frac{\partial(\rho E_\nu)}{\partial x}\left[\frac{\partial \hat{L}}{\partial x} - \frac{2}{x}\hat{L}\right] , \end{aligned} \tag{F.40}$$

where $E_\nu = \nu/R_\odot^2\Omega_{eq}$. We include the derivation of the second derivatives of u_ϕ with respect to θ and with respect to μ in Appendix C.

Alternatively, we can derive $F_{Viscous}$ by performing the change of variables in earlier steps than in the previous derivation. Let us start by rewriting the components of the stress

tensor in terms of the non-dimensional variable $\hat{L}$ and the coordinates x and μ, as follows:

$$u_\phi(r,\theta) = R_\odot^2 \Omega_{eq} \frac{\hat{L}}{r\sin\theta} \tag{F.41}$$

$$u_\phi(x,\mu) = R_\odot \Omega_{eq} \frac{1}{x\sqrt{1-\mu^2}} \hat{L} \tag{F.42}$$

$$\frac{u_\phi(x,\mu)}{x} = \Omega_{eq} \frac{1}{x^2\sqrt{1-\mu^2}} \hat{L} \tag{F.43}$$

$$\frac{\partial u_\phi(r,\theta)}{\partial r} = \frac{R_\odot^2 \Omega_{eq}}{r\sin\theta} \left(\frac{\partial \hat{L}}{\partial r} - \frac{1}{r}\hat{L} \right) \tag{F.44}$$

$$\frac{\partial u_\phi(x,\mu)}{\partial x} = \frac{\Omega_{eq}}{x\sqrt{1-\mu^2}} \left(\frac{\partial \hat{L}}{\partial x} - \frac{1}{x}\hat{L} \right) \tag{F.45}$$

$$\frac{\partial u_\phi(r,\theta)}{\partial \theta} = \frac{R_\odot^2 \Omega_{eq}}{r\sin\theta} \left(\frac{\partial \hat{L}}{\partial \theta} - \frac{\cos\theta}{\sin\theta}\hat{L} \right) \tag{F.46}$$

$$-\sqrt{1-\mu^2}\frac{\partial u_\phi(x,\mu)}{\partial \mu} = -\frac{R_\odot \Omega_{eq}}{x} \left(\frac{\partial \hat{L}}{\partial \mu} + \frac{\mu}{1-\mu^2}\hat{L} \right) \tag{F.47}$$

$$\Pi_{r\phi}(r,\theta) = \rho\nu \left[\frac{\partial u_\phi(r,\theta)}{\partial r} - \frac{1}{r} u_\phi(r,\theta) \right] \tag{F.48}$$

$$\Pi_{x\phi}(x,\mu) = \rho\nu\Omega_{eq} \frac{1}{x\sqrt{1-\mu^2}} \left[\frac{\partial \hat{L}}{\partial x} - \frac{2}{x}\hat{L} \right] \tag{F.49}$$

$$\Pi_{\theta\phi}(r,\theta) = \rho\nu \left[\frac{1}{r}\frac{\partial u_\phi(r,\theta)}{\partial \theta} - \frac{\cos\theta}{r\sin\theta} u_\phi(r,\theta) \right] \tag{F.50}$$

$$\Pi_{\mu\phi}(x,\mu) = -\rho\nu\Omega_{eq} \left[\frac{1}{x^2}\frac{\partial \hat{L}}{\partial \mu} + \frac{2\mu}{x^2(1-\mu^2)}\hat{L} \right] . \tag{F.51}$$

Now, we can express the ϕ-component of the viscous stress tensor in terms of $\hat{L}$, x, and μ:

$$
\begin{aligned}
(\nabla\cdot\mathbf{\Pi})_\phi(r,\theta) &= \frac{\partial\Pi_{r\phi}}{\partial r}+\frac{1}{r}\frac{\partial\Pi_{\theta\phi}}{\partial\theta}+\frac{3}{r}\Pi_{r\phi}+\frac{2\cos\theta}{r\sin\theta}\Pi_{\theta\phi} && \text{(F.52)}\\
R_\odot(\nabla\cdot\mathbf{\Pi})_\phi(x,\mu) &= \frac{\partial\Pi_{x\phi}}{\partial x}-\frac{\sqrt{1-\mu^2}}{x}\frac{\partial\Pi_{\mu\phi}}{\partial\mu}+\frac{3}{x}\Pi_{x\phi}+\frac{2\mu}{x\sqrt{1-\mu^2}}\Pi_{\mu\phi} && \text{(F.53)}\\
&= \rho\nu\Omega_{eq}\frac{1}{\sqrt{1-\mu^2}}\left(\frac{1}{x}\frac{\partial^2\hat{L}}{\partial x^2}-\frac{2}{x^2}\frac{\partial\hat{L}}{\partial x}+\frac{2}{x^3}\hat{L}-\frac{1}{x^2}\frac{\partial\hat{L}}{\partial x}+\frac{2}{x^3}\hat{L}\right)\\
&\quad+\rho\nu\Omega_{eq}\frac{\sqrt{1-\mu^2}}{x^3}\left(\frac{\partial^2\hat{L}}{\partial\mu^2}+\frac{2\mu}{1-\mu^2}\frac{\partial\hat{L}}{\partial\mu}+\hat{L}\frac{\partial}{\partial\mu}\left[\frac{2\mu}{1-\mu^2}\right]\right)\\
&\quad+\rho\nu\Omega_{eq}\frac{3}{x^2\sqrt{1-\mu^2}}\left(\frac{\partial\hat{L}}{\partial x}-\frac{2}{x}\hat{L}\right)\\
&\quad-\rho\nu\Omega_{eq}\frac{2\mu}{x^3\sqrt{1-\mu^2}}\left(\frac{\partial\hat{L}}{\partial\mu}+\frac{2\mu}{1-\mu^2}\hat{L}\right)\\
&\quad+\Omega_{eq}\frac{1}{x\sqrt{1-\mu^2}}\frac{\partial(\rho\nu)}{\partial x}\left(\frac{\partial\hat{L}}{\partial x}-\frac{2}{x}\hat{L}\right)\ , && \text{(F.54)}
\end{aligned}
$$

which reduces to:

$$
\begin{aligned}
R_\odot(\nabla\cdot\mathbf{\Pi})_\phi(x,\mu) &= \rho\nu\Omega_{eq}\frac{1}{x\sqrt{1-\mu^2}}\left[\frac{\partial^2\hat{L}}{\partial x^2}-\frac{2}{x^2}\hat{L}+\frac{(1-\mu^2)}{x^2}\frac{\partial^2\hat{L}}{\partial\mu^2}\right.\\
&\quad\left.+\frac{(1-\mu^2)}{x^2}\hat{L}\frac{\partial}{\partial\mu}\left(\frac{2\mu}{1-\mu^2}\right)-\frac{4\mu^2}{x^2(1-\mu^2)}\hat{L}\right]\\
&\quad+\Omega_{eq}\frac{1}{x\sqrt{1-\mu^2}}\frac{\partial(\rho\nu)}{\partial x}\left[\frac{\partial\hat{L}}{\partial x}-\frac{2}{x}\hat{L}\right] && \text{(F.55)}\\
R_\odot(\nabla\cdot\mathbf{\Pi})_\phi(x,\mu) &= \rho\nu\Omega_{eq}\frac{1}{\sqrt{1-\mu^2}}\left[\frac{\partial^2\hat{L}}{\partial x^2}+\frac{(1-\mu^2)}{x^2}\frac{\partial^2\hat{L}}{\partial\mu^2}-\frac{2}{x^2}\hat{L}+\frac{2}{x^2}\hat{L}\right.\\
&\quad\left.+\frac{(1-\mu^2)}{x^2}(2\mu)\frac{(2\mu)}{(1-\mu^2)}\hat{L}-\frac{4\mu^2}{x^2(1-\mu^2)}\hat{L}\right]\\
&\quad+\Omega_{eq}\frac{1}{x\sqrt{1-\mu^2}}\frac{\partial(\rho\nu)}{\partial x}\left[\frac{\partial\hat{L}}{\partial x}-\frac{2}{x}\hat{L}\right]\ , && \text{(F.56)}
\end{aligned}
$$

to finally yield:

$$
\begin{aligned}
\frac{(\nabla\cdot\mathbf{\Pi})_\phi}{R_\odot\Omega_{eq}^2} &= \frac{\rho E_\nu}{x\sqrt{1-\mu^2}}\left[\frac{\partial^2\hat{L}}{\partial x^2}+\frac{(1-\mu^2)}{x^2}\frac{\partial^2\hat{L}}{\partial\mu^2}\right]\\
&\quad+\frac{1}{x\sqrt{1-\mu^2}}\frac{\partial(\rho E_\nu)}{\partial x}\left[\frac{\partial\hat{L}}{\partial x}-\frac{2}{x}\hat{L}\right]\ . && \text{(F.57)}
\end{aligned}
$$

Then, the viscous stresses in the azimuthal direction are computed from $L_m(x)$ and its derivatives with respect to x and with respect to μ. The second derivatives are obtained with the following relationships:

$$\begin{aligned}
\frac{\partial^2 \hat{L}(x,\mu)}{\partial x^2} &= (1-\mu^2)\sum_{n=1}^{N}\left(\frac{dL_n[i+1]-dL_n[i]}{x[i+1]-x[i]}\right)T_{2n-2}(\mu) \\
&= (1-\mu^2)\sum_{m=0}^{N-1}\left(\frac{dL_m[i+1]-dL_m[i]}{x[i+1]-x[i]}\right)T_{2m}(\mu) \\
\frac{\partial^2 \hat{L}(x,\mu)}{\partial \mu^2} &= \sum_{n=1}^{N} L_n(x)\left[(1-\mu^2)\frac{\partial^2 T_{2n-2}(\mu)}{\partial \mu^2} - 4\mu\frac{\partial T_{2n-2}(\mu)}{\partial \mu} - 2T_{2n-2}(\mu)\right] \\
&= \sum_{m=0}^{N-1} L_m(x)\left[(1-\mu^2)\frac{\partial^2 T_{2m}(\mu)}{\partial \mu^2} - 4\mu\frac{\partial T_{2m}(\mu)}{\partial \mu} - 2T_{2m}(\mu)\right] \qquad \text{(F.58)}
\end{aligned}$$

along with the identities for Chebyshev polynomials included in Appendix C.

F.2 Balances from the vorticity equation

The vorticity equation is obtained by taking the curl of the momentum equation

$$\rho\frac{\partial \mathbf{u}}{\partial t} = -\rho\mathbf{u}\cdot\nabla\mathbf{u} - 2\mathbf{\Omega}_\odot\times\mathbf{u} - \nabla p - \rho\mathbf{g} + \mathbf{j}\times\mathbf{B} + \nabla\cdot\mathbf{\Pi}\ . \qquad \text{(F.59)}$$

The vorticity and the momentum equations are perturbed with respect to a background in hydrostatic equilibrium, and numerically solved within a spherical framework rotating with angular velocity Ω_0. We assume a system in steady state with axial symmetry, and with meridional flows generated in the convection zone by a force, $(\mathbf{u}-\mathbf{u}_C Z)/\tau$, driven by the differential rotation estimated from helioseismic observations.

We now derive the ϕ- component of the vorticity equation by taking the curl of each term of the momentum equation, $\nabla\times F$, which we later express in terms of Chebyshev polynomials to verify force and torque balances.

F.2.1 Coriolis term

We define the components of the velocity field in terms of non-dimensional variables by using:

$$u_r = R_\odot \Omega_{eq} \hat{u} \tag{F.60}$$

$$u_\theta = \frac{R_\odot \Omega_{eq}}{\sin\theta} \hat{v} \tag{F.61}$$

$$u_\phi = R_\odot^2 \Omega_{eq} \frac{\hat{L}}{r \sin\theta} \ . \tag{F.62}$$

Then, the ϕ-component of the Coriolis torque (divided by $\bar{\rho}$), can be expressed as:

$$\begin{aligned} \nabla \times F_{Coriolis} &= \frac{2\Omega_\odot}{R_\odot} \left[\mu \frac{\partial u_\phi}{\partial x} + \frac{(1-\mu^2)}{x} \frac{\partial u_\phi}{\partial \mu} \right] \\ &= \frac{2\Omega_\odot \Omega_{eq}}{x\sqrt{1-\mu^2}} \left[\mu \frac{\partial \hat{L}}{\partial x} + \frac{(1-\mu^2)}{x} \frac{\partial \hat{L}}{\partial \mu} \right] \ , \end{aligned} \tag{F.63}$$

where $\mu = \cos\theta$ and $x = r/R_\odot$. Since $\Omega_0 = 1 - \Omega_\odot/\Omega_{eq}$ (see the Appendix in Note_003),

$$\frac{\nabla \times F_{Coriolis}}{\Omega_{eq}^2} = \frac{2(1-\Omega_0)}{x\sqrt{1-\mu^2}} \left[\mu \frac{\partial \hat{L}}{\partial x} + \frac{(1-\mu^2)}{x} \frac{\partial \hat{L}}{\partial \mu} \right] \ . \tag{F.64}$$

We need $\hat{L}$ and its derivatives with respect to x and with respect to μ to be expressed in terms of Chebyshev polynomials:

$$\begin{aligned}
\hat{L}(x,\mu) &= (1-\mu^2)\sum_{n=1}^{N} L_n(x)T_{2n-2}(\mu) \\
&= (1-\mu^2)\sum_{m=0}^{N-1} L_m(x)T_{2m}(\mu) \qquad \text{(F.65)} \\
\frac{\partial\hat{L}(x,\mu)}{\partial x} &= (1-\mu^2)\sum_{n=1}^{N} dL_n(x)T_{2n-2}(\mu) \\
&= (1-\mu^2)\sum_{m=0}^{N-1} dL_m(x)T_{2m}(\mu) \qquad \text{(F.66)} \\
\frac{\partial\hat{L}(x,\mu)}{\partial \mu} &= \sum_{n=1}^{N} L_n(x)\frac{\partial}{\partial\mu}[(1-\mu^2)T_{2n-2}(\mu)] \\
&= \sum_{n=1}^{N} L_n(x)[(n-2)T_{|2n-3|}(\mu) - nT_{2n-1}(\mu)] \\
&= \sum_{m=0}^{N-1} L_m(x)[(m-1)T_{|2m-1|}(\mu) - (m+1)T_{2m+1}(\mu)]\ . \qquad \text{(F.67)}
\end{aligned}$$

This way, we will compute $\nabla\times F_{Coriolis}$ from $L_m(x)$ and $dL_m(x)$.

F.2.2 Advection term

We write the ϕ-component of the advection term (divided by $\hat{\rho}$) in the vorticity equation as:

$$\begin{aligned}
\nabla\times F_{Advection} &= \frac{2}{R_\odot^2}\left[\frac{\mu}{x\sqrt{1-\mu^2}}u_\phi\frac{\partial u_\phi}{\partial x} + \frac{\sqrt{1-\mu^2}}{x^2}u_\phi\frac{\partial u_\phi}{\partial\mu}\right] \\
&= \frac{2\Omega_{eq}^2}{x\sqrt{1-\mu^2}}\left[\frac{\mu}{x^2(1-\mu^2)}\hat{L}\frac{\partial\hat{L}}{\partial x} + \frac{1}{x^3}\hat{L}\frac{\partial\hat{L}}{\partial\mu}\right]\ , \qquad \text{(F.68)}
\end{aligned}$$

which simplifies to:

$$\frac{\nabla\times F_{Advection}}{\Omega_{eq}^2} = \frac{2}{x\sqrt{1-\mu^2}}\left[\frac{\mu}{x^2(1-\mu^2)}\hat{L}\frac{\partial\hat{L}}{\partial x} + \frac{1}{x^3}\hat{L}\frac{\partial\hat{L}}{\partial\mu}\right]\ . \qquad \text{(F.69)}$$

We compute $\nabla\times F_{Advection}$ from modes $L_m(x)$ and $dL_m(x)$.

F.2.3 Thermal Wind, Stratification, and Baroclinicity terms

Taking the curl of the gradient pressure divided by density as well as the curl of the gravity forces divided by density yields the following expression:

$$\begin{aligned}
\nabla \times F_{thermalstrat} &= -\frac{1}{R_\odot^2}\frac{\sqrt{1-\mu^2}}{x}\frac{\bar{p}}{\bar{\rho}^2}\frac{\partial\bar{\rho}}{\partial x}\left[\frac{1}{\bar{T}}\frac{\partial T}{\partial\mu}+\frac{1}{\bar{\rho}}\frac{\partial\tilde{\rho}}{\partial\mu}\right] \\
&\quad -\frac{1}{R_\odot}\frac{\sqrt{1-\mu^2}}{x}\frac{\bar{g}}{\bar{\rho}}\frac{\partial\tilde{\rho}}{\partial x} \\
&= -\frac{1}{R_\odot^2 x\sqrt{1-\mu^2}}\left[(1-\mu^2)\frac{\bar{p}}{\bar{\rho}^2}\frac{\partial\bar{\rho}}{\partial x}\left(\frac{1}{\bar{T}}\frac{\partial T}{\partial\mu}+\frac{1}{\bar{\rho}}\frac{\partial\tilde{\rho}}{\partial\mu}\right)\right] \\
&\quad -\frac{1}{R_\odot x\sqrt{1-\mu^2}}\left[(1-\mu^2)\frac{\bar{g}}{\bar{\rho}}\frac{\partial\tilde{\rho}}{\partial x}\right] \ , \qquad \text{(F.70)}
\end{aligned}$$

where the quantities with bars correspond to the background state, whereas the quantities with tilde or without marks correspond to the perturbed thermodynamical variables. We obtain then the non-dimensional expression:

$$\begin{aligned}
\frac{\nabla \times F_{thermalstrat}}{\Omega_{eq}^2} &= -\frac{1}{R_\odot^2\Omega_{eq}^2 x\sqrt{1-\mu^2}}\left[(1-\mu^2)\frac{\bar{p}}{\bar{\rho}^2}\frac{\partial\bar{\rho}}{\partial x}\left(\frac{1}{\bar{T}}\frac{\partial T}{\partial\mu}+\frac{1}{\bar{\rho}}\frac{\partial\tilde{\rho}}{\partial\mu}\right)\right] \\
&\quad -\frac{1}{R_\odot\Omega_{eq}^2 x\sqrt{1-\mu^2}}\left[(1-\mu^2)\frac{\bar{g}}{\bar{\rho}}\frac{\partial\tilde{\rho}}{\partial x}\right] \ , \qquad \text{(F.71)}
\end{aligned}$$

F.2.4 Lorentz term

We non-dimensionalize the Lorentz torque expression by using[2]:

$$\begin{aligned}
B_r &= B_0\hat{B} \\
B_\theta &= \frac{B_0}{\sin\theta}\hat{b} \\
B_\phi &= \frac{B_0 R_\odot}{r\sin\theta}\hat{S} \\
j_\phi &= \frac{B_0}{4\pi R_\odot}\frac{\hat{J}}{x\sqrt{1-\mu^2}} \\
\Lambda &= \frac{B_0^2}{4\pi\rho_0 R_\odot\Omega_{eq}^2} \ , \qquad \text{(F.72)}
\end{aligned}$$

[2]Note that we assume $\rho_0 = 1$ to simplify Λ.

so that taking the curl of the Lorentz force divided by $\bar{\rho}$ results in:

$$\begin{aligned}
\nabla \times F_{Lorentz} &= \frac{1}{R_\odot \bar{\rho}} \left[j_\phi \frac{\partial B_r}{\partial x} + B_r \frac{\partial j_\phi}{\partial x} - j_r \frac{\partial B_\phi}{\partial x} - B_\phi \frac{\partial j_r}{\partial x} \right] \\
&\quad + \frac{1}{R_\odot} \left(\frac{1}{x\bar{\rho}} - \frac{1}{\bar{\rho}^2} \frac{\partial \bar{\rho}}{\partial x} \right) [j_\phi B_r - j_r B_\phi] \\
&\quad + \frac{1}{R_\odot \bar{\rho}} \frac{\sqrt{1-\mu^2}}{x} \left[j_\theta \frac{\partial B_\phi}{\partial \mu} + B_\phi \frac{\partial j_\theta}{\partial \mu} - j_\phi \frac{\partial B_\theta}{\partial \mu} - B_\theta \frac{\partial j_\phi}{\partial \mu} \right] \\
&= \frac{B_0^2}{4\pi R_\odot^2} \frac{1}{x\sqrt{1-\mu^2}} \left\{ \frac{1}{\bar{\rho}} \left[\hat{J} \frac{\partial \hat{B}}{\partial x} + \hat{B} \frac{\partial \hat{J}}{\partial x} \right. \right. \\
&\quad - \frac{1}{x} \hat{J} \frac{\partial \hat{b}}{\partial \mu} - \frac{2\mu}{x(1-\mu^2)} \hat{J}\hat{b} - \frac{1}{x} \hat{b} \frac{\partial \hat{J}}{\partial \mu} \\
&\quad \left. \left. - \frac{2\mu}{x^2(1-\mu^2)} \hat{S} \frac{\partial \hat{S}}{\partial x} - \frac{2}{x^3} \hat{S} \frac{\partial \hat{S}}{\partial \mu} \right] - \frac{1}{\bar{\rho}^2} \frac{\partial \bar{\rho}}{\partial x} \left[\hat{J}\hat{B} + \frac{1}{x^2} \hat{S} \frac{\partial \hat{S}}{\partial \mu} \right] \right\} ,
\end{aligned} \tag{F.73}$$

which, by virtue of

$$\nabla \cdot \mathbf{B} = \frac{\partial \hat{B}}{\partial x} + \frac{2}{x} \hat{B} - \frac{1}{x} \frac{\partial \hat{b}}{\partial \mu} = 0 \tag{F.74}$$

simplifies to:

$$\begin{aligned}
\nabla \times \frac{F_{Lorentz}}{\Omega_{eq}^2} &= \frac{\Lambda}{x\sqrt{1-\mu^2}} \left\{ \frac{1}{\bar{\rho}} \left[\hat{B} \frac{\partial \hat{J}}{\partial x} - \frac{2}{x} \hat{J}\hat{B} - \frac{2\mu}{x(1-\mu^2)} \hat{J}\hat{b} - \frac{1}{x} \hat{b} \frac{\partial \hat{J}}{\partial \mu} \right. \right. \\
&\quad \left. \left. - \frac{2\mu}{x^2(1-\mu^2)} \hat{S} \frac{\partial \hat{S}}{\partial x} - \frac{2}{x^3} \hat{S} \frac{\partial \hat{S}}{\partial \mu} \right] - \frac{1}{\bar{\rho}^2} \frac{\partial \bar{\rho}}{\partial x} \left[\hat{J}\hat{B} + \frac{1}{x^2} \hat{S} \frac{\partial \hat{S}}{\partial \mu} \right] \right\} ,
\end{aligned} \tag{F.75}$$

Then, the required Chebyshev transformations of $\hat{B}$, $\hat{b}$, as well as $\hat{S}$, $\hat{J}$ and their

derivatives, are:

$$\begin{aligned}
\hat{B}(x,\mu) &= \sum_{n=1}^{N} B_n(x) T_{2n-1}(\mu) \\
&= \sum_{m=0}^{N-1} B_m(x) T_{2m+1}(\mu) \qquad \text{(F.76)} \\
\hat{b}(x,\mu) &= (1-\mu^2) \sum_{n=1}^{N} b_n(x) T_{2n-2}(\mu) \\
&= (1-\mu^2) \sum_{m=0}^{N-1} b_m(x) T_{2m}(\mu) \qquad \text{(F.77)} \\
\hat{S}(x,\mu) &= (1-\mu^2) \sum_{n=1}^{N} S_n(x) T_{2n-1}(\mu) \\
&= (1-\mu^2) \sum_{m=0}^{N-1} S_m(x) T_{2m+1}(\mu) \qquad \text{(F.78)} \\
\frac{\partial \hat{S}(x,\mu)}{\partial x} &= (1-\mu^2) \sum_{n=1}^{N} dS_n(x) T_{2n-1}(\mu) \\
&= (1-\mu^2) \sum_{m=0}^{N-1} dS_m(x) T_{2m+1}(\mu) \qquad \text{(F.79)} \\
\frac{\partial \hat{S}(x,\mu)}{\partial \mu} &= \sum_{n=1}^{N} S_n(x) \frac{\partial}{\partial \mu} [(1-\mu^2) T_{2n-1}(\mu)] \\
&= \sum_{n=1}^{N} S_n(x) \left[\frac{2n-3}{2} T_{2n-2}(\mu) - \frac{2n+1}{2} T_{2n}(\mu) \right] \\
&= \sum_{m=0}^{N-1} S_m(x) \left[\frac{2m-1}{2} T_{2m}(\mu) - \frac{2m+3}{2} T_{2m+2}(\mu) \right] , \qquad \text{(F.80)}
\end{aligned}$$

which we will use to obtain $\nabla \times F_{Lorentz}$ from $B_m(x)$, $b_m(x)$, $J_m(x)$, $S_m(x)$, and $dS_m(x)$.

F.2.5 Gyroscopic Pumping term

We write the term that drives zonal vorticity in the convection zone as:

$$\begin{aligned}
\nabla \times F_{Gyropump} &= -\frac{\Omega_{eq}}{R_\odot x \tau} \left[\sqrt{1-\mu^2} \frac{\partial u_r}{\partial \mu} + x \frac{\partial u_\theta}{\partial x} + u_\theta \right] \\
&= -\frac{\Omega_{eq}^2}{\tau x \sqrt{1-\mu^2}} \left[(1-\mu^2) \frac{\partial \hat{u}}{\partial \mu} + x \frac{\partial \hat{v}}{\partial x} + \hat{v} \right] , \qquad \text{(F.81)}
\end{aligned}$$

which reduces to:

$$\frac{\nabla \times F_{Gyropump}}{\Omega_{eq}^2} = -\frac{1}{\tau x\sqrt{1-\mu^2}}\hat{W} \ . \tag{F.82}$$

Here, we use the non-dimensional vorticity, $\hat{W} = (1-\mu^2)\frac{\partial \hat{u}}{\partial \mu} + x\frac{\partial \hat{v}}{\partial x} + \hat{v}$.

Then, we use the following Chebyshev transformations:

$$\begin{aligned}
\hat{u}(x,\mu) &= \sum_{n=1}^{N} \psi_n(x)\frac{\partial}{\partial \mu}[(1-\mu^2)T_{2n-1}(\mu)] \\
&= \sum_{n=1}^{N} \psi_n(x)\left[\frac{2n-3}{2}T_{2n-2}(\mu) - \frac{2n+1}{2}T_{2n}(\mu)\right] \\
&= \sum_{m=0}^{N-1} \psi_m(x)\left[\frac{2m-1}{2}T_{2m}(\mu) - \frac{2m+3}{2}T_{2m+2}(\mu)\right] \qquad \text{(F.83)} \\
\hat{v}(x,\mu) &= (1-\mu^2)\sum_{n=1}^{N} v_n(x)T_{2n-1}(\mu) \\
&= (1-\mu^2)\sum_{m=0}^{N-1} v_m(x)T_{2m+1}(\mu) \qquad \text{(F.84)}
\end{aligned}$$

to compute $\nabla \times F_{Gyropump}$ from the correspondig Chebyshev modes.

F.2.6 Viscous stress term

To compute the viscous torques on the azimuthal direction, we start from:

$$[\nabla \times (\nabla \cdot \mathbf{\Pi})]_\phi = \frac{1}{r}\frac{\partial}{\partial r}\left[r(\nabla \cdot \mathbf{\Pi})_\theta\right] - \frac{1}{r}\frac{\partial}{\partial \theta}\left[(\nabla \cdot \mathbf{\Pi})_r\right] \ , \tag{F.85}$$

which we transform into a non-dimensional expression by using the following relationships:

$$\Pi_{rr} = \bar{\rho}\nu\left[2\frac{\partial u_r}{\partial r} - \frac{2}{3}\nabla\cdot\mathbf{u}\right] \tag{F.86}$$

$$\Pi_{\theta\theta} = \bar{\rho}\nu\left[\frac{2}{r}\frac{\partial u_\theta}{\partial\theta} + \frac{2}{r}u_r - \frac{2}{3}\nabla\cdot\mathbf{u}\right] \tag{F.87}$$

$$\Pi_{\phi\phi} = \bar{\rho}\nu\left[\frac{2}{r}u_r + \frac{2\cos\theta}{r\sin\theta}u_\theta - \frac{2}{3}\nabla\cdot\mathbf{u}\right] \tag{F.88}$$

$$\Pi_{r\theta} = \bar{\rho}\nu\left[\frac{1}{r}\frac{\partial u_r}{\partial\theta} + \frac{\partial u_\theta}{\partial r} - \frac{1}{r}u_\theta\right] \tag{F.89}$$

$$\Pi_{r\phi} = \bar{\rho}\nu\left[\frac{\partial u_\phi}{\partial r} - \frac{1}{r}u_\phi\right] \tag{F.90}$$

$$\Pi_{\theta\phi} = \bar{\rho}\nu\left[\frac{1}{r}\frac{\partial u_\phi}{\partial\theta} - \frac{\cos\theta}{r\sin\theta}u_\phi\right] \tag{F.91}$$

$$\nabla\cdot\mathbf{u} = \Omega_{eq}\left[\frac{\partial\hat{u}}{\partial x} + \frac{2}{x}\hat{u} - \frac{1}{x}\frac{\partial\hat{v}}{\partial\mu}\right] \tag{F.92}$$

$$\nabla\cdot(\bar{\rho}\mathbf{u}) = \frac{\bar{\rho}}{x^2}\left[x^2\frac{\partial\hat{u}}{\partial x} + 2x\hat{u}\right] + \hat{u}\frac{\partial\bar{\rho}}{\partial x} - \frac{\bar{\rho}}{x}\frac{\partial\hat{v}}{\partial\mu} = 0\ . \tag{F.93}$$

Here we have a summary with the main expressions needed to compute the viscous torque, which we provide in the order we derived them:

$$\Pi_{rr} = \frac{\Omega_{eq}\bar{\rho}\nu}{R_\odot}\left[\frac{4}{3}\frac{\partial\hat{u}}{\partial x} - \frac{4}{3}\frac{1}{x}\hat{u} + \frac{2}{3}\frac{1}{x}\frac{\partial\hat{v}}{\partial\mu}\right] \tag{F.94}$$

$$\begin{aligned}\frac{\partial}{\partial x}(x^2\Pi_{rr}) &= \frac{\Omega_{eq}\bar{\rho}\nu}{R_\odot}\left[\frac{2}{3}\frac{\partial\hat{W}}{\partial\mu} + \frac{4}{3}x^2\frac{\partial^2\hat{u}}{\partial x^2}\right.\\ &\quad \left. -\frac{2}{3}(1-\mu^2)\frac{\partial^2\hat{u}}{\partial\mu^2} + \frac{4}{3}x\frac{\partial\hat{u}}{\partial x} + \frac{4}{3}\mu\frac{\partial\hat{u}}{\partial\mu} - \frac{4}{3}\hat{u}\right]\\ &\quad + \frac{1}{R_\odot}\frac{\partial(\bar{\rho}\nu)}{\partial x}\left[\frac{4}{3}x^2\frac{\partial\hat{u}}{\partial x} - \frac{4}{3}x\hat{u} + \frac{2}{3}x\frac{\partial\hat{v}}{\partial\mu}\right]\end{aligned} \tag{F.95}$$

$$\Pi_{r\theta} = \frac{\Omega_{eq}\bar{\rho}\nu}{R_\odot}\left[\frac{1}{x\sqrt{1-\mu^2}}\hat{W} - \frac{2\sqrt{1-\mu^2}}{x}\frac{\partial\hat{u}}{\partial\mu} - \frac{2}{x\sqrt{1-\mu^2}}\hat{v}\right] \tag{F.96}$$

$$\frac{\partial}{\partial\mu}(\sqrt{1-\mu^2}\Pi_{r\theta}) = \frac{\Omega_{eq}\bar{\rho}\nu}{R_\odot}\left[\frac{1}{x}\frac{\partial\hat{W}}{\partial\mu} - \frac{2(1-\mu^2)}{x}\frac{\partial^2\hat{u}}{\partial\mu^2} + \frac{4\mu}{x}\frac{\partial\hat{u}}{\partial\mu} - \frac{2}{x}\frac{\partial\hat{v}}{\partial\mu}\right] \tag{F.97}$$

$$\Pi_{\theta\theta} = \frac{\bar{\rho}\nu}{R_\odot}\left[-\frac{2}{3}\frac{\partial\hat{u}}{\partial x} + \frac{2}{3}\frac{1}{x}\hat{u} - \frac{4}{3}\frac{1}{x}\frac{\partial\hat{v}}{\partial\mu} - \frac{2\mu}{x(1-\mu^2)}\hat{v}\right] \tag{F.98}$$

$$\Pi_{\phi\phi} = \frac{\Omega_{eq}\bar{\rho}\nu}{R_\odot}\left[-\frac{2}{3}\frac{\partial\hat{u}}{\partial x} + \frac{2}{3}\frac{1}{x}\hat{u} + \frac{2}{3}\frac{1}{x}\frac{\partial\hat{v}}{\partial\mu} + \frac{2\mu}{x(1-\mu^2)}\hat{v}\right] \tag{F.99}$$

$$R_\odot(\nabla\cdot\mathbf{\Pi})_r = \frac{1}{x^2}\frac{\partial}{\partial x}(x^2\Pi_{rr}) - \frac{1}{x}\frac{\partial}{\partial\mu}(\sqrt{1-\mu^2}\Pi_{r\theta}) - \frac{1}{x}\Pi_{\theta\theta} - \frac{1}{x}\Pi_{\phi\phi}\ , \tag{F.100}$$

which yields the first two big terms to compute the viscous torque:

$$\begin{aligned}(\nabla\cdot\mathbf{\Pi})_r &= \\ &\quad \frac{\Omega_{eq}\bar{\rho}\nu}{R_\odot^2}\left[-\frac{1}{3}\frac{1}{x^2}\frac{\partial\hat{W}}{\partial\mu} + \frac{4}{3}\frac{\partial^2\hat{u}}{\partial x^2} + \frac{4}{3}\frac{(1-\mu^2)}{x^2}\frac{\partial^2\hat{u}}{\partial\mu^2}\right.\\ &\quad \left. +\frac{8}{3}\frac{1}{x}\frac{\partial\hat{u}}{\partial x} - \frac{8}{3}\frac{\mu}{x^2}\frac{\partial\hat{u}}{\partial\mu} - \frac{8}{3}\frac{1}{x^2}\hat{u} + \frac{8}{3}\frac{1}{x^2}\frac{\partial\hat{v}}{\partial\mu}\right]\\ &\quad + \frac{\Omega_{eq}}{R_\odot^2}\frac{\partial(\bar{\rho}\nu)}{\partial x}\left[\frac{4}{3}\frac{\partial\hat{u}}{\partial x} - \frac{4}{3}\frac{1}{x}\hat{u} + \frac{2}{3}\frac{1}{x}\frac{\partial\hat{v}}{\partial\mu}\right]\end{aligned} \tag{F.101}$$

$$\begin{aligned}\frac{\partial}{\partial\mu}(\nabla\cdot\mathbf{\Pi})_r &= \frac{\Omega_{eq}\bar{\rho}\nu}{R_\odot^2}\left[-\frac{1}{3}\frac{1}{x^2}\frac{\partial^2\hat{W}}{\partial\mu^2} + \frac{4}{3}\frac{\partial^3\hat{u}}{\partial x^2\partial\mu} + \frac{4}{3}\frac{(1-\mu^2)}{x^2}\frac{\partial^3\hat{u}}{\partial\mu^3} - \frac{16}{3}\frac{\mu}{x^2}\frac{\partial^2\hat{u}}{\partial\mu^2}\right.\\ &\quad \left. +\frac{8}{3}\frac{1}{x}\frac{\partial^2\hat{u}}{\partial x\partial\mu} - \frac{16}{3}\frac{1}{x^2}\frac{\partial\hat{u}}{\partial\mu} + \frac{8}{3}\frac{1}{x^2}\frac{\partial^2\hat{v}}{\partial\mu^2}\right]\\ &\quad + \frac{\Omega_{eq}}{R_\odot^2}\frac{\partial(\bar{\rho}\nu)}{\partial x}\left[\frac{4}{3}\frac{\partial^2\hat{u}}{\partial x\partial\mu} - \frac{4}{3}\frac{1}{x}\frac{\partial\hat{u}}{\partial\mu} + \frac{2}{3}\frac{1}{x}\frac{\partial 2\hat{v}}{\partial\mu^2}\right]\ .\end{aligned} \tag{F.102}$$

Then, other two big terms for the viscous torque expression will be derived by using the following relationships:

$$\begin{aligned}\frac{\partial}{\partial x}(x^2\Pi_{r\theta}) &= \\ &\frac{\Omega_{eq}\bar{\rho}\nu}{R_\odot^2}\left[\frac{x}{\sqrt{1-\mu^2}}\frac{\partial\hat{W}}{\partial x}-\frac{1}{\sqrt{1-\mu^2}}\hat{W}-2x\sqrt{1-\mu^2}\frac{\partial^2\hat{u}}{\partial x\partial\mu}\right] \\ &+\frac{\Omega_{eq}}{R_\odot^2}\frac{\partial(\bar{\rho}\nu)}{\partial x}\left[\frac{x}{\sqrt{1-\mu^2}}\hat{W}-2x\sqrt{1-\mu^2}\frac{\hat{u}}{\partial\mu}-\frac{2x}{\sqrt{1-\mu^2}}\hat{v}\right]\end{aligned} \tag{F.103}$$

$$\begin{aligned}\frac{\partial}{\partial\mu}(\sqrt{1-\mu^2}\Pi_{\theta\theta}) &= \\ &\frac{\Omega_{eq}\bar{\rho}\nu}{R_\odot^2}\left[-\frac{2}{3}\sqrt{1-\mu^2}\frac{\partial^2\hat{u}}{\partial x\partial\mu}+\frac{2}{3}\frac{\mu}{\sqrt{1-\mu^2}}\frac{\partial\hat{u}}{\partial x}\right. \\ &+\frac{2}{3}\frac{\sqrt{1-\mu^2}}{x}\frac{\partial\hat{u}}{\partial\mu}-\frac{2}{3}\frac{\mu}{x\sqrt{1-\mu^2}}\hat{u} \\ &\left.-\frac{4}{3}\frac{\sqrt{1-\mu^2}}{x}\frac{\partial^2\hat{v}}{\partial\mu^2}-\frac{2}{3}\frac{\mu}{x\sqrt{1-\mu^2}}\frac{\partial\hat{v}}{\partial\mu}-\frac{2}{x(1-\mu^2)^{3/2}}\hat{v}\right]\ ,\end{aligned} \tag{F.104}$$

which turn out to be:

$$
\begin{aligned}
(\nabla\cdot\mathbf{\Pi})_\theta \quad = \quad & \\
& \frac{\Omega_{eq}\bar{\rho}\nu}{R_\odot^2}\left[\frac{1}{x\sqrt{1-\mu^2}}\frac{\partial\hat{W}}{\partial x}-\frac{4}{3}\frac{\sqrt{1-\mu^2}}{x}\frac{\partial^2\hat{u}}{\partial x\partial\mu}\right. \\
& \left.-\frac{8}{3}\frac{\sqrt{1-\mu^2}}{x^2}\frac{\partial\hat{u}}{\partial\mu}+\frac{4}{3}\frac{\sqrt{1-\mu^2}}{x^2}\frac{\partial^2\hat{v}}{\partial\mu^2}\right] \\
& +\frac{\Omega_{eq}}{R_\odot^2}\frac{\partial(\bar{\rho}\nu)}{\partial x}\left[\frac{1}{x\sqrt{1-\mu^2}}\hat{W}-\frac{2\sqrt{1-\mu^2}}{x}\frac{\hat{u}}{\partial\mu}-\frac{2}{x\sqrt{1-\mu^2}}\hat{v}\right] \\
\frac{\partial}{\partial x}(\nabla\cdot\mathbf{\Pi})_\theta \quad = \quad & \\
& \frac{\Omega_{eq}\bar{\rho}\nu}{R_\odot^2}\left[\frac{1}{x\sqrt{1-\mu^2}}\frac{\partial^2\hat{W}}{\partial x^2}-\frac{1}{x^2\sqrt{1-\mu^2}}\frac{\partial\hat{W}}{\partial x}-\frac{4}{3}\frac{\sqrt{1-\mu^2}}{x}\frac{\partial^3\hat{u}}{\partial x^2\partial\mu}\right. \\
& -\frac{4}{3}\frac{\sqrt{1-\mu^2}}{x^2}\frac{\partial^2\hat{u}}{\partial x\partial\mu} \\
& \left.+\frac{16}{3}\frac{\sqrt{1-\mu^2}}{x^3}\frac{\partial\hat{u}}{\partial\mu}+\frac{4}{3}\frac{\sqrt{1-\mu^2}}{x^2}\frac{\partial^3\hat{v}}{\partial x\partial\mu^2}-\frac{8}{3}\frac{\sqrt{1-\mu^2}}{x^3}\frac{\partial^2\hat{v}}{\partial\mu^2}\right] \\
& +\frac{\Omega_{eq}}{R_\odot^2}\frac{\partial(\bar{\rho}\nu)}{\partial x}\left[\frac{2}{x\sqrt{1-\mu^2}}\frac{\partial\hat{W}}{\partial x}-\frac{3}{x^2\sqrt{1-\mu^2}}\hat{W}\right. \\
& -\frac{10}{3}\frac{\sqrt{1-\mu^2}}{x}\frac{\partial^2\hat{u}}{\partial x\partial\mu}-\frac{4}{3}\frac{\sqrt{1-\mu^2}}{x^2}\frac{\partial\hat{u}}{\partial\mu} \\
& \left.+\frac{4}{3}\frac{\sqrt{1-\mu^2}}{x^2}\frac{\partial^2\hat{v}}{\partial\mu^2}+\frac{4}{x^2\sqrt{1-\mu^2}}\hat{v}\right] \\
& +\frac{\Omega_{eq}}{R_\odot^2}\frac{\partial^2(\bar{\rho}\nu)}{\partial x^2}\left[\frac{1}{x\sqrt{1-\mu^2}}\hat{W}-\frac{2\sqrt{1-\mu^2}}{x}\frac{\partial\hat{u}}{\partial\mu}-\frac{2}{x\sqrt{1-\mu^2}}\hat{v}\right] \quad . \quad \text{(F.105)}
\end{aligned}
$$

Finally, we obtain the expression for the viscous stresses as follows:

$$\frac{x\sqrt{1-\mu^2}}{\Omega_{eq}^2}\left[\nabla\times\left(\frac{\nabla\cdot\mathbf{\Pi}}{\bar{\rho}}\right)\right]_\phi = \\ E_\nu\left[\frac{\partial^2\hat{W}}{\partial x^2}+\frac{(1-\mu^2)}{x^2}\frac{\partial^2\hat{W}}{\partial\mu^2}\right] \\ +\frac{\partial E_\nu}{\partial x}\left[2\frac{\partial\hat{W}}{\partial x}-\frac{2}{x}\hat{W}+\frac{2(1-\mu^2)}{x}\frac{\partial\hat{u}}{\partial\mu}+\frac{2}{x}\hat{v}\right] \\ \frac{E_\nu}{\bar{\rho}}\frac{\partial\bar{\rho}}{\partial x}\left[\frac{\partial\hat{W}}{\partial x}-\frac{2}{x}\hat{W}+\frac{2(1-\mu^2)}{x}\frac{\partial\hat{u}}{\partial\mu}+\frac{2}{x}\hat{v}\right] \\ +\left(\frac{\partial^2E_\nu}{\partial x^2}+\frac{E_\nu}{\bar{\rho}}\frac{\partial^2\bar{\rho}}{\partial x^2}\right)\left[\hat{W}-2(1-\mu^2)\frac{\partial\hat{u}}{\partial\mu}-2\hat{v}\right] \\ +\frac{1}{\bar{\rho}}\frac{\partial\bar{\rho}}{\partial x}\frac{\partial E_\nu}{\partial x}\left[\hat{W}-2\hat{v}\right] \\ +\frac{E_\nu}{\bar{\rho}^2}\left(\frac{\partial\bar{\rho}}{\partial x}\right)^2\left[-\hat{W}+\frac{8}{3}(1-\mu^2)\frac{\partial\hat{u}}{\partial\mu}+2\hat{v}\right]\ , \tag{F.106}$$

which we rewrite as:

$$\frac{x\sqrt{1-\mu^2}}{\Omega_{eq}^2}\left[\nabla\times\left(\frac{\nabla\cdot\mathbf{\Pi}}{\bar{\rho}}\right)\right]_\phi = \\ E_\nu\left[\frac{\partial^2\hat{W}}{\partial x^2}+\frac{(1-\mu^2)}{x^2}\frac{\partial^2\hat{W}}{\partial\mu^2}\right] \\ +2\frac{\partial E_\nu}{\partial x}\left[\frac{\partial\hat{W}}{\partial x}-\frac{\partial\hat{v}}{\partial x}\right]+\frac{E_\nu}{\bar{\rho}}\frac{\partial\bar{\rho}}{\partial x}\left[\frac{\partial\hat{W}}{\partial x}-2\frac{\partial\hat{v}}{\partial x}\right] \\ +\left(\frac{\partial^2E_\nu}{\partial x^2}-\frac{E_\nu}{\bar{\rho}^2}\left(\frac{\partial\bar{\rho}}{\partial x}\right)^2+\frac{E_\nu}{\bar{\rho}}\frac{\partial^2\bar{\rho}}{\partial x^2}\right) \\ \cdot\left[\hat{W}-2(1-\mu^2)\frac{\partial\hat{u}}{\partial\mu}-2\hat{v}\right] \\ +\frac{1}{\bar{\rho}}\frac{\partial\bar{\rho}}{\partial x}\frac{\partial E_\nu}{\partial x}\left[\hat{W}-2\hat{v}\right] \\ +\frac{2}{3}\frac{E_\nu}{\bar{\rho}^2}\left(\frac{\partial\bar{\rho}}{\partial x}\right)^2(1-\mu^2)\frac{\partial\hat{u}}{\partial\mu}\ . \tag{F.107}$$

F.2.7 High order derivatives of expressions involving $T_{2n-1}(\mu)$

Here, we have compiled the expressions needed to implement the IDL code to generate plots of each term in the vorticity equation. In the code listing included in the appendix, some derivatives are expressed in two or more ways depending on whether we used the Chebishev differential equation to simplify algebraic computations. Also, by writing some derivatives in more than one way, we were able to verify the accuracy of our computations.

We start by using the Chebyshev differential equation to reduce higher order derivatives of $T_{2n-1}(\mu)$, which show up when deriving high order derivatives of $\hat{u}$:

$$\hat{u}(x,\mu) = \sum_{n=1}^{N} \psi_n \frac{\partial}{\partial \mu}\left[(1-\mu^2)T_{2n-1}(\mu)\right] \tag{F.108}$$

$$\begin{aligned}\frac{\partial \hat{u}}{\partial \mu}(x,\mu) &= \sum_{n=1}^{N} \psi_n \frac{\partial^2}{\partial \mu^2}\left[(1-\mu^2)T_{2n-1}(\mu)\right] \\ &= \sum_{n=1}^{N} \psi_n \left[(1-\mu^2)\frac{\partial^2 T_{2n-1}(\mu)}{\partial \mu^2} - 4\mu\frac{\partial T_{2n-1}(\mu)}{\partial \mu} - 2T_{2n-1}(\mu)\right] ,\end{aligned} \tag{F.109}$$

from which we can obtain:

$$\frac{\partial \hat{u}}{\partial \mu}(x,\mu) = \sum_{n=1}^{N} \psi_n \left[-3\mu\frac{\partial T_{2n-1}(\mu)}{\partial \mu} - [2+(2n-1)^2]T_{2n-1}(\mu)\right] \tag{F.110}$$

$$\begin{aligned}\frac{\partial^2 \hat{u}}{\partial \mu^2}(x,\mu) &= \sum_{n=1}^{N} \psi_n \left\{-\left[\frac{3\mu^2}{1-\mu^2} + 5 + (2n-1)^2\right]\frac{\partial T_{2n-1}(\mu)}{\partial \mu}\right. \\ &\quad \left. + \frac{3\mu}{1-\mu^2}(2n-1)^2 T_{2n-1}(\mu)\right\}\end{aligned} \tag{F.111}$$

$$\begin{aligned}\frac{\partial^3 \hat{u}}{\partial \mu^3}(x,\mu) &= \sum_{n=1}^{N} \psi_n \left\{-\left[\frac{9\mu^3}{(1-\mu^2)^2} + \frac{11\mu - 2\mu(2n-1)^2}{1-\mu^2}\right]\frac{\partial T_{2n-1}(\mu)}{\partial \mu}\right. \\ &\quad \left. + \left[\frac{9\mu^2}{(1-\mu^2)^2} + \frac{8+(2n-1)^2}{1-\mu^2}\right](2n-1)^2 T_{2n-1}(\mu)\right\} .\end{aligned} \tag{F.112}$$

We use these expressions to compute the vorticity and its derivatives:

$$\frac{\partial \hat{v}}{\partial x}(x,\mu) = \sum_{n=1}^{N} dv_n(x)(1-\mu^2)T_{2n-1}(\mu) \tag{F.113}$$

$$\frac{\partial \hat{v}}{\partial \mu}(x,\mu) = \sum_{n=1}^{N} v_n(x)\left[(1-\mu^2)\frac{\partial T_{2n-1}(\mu)}{\partial \mu} - 2\mu T_{2n-1}(\mu)\right] \tag{F.114}$$

$$\frac{\partial^2 \hat{v}}{\partial \mu^2}(x,\mu) = \sum_{n=1}^{N} v_n\left[-3\mu\frac{\partial T_{2n-1}(\mu)}{\partial \mu} - [2+(2n-1)^2]T_{2n-1}(\mu)\right] \tag{F.115}$$

$$\frac{\partial^3 \hat{v}}{\partial x \partial \mu^2}(x,\mu) = \sum_{n=1}^{N} dv_n\left[-3\mu\frac{\partial T_{2n-1}(\mu)}{\partial \mu} - [2+(2n-1)^2]T_{2n-1}(\mu)\right] \tag{F.116}$$

$$\hat{W}(x,\mu) = (1-\mu^2)\frac{\partial \hat{u}}{\partial \mu} + x\frac{\partial \hat{v}}{\partial x} + \hat{v} \tag{F.117}$$

$$\frac{\partial \hat{W}}{\partial x}(x,\mu) = (1-\mu^2)\frac{\partial^2 \hat{u}}{\partial x \partial \mu} + x\frac{\partial^2 \hat{v}}{\partial x^2} + 2\frac{\partial \hat{v}}{\partial x} \tag{F.118}$$

$$\frac{\partial^2 \hat{W}}{\partial \mu^2}(x,\mu) = (1-\mu^2)\frac{\partial^3 \hat{u}}{\partial \mu^3} - 4\mu\frac{\partial^2 \hat{u}}{\partial \mu^2} - 2\frac{\partial \hat{u}}{\partial \mu} + x\frac{\partial^3 \hat{v}}{\partial x \partial \mu^2} + \frac{\partial^2 \hat{v}}{\partial \mu^2}\ . \tag{F.119}$$

The rest of the expressions we need are:

$$\hat{T}(x,\mu) = \sum_{n=1}^{N} \Theta_n(x) T_{2n-2}(\mu) \tag{F.120}$$

$$\frac{\partial \hat{T}}{\partial \mu}(x,\mu) = \sum_{n=1}^{N} \Theta_n(x) \frac{n-1}{1-\mu^2} [T_{2n-3}(\mu) - T_{2n-1}(\mu)] \tag{F.121}$$

$$\hat{\rho}(x,\mu) = \sum_{n=1}^{N} \rho_n(x) T_{2n-2}(\mu) \tag{F.122}$$

$$\frac{\partial \hat{\rho}}{\partial \mu}(x,\mu) = \sum_{n=1}^{N} \rho_n(x) \frac{n-1}{1-\mu^2} [T_{2n-3}(\mu) - T_{2n-1}(\mu)] \tag{F.123}$$

$$\hat{J}(x,\mu) = \sum_{n=1}^{N} J_n(x)(1-\mu^2) T_{2n-2}(\mu) \tag{F.124}$$

$$\hat{J}(x,\mu) = (1-\mu^2)\frac{\partial \hat{B}}{\partial \mu} + x\frac{\partial \hat{b}}{\partial x} + \hat{b} \tag{F.125}$$

$$\begin{aligned}
\frac{\partial^2 \hat{L}(x,\mu)}{\partial x^2} &= (1-\mu^2) \sum_{n=1}^{N} \left(\frac{dL_n[i+1] - dL_n[i]}{x[i+1] - x[i]} \right) T_{2n-2}(\mu) \\
&= (1-\mu^2) \sum_{m=0}^{N-1} \left(\frac{dL_m[i+1] - dL_m[i]}{x[i+1] - x[i]} \right) T_{2m}(\mu) \\
\frac{\partial^2 \hat{L}(x,\mu)}{\partial \mu^2} &= \sum_{n=1}^{N} L_n(x) \left[(1-\mu^2) \frac{\partial^2 T_{2n-2}(\mu)}{\partial \mu^2} - 4\mu \frac{\partial T_{2n-2}(\mu)}{\partial \mu} - 2T_{2n-2}(\mu) \right] \\
&= \sum_{m=0}^{N-1} L_m(x) \left[(1-\mu^2) \frac{\partial^2 T_{2m}(\mu)}{\partial \mu^2} - 4\mu \frac{\partial T_{2m}(\mu)}{\partial \mu} - 2T_{2m}(\mu) \right]
\end{aligned} \tag{F.126}$$

Some identities for Chebyshev polynomials are included in Appendix C.

Appendix G

NRK_ParaSol: The User's Guide

G.1 Description of the package

NRK_ParaSol is a parallel implementation of the commonly-used Newton-Raphson-Kantorovich (NRK) algorithm ((Garaud and Garaud , 2008),(Press et al. , 2007)) originally developed by Gough & Moore, which solves systems of I first order, nonlinear, coupled, ordinary differential equations (ODEs) in the two-point boundary value problem expressed as

$$\sum_{j=1}^{I} M_{ij}(x,\mathbf{y})\frac{\mathrm{d}y_j}{\mathrm{d}x} = f_i(x,\mathbf{y}) \text{ , where } i = \{1,2,\ldots I\} \text{ ,} \tag{G.1}$$

with boundary conditions

$$\begin{aligned} g_k(x_A,\mathbf{y}) &= 0 \text{ , where } k = \{1,2,\ldots k_A\} \text{ ,} \\ g_k(x_B,\mathbf{y}) &= 0 \text{ , where } k = \{k_A+1,\ldots I\} \text{ ,} \end{aligned} \tag{G.2}$$

for the vector of dependent variables $\mathbf{y} = \{y_1(x), y_2(x), \ldots y_I(x)\}$ on a discretized interval $[x_A, x_B] = \{x_1, x_2, \ldots x_N\}$. Here, $x_A = x_1$ and $x_B = x_N$, k_A is the number of conditions set at the boundary located at x_A, whereas $k_B = I - k_A$ is the number of conditions set at the boundary located at x_B. The code implementation requires that (1) the mesh be either mono-

tonically increasing or monotonically decreasing, and (2) the number of boundary conditions at the first meshpoint be greater than or equal to that at the second meshpoint[1]: $k_A \geq k_B$. Note that this version of the algorithm is second-order accurate in the spatial discretization.

G.1.1 Installation

To install the package, untar the file `NRK_ParaSol.tar`. This creates a directory structure with seven directories: five of them containing the examples provided in this guide, a `/templates` directory, and the directory `/docs` with the documentation.

Each example contains the software organized in two folders: `/src` and `/workdir`.

- The folder `/src` contains the subroutines organized in two sub-folders: the solver routines `/src_solver_routines`, which should not be modified, and the user routines `/src_user_routines`, which can be tailored at will.

- The folder `/workdir` contains the initialization `.h` file, and a sample `Makefile` and `PBS` file. This folder also contains all the output files organized in various directories (see below).

The directory `/templates` is organized in the same way as the example directories, but the subroutines in `/src_user_routines` should be completed by the user as explained in Section 1.3.

G.1.2 Directory `Workdir`

The directory `/workdir` is where the code is executed. It contains both input and output files and directories as described below. The `Makefile` provided is generic and should be modified to include the user's version of Fortran (`FORTRAN`). A `pp.pbs` file is provided if necessary (for users on the Pleiades supercomputer at Santa Cruz for example), though the code can be

[1] Note that if $k_B > k_A$, the user simply needs to reverse the mesh.

run directly using the standard `mpirun` command. Note that the user should verify that the number of processors used in the `mpirun` command matches that of the `init_simu.h` file.

G.1.2.1 Input files

The main input parameters are entered into the `init_simu.h` file:

- `ii`, the number of ordinary differential equations,
- `ka`, the number of conditions at the boundary x_A,
- `kb`, the number of conditions at the boundary x_B,
- `linearlhs`, an optimization flag which is set to 1 if the coefficients of the left-hand-side matrix M_{ij} are all independent of **y**.
- `nn`, the number of meshpoints,
- `xa`, the coordinate of the first boundary,
- `xb`, the coordinate of the second boundary,
- `nprev`, an indicator for the use of previous results as initial guess,
- `niter`, the maximum number of iterations to be attempted, and
- `nproc`, the number of processors.

The file `init_simu.h` can be modified to include any user-defined parameter if needed (see Example 4). All other input files/data should be stored for clarity in the directory `/workdir/inputfiles`.

G.1.2.2 Output files

The output files are organized in the following folders:

- `/guessd`: The NRK solver saves the initial guess in this folder.
- `/tempor`: The NRK solver saves the solution at each iteration in this folder.
- `/result`: The NRK solver saves the results in this folder once the accuracy criterion is satisfied.
- `/diagnosticfiles`: Solution errors are written in the file `ea.dat` included in this folder. The file `ea.dat` reports both the average error and the maximum error for each element of the computed vector $\mathbf{y}$.

G.1.3 User-defined subroutines

The directory `/src/src_user_routines` contains all user-modified routines. The driver routine is the `main.f`. Subroutines describing the ODEs and boundary conditions of the problem to be solved are `lhs.f`, `rhs.f`, and `bc.f`, respectively. In addition, the user should modify `mesh.f` where the mesh is created, `guess.f` where a guess is generated and `printresult.f` where results are printed to files.

- `main.f`: Driver routine.
- `rhs.f`: The user inputs the right hand side of equation (G.1), represented by the vector $\mathbf{f}$, into the array `f(i)`. The non-zero elements of the Jacobian, $\partial f_i/\partial y_j$, are input into the array `fd`(i, j). See examples for detail.
- `lhs.f`: The user inputs the non-zero elements of the matrix $\mathbf{M}$ corresponding to the left-hand-side of equation (G.1) through the function `am`(i, j). Likewise, the non-zero elements

of the left-hand-side Jacobian $\partial M_{ij}/\partial y_k$ are input through the function `amd`(i, j, k). See examples for detail.

- `bc.f`: The user inputs the boundary conditions, defined by the vector **g**, into the array `g(i)`. The user also inputs the non-zero elements of the Jacobian $\partial g_i/\partial y_j$ into the array `gs`(i, j). Finally, a permutation vector **v** is also defined in this subroutine to renumber the dependent variables to prevent formation of singular matrices. See Example 2b for detail.

- `mesh.f`: The user defines an array of meshpoints. A default file creating a linearly-spaced mesh is provided.

- `guess.f`: The user provides a trial solution either by writing a mathematical function, or by reading external files. A default file creating a constant initial guess is provided.

- `printresult.f`: The user specifies in this subroutine how the vector solution **y** is printed to files. A default file for printing is provided.

Some examples follow illustrating how to apply `NRK_ParaSol` under different circumstances.

G.2 Examples

G.2.1 Example 1

Let us consider first the following differential equation

$$\frac{\mathrm{d}^2 y}{\mathrm{d}x^2} + \frac{\mathrm{d}y}{\mathrm{d}x} - 2y = e^x \tag{G.3}$$

on the interval $(0, 1)$, under the following boundary conditions

$$\begin{aligned} y(0) &= 1\ , \\ y(1) &= 0\ . \end{aligned} \tag{G.4}$$

This second-order equation can be rewritten as two first-order equations, hence $I = 2$. We define the parameters for this case in the file `init_simu.h` as follows:

```
c Initialization file for the specific simulations

c Initialization of parameters specific to the system of ODEs to solve
      integer ii,ka,kb
      parameter(ii = 2)  ! Number of equations
      parameter(ka = 1)  ! Number of boundary conditions at first meshpoint
      parameter(kb = 1)  ! Number of boundary conditions at second meshpoint
      integer linearlhs
      parameter(linearlhs=1) !If the lhs is linear then 1, otherwise 0

c Initialization of parameters specific to the mesh used
      integer nn
      parameter(nn = 1000)     !number of meshpoints
      double precision xa,xb  ! First and last meshpoint
      parameter(xa=0.d0)
      parameter(xb=1.d0)

c Initialization of relaxation parameters
      integer nprev
      parameter(nprev = 0)      !use previous guess (1) or not (0)
      double precision ucy,acy
      parameter(ucy = 1.d0)     ! convergence speed (must be le 1.0)
      parameter(acy = 1.d-16)   ! accuracy required
      integer niter
      parameter(niter = 10)     ! number of iterations to try.

c Initialization of quantities specific to the parallel implementaion
      integer nproc,nbppmax
c Number of processors :
      parameter(nproc=4)
c Maximum number of blocks per processor
      parameter(nbppmax = (nn+1)/nproc +1 )
```

Note that this input file also specifies the number of processors to be 4.

G.2.1.1 Case 1a

By defining

$$\begin{aligned} y_1 &= y \,, \\ y_2 &= \frac{\mathrm{d}y}{\mathrm{d}x} \,, \end{aligned} \tag{G.5}$$

we can rewrite equation (G.3) in the following way

$$\frac{\mathrm{d}}{\mathrm{d}x}\begin{pmatrix} y_1 \\ \\ y_2 \end{pmatrix} = \begin{pmatrix} y_2 \\ \\ 2y_1 - y_2 + e^x \end{pmatrix} , \tag{G.6}$$

from which we can obtain the expressions for the RHS functions:

$$\begin{aligned} f_1 &= y_2 , \\ f_2 &= 2y_1 - y_2 + e^x . \end{aligned} \tag{G.7}$$

The Jacobian matrix is

$$\begin{pmatrix} \frac{\partial f_1}{\partial y_1} = 0 & \frac{\partial f_1}{\partial y_2} = 1 \\ \\ \frac{\partial f_2}{\partial y_1} = 2 & \frac{\partial f_2}{\partial y_2} = -1 \end{pmatrix} ,$$

for which only the non-zero terms need to be entered. Hence, the core part of the subroutine `rhs.f` is written as

```
f(1) = y(2)
fd(1,2) = 1.d0

f(2) = 2.d0*y(1)-y(2)+dexp(x)
fd(2,1) = 2.d0
fd(2,2) = -1.d0
```

The corresponding boundary conditions can be expressed within the subroutine `bc.f` as

$$\begin{aligned} g_1 &= y(x_A) - 1 = y_1(x_A) - 1 , \\ g_2 &= y(x_B) - 0 = y_1(x_B) - 0 . \end{aligned} \tag{G.8}$$

We define $y_1(x_A)$ as `ya(1)` and $y_2(x_A)$ as `ya(2)`. Similarly, $y_1(x_B)$ is `yb(1)` and $y_2(x_B)$ is `yb(2)`. Hence, these functions along with their corresponding derivatives are coded in the subroutine `bc.f` as

```
g(1) = ya(1)-1.d0
gs(1,1) = 1.d0

g(2) = yb(1)
gs(2,1) = 1.d0
```

In a similar fashion, the subroutine `lhs.f` contains the expressions for M_{ij} and $\partial M_{ij}/\partial y_k$. By contrast with `rhs.f` and `bc.f` these quantities are returned through function calls, M_{ij} in `am` and $\partial M_{ij}/\partial y_k$ in `amd`. This is done to ease the memory requirement for very large systems of ODEs. In this example, the M_{ij} matrix is unity. This can be input as:

```
am=0.d0
if(i.eq.j) am=1.d0
```

in the `am` function. The `amd` function needs not to be entered if M_{ij} is independent of $\mathbf{y}$ (i.e. if `linearlhs = 1`).

All the corresponding subroutines adapted for this example are included in the directory `/example1a/src/src_user_routines`.

G.2.1.2 Case 1b

Alternatively, we can express equation (G.3) as

$$\begin{pmatrix} 1 & 0 \\ 1 & 1 \end{pmatrix} \frac{\mathrm{d}}{\mathrm{d}x} \begin{pmatrix} y_1 \\ y_2 \end{pmatrix} = \begin{pmatrix} y_2 \\ 2y_1 + e^x \end{pmatrix} , \tag{G.9}$$

from which we can obtain the expressions for the subroutines `rhs.f`, `bc.f`, and `lhs.f` to be slightly different. In the case of `lhs.f`, for example, the nonzero elements of the matrix $\mathbf{M}$ are now input as

```
am=0.d0
if(i.eq.j) am=1.d0
if(i.eq.2 .and. j.eq.1) am=1.d0
```

The user may compare the subroutines `rhs.f`, `bc.f`, and `lhs.f` in the directory `/example1b/src/src_user_routines`

with the corresponding subroutines at

`/example1a/src/src_user_routines`.

G.2.1.3 Result comparison

When the code for this example is executed, the exact solution is written along with the numerical one in the file `Y001.dat` both in the directory

`/example1a/workdir/result`

and

`/example1b/workdir/result`.

G.2.2 Example 2

NRK can also be used to find solutions to eigenvalue problems. Let us consider now the following eigenvalue differential equation

$$\frac{\mathrm{d}^2 y}{\mathrm{d}x^2} + \omega^2 y = 0 \tag{G.10}$$

on the interval $(0, 1)$, under the following boundary conditions

$$\begin{aligned} y(0) &= 0 \,, \\ y(1) &= 0 \,, \\ \frac{\mathrm{d}y}{\mathrm{d}x}(0) &= 1 \,. \end{aligned} \tag{G.11}$$

G.2.2.1 Case 2a

By defining

$$\begin{aligned} y_1 &= y \,, \\ y_2 &= \frac{\mathrm{d}y}{\mathrm{d}x} \,, \\ y_3 &= \omega \,, \end{aligned} \tag{G.12}$$

we can rewrite equation (G.10) in the following way

$$\frac{\mathrm{d}}{\mathrm{d}x}\begin{pmatrix} y_1 \\ y_2 \\ y_3 \end{pmatrix} = \begin{pmatrix} y_2 \\ -y_3^2 y_1 \\ 0 \end{pmatrix} \tag{G.13}$$

from which we can obtain the expressions for the subroutine `rhs.f`:

$$\begin{aligned} f_1 &= y_2 \ , \\ f_2 &= -y_3^2 y_1 \ , \\ f_3 &= 0 \ . \end{aligned} \tag{G.14}$$

Hence, the core part of the subroutine `rhs.f` is written as

```
f(1) = y(2)
fd(1,2) = 1.d0

f(2) = -y(3)**2*y(1)
fd(2,1) = -y(3)**2
fd(2,3) = -2*y(3)*y(1)

f(3) = 0.d0
```

Likewise, the corresponding boundary conditions can be expressed within the subroutine `bc.f` as

$$\begin{aligned} g_1 &= y(x_A) - 0 = y_1(x_A) = y_A(1) \ , \\ g_2 &= \frac{\mathrm{d}y}{\mathrm{d}x}(x_A) - 1 = y_2(x_A) - 1 = y_A(2) - 1 \ , \\ g_3 &= y(x_B) - 0 = y_1(x_B) = y_B(1) \ . \end{aligned} \tag{G.15}$$

These functions along with their corresponding derivatives are coded in the subroutine `bc.f` as

```
g(1) = ya(1)
gs(1,1) = 1.d0

g(2) = ya(2) - 1.d0
gs(2,2) = 1.d0
```

```
g(3) = yb(1)
gs(3,1) = 1.d0
```

Finally, the subroutine `lhs.f` contains the expressions for M_{ij} and $\partial M_{ij}/\partial y_j$, which reduce to `am=1` for the elements on the diagonal of the matrix $\mathbf{M}$. As in Example 1, `amd` needs not to be entered if the problem in `lhs.f` is linear.

Note that since this is an eigenvalue problem, we expect a number of solutions. Typically, different solutions are found starting from different initial guesses. The user can modify the subroutine `guess.f` to find solutions corresponding to different eigenvalues. We change the default values in `guess.f` to solve case 2b to obtain a specific eigenvalue solution. For example, if y_3 is set to 7 for all $x(i)$ in `guess.f`, then we get the eigenvalue y_3 closest to 7 and its corresponding solution y_1.

G.2.2.2 Case 2b

This example illustrates the use of the permutation vector. By defining

$$\begin{aligned} y_1 &= \omega \ , \\ y_2 &= y \ , \\ y_3 &= \frac{\mathrm{d}y}{\mathrm{d}x} \ , \end{aligned} \tag{G.16}$$

we can rewrite equation (G.10) in the following way

$$\frac{\mathrm{d}}{\mathrm{d}x}\begin{pmatrix} y_1 \\ y_2 \\ y_3 \end{pmatrix} = \begin{pmatrix} 0 \\ y_3 \\ -y_1^2 y_2 \end{pmatrix} \tag{G.17}$$

from which we can obtain the expressions for the subroutine `rhs.f`:

$$\begin{aligned} f_1 &= 0 \,, \\ f_2 &= y_3 \,, \\ f_3 &= -y_1^2 y_2 \,. \end{aligned} \tag{G.18}$$

Hence, the core part of the subroutine `rhs.f` is finally written as

```
f(2) = y(3)
fd(2,3) = 1.d0

f(3) = -y(1)**2*y(2)
fd(3,2) = -y(1)**2
fd(3,1) = -2*y(1)*y(2)

f(1) = 0.d0
```

Similarly the boundary conditions are now

```
g(1) = ya(2)
gs(1,2) = 1.d0

g(2) = ya(3) - 1.d0
gs(2,3) = 1.d0

g(3) = yb(2)
gs(3,2) = 1.d0
```

Note that in this case, the Jacobian matrix `gs` becomes

$$\mathtt{gs}(I,I) = \left(\begin{array}{cc|c} \mathbf{0} & \mathbf{1} & 0 \\ \mathbf{0} & \mathbf{0} & 1 \\ \hline 0 & 1 & 0 \end{array}\right) \tag{G.19}$$

We then see that the submatrix associated with the boundary conditions at x_A, namely

$$\mathtt{gs}(k_A,k_A) = \left(\begin{array}{cc} \mathbf{0} & \mathbf{1} \\ \mathbf{0} & \mathbf{0} \end{array}\right) \tag{G.20}$$

is singular. The matrix `gs(`k_A, k_A`)` must be non-singular for this parallel algorithm to work. Hence, we create a permutation of the columns of `gs(`I, I`)` (which is equivalent to renumbering the dependent variables) to make the new `gs(`k_A, k_A`)` non-singular:

$$\begin{pmatrix} \mathbf{0} & \mathbf{1} & 0 \\ \mathbf{0} & \mathbf{0} & 1 \\ 0 & 1 & 0 \end{pmatrix} \xrightarrow{v^T=[2,3,1]} \begin{pmatrix} \mathbf{1} & 0 & \mathbf{0} \\ \mathbf{0} & 1 & \mathbf{0} \\ 1 & 0 & 0 \end{pmatrix}, \tag{G.21}$$

where `v(I)` is the permutation vector, whose subroutine is in the last part of the file `bc.f`:

```
      subroutine pervector(v)

c ***********************************************************************
c Subroutine where the permutation vector for the boundary condition
c functions is input
c ***********************************************************************

      implicit none
      include 'init_simu.h'

      integer v
      dimension v(ii)

      integer i

      v(1) = 2
      v(2) = 3
      v(3) = 1

      return
      end
```

Finally, the subroutine `lhs.f` contains the expressions for M_{ij} and $\partial M_{ij}/\partial y_j$, which reduce to `am=1` for the elements on the diagonal of the matrix $\mathbf{M}$.

G.2.3 Example 3

Let us consider now the Chebishev differential equation ((Rivlin , 1974)):

$$(1-x^2)\frac{\mathrm{d}^2y}{\mathrm{d}x^2} - x\frac{\mathrm{d}y}{\mathrm{d}x} + \omega^2 y = 0 \tag{G.22}$$

under the following boundary conditions

$$\begin{aligned} y(0) &= 0 \,, \\ y(1) &= 1 \,, \\ \frac{\mathrm{d}y}{\mathrm{d}x}(0) &= -3 \,. \end{aligned} \tag{G.23}$$

By defining

$$\begin{aligned} y_1 &= y \,, \\ y_2 &= \frac{\mathrm{d}y}{\mathrm{d}x} \,, \\ y_3 &= \omega \,, \end{aligned} \tag{G.24}$$

we can rewrite equation (G.22) in the following way

$$\begin{pmatrix} 1 & 0 & 0 \\ 0 & (1-x^2) & 0 \\ 0 & 0 & 1 \end{pmatrix} \frac{\mathrm{d}}{\mathrm{d}x} \begin{pmatrix} y_1 \\ y_2 \\ y_3 \end{pmatrix} = \begin{pmatrix} y_2 \\ xy_2 - y_3^2 y_1 \\ 0 \end{pmatrix} \,, \tag{G.25}$$

from which we can obtain the expressions for the subroutine `rhs.f`:

$$\begin{aligned} f_1 &= y_2 \,, \\ f_2 &= xy_2 - y_3^2 y_1 \,, \\ f_3 &= 0 \,. \end{aligned} \tag{G.26}$$

The core part of the subroutine `rhs.f` is

```
f(1) = y(2)
fd(1,2) = 1.d0

f(2) = x*y(2)-y(3)**2.d0*y(1)
fd(2,1) = -y(3)**2.d0
fd(2,2) = x
fd(2,3) = -2.d0*y(3)*y(1)

f(3) = 0.d0
```

Likewise, the corresponding boundary conditions can be expressed within the subroutine `bc.f` as

$$\begin{aligned} g_1 &= y(x_A) - 0 = y_1(x_A) = y_A(1) \ , \\ g_2 &= \frac{\mathrm{d}y}{\mathrm{d}x}(x_A) + 3 = y_2(x_A) + 3 = y_A(2) + 3 \ , \\ g_3 &= y(x_B) - 1 = y_1(x_B) - 1 = y_B(1) - 1 \ . \end{aligned} \tag{G.27}$$

These functions along with their corresponding derivatives are coded in the subroutine `bc.f` as

```
g(1) = ya(1)
gs(1,1) = 1.d0

g(2) = ya(2) + 3.d0
gs(2,2) = 1.d0

g(3) = yb(1) - 1.d0
gs(3,1) = 1.d0
```

As in previous examples, the subroutine `lhs.f` contains the expressions for M_{ij} and $\partial M_{ij}/\partial y_j$. This example requires setting $M_{2,2} = (1 - x^2)$. This is done as:

```
am=0.d0

if(i.eq.j) am=1.d0
if(i.eq.2 .and. j.eq.2) am=1.d0-x**2.d0
```

The exact solution is written along with the numerical one in the file `Y001.dat` in the directory `/example3/workdir/result`. The file `Y003.dat` in the same directory shows the eigenvalue numerically computed, and the eigenvalue which corresponds to the exact solution provided in the file `Y001.dat`.

G.2.4 Example 4

Let us consider now the van der Pol's differential equation ((Fogiel , 1996)):

$$\frac{\mathrm{d}^2 y}{\mathrm{d}x^2} - \epsilon(1-y^2)\frac{\mathrm{d}y}{\mathrm{d}x} + \frac{1}{4}u_0^2 y = 0 \tag{G.28}$$

under the following boundary conditions

$$\begin{aligned} y(0) &= 0 \ , \\ \frac{\mathrm{d}y}{\mathrm{d}x}(0) &= u_0 \ . \end{aligned} \tag{G.29}$$

In this example, the parameters u_0 and ϵ are entered in the `init_simu.h` file as

```
c Initialization of model-specific parameters
      double precision epsil,u0
      parameter(epsil=1.d-6)
      parameter(u0=1.d0)
```

By defining

$$\begin{aligned} y_1 &= y \ , \\ y_2 &= \frac{\mathrm{d}y}{\mathrm{d}x} \ , \end{aligned} \tag{G.30}$$

we can rewrite equation (G.28) in the following way

$$\begin{pmatrix} 1 & 0 \\ -\epsilon(1-y_1^2) & 1 \end{pmatrix} \frac{\mathrm{d}}{\mathrm{d}x} \begin{pmatrix} y_1 \\ y_2 \end{pmatrix} = \begin{pmatrix} y_2 \\ \frac{1}{4}u_0^2 y_1 \end{pmatrix} \ , \tag{G.31}$$

from which we can obtain the expressions for the subroutine `rhs.f`:

$$\begin{aligned} f_1 &= y_2 \ , \\ f_2 &= \frac{1}{4}u_0^2 y_1 \ . \end{aligned} \tag{G.32}$$

The core part of the subroutine `rhs.f` is

```
f(1) = y(2)
fd(1,2) = 1.d0

f(2) = 0.25d0*u0**2.d0*y(1)
fd(2,1) = 0.25d0*u0**2.d0
```

Likewise, the corresponding boundary conditions can be expressed within the subroutine `bc.f` as

$$\begin{aligned} g_1 &= y(x_A) - 0 = y_1(x_A) = y_A(1) \ , \\ g_2 &= \frac{\mathrm{d}y}{\mathrm{d}x}(x_A) - u_0 = y_2(x_A) - u_0 = y_A(2) - u_0 \ . \end{aligned} \tag{G.33}$$

These functions along with their corresponding derivatives are coded in the subroutine `bc.f` as

```
g(1) = ya(1)
gs(1,1) = 1.d0

g(2) = ya(2) - u0
gs(2,2) = 1.d0
```

The subroutine `lhs.f` contains the expressions for M_{ij} and $\partial M_{ij}/\partial y_j$. This example no longer has a linear left-hand-side. Indeed,

$$M_{2,1} = -\epsilon(1 - y_1^2) \ , \tag{G.34}$$

$$\frac{\partial M_{2,1}}{\partial y_1} = 2\epsilon y_1 \ , \tag{G.35}$$

As a result, we must set `linearlhs=0` in the file `/workdir/init_simu.h`. The LHS is then coded as

```
double precision function am(i,j,x,y,in)
implicit none
include 'init_simu.h'

integer i,j,in
double precision x,y
```

```
      dimension y(*)

      am=0.d0

      if(i.eq.j) am=1.d0
      if(i.eq.2 .and. j.eq.1) am=-epsil*(1.d0-y(j)**2)

      return
      end

c ************************************************************
      double precision function amd(i,j,l,x,y,in)
      implicit none
      include 'init_simu.h'

      integer i,j,l,in
      double precision x,y
      dimension y(*)

      amd=0.d0
      if(i.eq.2 .and. j.eq.1 .and. l.eq.1) amd=2.d0*epsil*y(j)

      return
      end
```

The first-order approximate solution (for $\epsilon \to 0$) is written along with the numerical one in the file `Y001.dat` in the directory `/example4/workdir/result`.